

Dynamics of active surfaces

DISSERTATION

zur Erlangung des akademischen Grades

Doctor rerum naturalium

vorgelegt

dem Bereich Mathematik und Naturwissenschaften
der Technischen Universität Dresden

von

Dipl.-Phys. Alexander Mietke
geboren am 18.06.1989 in Zittau



center for
systems biology
dresden



CBG
Max Planck Institute
of Molecular Cell Biology
and Genetics

Technische Universität Dresden
Max-Planck-Institut für Physik komplexer Systeme
Zentrum für Systembiologie Dresden
Max-Planck-Institut für molekulare Zellbiologie und Genetik

Dresden, 2018

Eingereicht am 31.08.2018

Verteidigt am 28.11.2018

Gutachter:

Prof. Dr. Frank Jülicher

Prof. Dr. Stephan W. Grill

Prof. Dr. Jaume Casademunt

Acknowledgements

First of all, I want to thank my supervisors Frank Jülicher and Ivo Sbalzarini. Ivo, I am grateful to you for ‘luring’ me into this PhD and leading me deep into the rabbit hole of computational methods. Frank, I am grateful to you for giving me the opportunity to work on this project and for your invaluable scientific support all along the way. I am greatly indebted for the opportunity you both gave me here in Dresden.

I thank all members of the Biological Physics group at the Max Planck Institute for the Physics of Complex Systems. Many people at the PKS have supported me during this PhD in different ways and I am deeply grateful for that. In random order, I want to thank Wolfram Pönisch for being the most entertaining office mate. I want to thank Anna Erzberger for introducing me to the topic of surface mechanics and for always taking time to answer my questions, while you actually had a thesis to write yourself. I want to thank Steffen Werner and Matthias Merkel for their extremely warm welcome when I joined the group. I want to thank David Oriola for many enlightening scientific discussions. I want to thank Johanna for always smiling and sharing her happiness. I thank Charlie, Johnathan, Suropriya and Izaak for carefully reading through this thesis.

I am equally thankful to all members of the MOSAIC group. In random order, I want to thank Sophie, Josefine, Yaser, Bevan, Pietro, Ulrik – you have been there from the beginning and supported me to get started and find my way. I am grateful to you all for making my PhD such an exciting endeavour. I also thank all the current members (with overlaps) for always providing a great atmosphere to work in.

I thank my collaborators Alicia Daeden and the Marcos González-Gaitán Lab for sharing their inspiring experimental work and for always being great hosts when I was visiting in Geneva. I want to thank Stefan, Teije and Lokesh for many interesting personal and scientific interactions and I also thank the whole Grill Lab for always welcoming me warmly during group meetings.

I want to thank Oliver Otto for being not only my supervisor for life, but also for being a fantastic friend. I am deeply thankful to my mother Kerstin and my Opa, as well as my sister Claudi and her husband Tino with Lukas, Leon, Niklas und Julian. I would have to thank you all every day for how much you always support me.

And saving the best for last: I want to thank my wonderful wife Amélie. Without your support, encouragement, patience and love this thesis would not have been possible.

Abstract

Mechano-chemical processes in biological systems play an important role during the morphogenesis of cells and tissues. In particular, they are responsible for the dynamic organisation of active stress, which itself results from non-equilibrium processes and leads to flows and deformations of material. The generation of active stress often occurs in thin biological structures, such as the cellular cortex or epithelial tissues, which motivates the theoretical concept of an active surface. In this thesis, we study the dynamics of curved and deforming active surfaces. More specifically, we are interested in the dynamics of mechano-chemical processes on these surfaces, as well as in their interaction with the surface shape and external forces.

To study the interplay of mechano-chemical processes with shape changes of the material, we consider the fully self-organised shape dynamics using the theory of active fluids on deforming surfaces. We then develop a numerical approach to solve the corresponding force and torque balance equations. We further examine how the stability of surface shapes is affected by mechano-chemical processes. We show that the tight coupling between chemical processes and surface mechanics gives rise to the spontaneous generation of specific surface shapes, to shape oscillations and to directed surface flows that resemble peristaltic motion.

In the following part, we explore the mechano-chemical self-organisation of active fluids on fixed surfaces, focussing on mechanical interactions with surrounding material. We introduce a description in which active surface flows set a surrounding passive fluid into motion. We then study two scenarios. First, inspired by the cellular cortex and its interactions with the cytoplasm, we consider a fluid that is enclosed by the surface. We find that mechanical interactions with the surrounding passive fluid enable an isotropic active surface to spontaneously generate patterns with polar asymmetry and to form a contractile ring in a fully self-organised fashion. Second, we consider the case where the passive fluid surrounds the active surface on the outside. This description leads to the model of a microswimmer, which is characterised by an onset of motion due to spontaneous symmetry breaking on the active surface.

Most biological materials are viscoelastic, such that they show viscous and elastic responses if mechanical stress is applied on different time scales. In the final part of this thesis, we therefore consider a surface whose response to self-organised active stress is described by a Maxwell model. We identify a minimal time scale for the relaxation of elastic stress, beyond which spatio-temporal, mechano-chemical oscillations on the surface can spontaneously emerge.

In summary, we identify and characterise in this thesis various processes that result from the self-organisation of active surfaces. The underlying coupling between surface mechanics and a chemical organisation of stress in the material represents a key feature of morphogenetic processes in biology. Furthermore, we develop several numerical approaches that will enable to study alternative constitutive relations of active surfaces in the future. Overall, we contribute theoretical insights and numerical tools to further the understanding of the emerging spatial organisation and shape generation of active surfaces.

Kurzzusammenfassung

Mechanochemische Prozesse spielen eine wichtige Rolle für die Morphogenese von biologischen Zellen und Geweben. Sie sind insbesondere verantwortlich für die dynamische Organisation von aktiver mechanischer Spannung, welche Nicht-Gleichgewichtsprozessen entstammt und zu Flüssen und Verformungen von Material führt. Aktive mechanische Spannung wird häufig in dünnen biologischen Strukturen erzeugt, wie zum Beispiel dem Zellkortex oder dem Epithelgewebe, was die Einführung von aktiven Flächen als theoretisches Konzept motiviert. In der vorliegenden Arbeit untersuchen wir die Dynamik von gekrümmten und sich verformenden aktiven Flächen. Dabei interessieren wir uns insbesondere für die Dynamik mechanochemischer Prozesse auf diesen Flächen, sowie für deren Wechselwirkung mit der Flächenform und externen Kräften.

Zur Untersuchung der Wechselwirkung zwischen mechanochemischen Prozessen und Flächenverformungen nutzen wir die hydrodynamische Theorie aktiver Fluide auf sich verformenden Flächen und betrachten eine vollständig selbstorganisierte Flächendynamik. Wir entwickeln eine Methode zur Bestimmung numerischer Lösungen des Kräfte- und Drehmomentgleichgewichts auf Flächen und untersuchen wie die Stabilität von Flächenformen durch mechanochemische Prozesse beeinflusst wird. Wir zeigen, dass die enge Kopplung zwischen chemischen Prozessen und der Mechanik von Flächen zur spontanen Erzeugung spezifischer Formen, zu Formoszillationen und zu gerichteten Flüssen führt, welche eine peristaltische Bewegung nachbilden.

Im Folgenden untersuchen wir die mechanochemische Selbstorganisation aktiver Fluide auf festen Flächen und betrachten mechanische Wechselwirkungen mit umgebendem Material. Dazu beschreiben wir ein umgebendes passives Fluid, welches durch aktive Flüsse auf der Fläche in Bewegung versetzt wird. Im Rahmen dieser Beschreibung untersuchen wir zwei Szenarien. Inspiriert durch die Wechselwirkung des Zellkortex mit dem Zytoplasma, betrachten wir zuerst ein Fluid, welches durch die Fläche eingeschlossen wird. Wir zeigen, dass die mechanische Wechselwirkung einer isotropen, aktiven Fläche mit dem umgebenden Fluid es ermöglicht, Muster mit einer polaren Asymmetrie, sowie einen kontraktilen Ring spontan und selbstorganisiert zu bilden. Danach betrachten wir ein passives Fluid, welches die Fläche außen umgibt. Diese Beschreibung führt zu einem Modell für einen Mikroschwimmer, welcher durch eine spontane Symmetriebrechung auf der aktiven Fläche beginnt sich durch das passive Fluid zu bewegen.

Die meisten biologischen Materialien verhalten sich viskoelastisch, sodass deren mechanische Antwort je nach Zeitskala einer applizierten mechanischen Spannung viskos und elastisch ausfallen kann. Im abschließenden Teil dieser Arbeit betrachten wir daher eine Fläche, deren mechanische Antwort auf aktive Spannung durch ein Maxwell-Modell beschrieben wird. Wir bestimmen eine minimale Zeitskala für die Relaxation von elastischer Spannung, welche das spontane Einsetzen räumlich-zeitlicher Oszillationen aktiver mechanischer Spannung kennzeichnet.

Zusammengefasst identifizieren und charakterisieren wir in dieser Arbeit eine Reihe von

Prozessen, welche der Selbstorganisation aktiver Flächen entspringen. Die zugrundeliegende Kopplung zwischen der Mechanik von Flächen und einer chemischen Organisation aktiver mechanischer Spannung stellen ein Schlüsselprinzip morphogenetischer Vorgänge in der Biologie dar. Zusätzlich entwickeln wir eine Reihe numerischer Methoden, welche es in Zukunft erlauben weitere Beschreibungen aktiver Flächen zu untersuchen. Damit trägt diese Arbeit neue theoretische Einsichten und numerische Algorithmen zur Verbesserung des Verständnisses der emergenten räumlichen Organisation und Formerzeugung aktiver Flächen bei.

Contents

1	Introduction	1
1.1	Active forces in biological systems	1
1.1.1	The actin cortex of animal cells	2
1.1.2	Epithelial tissues	5
1.2	Hydrodynamic theories of active matter	7
1.2.1	Conservation laws	8
1.2.2	Irreversible thermodynamics	9
1.2.3	Active fluids and viscoelastic gels	11
1.2.4	Active surfaces	12
1.3	Chemical regulation of active stress	15
1.4	Overview of this thesis	16
2	Self-organised shape dynamics of active fluid surfaces	18
2.1	Geometry and mechanics of self-organised active fluid surfaces	18
2.1.1	Force and torque balance equations on curved surfaces	19
2.1.2	Constitutive relation of an active fluid surface	20
2.1.3	Chemical regulation of active tension	21
2.2	Dynamic representation of deforming axisymmetric surfaces	22
2.2.1	Arc length surface parameterisation	22
2.2.2	Time-dependent coordinate transformation	23
2.2.3	Dynamic equations for geometric surface properties	24
2.3	Mechano-chemical self-organisation of spherical surfaces	25
2.3.1	Linear stability analysis	26
2.3.2	Spontaneous shape formation	28
2.4	Mechano-chemical self-organisation of tubular surfaces	28
2.4.1	Linear stability analysis	30
2.4.2	Spontaneous constriction and shape oscillations	33
2.4.3	Directed flows and peristaltic surface dynamics	34
2.4.4	Neck radii of tubular surfaces with bending rigidity	35
2.5	Discussion	37

3	Symmetry breaking on an active fluid surfaces in viscous environments	40
3.1	Self-organised active fluid surface in a viscous environment	41
3.1.1	Constitutive relations and governing equations for the active surface	41
3.1.2	Mechanical interactions of surfaces with a surrounding fluid	42
3.1.3	Closed solution of the nonlinear problem	44
3.2	Mechano-chemical symmetry breaking in the cellular cortex	47
3.2.1	Linear stability analysis	47
3.2.2	Spontaneous formation of a contractile ring	50
3.2.3	Interactions of patterns with an inhomogeneous external cue	51
3.3	Spontaneous motion of an active surface swimmer	54
3.3.1	Spontaneous onset of translational motion	55
3.3.2	Analytic approximation of the propagation velocity	56
3.3.3	Bifurcation analysis at the spontaneous onset of motion	60
3.4	Discussion	62
4	Self-organised contractility oscillations on an active viscoelastic surface	65
4.1	Constitutive relation of an active viscoelastic surface	65
4.2	Linear stability analysis	67
4.2.1	Derivation of the Jacobian	67
4.2.2	Critical Maxwell time	71
4.3	Nonlinear dynamics of contractility oscillations	71
4.4	Discussion	74
5	Conclusion and Outlook	77
 Appendices		
A	Differential geometry of embedded surfaces	81
A.1	Definitions and basic identities	81
A.1.1	Parametrisation of an embedded surface	81
A.1.2	Invariants of surface tensors	82
A.1.3	Differentiation on curved surfaces	84
A.2	Geometric surface variation under small deformations	85
A.2.1	Dynamic equations of geometric surface properties	86
A.3	Parametrisation of axisymmetric surfaces	87
A.3.1	Arc length surface parametrisation	87
A.3.2	Parametrisation of the unit sphere	88
B	Definitions and applications of spherical harmonics	90
B.1	Definitions and basic identities	90
B.1.1	Scalar spherical harmonics	90

B.1.2	Vector spherical harmonics	91
B.1.3	Tensor spherical harmonics	93
B.2	Solution of the Stokes equation in terms of vector spherical harmonics	94
B.2.1	General solution	95
B.2.2	Solution of the boundary value problem	95
B.2.3	The hydrodynamic stress on a spherical surface	96
B.2.4	Generalised Stokes drag	98
B.3	Further relations used in this thesis	100
B.3.1	Harmonic projection of the nonlinear advection term	100
B.3.2	Harmonic decomposition of the surface strain rate tensor	101
C	Strain rate tensor and viscous stress in deforming thin films	103
C.1	General expression for the strain rate tensor in a thin film	103
C.2	Discussion of the symmetric part	105
C.2.1	Viscous stress in compressible thin films	106
C.2.2	Viscous stress in incompressible thin films	106
C.3	Discussion of the antisymmetric part	107
D	Active fluid dynamics on deforming surfaces	109
D.1	Dynamic representation of deforming axisymmetric surfaces	109
D.2	Governing equations for axisymmetric active fluid surfaces	112
D.2.1	Force and torque balance equations	112
D.2.2	Dynamic equation for the concentration field	114
D.2.3	Analytic limits at the poles of axisymmetric spherical surfaces	114
D.3	Boundary conditions and global constraints	115
D.3.1	Closure conditions on spherical axisymmetric surfaces	115
D.3.2	Conservation of the enclosed volume	116
D.3.3	Translational invariance and choice of reference frame	117
D.4	Linearisation of the dynamics of deforming active fluid surfaces	117
D.4.1	Coordinate-free form of the governing equations	118
D.4.2	Linearisation on spherical surfaces	120
D.4.3	Linearisation on tubular surfaces	122
D.5	Neck radius scaling of tubular surfaces with bending rigidity	124
D.6	Details of the numerical approach	127
D.6.1	Numerical discretisation	128
D.6.2	Grid convergence analysis and simulation code validation	129
D.6.3	Parameters used for numerical results	130

E	Active fluid dynamics on a sphere	131
E.1	Active surface swimmer	131
E.1.1	Steady-state solutions	131
E.1.2	Characterisation of the spontaneous onset of motion	133
E.2	Active viscoelastic surface theory	134
E.2.1	Lagrangian derivative on curved surfaces	134
E.2.2	Analysis of the Jacobian	138
E.3	Details of the numerical approach	141
E.3.1	Least-square fitting of scalar and tensor spherical harmonics	141
E.3.2	Viscous surface dynamics	144
E.3.3	Viscoelastic surface dynamics	145
Bibliography		150

Chapter 1

Introduction

The development of multicellular organisms from a single cell is a remarkable process. It involves a large number of steps gradually specifying the spatial organisation of the organism; a process called *morphogenesis*.

Morphogenesis encompasses two important aspects of spatial organisation: the generation and organisation of different shapes, as well as the general patterning of otherwise homogeneous structures. These concepts have been brought forward as key elements of morphogenetic processes in the seminal works of Thompson [1] and Turing [2]. The generation of shapes generally requires mechanical forces to move and deform material, while spatial patterns in biological cells and tissues are often chemical in nature. By organising mechanical forces directly through chemical processes, biological systems demonstrate the fascinating ability to couple the generation of forces with the formation of patterns in a material.

In this introductory chapter, we first present two concrete examples of such biological systems whose properties motivate large parts of the theoretical work presented in this thesis (Section 1.1). We then introduce general theoretical concepts that are required to describe the non-equilibrium properties of biological materials (Section 1.2). Finally, we explain how the mechano-chemical organisation of biological systems can be integrated into a theoretical description (Section 1.3). We conclude with a brief overview of the problems that are studied in this thesis (Section 1.4).

1.1 Active forces in biological systems

Biological systems are unique in their ability to generate forces that act at molecular scales and lead to macroscopic motion, flows and material deformations. During these processes, energy is constantly transduced, such that biological systems are maintained away from thermodynamic equilibrium [3–5]. Therefore, they are *active* systems and the associated forces are referred to as active forces [6]. This is in contrast to ‘dead’ matter, which does not transduce energy and only responds to external forces with its passive material properties.

In the following, we present two examples of highly abundant biological systems that

are particularly interesting to study the dynamics of active mechanical processes: the actin cortex of animal cells (Section 1.1.1) and epithelial tissues (Section 1.1.2). Both are involved in a large number of morphogenetic events, and the key principles of their spatio-temporal organisation inspired most of the theoretical work presented in this thesis.

1.1.1 The actin cortex of animal cells

Actin is a major component of the animal cells' cytoskeleton, which is additionally constituted by microtubules and intermediate filaments [7]. The actin cortex is a thin actin-rich structure, which is physically attached to the lipid membrane that forms the outer boundary of cells. The thickness of the actin cortex is on the order of 100 nm [8], which compares against a cell diameter of animal cells roughly on the order of $10\ \mu\text{m}$ [9]. The actin cortex consists of semi-flexible polymeric filaments that are structurally polar and dynamic. Indeed, actin-binding proteins use energy from the hydrolysis of adenosine triphosphate (ATP) into adenosine diphosphate (ADP) to polymerise actin filaments at one end, while the release of a phosphate leads to depolymerisation at the other end. A polymerisation force can be generated by this process; thus driving, for example, membrane protrusions in migrating cells [10, 11].

Due to actin turnover and to the transient binding dynamics of cross-linking proteins, the cortex has viscoelastic material properties [12, 13]. The corresponding relaxation time scales depend on the constituent's turnover rates. The time scale of actin turnover is on the order of tens of seconds [14, 15], and cross-linking proteins typically bind and unbind on time scales below a second [16]. Quantitative *in-vivo* measurements of the cortex determined relaxation time scales of approximately five seconds [13]. However, the general rheology of the cortex is complex, and some experiments suggest a power law distribution of relaxation times [17, 18]. The cortical rheology and material properties are additionally affected by active processes [19–21], which we introduce and discuss in the remainder of Section 1.1.1.

Active stress generation in the cortex

Besides mechanical integrity, the actin network provides tracks for myosin motor proteins. The latter can cross-link and move along actin filaments [9, 22], thus forming a dynamic actin-myosin meshwork called the *actomyosin cortex* (Fig. 1.1). Molecular motors use the hydrolysis of ATP as an energy source to exert forces between filaments and thereby transduce chemical energy into mechanical work [23, 24] (Fig. 1.1 b). This microscopic dynamics leads macroscopically to the generation of *active stress*.

Active stress generation has been the focus of a wide range of experimental *in-vivo* and *in-vitro* studies, which found that the active stress in the actomyosin systems is typically contractile [8, 22, 25–29]. In general, its amplitude depends on the architecture of the actin network [8, 25, 28, 30] and on the local concentration of myosin motors [29, 31–33]. Active stress vanishes in the absence of myosin or when the actomyosin system is depleted of ATP [25].

At the cellular scale, active stress can lead to motion and shear of the actin cortex, a

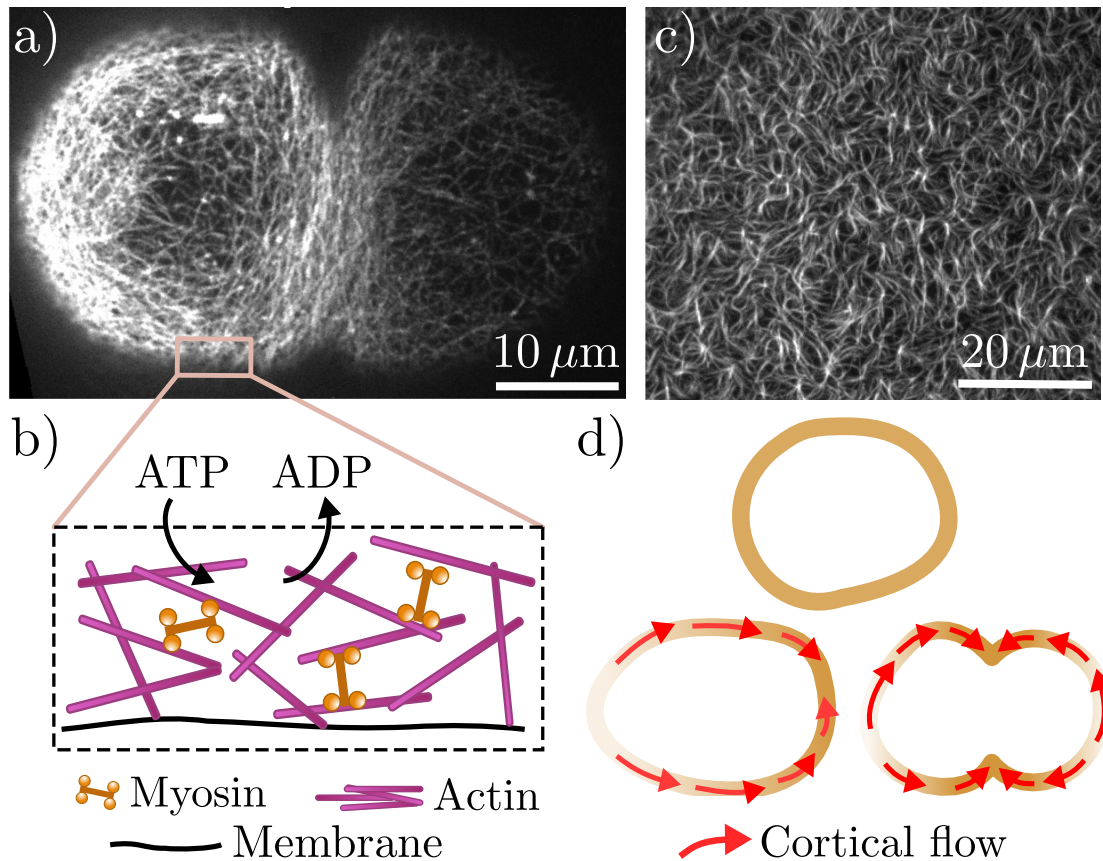


Figure 1.1: Overview of the actomyosin cortex. **a)** Fluorescence image of actin taken from the actomyosin cortex of a *C. elegans* single-cell embryo during the onset of cytokinesis (image: adapted from [33]). *C. elegans* is a worm that reaches about 1 mm in length at maturity. Its ease of manipulation in the lab and the fact that it is transparent make it a popular model organism in developmental biology. **b)** Schematic of the actomyosin cortex. The actomyosin cortex is attached to a lipid membrane that forms the outer boundary of animal cells. Myosin filaments dynamically cross-link actin filaments and exert forces between them. For this, myosin motors use the hydrolysis of adenosine triphosphate (ATP) into adenosine diphosphate (ADP) and transduce chemical energy into mechanical work. Macroscopically, this leads to the generation of active stress. **c)** Fluorescently labelled bundles of actin filaments in a reconstituted actomyosin system (image: adapted from [26]). Reconstituted systems allow studying organisation principles of actomyosin systems in a more controlled setting. **d)** Schematic cross sections through cells with different distributions of actomyosin density. The latter provides an indicator for the local amplitude of active stress in the cortex. An asymmetric distribution of actomyosin effectively polarises the cell and leads to cortical flows towards one pole (bottom left). A contractile actomyosin ring is formed during cytokinesis (bottom right). This causes cortical flows into the ring and cell shape changes that ultimately lead to the division of a single cell into two daughter cells.

process known as cortical flow [31, 32, 34–36] (Fig. 1.1 d). Importantly, active stress can also lead to cell shape changes [12, 33, 34, 37], even in the absence of external forces.

Organisation of the cortex during cytokinesis of animal cells

A well-studied phenomenon where active cortical flows and cell shape changes play an important role is *cytokinesis*: the separation of a mother cell into two daughter cells. Cytokinesis is an essential process for the development and maintenance of an organism. For example, cells in the human body undergo an estimated 10^{16} cell divisions during an average life time [38].

Cytokinesis proceeds in several steps, during which the actomyosin cortex contributes mechanical forces that are required for cell shape changes and cell division [12, 39–41]. First, animal cells round up due to an increase of active stress in the actomyosin cortex [42–44], which facilitates the distribution of genetic material – the *Deoxyribonucleic acid* (DNA) – within the cell [45]. This is followed by an accumulation of actin and myosin in a narrow band surrounding the cell, which is called the *contractile ring* [34, 46, 47] (Fig. 1.1 d, bottom right). The formation of a contractile ring is facilitated by a recruitment of actin and myosin towards the ring zone [48–50], as well as in some cell types by a targeted reduction of actomyosin density from the poles of the cell [51, 52]; The latter process is called *polar relaxation*. Due to increased contractile stress in the contractile ring, a cleavage furrow forms and the cortex ingresses [39, 41], leading finally to the separation of the two daughter cells [53].

Cytokinesis is tightly regulated by biochemical signalling processes that guide cells through the different steps just described [39, 54, 55]. We refer to *signalling processes* or *signals* here generically as processes that are determined by genetic programs upstream of the dynamics that we explicitly describe. Conceptually, one can consider them as an ‘external field’ that is added to the system by some underlying biochemical regulation. Importantly, these signalling processes can also act inhomogeneously across the cortex and thereby break the global isotropic symmetry of the cell. During cytokinesis, inhomogeneous signals originate from the spindle apparatus, a cytoskeletal structure made of microtubules that facilitates the even distribution of the genetic material to the two daughter cells [9]. The spindle geometry defines the cell division axis: signals from the central part of the spindle support the formation of the contractile ring [39, 48, 56] and signals from the polar regions of the spindle lead to the polar relaxation described above [52].

An important spindle-independent patterning process of the cortex is *cell polarisation*. In this case, high concentrations of different proteins in two disjoint domains of the cortex can act as molecular ‘labels’, and polarise cells before cytokinesis [57, 58]. The two daughter cells that emerge from the following division are of distinct cell types, and the division is thus called *asymmetric cell division*. The protein family that mainly regulates cell polarisation, the PAR family, is conserved across many different animal species and cell types [59]. However, the underlying symmetry breaking event occurs in different ways. For example, in embryonic cells of the nematode *Caenorhabditis elegans*, a distinct cortical region is molec-

ularly marked by the sperm entry point into the unfertilised egg, which later defines a polar asymmetry [35, 60, 61]. Another scenario is provided by cells that are embedded in a tissue, where the cellular polarisation can be determined by signalling cues that are organised on the tissue level [62–64].

Mechanical interactions of the cortex with the cytoplasm

During and outside of the context of cell division, the dynamics of the actomyosin cortex is additionally influenced by its mechanical interactions with surrounding material. Towards the inside of the cell, the cortex is in contact with the cytoplasm, a crowded fluid that consists of 80 % water [65]. By manipulating the cytoplasm mechanically, it has been shown that cytoplasmic flows can directly affect the dynamics of cortical material and the distribution of proteins within it [66]. Similar cytoplasmic flows can appear spontaneously due to active processes within the cytoplasm [67–69]. The reverse scenario, in which active cortical flows set the cytoplasmic fluid into motion, has also been observed experimentally [66, 70, 71]. This suggests that active stress, which is generated in the actomyosin cortex, can affect the dynamics of the cytoplasmic fluid and *vice versa*.

1.1.2 Epithelial tissues

In multicellular organisms, cells are the building blocks of biological tissues. The epithelium is an example of a tissue type that is involved in a large range of morphogenetic processes [72, 73]. Epithelial tissues are multicellular sheets in which cells are tightly connected by adherens junction proteins [74] (Fig. 1.2 b). The material properties of an epithelium emerge as a net response that results from contributions of single cell mechanical properties and from the mechanical connectivity of the tissue [72]. In general, the epithelium can be considered as a complex viscoelastic material [75–77]. The time scale of stress relaxation in tissues can be related to the cell division rate [78], but collective memory effects in a developing epithelial tissue have also been identified [79, 80]. Cell growth, rearrangements of cells due to neighbour exchanges, and active processes can additionally change the distribution of mechanical stress in the tissue [80, 81].

Active stress in epithelial tissue

The mechanical connectivity between cells within an epithelium enables the transmission of locally generated active stress across the tissue [85]. As a result, the mechanical activity of a few cells can lead in this assembly to morphogenetic transformations on multicellular scales [72, 73, 86]. These include collective cellular motion or tissue flows [79, 87–90], as well as the formation of tissue folds and invaginations with various geometries that appear during the development of an organism [72, 86, 91–95] (Fig. 1.2 a). In most of these processes, a local increase in the actomyosin density correlates with the appearance of tissue deformations.

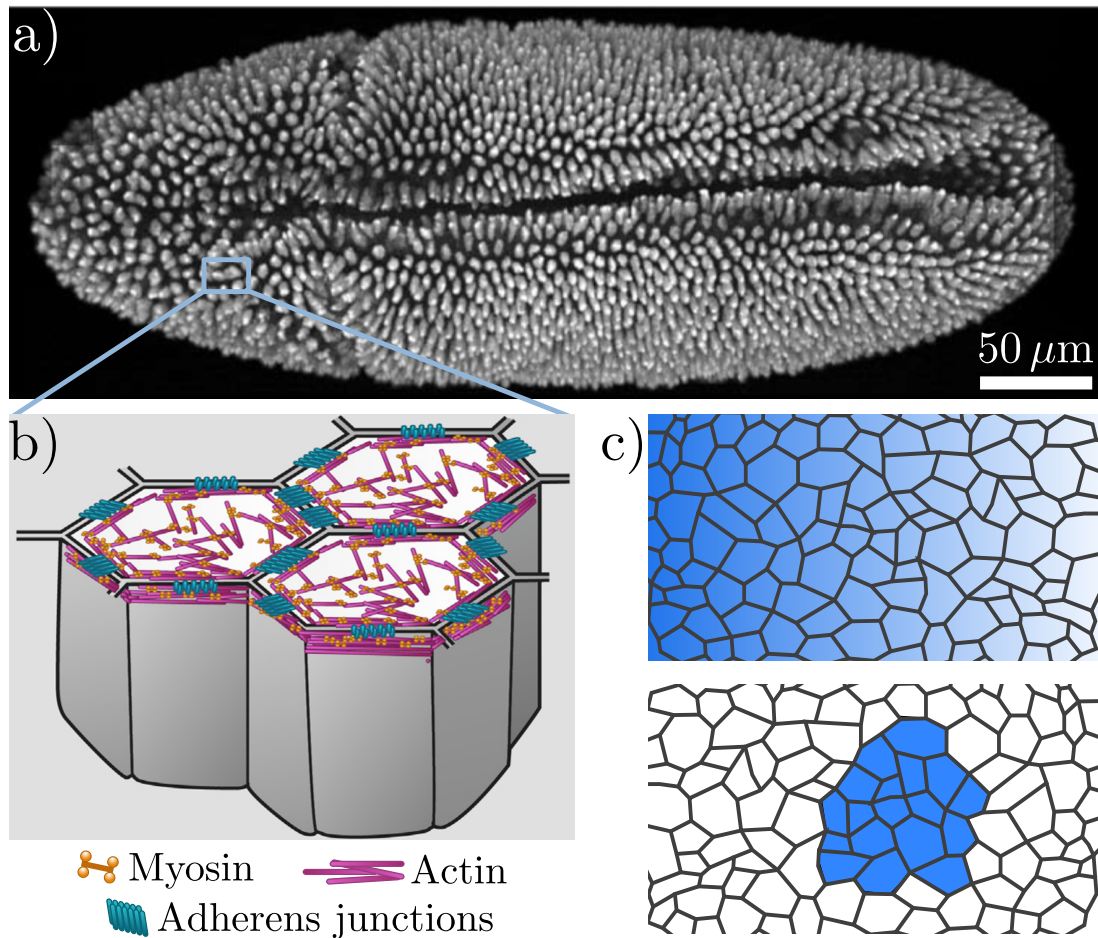


Figure 1.2: Overview of an epithelial tissue. **a)** Light-sheet fluorescence microscopy image of the *Drosophila melanogaster* fly embryo during early development (image: adapted from [82]). The fruit fly *D. melanogaster* represents one of the most popular model organism to study questions in developmental biology. The fluorescent label is attached to deoxyribonucleic acid (DNA) in the embryo, such that each distinct bright region represents a cell within the tissue. At this stage, the tissue has started forming several invaginations. For example, the central horizontal streak (ventral furrow) will later turn into a part of the adult fly’s digestive tract. **b)** Schematic of connected cells in an epithelial tissue (image: adapted from [73]). Adherens junctions provide a mechanical connectivity between cells in the tissue. Active stress, which is locally generated in the actomyosin cortex of cells (Section 1.1.1), can therefore be transmitted through the tissue. **c)** Schematics of mechanisms that allow for a spatial organisation of an epithelial tissue. These are required to guide and coordinate morphogenetic processes during development. Diffusible signalling molecules, which interact with cells in a concentration-dependent manner (morphogens), can spread inhomogeneously across the tissue and thereby provide an implicit spatial ‘map’ [83,84] (top). Inhomogeneous physical properties of epithelial cells can lead to the formation of immiscible groups of cells, which is called compartmentalisation [72] (bottom).

Biochemical perturbations of the global actomyosin machinery lead to the disruption or failure of these processes [92,93], which altogether suggests that the active stress required for morphogenetic processes in epithelial tissues is largely generated in the actomyosin cortex of the epithelial cells.

Several mechanisms contribute to the spatio-temporal organisation of active stress associated with morphogenetic processes in epithelial tissues. These include feedback mechanisms that couple the cellular secretion of signalling molecules to the local stress in the tissue, a process called *mechanotransduction* [96,97]. Furthermore, tissues can be patterned already during early development, thus later instructing multicellular morphogenetic transformations to appear at the desired tissue location [72,98]. The origin of these early patterns can be of biochemical nature, as it is the case for mechanisms that involve *morphogens*, diffusible molecular species that interact with cells in a concentration-dependent manner. These can spread inhomogeneously across the tissue and thereby provide an implicit spatial ‘map’ [2,58,73,83,98] (Fig. 1.2 c, top). Inhomogeneous physical properties of epithelial cells can also contribute to an effective patterning of tissues by forming patches of immiscible groups of cells, a process called *compartmentalisation* [72] (Fig. 1.2 c, bottom).

1.2 Hydrodynamic theories of active matter

In the previous section, we have introduced the complex material properties of the actomyosin cortex and epithelial tissues. These systems represent examples of soft condensed matter that is maintained away from thermodynamic equilibrium by chemical processes [5]. A powerful framework to systematically develop a theoretical description of such systems is provided by a hydrodynamic approach that is based on irreversible thermodynamics [5,99,100]. Theories of active matter that have been developed using this framework, were later successfully applied to quantitatively describe a wide range of dynamic processes in the actomyosin cortex [29,31–33,36,41,101] and in epithelial tissues [79,80,88–90].

In general, hydrodynamics theories describe slowly varying, long-lived processes that emerge from a system with a large number of degrees of freedom. The corresponding hydrodynamic modes are determined by conservation laws and continuous broken symmetries [99,100,102]. From the entropy production in the system, conjugate pairs of generalised thermodynamic fluxes and forces can be identified [5]. Close to thermodynamic equilibrium, linear constitutive relations can be written by expanding generalised fluxes in terms of generalised forces [103]. Because the hydrodynamic approach is solely built on conservation laws and symmetries, the resulting constitutive relations are generic and do not depend on the microscopic details of the system [5].

In the following, we present the basic conservation laws (Section 1.2.1) and briefly introduce the theoretical concepts of irreversible thermodynamics (Section 1.2.2). We then review constitutive relations of active isotropic materials that have been obtained previously (Sec-

tion 1.2.3). Note that for the purpose of this introduction, we present these aspects for three-dimensional systems in Euclidean space. Finally, we discuss the description of active materials that prescribe effectively two-dimensional, moving and deforming geometries: *active surfaces* (Section 1.2.4).

1.2.1 Conservation laws

The dynamics of the microscopic degrees of freedom of molecular components has to obey a set of conservation laws that are generically valid at, but also away from thermodynamic equilibrium [5]. In the continuum limit, these conservation laws can be expressed as continuity equations that are introduced in the following.

Conservation of mass implies the continuity equation

$$\partial_t \bar{\rho} + \partial_\alpha (\bar{\rho} v_\alpha) = 0, \quad (1.1)$$

where $\bar{\rho}$ is the mass density in units of mass per volume and v_α is the local center-of-mass velocity of volume elements. Greek indices denote Cartesian coordinates $\{x, y, z\}$ and the Einstein summation convention is used.

Conservation of momentum can be written as

$$\partial_t g_\alpha - \partial_\beta \sigma_{\alpha\beta}^{\text{tot}} = 0, \quad (1.2)$$

where $g_\alpha = \bar{\rho} v_\alpha$ denotes the momentum density and the total stress tensor $-\sigma_{\alpha\beta}^{\text{tot}}$ corresponds to the total momentum flux. The stress tensor in the comoving reference frame of volume elements is given by $\sigma_{\alpha\beta} = \sigma_{\alpha\beta}^{\text{tot}} + \bar{\rho} v_\alpha v_\beta$, for which the momentum balance Eq. (1.2) takes the form

$$\bar{\rho} \frac{d}{dt} v_\alpha = \partial_\beta \sigma_{\alpha\beta}. \quad (1.3)$$

Here, Eq. (1.1) was used and $\frac{d}{dt} = \partial_t + v_\gamma \partial_\gamma$ denotes the convected time derivative.

Conservation of energy reads [5]

$$\partial_t \bar{e} + \partial_\alpha J_\alpha^e = 0, \quad (1.4)$$

where \bar{e} is the energy density and J_α^e denotes the energy flux.

Similarly, a conservation law of angular momentum can be expressed in terms of a continuity equation for the total angular momentum density [5]. For isotropic systems that are studied in this thesis, angular momentum conservation implies that the stress tensor $\sigma_{\alpha\beta}^{\text{tot}}$ is symmetric. Hence, also the stress tensor $\sigma_{\alpha\beta}$ in the comoving reference frame has to be symmetric.

1.2.2 Irreversible thermodynamics

Local thermodynamic equilibrium

A system with a large number of degrees of freedom, which is globally at thermodynamic equilibrium, can be described in terms of thermodynamic potentials that depend only on a small number of state variables [104]. In the framework of irreversible thermodynamics, one considers a *local thermodynamic equilibrium*: local volume elements are at thermodynamic equilibrium, while the global system can be maintained away from it [5, 102]. This requires the equilibration within volume elements to be fast compared to the dynamics of the hydrodynamic modes. If this condition is met, thermodynamic potentials and state variables are well-defined in each of the volume elements. The sum of extensive thermodynamic quantities defined in each volume element therefore yields meaningful physical quantities. In particular, one can determine the free energy F of a finite volume of material from

$$F = \int \bar{f} dV, \quad (1.5)$$

where \bar{f} is the free energy density. The entropy S can be determined similarly from an integral over the corresponding entropy volume density \bar{s} .

Entropy production

At thermodynamic equilibrium the entropy S is maximal. If a system that is globally out of thermodynamic equilibrium is left to equilibrate, entropy will be produced until the state of maximal entropy is reached. In the following, we explain how an explicit expression for this entropy production, and therefore information about irreversible processes in the system, can be obtained from the free energy given in Eq. (1.5).

Consider the general balance equations for the free energy density and entropy density given by

$$\partial_t \bar{f} + \partial_\alpha J_\alpha^f = \bar{\theta}_f \quad (1.6)$$

$$\partial_t \bar{s} + \partial_\alpha J_\alpha^s = \bar{\theta}, \quad (1.7)$$

where $\bar{\theta}_f$ and $\bar{\theta}$ denote sources of free energy and the local rate of entropy production, respectively [5, 103]. For a given free energy density \bar{f} that characterises the local equilibrium properties of the system, an explicit expression for $\bar{\theta}_f$ can be found by computing $\frac{d}{dt}F$ using Eq. (1.5) and identifying bulk and surface terms according to

$$\frac{d}{dt}F = \int \bar{\theta}_f dV - \int J_\alpha^f dA_\alpha. \quad (1.8)$$

The rate of local entropy production $\bar{\theta}$ can then be determined from $\bar{\theta}_f$ as follows. First, we note that the thermodynamic relation $\bar{e} = \bar{f} + T\bar{s}$ is valid in each volume element and

the energy flux in Eq. (1.4) is accordingly related to fluxes of free energy and entropy by $J_\alpha^e = J_\alpha^f + T J_\alpha^s$. Here, T is the temperature and we consider for simplicity an isothermal system. From the conservation of energy Eq. (1.4) and the balance Eqs. (1.6) and (1.7) it then follows that the rate of local entropy production is related to sources of free energy by [103]

$$T\bar{\theta} = -\bar{\theta}_f. \quad (1.9)$$

Determining $\bar{\theta}_f$ as outlined above, is therefore sufficient to find an explicit expression for the rate of local entropy production $\bar{\theta}$.

Onsager relations

The rate of local entropy production $\bar{\theta}$, or alternatively the rate of dissipation of free energy $T\bar{\theta}$, generally takes the form [5, 102, 103, 105]

$$T\bar{\theta} = \sum_k J_k X_k. \quad (1.10)$$

Here, J_k and X_k represent conjugate pairs of generalised thermodynamic fluxes and forces, respectively, which must vanish at thermodynamic equilibrium [102]. Close to thermodynamic equilibrium we can write *linear constitutive relations*

$$J_k = \sum_l L_{kl} X_l, \quad (1.11)$$

where the coupling constants L_{kl} represent phenomenological coefficients [103]. As explained in the following, one can deduce from physical considerations that not all coefficients L_{kl} can be set independently and certain constraints have to be obeyed.

Based on the signature of the generalised fluxes and forces under time-reversal, one distinguishes between reactive and dissipative couplings [5, 102]. If the time-reversal signatures of J_k and X_l are equal (different), the coefficient L_{kl} represents a reactive (dissipative)¹ coupling and is denoted by L_{kl}^r (L_{kl}^d). *Onsager reciprocal relations* follow from the assumption of microscopic irreversibility and can be stated as $L_{kl}^r = -L_{lk}^r$ and $L_{kl}^d = L_{lk}^d$ [102, 105, 106]. Hence, it follows from Eqs. (1.10) and (1.11) that only dissipative couplings L_{kl}^d contribute to the rate of entropy production.

The second law of thermodynamics imposes additional algebraic constraints on the coefficients L_{kl}^d [102]. In order to ensure $T\bar{\theta} \geq 0$, the dissipative coefficients must fulfil $L_{kk}^d \geq 0$ and $L_{kl}^d \leq (L_{kk}^d L_{ll}^d)^{1/2}$ (no summation). These conditions guarantee the positive definiteness of the quadratic form that is defined by Eqs. (1.10), (1.11), and the Onsager relations.

Additionally, the expansion given in Eq. (1.11) has to respect the spatial symmetries of

¹This notion can be illustrated by considering the equation of a damped oscillator: $\ddot{x} + \gamma\dot{x} + \omega^2 x = 0$. Albeit not a thermodynamic example, the dissipative nature of the term $\gamma\dot{x}$ is in accordance with the fact that its signature under time-reversal is different from the signature of the other terms in this equation.

the system, which is known as *Curie's symmetry principle* [107]. Formally, this implies that the transformation properties of scalars, vectors and tensors have to be respected [5].

1.2.3 Active fluids and viscoelastic gels

The approach outlined in Section 1.2.2 can be used to derive constitutive relations for active fluids and gels [108–111]. In the case of an isotropic active fluid, conjugate pairs of generalised fluxes and forces $J_k \leftrightarrow X_k$ have been identified as [5]

$$\sigma_{\alpha\beta}^d \leftrightarrow v_{\alpha\beta} \quad (1.12)$$

$$r \leftrightarrow \Delta\mu. \quad (1.13)$$

In Eq. (1.12), $\sigma_{\alpha\beta}^d$ denotes the deviatoric stress tensor $\sigma_{\alpha\beta}^d = \sigma_{\alpha\beta} - P\delta_{\alpha\beta}$, where P is an isotropic equilibrium stress, and $v_{\alpha\beta} = (\partial_\alpha v_\beta + \partial_\beta v_\alpha)/2$ denotes the symmetric part of the strain rate tensor $\partial_\alpha v_\beta$. In Eq. (1.13), r denotes the rate at which a chemical fuel species is converted into a product species whose chemical potential difference is $\Delta\mu = \mu_f - \mu_p$ [112].

Using the conjugate pairs of fluxes and forces Eqs. (1.12) and (1.13) and following Eq. (1.11), a linear constitutive relation for the deviatoric stress tensor of an *isotropic active fluid* can be written as [4, 5]

$$\sigma_{\alpha\beta}^{d,f} = 2\bar{\eta}_s \left(v_{\alpha\beta} - \frac{1}{3} v_{\gamma\gamma} \delta_{\alpha\beta} \right) + \bar{\eta}_b v_{\gamma\gamma} \delta_{\alpha\beta} + \bar{\xi} \Delta\mu \delta_{\alpha\beta}. \quad (1.14)$$

The phenomenological Onsager coefficients $\bar{\eta}_s$, $\bar{\eta}_b$ correspond to shear and bulk viscosities of the fluid, respectively, the coefficient $\bar{\xi}$ describes the generation of isotropic stress in the material due to chemical reactions. In the absence of the latter, Eq. (1.14) leads together with the momentum balance Eq. (1.3) to the Navier-Stokes equations of a compressible fluid [111, 113].

Using the hydrodynamic approach, it is also possible to describe active materials with viscoelastic properties, as we briefly sketch in the following. Constitutive relation for viscoelastic gels can be derived by considering a free energy density \bar{f} that depends additionally on the elastic strain $u_{\alpha\beta}$ in the material [5, 110]. Besides the conjugate pairs given Eqs. (1.12) and (1.13), the local entropy production $\bar{\theta}$ then contains an additional pair of conjugate fluxes and forces $J_k \leftrightarrow X_k$ that is given by

$$\frac{D}{Dt} u_{\alpha\beta} \leftrightarrow -\sigma_{\alpha\beta}^{\text{el}}, \quad (1.15)$$

where $\sigma_{\alpha\beta}^{\text{el}}$ is the stress of the elastic material components. The convected corotational time derivative

$$\frac{D}{Dt} u_{\alpha\beta} = \partial_t u_{\alpha\beta} + v_\gamma \partial_\gamma u_{\alpha\beta} + \omega_{\alpha\gamma} u_{\gamma\beta} + \omega_{\beta\gamma} u_{\alpha\gamma} \quad (1.16)$$

evaluates temporal changes of elastic strain in the comoving, corotating reference frame

of volume elements [5]. Here, $\omega_{\alpha\beta} = (\partial_\alpha v_\beta - \partial_\beta v_\alpha)/2$ denotes the antisymmetric part of the strain rate tensor. Taking into account the conjugate pairs given in Eqs. (1.12) and Eq. (1.15), a constitutive relation for $Du_{\alpha\beta}/Dt$ can be written. Assuming linear behaviour of the elastic material components, $\sigma_{\alpha\beta}^{\text{el}} \sim u_{\alpha\beta}$, the constitutive relation for $Du_{\alpha\beta}/Dt$ leads to an constitutive relation for $\sigma_{\alpha\beta}^{\text{el}}$ in the form [5,110]

$$\left(1 + \tau_M \frac{D}{Dt}\right) \sigma_{\alpha\beta}^{\text{el}} = 2\bar{\eta}'_s \left(v_{\alpha\beta} - \frac{1}{3}v_{\gamma\gamma}\delta_{\alpha\beta}\right) + \bar{\eta}'_b v_{\gamma\gamma}\delta_{\alpha\beta}. \quad (1.17)$$

Here, $\bar{\eta}'_s$ and $\bar{\eta}'_b$ denote shear and bulk viscosities of the gel. Equation (1.17) corresponds to a classical Maxwell model for the stress $\sigma_{\alpha\beta}^{\text{el}}$ with a *Maxwell relaxation time* τ_M [111,114]. This relation describes a predominantly elastic behaviour on time scales shorter than τ_M and viscous behaviour on longer time scales. With this, the deviatoric stress tensor for an *isotropic active viscoelastic gel* can be written as [4,111]

$$\sigma_{\alpha\beta}^{d,g} = \sigma_{\alpha\beta}^{\text{el}} + \bar{\xi}\Delta\mu\delta_{\alpha\beta}. \quad (1.18)$$

Note that we have for simplicity ignored couplings with $\Delta\mu$ in Eq. (1.17) and with $v_{\alpha\beta}$ in Eq. (1.18).

1.2.4 Active surfaces

In Section 1.1, we have introduced the fascinating properties of the actomyosin cortex and epithelial tissues and discussed their important roles in morphogenetic processes. These structures represent active materials that are organised into effectively two-dimensional geometries: active surfaces (Fig 1.3). In this section, we present a basic overview of the geometric and mechanical description of active surfaces. We begin by discussing the description of deformations in thin layers of material [115] and introduce the geometric representation of the associated midplane-surfaces. Then, we explain how constitutive relations for active surfaces can be obtained from the constitutive relations presented in the previous section [13,36]. Finally, we briefly discuss a more general approach to derive constitutive relations for active surfaces [112].

Deformations and shear of the three-dimensional material are described by the strain rate tensor $\partial_\alpha v_\beta$. In order to determine a representation of this tensor on a two-dimensional surface, we require additional assumptions about the material degrees of freedom normal to the midplane. We adapt in this thesis the classical thin shell assumption that can be analogously formulated for a thin fluid film: points on a straight line along the normal of the initial surface, remain on a straight line along the normal of the deformed surface [115]. In the case of a fluid film, further assumptions are required about flows parallel to the midplane that are not associated with midplane deformations (Appendix C). We also show in Appendix C how the three-dimensional strain rate tensor $\partial_\alpha v_\beta$ can be rigorously mapped onto a strain

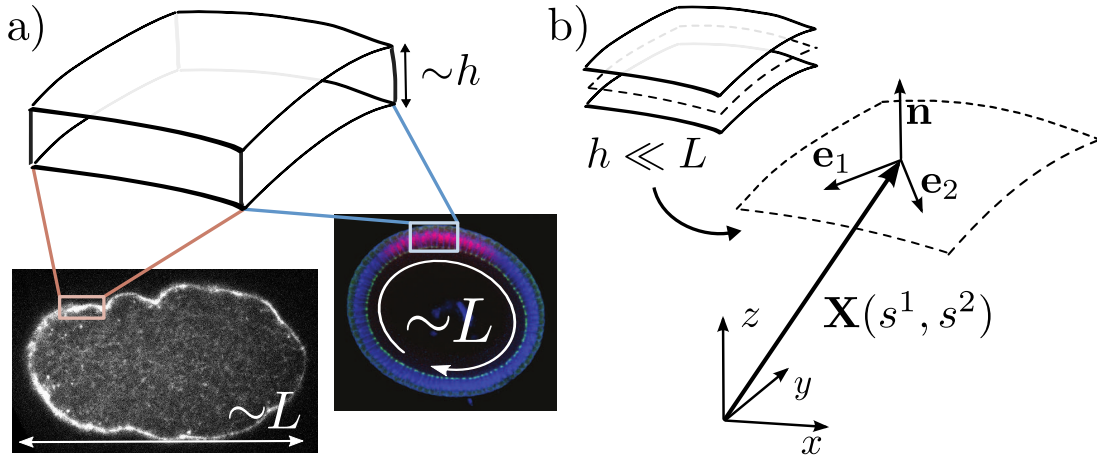


Figure 1.3: Representation of biological structures as two-dimensional surfaces. **a)** The height h of the cellular cortex and epithelial tissue is typically much smaller than their lateral extensions L . Left: Fluorescence image of actin in the median cross section of a *C.elegans* single-cell embryo (image: courtesy of Anne-Cecile Reymann). The increased brightness in the outline of the cell indicates the high actin concentration in the cortex. Right: Fluorescence image of a transverse cross section of the *Drosophila melanogaster* fly embryo (image: adapted from [116]). The blue color marks the DNA content in cells, which form the epithelial tissue. The red color shows signals that instruct subsequent morphogenetic processes. **b)** In these geometries, a description of the two-dimensional midplane (dashed outline) is sufficient to capture the essential geometry of the three-dimensional structure. A two-dimensional surface can be described by a parametrisation $\mathbf{X}(s^1, s^2)$, which defines a local basis $\{\mathbf{e}_1, \mathbf{e}_2, \mathbf{n}\}$ on the surface.

rate tensor of a two-dimensional surface that represents the midplane of a thin fluid film.

A geometric representation of a general two-dimensional surfaces is given by a surface parametrisation $\mathbf{X}(s^1, s^2)$, where $\{s^1, s^2\}$ are generalised coordinates on the surface. This parametrisation defines a local basis with tangent vectors $\mathbf{e}_i = \partial_i \mathbf{X}$ ($\partial_i = \partial/\partial s^i$) and surface normal $\mathbf{n} = \mathbf{e}_1 \times \mathbf{e}_2 / |\mathbf{e}_1 \times \mathbf{e}_2|$ with Cartesian components $(\mathbf{e}_i)_\alpha$ and n_α , respectively (Fig. 1.3b).

An effective description of the forces within a two-dimensional surface can be determined from a given stress tensor $\sigma_{\alpha\beta}$ of the three-dimensional sheet as follows. We begin by describing a force $\mathbf{F} = F^i \mathbf{e}_i$ that acts within the surface. For this, we introduce a tension tensor t_{ij} that is defined by the relation

$$F_j = ds \nu^i t_{ij}. \quad (1.19)$$

Here, $\nu = \nu^i \mathbf{e}_i$ is a unit vector that is orthogonal to a line element of length ds on which the force \mathbf{F} acts.¹ The force \mathbf{F} on the other hand can directly be determined from the stress $\sigma_{\alpha\beta}$ in the material (Fig. 1.4) [115]. For this, we use the projected stress tensor $\sigma_{ij} = \sigma_{\alpha\beta} (\mathbf{e}_i)_\alpha (\mathbf{e}_j)_\beta$

¹This is analogous to a stress tensor $\sigma_{\alpha\beta}$ in three dimensions that is defined by $F_\alpha = dA \sigma_{\alpha\beta} \bar{n}_\beta$, where the force F_α acts on a surface element with surface normal $\bar{\mathbf{n}}$ (corresponding to the line element with in-plane normal ν).

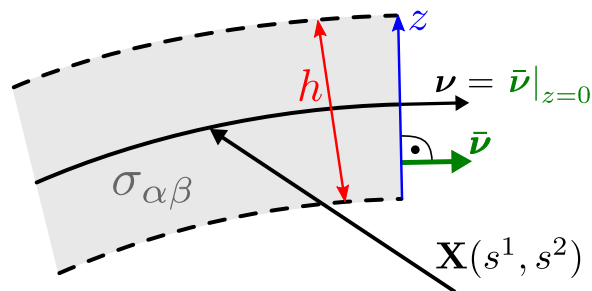


Figure 1.4: Schematic of a cut through the material. The mechanical properties of the three-dimensional material are described by the stress tensor $\sigma_{\alpha\beta}$. Cross-sectional surfaces (along the z -axis marked in blue) are characterised by a unit normal $\bar{\nu}$, which is denoted ν on the midplane at $z = 0$. By integrating the stress that acts on this cross-sectional surface over the height h (Eq. (1.20)), effective mechanical properties associated with the midplane surface can be determined.

and compute the force \mathbf{F} from an integral over the finite height h given by

$$F_j = ds \int_{-h/2}^{h/2} dz \bar{\nu}^i \sigma_{ij}. \quad (1.20)$$

Here, the midplane is located at $z = 0$ such that $\nu^i = \bar{\nu}^i|_{z=0}$ and $\bar{\nu} = \bar{\nu}^i \mathbf{e}_i$ is the unit normal on the cross-sectional surface that is also defined away from the midplane.¹ Expanding the integrand in Eq. (1.20) in z and using the definition of the tension tensor Eq. (1.19), we can identify to lowest order in the height

$$t_{ij} \approx h \sigma_{ij}^{(0)}, \quad (1.21)$$

where $\sigma_{ij}^{(0)}$ corresponds to the constant zeroth order contribution of the expansion of σ_{ij} in z .

The projected stress tensor σ_{ij} , together with Eq. (1.21), provide a connection between the constitutive relations of active isotropic materials introduced in Section 1.2.3 and an effective description of such materials on a two-dimensional surface. For example, we can directly infer that the isotropic active stress $\sigma_{\alpha\beta}^a = \bar{\xi} \Delta \mu \delta_{\alpha\beta}$ leads to

$$t_{ij}^a \approx h \bar{\xi} \Delta \mu^{(0)} \delta_{\alpha\beta} (\mathbf{e}_i)_\alpha (\mathbf{e}_j)_\beta \quad (1.22)$$

$$= \xi_a g_{ij}, \quad (1.23)$$

which corresponds to an effective isotropic active tension t_{ij}^a in the surface description. Here, we have introduced the metric tensor $g_{ij} = \mathbf{e}_i \cdot \mathbf{e}_j$ and collected prefactors that are constant along the midplane surface normal into $\xi_a = h \bar{\xi} \Delta \mu^{(0)}$. Variations of active stress along the midplane surface normal lead in this limit to active bending moments that are not considered further in this thesis [115].

An alternative approach to determine constitutive relations of active matter specifically

¹Torques and related bending moments within a surface can be described in a similar fashion [115].

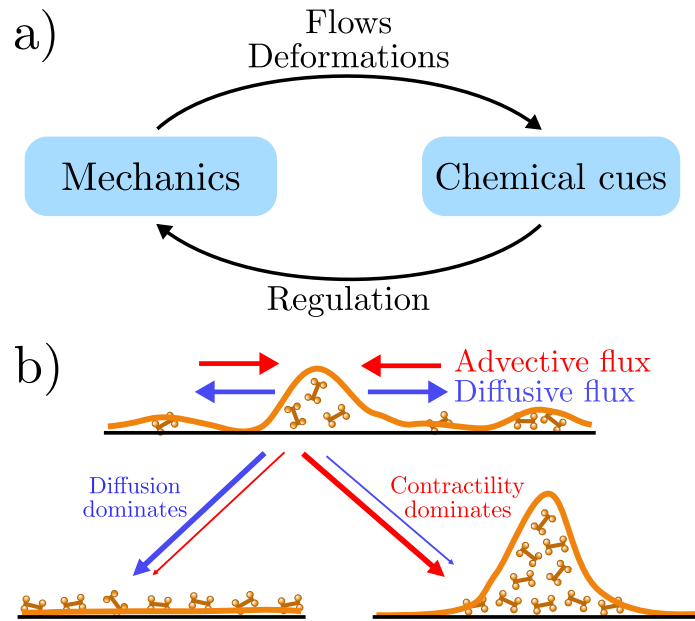


Figure 1.5: Mechano-chemical feedback. **a)** Schematic overview of the mechano-chemical feedback loop in biological systems. Mechanical stress is regulated by chemical cues and leads to flows and deformations of material. In turn, this affects the distribution of the chemical cues in the material. **b)** Theoretical conceptualisation of the mechano-chemical feedback loop. Gradients of a stress-regulating molecular species lead to contractile advective flows that increase the local concentration of stress regulator. Diffusion homogenises the concentration. Depending on the relative strength of advective and diffusive fluxes a mechano-chemical instability can appear. This leads to inhomogeneous steady state distributions of the stress regulating species and thus, of contractile stress [117].

for surfaces is to apply the general concepts of irreversible thermodynamics (Section 1.2.2) directly to moving and deforming surfaces [112]. This leads to a fully covariant theory of the mechanics of active surfaces. The covariant framework gives rise to a rich family of additional active terms, including explicit couplings of the surface curvature with internal chemical processes [112]. The fully covariant theory contains as a special case constitutive relations for an isotropic active fluid film, which can alternatively be obtained as outlined above and which represents the scenario we focus on in this thesis. The specific constitutive relations used will be introduced in detail together with the concrete problems that are studied in the main part of the thesis.

1.3 Chemical regulation of active stress

We have seen in Section 1.1 that the generation of active stress in the actomyosin cortex and epithelial tissues is tightly coupled to chemical processes. This provides the elements for a *mechano-chemical* feedback mechanism, in which chemically regulated active stress induces motion of material, which in turn can affect the distribution of the chemical regulators

(Fig. 1.5 a).¹ Such a mechanism has been previously conceptualised in [117]. There, the authors studied the dynamics of an active fluid as introduced in Eq. (1.14) in one dimension and considered a contractile active stress $\bar{\xi}\Delta\mu(c) \geq 0$ that depends additionally on the local concentration c of a stress-regulating molecular species. For a given distribution of active stress $\bar{\xi}\Delta\mu(c)$, the force balance² $\partial_\beta\sigma_{\alpha\beta} = 0$ leads to a finite flow velocity v_α of the material. These flows lead in turn to a change in the concentration c of stress regulator, which can be described by an advection-diffusion equation

$$\partial_t c = -\partial_\alpha (c v_\alpha) + D \partial_\alpha^2 c, \quad (1.24)$$

where D is the diffusion constant. This generic description gives rise to a mechano-chemical instability that depends on the competition between active contractile flows that locally lead to an accumulation of stress regulator and its homogenisation due to diffusion [117] (Fig. 1.5 b).

Several descriptions of self-organised active materials that followed a similar approach have been studied in fixed domains and in the absence of curvature. These include theoretical studies [119–121], but also the description of experimental results related to the cellular cortex [122], epithelial tissues [123–125] and *in-vitro* actomyosin systems [126]. More recently, also stationary stress distributions that emerge from self-organised active stress on a sphere have been used to determine deformations in a linear approximation [37, 127].

The chemical regulation and resulting self-organisation of active stress is one of the key concepts we explore in this thesis to study the *dynamics of active surfaces*.

1.4 Overview of this thesis

In this thesis, we study the dynamics of curved and deforming active surfaces. More specifically, we are interested in the dynamics of mechano-chemical processes on these surfaces, as well as in their interaction with the surface shape and external forces. We formalise this using the hydrodynamic theory of active surfaces and study minimal models that resemble key principles of the mechano-chemical self-organisation observed in biological systems.

The remaining parts of this thesis are organised as follows. In Chapter 2, we introduce a hydrodynamic description of self-organised active surfaces and develop a numerical framework to study the full nonlinear shape dynamics. We identify mechano-chemical shape instabilities and describe the spontaneous generation of non-trivial surface shapes, shape oscillations and directed surface flows that resemble peristaltic waves. In Chapter 3, we study the effects of ex-

¹In the context of biological systems one may critically argue that morphogenetic processes are predominantly guided by ‘hard-coded’ biochemical signalling networks that operate constantly in the background, while mechano-chemical processes are only secondary downstream effects. However, there is strong evidence that the mechanical properties of biological materials and their dynamic chemical organisation are themselves an integral component of the morphogenesis machinery [118].

²Throughout the thesis we neglect inertial effects, which is typically a valid simplification for the dynamics of cells and tissues due to the small length scales and strong viscous damping associated with these systems [41, 89]. The force balance given here then follows from Eq. (1.3).

ternal viscous forces on the self-organisation of an active fluid film on the surface of a sphere. We show that external shear stress from a passive fluid enables the spontaneous formation of a stable, contractile ring. We also characterise a microswimmer that is described by this model, and which can spontaneously propagate through the surrounding fluid. In Chapter 4, we study an active viscoelastic material on a sphere. We identify a critical stress relaxation time that indicates the emergence of spontaneous contractility oscillations and, we study the nonlinear dynamics of these oscillations. We conclude in Chapter 5 by summarising the main results of this thesis and pointing out possible directions for future work.

Chapter 2

Self-organised shape dynamics of active fluid surfaces

In this chapter, we study the dynamics of shapes that arises from the self-organisation of mechano-chemical processes on an active fluid surface.

In Section 2.1, we introduce the description of a self-organised active fluid surface. On this surface, active stress is dynamically regulated by the concentration field of a diffusible and advected regulator. We first present the force and torque balance equations on surfaces and then present constitutive relations for the active fluid surface, as well as a dynamic equation for the stress regulator. In Section 2.2, we develop a framework to capture the dynamics of deforming axisymmetric surfaces, which also forms the basis of the numerical approach we use to obtain solutions of the non-linear shape dynamics. In Sections 2.3 and 2.4, we then study the shape dynamics of self-organised active surfaces with spherical and tubular topology, respectively. In each case, we perform a linear stability analysis and examine the full non-linear surface dynamics using our numerical approach. In Section 2.5, we summarise and discuss the main results of this chapter.

2.1 Geometry and mechanics of self-organised active fluid surfaces

In this section, we introduce the description of a self-organised active fluid surface. We represent the corresponding time-dependent surface $\Gamma \subset \mathbb{R}^3$ by a parametrisation $\mathbf{X}(s^1, s^2, t)$, where the parameters (s^1, s^2) and t denote generalised surface coordinates and time, respectively. Using the surface basis vectors introduced in Section 1.2.4, vector fields on the surface can be decomposed into tangential and normal parts $\mathbf{a} = \mathbf{a}_{\parallel} + \mathbf{a}_{\perp}$, where $\mathbf{a}_{\parallel} = a^i \mathbf{e}_i$ and $\mathbf{a}_{\perp} = a_n \mathbf{n}$. Derivatives of the basis vectors are given by the Gauss-Weingarten relations [128]

$$\partial_i \mathbf{e}_j = -C_{ij} \mathbf{n} + \Gamma_{ij}^k \mathbf{e}_k \quad (2.1)$$

$$\partial_i \mathbf{n} = C^j_i \mathbf{e}_j, \quad (2.2)$$

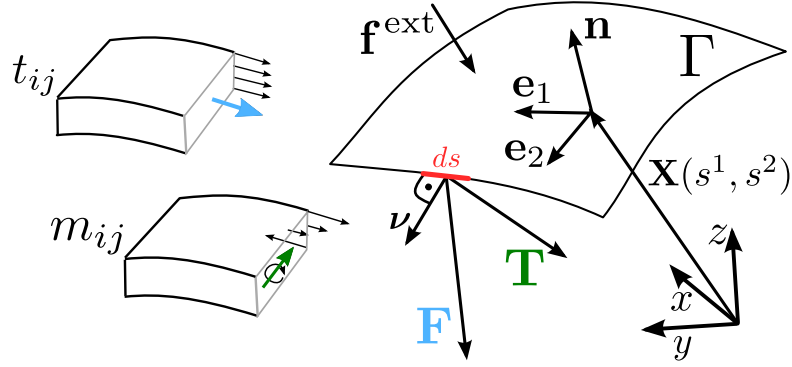


Figure 2.1: Description of the forces and torques on curved surfaces. The geometry of a curved surface Γ embedded in \mathbb{R}^3 can be described by a parametrisation $\mathbf{X}(s^1, s^2)$. The tension tensor t_{ij} and moment tensor m_{ij} are used to describe forces \mathbf{F} and torques \mathbf{T} in the surface that act on a line element ds .

where C_{ij} is the curvature tensor and Γ_{ij}^k denotes Christoffel symbols. The mean curvature H and Gaussian curvature K are defined by $H = C^k_k/2$ and $K = \det(C^j_i)$.

2.1.1 Force and torque balance equations on curved surfaces

To describe deformations of the surface Γ as a result of internal mechanical stresses and external forces, surface configurations have to obey force and torque balance equations that we introduce in the following.

General forces in the surface acting on a line element of length ds can be written as $\mathbf{F} = ds\nu_i \mathbf{t}^i$ (Fig. 2.1, [129]). This defines the in-plane tension tensor t_{ij} , as well as normal forces t_n^i in the surface by $\mathbf{t}^i = t^{ij} \mathbf{e}_j + t_n^i \mathbf{n}$. Normal forces arise from torques $\mathbf{T} = ds\nu_i \mathbf{m}^i$ and associated bending moments $\mathbf{m}^i = m^{ij} \mathbf{e}_j + m_n^i \mathbf{n}$ within the surface. Additionally, external forces $\mathbf{f}^{\text{ext}} = f^{\text{ext},i} \mathbf{e}_i + f_n^{\text{ext}} \mathbf{n}$ can act onto the surface. With these definitions, the force and torque balance equations read [112, 115, 129]:

$$\nabla_i t^{ij} + C_i^j t_n^i = -f^{\text{ext},j} \quad (2.3)$$

$$\nabla_i t_n^i - C_{ij} t^{ij} = -f_n^{\text{ext}} \quad (2.4)$$

$$\nabla_i m^{ij} + C_i^j m_n^i = \epsilon_i^j t_n^i \quad (2.5)$$

$$\nabla_i m_n^i - C_{ij} m^{ij} = -\epsilon_{ij} t^{ij}, \quad (2.6)$$

where ∇_i denotes the covariant derivative, ϵ_{ij} denotes the covariant Levi-Civita tensor (Appendix A.1) and we have neglected inertial terms. Equations (2.3) and (2.4) describe the force-balance in the directions tangential and normal to the surface, respectively. Equation (2.5) determines how bending moments in the surface produce normal forces t_n^i , and Eq. (2.6) determines their coupling to the antisymmetric part of the tension tensor t_{ij} . Constitutive relations of the material provide expressions for the tension and moment tensors t_{ij}, m_{ij}, m_n^i [112]. These constitutive relations may contain passive elastic contributions, but

also active material properties that take into account the active stress generation observed in biological materials.

2.1.2 Constitutive relation of an active fluid surface

In order to define the active thin film description studied in this chapter, we first introduce the equilibrium properties of the surface. We consider here a surface with constant surface tension γ and bending rigidity κ , described by the Helfrich free energy [130]

$$F_H = \int dA \left[\gamma + \kappa \left(C_k^k \right)^2 \right]. \quad (2.7)$$

The tension and moment tensors of a surface described by Eq. (2.7) read [129]

$$t_{ij}^H = \gamma g_{ij} + \kappa C_k^k \left(C_k^k g_{ij} - 2C_{ij} \right) \quad (2.8)$$

$$m_{ij}^H = 2\kappa C_k^k \epsilon_{ij}. \quad (2.9)$$

Spontaneous curvature and Gaussian bending rigidity lead to additional terms in Eqs. (2.8) and (2.9), which we do not consider here for simplicity [112]. Note that the moments in Eq. (2.9) generate normal forces in the surface given by Eq. (2.5) and the normal force balance Eq. (2.4) yields the well-known shape equation of membranes [129].

To characterise flows and deformations of the thin film, we use the symmetric part of the in-plane strain rate tensor $\mathbf{e}_j \cdot \partial_i \mathbf{v}$, which reads [112]:

$$v_{ij} = \frac{1}{2} (\nabla_i v_j + \nabla_j v_i) + C_{ij} v_n. \quad (2.10)$$

Here, v_i denotes components of the in-plane flow field $\mathbf{v}_{\parallel} = v^i \mathbf{e}_i$, $\mathbf{v}_{\perp} = v_n \mathbf{n}$ describes deformations of the surface, and $\mathbf{v} = \mathbf{v}_{\parallel} + \mathbf{v}_{\perp}$ represents the center-of-mass flow velocity of surface elements. The deformation field v_n contributes to strains that are generated when deforming curved surface regions, such that curvature becomes a natural element of the constitutive equations of a deforming surface.¹ The deviatoric tension of an isotropic active thin film is given by [32, 112]

$$t_{ij}^d = 2\eta_s \left(v_{ij} - \frac{1}{2} v_k^k g_{ij} \right) + \eta_b v_k^k g_{ij} + \xi_a g_{ij}. \quad (2.11)$$

Here, η_s and η_b are the shear and bulk viscosities. The contractility $\xi_a \geq 0$ describes an isotropic active tension. The viscous terms in Eq. (2.11) can be obtained from a thin film limit, if additional assumptions about the flows in the three-dimensional fluid film are made (Appendix C). Furthermore, note that an effective in-plane compressibility can even arise

¹Equation (2.10) shows that the anisotropy of if the strain (rate) induced by a deformation is directly related to the anisotropy of the surface curvature. To see this qualitatively, consider the homogeneous inflation of a sphere and a cylinder along their surface normals. In the case of the sphere the surface area expands homogeneously, because the curvature is isotropic. In the case of the cylinder, strain is only induced along the azimuthal circumference, in accordance with the anisotropy of its surface curvature.

in a fluid film that is incompressible in three dimensions and is in this case linked to an exchange of surface material with the environment or surface height changes [13, 41, 112].

The complete constitutive relations are finally given by:

$$t_{ij} = t_{ij}^H + t_{ij}^d \quad (2.12)$$

$$m_{ij} = m_{ij}^H, \quad (2.13)$$

with the tension and moment tensors given by Eqs (2.8), (2.9), and (2.11). Furthermore, we assume that the volume enclosed by the surface is conserved, which defines a pressure p that enters the normal force balance Eq. (2.4) as $f_{\text{ext},n} = p$.

Finally, note that the normal torque balance Eq. (2.6) implies for the moment tensor m_{ij}^H given in Eq. (2.9) that t_{ij} has no antisymmetric part. Additionally, the in-plane torque balance Eq. (2.5) can be used to eliminate normal forces t_n^i in the force balance Eqs. (2.3) and (2.4). With this, we guarantee that the torque balance equations are always satisfied, and we are only left with force balance equations given by

$$\nabla^i t_{ij}^d = 0 \quad (2.14)$$

$$\epsilon^{jk} \nabla_k \nabla^i m_{ij}^H + C^{ij} t_{ij}^H + C^{ij} t_{ij}^d = p, \quad (2.15)$$

where m_{ij}^H , t_{ij}^H and t_{ij}^d are given in Eqs (2.8), (2.9), and (2.11), respectively.

2.1.3 Chemical regulation of active tension

We consider an active tension amplitude of the form $\xi_a = \xi f(c)$, where ξ is the contractility and c is a concentration field that regulates the strength of the local active tension. Following previous works [31, 117, 120, 131], this regulation is modelled using a saturating Hill function

$$f(c) = \frac{c^m}{c_0^m + c^m}. \quad (2.16)$$

The concentration field c is changing over time due to advective transport, reactions, and diffusion and therefore plays a crucial role for the self-organisation of the surface dynamics. These processes are captured by the dynamic equation for the concentration field [112, 132]

$$\partial_t c = -\nabla_i (c v^i) - 2H v_n c + D \Delta_\Gamma c - k_{\text{off}} c + k_{\text{on}}. \quad (2.17)$$

The first term on the right-hand side describes advection due to in-plane flows. The second term describes dilution and accumulation due to local surface expansion ($H v_n > 0$) or compression ($H v_n < 0$), respectively, that occurs during deformations of surface regions with non-vanishing mean curvature H . Isotropic in-plane diffusion with diffusion constant D is incorporated using the Laplace-Beltrami operator $\Delta_\Gamma = g^{ij} \nabla_i \nabla_j$. The last two terms describe production and degradation, defining a characteristic concentration $c_0 = k_{\text{on}}/k_{\text{off}}$.

For convenience, we choose in the following $k = k_{\text{off}}$ and c_0 as model parameters and write $k_{\text{on}} - k_{\text{off}}c = k(c_0 - c)$.

The dynamics of the concentration field given in Eq. (2.17) depends on flows v_i and deformations v_n on and of the surface. For a given geometry, these flow fields can be determined by solving the force balance Eqs. (2.14) and (2.15) of the active fluid surface. To close this model, we have to solve additionally for the dynamics of the surface geometry that depends on the deformation field v_n . In the next section, we therefore present a general framework to evolve the shape of surfaces for a given deformation field v_n , where we consider the dynamics of axisymmetric surfaces.

2.2 Dynamic representation of deforming axisymmetric surfaces

The dynamic equation of the deforming surface Γ is given by

$$\frac{d\mathbf{X}}{dt} = v_n \mathbf{n}, \quad (2.18)$$

where v_n denotes the deformation velocity and $\frac{d}{dt}$ the total time derivative. In the following, we consider deformations of axisymmetric surfaces and develop a framework to numerically solve Eq. (2.18) and general vector-valued differential equations on this surface.

2.2.1 Arc length surface parameterisation

An arbitrary axisymmetric surface can be represented explicitly using an arc length parameterisation

$$\mathbf{X}(\varphi, s, t) = \rho(s, t) \bar{\mathbf{e}}_\rho(\varphi) + z(s, t) \bar{\mathbf{e}}_z, \quad (2.19)$$

where $\{\bar{\mathbf{e}}_\rho, \bar{\mathbf{e}}_\varphi, \bar{\mathbf{e}}_z\}$ is the normalised standard basis $\bar{\mathbf{e}}_\alpha \cdot \bar{\mathbf{e}}_\beta = \delta_{\alpha\beta}$ with $\alpha, \beta \in \{\rho, \varphi, z\}$ in cylindrical coordinates, $\varphi = s^1 \in [0, 2\pi]$ is the azimuthal angle, and $s = s^2 \in [0, L(t)]$ is the arc length parameter of the meridional outline (Fig. 2.2). In the following, we use φ and s explicitly as covariant indices. From Eq. (2.1) it follows that $C_{s\varphi} = C_{\varphi s} = 0$ and

$$C_s^s(s, t) = \partial_s \psi, \quad (2.20)$$

$$C_\varphi^\varphi(s, t) = \frac{\sin \psi}{\rho} \quad (2.21)$$

where $\psi(s)$ is the tangent angle defined by $(\partial_s \rho, \partial_s z) = (\cos \psi, \sin \psi)$. This implies that the full shape information about Γ is encoded in the meridional curvature C_s^s , together with a point $\mathbf{X}(t)|_{s=0}$. Indeed, for given C_s^s , we can compute the tangent angle from Eq. (2.20) as:

$$\psi(s, t) = \psi(t)|_{s=0} + \int_0^s C_s^s(s', t) ds' \quad (2.22)$$

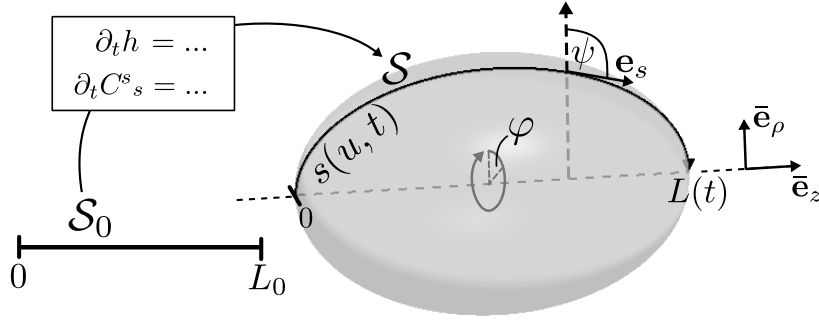


Figure 2.2: Representation of a deforming axisymmetric surface. The dynamic coordinate transformation h defines an arc length parameter $s(u, t) : \mathcal{S}_0 \rightarrow \mathcal{S}$, where u is a coordinate from a fixed Eulerian parametrisation of the meridional outline. The vectors $\{\bar{\mathbf{e}}_\rho, \bar{\mathbf{e}}_\varphi, \bar{\mathbf{e}}_z\}$ denote the normalised standard basis in cylindrical coordinates. The vector field $\mathbf{e}_s = \partial_s \mathbf{X}$ denotes the meridional tangent vector. The field $\psi(s)$ denotes the tangent angle defined by $\cos \psi = \mathbf{e}_s \cdot \bar{\mathbf{e}}_\rho$. The time-dependent coordinate transformation h and the meridional curvature C_s^s change with the deforming surface according to Eqs. (2.28) and (2.29). If required, the surface can be independently reconstructed using Eqs. (2.22)–(2.24).

and reconstruct Γ via

$$\rho(s, t) = \rho(t)|_{s=0} + \int_0^s \cos[\psi(s', t)] ds' \quad (2.23)$$

$$z(s, t) = z(t)|_{s=0} + \int_0^s \sin[\psi(s', t)] ds' \quad (2.24)$$

from the meridional curvature. Consequently, the shape of the surface Γ during deformations, and therefore the solution to Eq. (2.18), is encoded in the time evolution of the meridional curvature C_s^s and in the values of ψ , ρ and z at $s = 0$.

2.2.2 Time-dependent coordinate transformation

An arc length parametrisation $s \in \mathcal{S}(t) = [0, L(t)]$ simplifies the parametric form of covariant equations and the shape reconstruction via Eqs. (2.22)–(2.24). However, the time dependence of the domain $\mathcal{S}(t)$ makes it difficult to evaluate the total time derivative in the equation of the shape dynamics, Eq. (2.18). This renders the arc length parametrisation impractical for the numerical treatment of differential equations on a deforming surface. We therefore introduce additionally an Eulerian parametrisation of Γ given by

$$\mathbf{X}_e(\varphi, u, t) = \rho(u, t) \bar{\mathbf{e}}_\rho(\varphi) + z(u, t) \bar{\mathbf{e}}_z, \quad (2.25)$$

where u is a parameter on an interval $\mathcal{S}_0 = [0, L_0]$ that remains fixed during surface deformations (Fig. 2.2). For convenience, we chose $L_0 = L|_{t=0}$. The azimuthal angle φ is defined as in Eq. (2.19). Note that \mathbf{X} and \mathbf{X}_e represent the same surface Γ , but for the Eulerian

parametrisation, the shape dynamics Eq. (2.18) can be written as

$$\frac{\partial \mathbf{X}_e}{\partial t} = v_n \mathbf{n}. \quad (2.26)$$

The surface coordinates s and u are then related by a time-dependent coordinate transformation $h(u, t)$ that is defined by

$$s(u, t) = \int_0^u h(u', t) du'. \quad (2.27)$$

To obtain a dynamic equation for $h(u, t)$, we first note that $g_{ss} = h^{-2}g_{uu} = 1$, which represents a standard coordinate transformation of tensor components and leads to $g_{uu} = h^2$. Furthermore, it follows from Eq. (2.26) and the definition of the metric tensor that for an Eulerian parametrisation $\partial_t g_{ij} = 2C_{ij}v_n$ (see Appendix A.2.1), which implies

$$\partial_t h(u, t) = hC_s^s v_n. \quad (2.28)$$

Here, we have used $C_{uu} = h^2 C_s^s$. Recall that we had chosen $\mathcal{S}_0 = \mathcal{S}|_{t=0}$ for the fixed interval, which implies that h is uniquely determined as the solution of Eq. (2.28) with initial condition $h|_{t=0} = 1$.

2.2.3 Dynamic equations for geometric surface properties

Finally, we present a set of dynamic equations that we use to evolve the surface geometry and to formulate the covariant force balance equations of the active fluid film on an axisymmetric surface. Detailed derivations of the following dynamic equations can be found in Appendix D.1.

Time-dependence of the curvature tensor

In order to reconstruct the deforming surface via Eqs. (2.22)–(2.24), we require the time-dependence of the meridional curvature C_s^s , which is given by:

$$\partial_t C_s^s(u, t) = -(C_s^s)^2 v_n - \frac{1}{h} \partial_u \left(\frac{1}{h} \partial_u v_n \right). \quad (2.29)$$

The first term captures curvature changes due to stretching of the meridional outline, the second term describes the outline's bending due to an inhomogeneous deformation velocity v_n . Similarly, the dynamic equation for C_φ^φ reads:

$$\partial_t C_\varphi^\varphi(u, t) = -(C_\varphi^\varphi)^2 v_n - \frac{1}{h^2} \Gamma_{\varphi u}^\varphi \partial_u v_n, \quad (2.30)$$

where the Christoffel symbol $\Gamma_{\varphi u}^\varphi$ is defined by Eq. (2.1). Equations (2.29) and (2.30) describe the dynamics of the principal curvature fields, C_s^s and C_φ^φ , which capture the full extrinsic

geometry of the deforming axisymmetric surface for a given deformation field v_n .

Time-dependence of the Christoffel symbols

In order to explicitly express the covariant force balance equations on a parametrised surface, we additionally require the Christoffel symbols as a function of time. From the definition of the Christoffel symbols it follows that:

$$\partial_t \Gamma_{\varphi u}^{\varphi}(u, t) = \partial_u \left(C_{\varphi}^{\varphi} v_n \right) \quad (2.31)$$

$$\partial_t \Gamma_{\varphi \varphi}^u(u, t) = \frac{g_{\varphi \varphi}}{h^2} \left(v_n \partial_u C_{\varphi}^{\varphi} - C_{\varphi}^{\varphi} \partial_u v_n \right). \quad (2.32)$$

The remaining Christoffel symbols either vanish ($\Gamma_{\varphi \varphi}^{\varphi}, \Gamma_{uu}^{\varphi}, \Gamma_{u\varphi}^u = 0$) or they are not explicitly required, which is the case for Γ_{uu}^u .

For a given deformation field v_n , Eqs. (2.28)–(2.32) provide a framework solve the dynamic equation for the surface shape Eq. (2.26). By virtue of the dynamic coordinate transformation, these equations represent partial differential equations on a fixed spatial interval $[0, L_0]$ that can be solved using standard numerical approaches. If required, the surface can be independently reconstructed using Eqs. (2.22)–(2.24). Details on the numerical discretisation are presented in Appendix D.6.

2.3 Mechano-chemical self-organisation of spherical surfaces

In the following, we study self-organised deformations of active surfaces. The present section is dedicated to the analysis of spherical surfaces. The dynamics of tubular surfaces is discussed in Section 2.4. In both cases, we solve the force balance Eqs. (2.14) and (2.15) to obtain the deformation field v_n and in-plane flows \mathbf{v}_{\parallel} . The explicit form of these equations on a parametrised axisymmetric surface can be found in Appendix D.2.1. The dynamics of the concentration field is determined by solving Eq. (2.17), whose explicit form on an axisymmetric surface is given in Appendix D.2.2. Note that these equations are Galilei invariant and all velocities are determined up to a constant velocity vector.¹ The surface shape and intrinsic geometric properties evolve according to Eqs. (2.27)–(2.32). This system represents the full mechano-chemical feedback of flow-generation and reorganisation of active stresses and integrates geometry into the self-organisation process.

In the following, we first perform a linear stability analysis of the homogeneous state of a sphere to determine parameter regimes, where the surface is unstable (Section 2.3.1). In

¹Unique solutions can be found by choosing an appropriate reference frame. Because every reference frame is equally physical, we chose reference frames in which the numerical approach is most robust. This is explained in detail in Appendix D.3.3.

order to characterise mechano-chemical instabilities, we introduce a *contractility parameter*

$$\alpha = \frac{\xi}{\gamma} c_0 \partial_c f(c_0). \quad (2.33)$$

In the second step, we use the framework introduced in the previous section to study the full non-linear surface dynamics (Section 2.3.2).

2.3.1 Linear stability analysis

We consider axisymmetric surfaces of spherical topology and analyse the linear stability of the homogeneous steady state with $c = c_0$ and $\mathbf{v} = 0$ on a sphere with radius $R = R_0$. The sphere is parametrised by polar and azimuthal angles θ and φ . We expand small, axisymmetric perturbations $\delta c(\theta)$, $\delta R(\theta)$ and $\delta \mathbf{v}_{\parallel}(\theta)$ of this state as

$$\delta c = \sum_{l=0}^{\infty} \delta c_l Y_l \quad (2.34)$$

$$\delta R = \sum_{l=0}^{\infty} \delta R_l Y_l \quad (2.35)$$

$$\delta \mathbf{v}_{\parallel} = \sum_{l=1}^{\infty} \left(\delta v_l^{(1)} \boldsymbol{\Psi}_l + \delta v_l^{(2)} \boldsymbol{\Phi}_l \right). \quad (2.36)$$

Here, $Y_l(\theta)$, $\boldsymbol{\Psi}_l(\theta)$ and $\boldsymbol{\Phi}_l(\theta)$ denote axisymmetric modes of scalar spherical harmonics and vector spherical harmonics¹ that are labelled with mode numbers $l \in \mathbb{N}_0$. Note also that $\delta v_n = \partial_t \delta R$ to linear order. In the next step, we expand the force balance Eqs. (2.14) and (2.14), as well as the dynamic Eq. (2.17) for the concentration field to linear order in the perturbations given in Eqs. (2.34)–(2.36) (see Appendix D.4 for details). From the force balance equations we find $\delta v_l^{(2)} = 0$ and

$$\frac{\eta_s}{R_0^2} (1-l)(l+2) \delta v_l^{(1)} + \left[\frac{\eta_b}{R_0^2} (2\delta \dot{R}_l - l(l+1) \delta v_l^{(1)}) + \frac{\xi}{R_0} \partial_c f(c_0) \delta c_l \right] = 0 \quad (2.37)$$

$$\begin{aligned} \frac{2\eta_b}{R_0^2} (2\delta \dot{R}_l - l(l+1) \delta v_l^{(1)}) + \frac{2\xi}{R_0} \partial_c f(c_0) \delta c_l \\ + \left[\frac{2\kappa}{R_0^4} l(l+1) + \frac{\gamma + \xi f(c_0)}{R_0^2} \right] (l-1)(l+2) \delta R_l = 0, \end{aligned} \quad (2.38)$$

where we denoted $\delta \dot{R}_l = \frac{d}{dt} \delta R_l$. The linearisation of the dynamic equation of the concentration field given in (2.17) reads for each mode

$$\delta \dot{c}_l + \frac{c_0}{R_0} (2\delta \dot{R}_l - l(l+1) \delta v_l^{(1)}) + \left(\frac{D}{R_0^2} l(l+1) + k \right) \delta c_l = 0, \quad (2.39)$$

¹General scalar spherical harmonics $Y_{lm}(\theta, \varphi)$ and vector spherical harmonics $\{\boldsymbol{\Psi}^{(lm)}, \boldsymbol{\Phi}^{(lm)}\}$ are defined in Appendices B.1.1 and B.1.2, respectively. For each l , $2l$ non-axisymmetric modes exist that are labelled with mode numbers $|m| \leq l$, where $m \in \mathbb{Z}$. Axisymmetric harmonics correspond to modes with $m = 0$.

where $\delta\dot{c}_l = \frac{d}{dt}\delta c_l$. Note that the same linearised equations can be found, if non-axisymmetric perturbations are included in Eqs. (2.34)–(2.36) (Appendix D.4.2). Hence, the linear stability properties presented here also hold for non-axisymmetric perturbations.

The mode $l = 1$

Perturbations with $l = 1$ correspond to pure translations of the surface if $\delta\dot{R}_1 = \delta v_1^{(1)}$. Any perturbation that leads to $\delta\dot{R}_1 \neq \delta v_1^{(1)}$ contributes to an inhomogeneous compression or expansion of the surface to linear order. According to the force balance Eqs. (2.37) and (2.38), these surface compressions are related to perturbations of the concentration field δc_1 , which can be used in the dynamic equation of the concentration field Eq. (2.39). From this, we find a linear dynamic equation for the concentration mode δc_1 given by

$$\frac{d}{dt}\delta c_1 = \left(-\frac{2D}{R_0^2} - k + \frac{\xi c_0 \partial_c f(c_0)}{\eta_b} \right) \delta c_1. \quad (2.40)$$

Considering an ansatz $\delta c_1 = \delta c_1^{(0)} \exp(\mu_1^s t)$, the term in brackets on the right-hand side of Eq. (2.40) can be identified as the growth rate μ_1^s of the perturbation. The condition $\mu_1^s = 0$ defines a critical contractility parameter α_s^* . For increasing contractility parameter α , defined in Eq. (2.33), the mode $l = 1$ becomes unstable at $\alpha = \alpha_s^*$ with

$$\alpha_s^* = \frac{\eta_b}{\gamma} \left(\frac{2D}{R_0^2} + k \right). \quad (2.41)$$

Note that the perturbation δR_1 does not change the mean curvature to first order, such that α_s^* is independent of the bending rigidity κ .

Higher modes $l \geq 2$

For modes with $l \geq 2$, we find from the linearised force balance Eqs. (2.37) and (2.38)

$$\delta v_l^{(1)} = \frac{1}{2\eta_s} \left[\frac{2\kappa}{R_0^2} l(l+1) + \gamma + \xi f(c_0) \right] \delta R_l. \quad (2.42)$$

This relation shows that on a viscous fluid surface in-plane flows and shape changes are intimately linked. As explained above, the linearised force balance equations are valid for non-axisymmetric perturbations as well, such that Eq. (2.42) also holds more generally for non-axisymmetric shape changes and surface flows (Appendix D.4.2). It is interesting to note that Eq. (2.42) is independent of inhomogeneities in the active tension, which was already found in a similar description of an active fluid surface [37]. More generally, the coupling between flows and shape changes is to linear order exclusively related to anisotropic flows, which can be seen from the fact that only the shear viscosity η_s appears in Eq. (2.42), but not the bulk viscosity η_b .

Equation (2.42) can be used to eliminate $\delta v_l^{(1)}$ in Eqs. (2.38) and (2.39). This leads for

each mode to a two-dimensional Jacobian \mathbf{J}_s^l for the dynamics of the mode coefficients δR_l and δc_l (Appendix D.4.2). From an analysis of the eigenvalues of \mathbf{J}_s^l , we find that the mode $l = 1$ discussed above always has the largest growth rate and becomes unstable first when increasing the contractility parameter α .

2.3.2 Spontaneous shape formation

Surface relaxation for $\alpha < \alpha_s^*$

For $\alpha < \alpha_s^*$ the homogeneous concentration on the sphere represents a stable solution. This is revealed by the relaxation of a deformed sphere towards this stable steady state. Such a relaxation is depicted in Fig. 2.3 b, where we use a spheroidal surface with a homogeneous concentration as initial condition. During the relaxation process, we observe the transient formation of concentration maxima at the poles. These maxima appear as a consequence of the large mean curvature at those locations, which leads to a locally increased surface compression during deformations (see Eq. (2.17)).

Spontaneous formation of shapes and patterns with polar asymmetry for $\alpha > \alpha_s^*$

The growing mode $l = 1$ characterises a polar asymmetry. Using a randomly perturbed concentration field as initial condition in our numerical approach, we find that for $\alpha > \alpha_s^*$ the instability leads to the spontaneous formation of a single patch of stress regulator and an asymmetric surface shape that deviates from a sphere (Fig. 2.3 c). At the final steady state the advective in-flux of stress regulator into the contractile region is balanced by a diffusive out-flux away from it. The resulting inhomogeneous tension across the surface leads to an oblate shape with broken mirror symmetry with respect to the z -axis and thus spatially varying curvature (Fig. 2.3 d).

2.4 Mechano-chemical self-organisation of tubular surfaces

In this section, we study the mechano-chemical self-organisation of tubular surfaces. We proceed in similar steps as in the previous section. We first perform a linear stability analysis of the homogeneous state (Section 2.4.1) and use the contractility parameter α defined in Eq. (2.33) to characterise mechano-chemical instabilities. In the next step, we use the framework described in Section 2.2 to obtain solutions of the full non-linear surface dynamics for tubular surfaces without and with bending rigidity (Sections 2.4.2 and 2.4.3). Finally, we introduce a toy model to quantitatively describe tubular surface shapes that appear as steady states in the nonlinear description (Section 2.4.4).

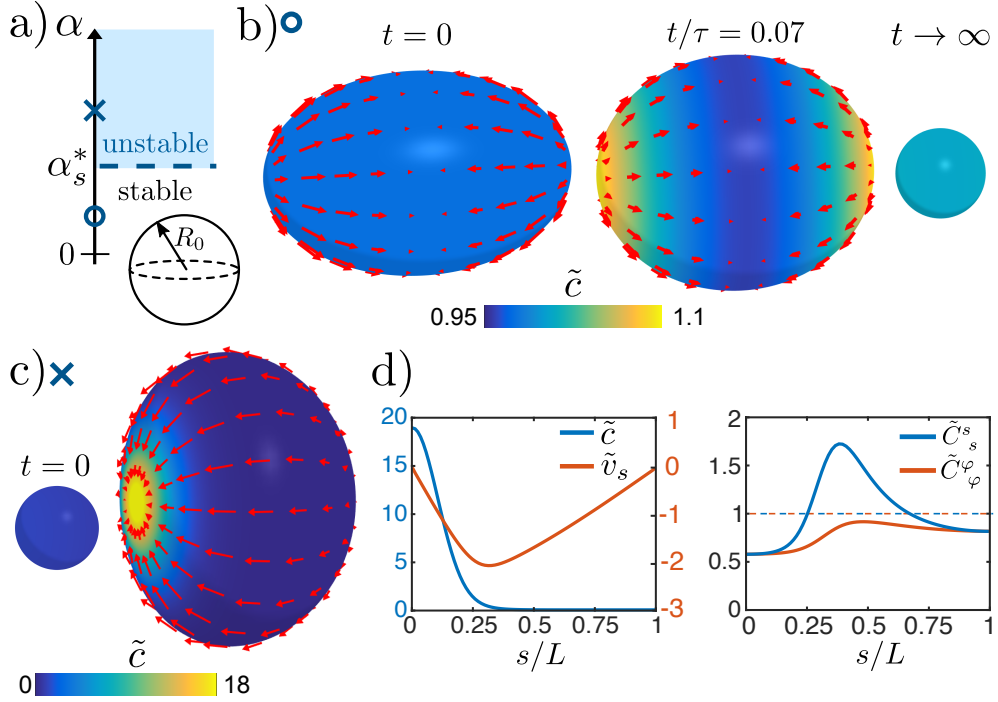


Figure 2.3: Shape dynamics of spherical surfaces with concentration-dependent active tension. **a)** Schematic stability diagram of the system. **b)** Relaxation dynamics of a mechano-chemically stable surface with $\alpha < \alpha_s^*$, starting with a spheroidal shape with eccentricity 0.75. To contractility parameter α is defined in Eq. (2.33) and the critical contractility α_c^* is given in Eq. (2.41). Inhomogeneities in the initial mean curvature ($t = 0$) lead to transient inhomogeneities in the concentration field ($t/\tau = 0.07$) due to a deformation-induced local expansion and compression of the surface (see Eq. 3.4). The stable steady state of a sphere is reached at long times ($t \rightarrow \infty$, not so scale). **c)** Mechano-chemically unstable surface with $\alpha > \alpha_s^*$. After a small concentration perturbation on a sphere ($t = 0$, not to scale), a deformed steady-state shape emerges with a localised patch of stress regulator. The final steady state corresponds to an oblate shape with broken mirror symmetry with respect to the z -axis. Red arrows denote the in-plane flow field. **d)** Profiles of the concentration $\tilde{c} = c/c_0$, in-plane flow $\tilde{v}_s = \mathbf{e}_s \cdot \mathbf{v}\tau/R_0$ ($\tau = \eta_b/\gamma$) and principle curvatures $\tilde{C}_s^s = R_0 C_s^s$, $\tilde{C}_s^\varphi = R_0 C_s^\varphi$ of the steady-state surface shown in c). In the steady state, the diffusive out-flux away from the contractile patch is balanced by an advective in-flux. The resulting tension across the surface is inhomogeneous, which leads to a deformed steady state shape. Surface flows in b) and c) and plotted values of \tilde{v}_s in d) are shown in the reference frame where the pole velocities satisfy $\mathbf{v}(s=0) = -\mathbf{v}(s=L)$ (see Appendix D.3.3). The parameters used in these simulations are given in the Appendix D.6.3.

2.4.1 Linear stability analysis

We now study the self-organisation of an active surface with a tubular geometry. We analyse the linear stability of the homogeneous steady state with $c = c_0$ and $\mathbf{v} = 0$ on a cylinder with radius ρ_0 and length L_0 , and we consider periodic boundary conditions. We expand small axisymmetric perturbations of this state as

$$\delta c = \sum_{n=-\infty}^{\infty} \delta c_n \exp(ik_n z) \quad (2.43)$$

$$\delta \rho = \sum_{n=-\infty}^{\infty} \delta \rho_n \exp(ik_n z) \quad (2.44)$$

$$\delta \mathbf{v}_{\parallel} = \bar{\mathbf{e}}_z \sum_{n=-\infty}^{\infty} \delta v_n^z \exp(ik_n z) \quad (2.45)$$

with wave numbers

$$k_n = \frac{2\pi n}{L_0}. \quad (2.46)$$

For the deformation field, we have $\delta v_n = \partial_t \delta \rho$ to linear order. From the corresponding expansion of the force balance Eqs. (2.14) and (2.15) we find

$$-(\eta_b + \eta_s) k_n^2 \delta v_n^z + (\eta_b - \eta_s) \frac{ik_n}{\rho_0} \delta \dot{\rho}_n + ik_n \xi \partial_c f(c_0) \delta c_n = 0 \quad (2.47)$$

$$i(\eta_b - \eta_s) \frac{k_n}{\rho_0} \delta v_n^z + (\eta_b + \eta_s) \frac{1}{\rho_0^2} \delta \dot{\rho}_n + \frac{\xi}{\rho_0} \partial_c f(c_0) \delta c_n + \left[\frac{\gamma + \xi f(c_0)}{\rho_0^2} (k_n^2 \rho_0^2 - 1) \right] \delta \rho_n = 0. \quad (2.48)$$

Here, we denote $\delta \dot{\rho}_n = \frac{d}{dt} \delta \rho_n$ and we have for simplicity of the following discussion chosen $\kappa = 0$. The derivation of the fully general linearisation is detailed in Appendix D.4.3. The linearised form of the dynamic equation of the concentration field Eq. (2.17) is given by

$$\delta \dot{c}_n + c_0 \left(ik_n \delta v_n^z + \frac{\delta \dot{\rho}_n}{\rho_0} \right) + \left(\frac{D}{\rho_0^2} k_n^2 \rho_0^2 + k \right) \delta c_n = 0, \quad (2.49)$$

where $\delta \dot{c}_n = \frac{d}{dt} \delta c_n$. To determine the Jacobian of this system, we eliminate δv_n^z and rewrite Eqs. (2.48) and (2.49) into a linear dynamical system for the variables $\delta \rho_n / \rho_0$ and $\delta c_n / c_0$, given by

$$\frac{d}{dt} \frac{\delta \rho_n}{\rho_0} = \frac{\eta_s + \eta_b}{4\eta_b \eta_s} [\gamma + \xi f(c_0)] \left(1 - k_n^2 \rho_0^2 \right) \frac{\delta \rho_n}{\rho_0} - \frac{\xi c_0 \partial_c f(c_0)}{2\eta_b} \frac{\delta c_n}{c_0} \quad (2.50)$$

$$\frac{d}{dt} \frac{\delta c_n}{c_0} = -\frac{1}{2\eta_b} [\gamma + \xi f(c_0)] \left(1 - k_n^2 \rho_0^2 \right) \frac{\delta \rho_n}{\rho_0} + \left(\frac{\xi c_0 \partial_c f(c_0)}{\eta_b} - D k_n^2 - k \right) \frac{\delta c_n}{c_0}. \quad (2.51)$$

The coefficients of this linear system define the Jacobian \mathbf{J}_c^n for each mode n , whose eigenvalues indicate the stability of the homogeneous cylindrical surface for a given perturbation. In the remainder of this section, we briefly discuss analytic insights that can be gained from this Jacobian and finally present the global stability diagram. Note that the Jacobian is invariant under $n \leftrightarrow -n$, such that we restrict this analysis without loss of generality to $n \geq 0$. We again use the contractility parameter α defined in Eq. (2.33) to characterise mechano-chemical instabilities of the surface.

Plateau-Rayleigh instability

In the absence of regulation of active tension, $\partial_c f = 0$ or equivalently for $\alpha = 0$, the dynamics of shape perturbations described by Eq. (2.50) becomes independent of the concentration modes δc_n and we have

$$\frac{d}{dt} \delta \rho_n = \frac{\eta_s + \eta_b}{4\eta_b \eta_s} [\gamma + \xi f(c_0)] (1 - k_n^2 \rho_0^2) \delta \rho_n. \quad (2.52)$$

Using an ansatz $\delta \rho_n = \delta \rho_n^{(0)} \exp(\mu_n^c t)$, the prefactor of $\delta \rho_n$ on the right-hand side of Eq. (2.52) can be identified as the growth rate

$$\mu_n^c = \frac{\eta_s + \eta_b}{4\eta_b \eta_s} [\gamma + \xi f(c_0)] (1 - k_n^2 \rho_0^2) \quad (2.53)$$

of shape perturbations. Consider now a ‘short’ stable cylindrical surface for which $k_n^2 \rho_0^2 > 1$, such that we have $\mu_n^c < 0$. When continuously increasing the length L_0 of this cylinder, the smallest available wave number $k_1 = 2\pi/L_0$ becomes eventually small enough such that $\mu_1^c = 0$. At this point, the aspect ratio L_0/ρ_0 of the cylinder takes the value 2π . For aspect ratios with $L_0/\rho_0 > 2\pi$, we have $\mu_1^c > 0$ and the cylindrical surface is unstable. This represents the classical Plateau-Rayleigh scenario, in which the instability of the surface is fully determined by the surface geometry and is independent of the material properties of the surface [133, 134].

Onset of contractile instability

We now consider $\partial_c f(c_0) > 0$, or equivalently $\alpha > 0$, and analyse how the regulation of active tension affects the stability properties of the cylindrical surface. To gain first analytic insights into this questions, we analyse the trace of the Jacobian \mathbf{J}_c^n defined by Eqs. (2.50) and (2.51), which reads

$$\text{tr}(\mathbf{J}_c^n) = - \left(\hat{\nu} \frac{\gamma + \xi f(c_0)}{\eta_b} + \frac{D}{\rho_0^2} \right) k_n^2 \rho_0^2 + \hat{\nu} \frac{\gamma + \xi f(c_0)}{\eta_b} + \frac{\xi c_0 \partial_c f(c_0)}{\eta_b} - k. \quad (2.54)$$

Here, we have introduced $\hat{\nu} = (\eta_b + \eta_s)/(4\eta_s)$. To determine aspect ratios at which tubular surfaces with $\alpha > 0$ become unstable, we first have to establish a few equivalences. We start

by introducing a critical wavenumber k^* that is defined by $\text{tr}(\mathbf{J}_c^n) = 0$ and reads

$$k^* = \pm \frac{1}{\rho_0} \sqrt{\frac{\alpha\gamma - \eta_b k + \hat{\nu}[\gamma + \xi f(c_0)]/2}{\eta_b D/\rho_0^2 + \hat{\nu}[\gamma + \xi f(c_0)]/2}}. \quad (2.55)$$

Here, we have used the definition of the contractility parameter α given in Eq. (2.33). In the following, we consider parameters for which k^* is real.¹ We then conclude from Eq. (2.54) that

$$\text{tr}(\mathbf{J}_c^n) > 0 \quad \Leftrightarrow \quad |k_n| < |k^*|. \quad (2.56)$$

We note at this point that $\text{tr}(\mathbf{J}_c^n) > 0$ is a *sufficient condition* for an instability to occur [135]. Thus, if the length of a cylindrical surface is continuously increased, the smallest available wavenumber, $k_1 = 2\pi/L_0$, is eventually small enough such that $k_1 < |k^*|$ and the surface is guaranteed to be unstable. The critical wavenumber that is analogous to the Plateau-Rayleigh criterion, $|k^*|_{\rho_0} = 1$, defines via Eq. (2.55) a critical contractility parameter

$$\alpha_c^* = \frac{\eta_b}{\gamma} \left(\frac{D}{\rho_0^2} + k \right), \quad (2.57)$$

for which we see from Eq. (2.55) that

$$\alpha > \alpha_c^* \quad \Leftrightarrow \quad |k^*|_{\rho_0} > 1. \quad (2.58)$$

Hence, if $\alpha > \alpha_c^*$, there can exist a wavenumber k_1 with the property $|k^*|_{\rho_0} > k_1 \rho_0 > 1$ that belongs to an unstable cylindrical surface (because of Eq. (2.56)) with an aspect ratio $L_0/\rho_0 < 2\pi$. In other words, for a sufficiently large contractility parameter $\alpha > \alpha_c^*$, the aspect ratio L_0/ρ_0 at which cylindrical surfaces become unstable is decreased compared to the Plateau-Rayleigh value of 2π .

Even though the argument presented here seems rather coarse, the general stability diagram reveals that α_c^* given in Eq. (2.57) indeed specifies the minimal contractility parameter at which the mechano-chemical self-organisation of the surface becomes relevant.

General stability diagram

A general, representative stability diagram as a function of the contractility parameter α and the aspect ratio L_0/ρ_0 (normalised to 2π) is shown in Fig. 2.4. For $\kappa = 0$ the cylinder surface is unstable in the blue-shaded region. For $\alpha < \alpha_c^*$ with α_c^* given in Eq. (2.57), the instability occurs when the aspect ratio L_0/ρ_0 increases beyond a critical value that equals 2π and is independent of the contractility parameter α . This instability corresponds to the geometric Plateau-Rayleigh instability and is not driven by the self-organisation of the stress regulator. As discussed above, the case $\alpha = 0$ and $\kappa = 0$ exactly represents the classical

¹Further analysis of the determinant of \mathbf{J}_c^n shows that the contractility regulation is irrelevant for the surface stability if k^* is complex.

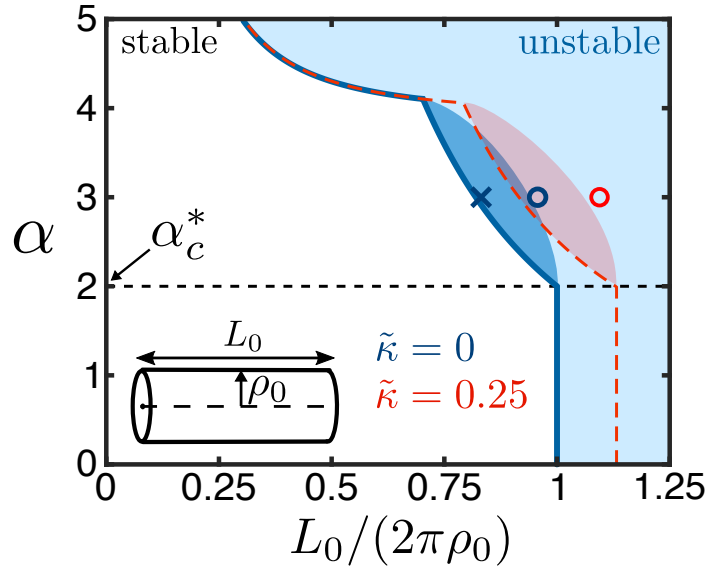


Figure 2.4: Representative stability diagram of a cylindrical active fluid surfaces with concentration-dependent active tension. Stable and unstable regions are separated by the blue curve for $\kappa = 0$ and the dashed line for $\tilde{\kappa} = 0.25$, where $\tilde{\kappa} = \kappa/(\gamma r_0^2)$. For $\kappa = 0$ the dark blue shaded region indicates parameter regimes where eigenvalues of the Jacobian defined by Eqs. (2.50) and (2.51) are complex. The red shaded region indicates complex eigenvalues of the Jacobian for $\tilde{\kappa} = 0.25$. To contractility parameter α is defined in Eq. (2.33) and the critical contractility α_c^* is given in Eq. (2.57). For $\alpha < \alpha_c^*$ unstable aspect ratios are independent of α , corresponding to a Plateau-Rayleigh instability. For $\alpha > \alpha_c^*$ instabilities are driven by the mechano-chemical self-organisation of the surface. The cross and the two circles depict parameter values for which we discuss the corresponding nonlinear dynamics in Sections 2.4.2 and 2.4.3. Parameters used for the stability: $k\tau = 1.95$, $D\tau/\rho_0^2 = 0.05$, $\eta_s/\eta_b = 1$, $f(c_0) = 1/2$, where $\tau = \eta_b/\gamma$ denotes the characteristic time scale.

Plateau-Rayleigh scenario [133]. For $\alpha > \alpha_c^*$ instabilities are driven by the mechano-chemical self-organisation of the fluid surface. In this regime the aspect ratio L_0/ρ_0 at which the cylinder surface becomes unstable is smaller than 2π and decreases for increasing contractility parameter α . Furthermore, the linear stability analysis reveals a region where eigenvalues are complex (dark blue-shaded area in Fig. 2.4), which indicates oscillatory behaviour at the instability. These characteristics of the stability diagram remain qualitatively unchanged when the bending rigidity κ is finite. The instability line for $\kappa = 0.25\gamma\rho_0^2$ is shown as a red dashed line in Fig. 2.4. The red-shaded region indicates complex eigenvalues. Note that the value of α_c^* in general depends on κ (Appendix D.4.3).

2.4.2 Spontaneous constriction and shape oscillations

We now study the surface dynamics beyond the linear regime using our numerical approach. For $\kappa = 0$, $\alpha > \alpha_c^*$ and aspect ratios L_0/ρ_0 inside the unstable region of the stability diagram (blue circle in Fig. 2.4), the cylinder surface constricts and generates a thin cylindrical neck region with decreasing radius (Fig. 2.5 a). The numerical analysis indicates that this

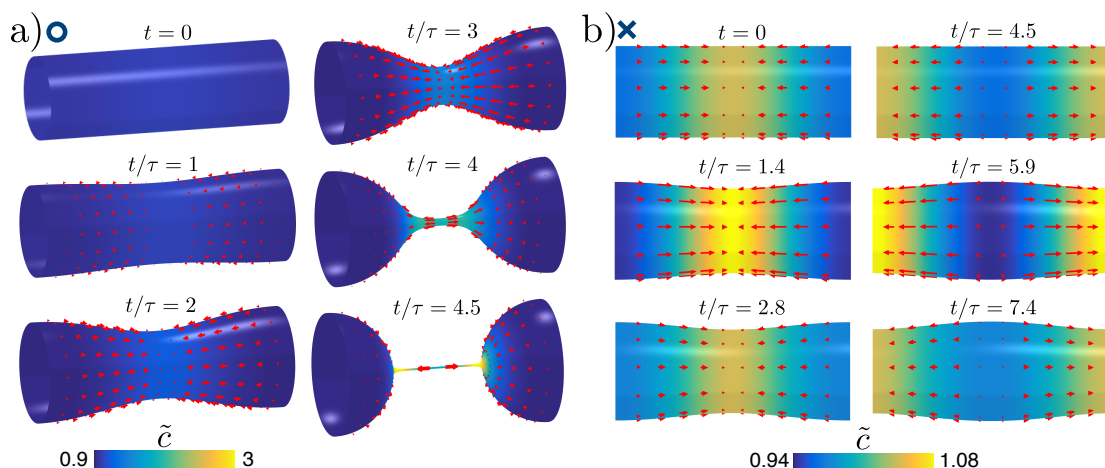


Figure 2.5: Self-organised tubular surface dynamics for $\kappa = 0$. **a)** Concentration $\tilde{c} = c/c_0$ and in-plane flow \mathbf{v}_{\parallel} (red arrows) during the spontaneous formation of a contractile ring for parameters indicated with a blue circle in the stability diagram Fig. 2.4. As characteristic time we use $\tau = \eta_b/\gamma$. The self-organised contractile ring can constrict surfaces with aspect ratios L_0/ρ_0 below the Plateau-Rayleigh threshold of 2π . **b)** Concentration and in-plane flow over one oscillation period for parameters indicated with a blue cross in the stability diagram Fig. 2.4. Oscillations result from the interplay between geometric stability of cylinder surfaces with $L_0/\rho_0 < 2\pi$ and the mechano-chemical instability of the active, contractile fluid film. Surface flows are shown in the reference frame where $\int_0^L v_s ds = 0$ (see Appendix D.3.3). The parameters used in these simulations are given in Appendix D.6.3.

radius vanishes at finite time. The concentration of the stress regulator increases along the tubular neck. For parameters that correspond to complex eigenvalues in the linear stability diagram (blue cross in Fig. 2.4), the cylinder constricts and expands periodically (Fig. 2.5 b) with increasing amplitude until the neck radius vanishes. For $\alpha < \alpha_c$ the instability also leads to a tubular neck with vanishing radius, however not driven by contractility but by surface tension γ due to the Plateau-Rayleigh character of the instability in this parameter regime. In this case, the concentration of stress regulator increases in the neck predominantly because of a local reduction of surface area.

2.4.3 Directed flows and peristaltic surface dynamics

For $\kappa > 0$, an unstable cylinder surface constricts and reaches a finite neck radius together with a homogeneous concentration of stress regulator on the surface. For $\alpha < \alpha_c^*$ this remains the stationary state at long times. For $\alpha > \alpha_c^*$ a high concentration of stress regulator builds up in the neck region at long times. The concentration pattern and surface flows that emerge spontaneously break the mirror symmetry with respect to the z -axis (Fig. 2.6 a). As a consequence, average flows directed along the z -axis occur in a reference frame, where the constriction does not move. Numerical results reveal that such directed flows emerge in all parameter regimes for which the cylinder surface is linearly unstable and $\alpha > \alpha_c^*$. For $\alpha < \alpha_c^*$ no directed flows occur. To finally test if the stabilisation of a finite neck radius is sufficient

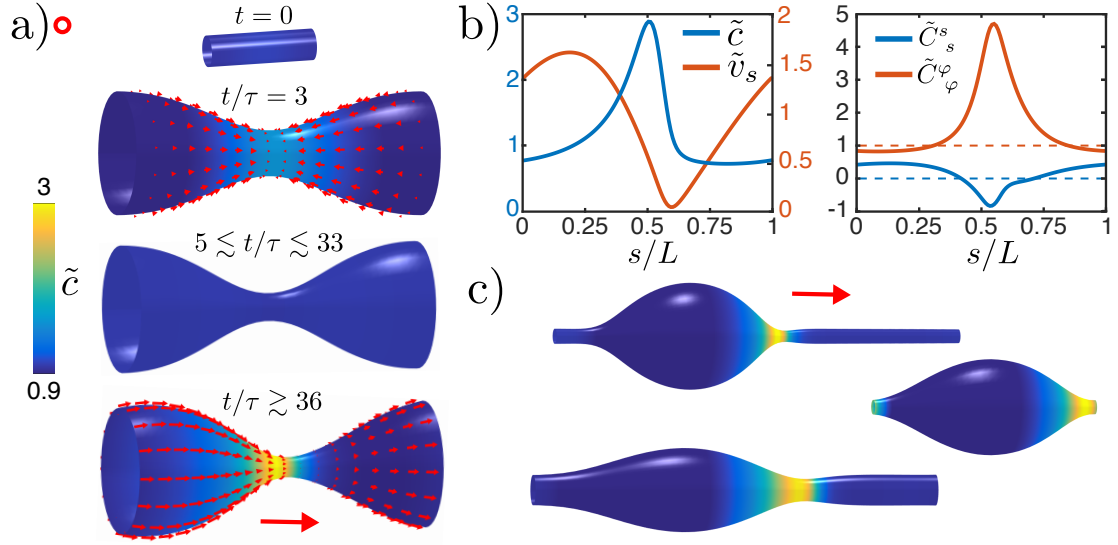


Figure 2.6: Emergence of directed flows on tubular surfaces with $\kappa > 0$. **a)** Concentration $\tilde{c} = c/c_0$ and in-plane flow \mathbf{v}_{\parallel} (red arrows) during the spontaneous formation of directed surface flows for parameters indicated with a red circle in the stability diagram Fig. 2.4. After a perturbation that is mirror-symmetric in z -direction, the tubular surface ingresses and forms a homogeneous, transiently stationary shape. At long times (for the parameters chosen here $t/\tau \gtrsim 36$, $\tau = \eta_b/\gamma$), the mirror symmetry is broken and a steady state emerges that shows directed surface flows relative to a constricted shape. **b)** In-plane flow velocity $\tilde{v}_s = \mathbf{e}_s \cdot \mathbf{v}\tau/\rho_0$ and principle curvatures $\tilde{C}_s^s = \rho_0 C_s^s$, $\tilde{C}_\varphi^\varphi = \rho_0 C_\varphi^\varphi$ of the final steady state shown in a). Surface flows in a) and b) are shown in the reference frame where the constriction does not move (see Appendix D.3.3). **c)** Exemplary surface shapes and concentration profiles of tubular surfaces at steady state with varying bending rigidities and aspect ratios (all other parameters are the same). The single red arrow indicates the average flow direction (also depicted in a)). From top to bottom: $\kappa/(\gamma\rho_0^2) = \{0.25, 0.25, 0.8\}$ and $L/\rho_0 = \{5\pi, 2.2\pi, 5\pi\}$. A complete overview of the parameters used in these simulations is given in Appendix D.6.3.

for directed flows to occur via spontaneous symmetry breaking, we chose $\kappa = 0$ and consider instead an external force $\mathbf{f}^{\text{ext}} = F_0(\rho_0/\rho - 1)\bar{\mathbf{e}}_r$ that also stabilises small neck radii. In this setting, we again find the formation of directed flows relative to the constricted shape. This shows that the spontaneous symmetry breaking for $\alpha > \alpha_c^*$ is an intrinsic property of the self-organised active fluid film and its tight coupling to the surface geometry.

2.4.4 Neck radii of tubular surfaces with bending rigidity

As described in the previous section, unstable cylindrical surfaces with bending rigidity form transiently stationary surfaces with finite neck radii at long times. The onset of directional flows hardly changes the transiently stable surface geometry (Fig 2.6a). Here, we study the scaling of the neck radii of these surfaces. To this end, we introduce a toy model for tubular surface shapes and neglect for simplicity local inhomogeneities in tension due to contractility and flows. Instead, we consider an effective homogeneous tension $\bar{\gamma}$, such that force-balanced

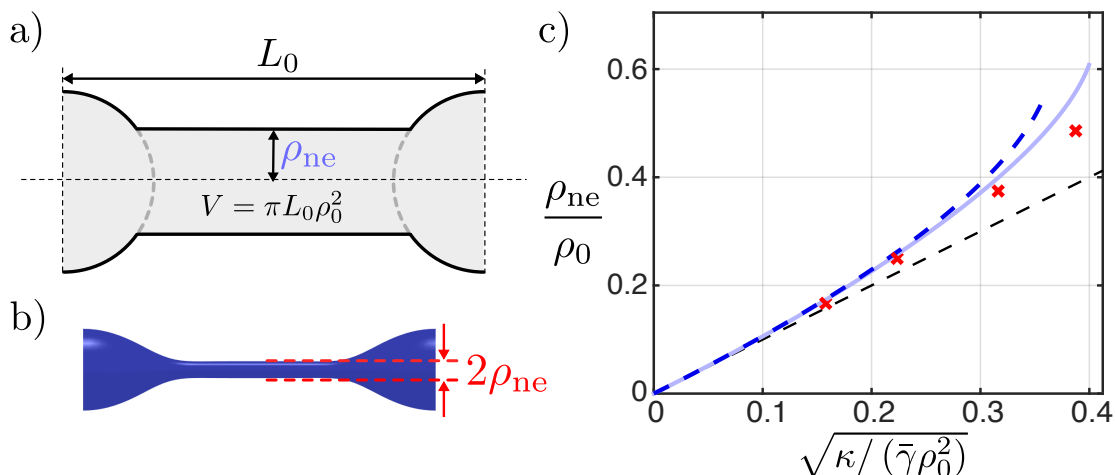


Figure 2.7: Quantitative description of tubular neck radii. **a)** Parameters used to approximate tubular surface geometries in a toy model, which consists of two inverted spherical caps that are connected by a cylinder with neck radius ρ_{ne} . For fixed total length L_0 and volume $V = \pi L_0 \rho_0^2$, the neck radius ρ_{ne} is the only free parameter to uniquely describe this geometry. **b)** Pictorial definition of the neck radius for stationary tubular surfaces that are extracted from numerical solutions of the full nonlinear surface description (red crosses in c). **c)** Comparison of the toy-model with numerical results. The solid blue line depicts minima of the Helfrich energy Eq. (2.7) parametrised by the geometry shown in a). The blue dashed line corresponds to minima of the expansion of F_H in the neck radius Eq. (2.60). As a reference, we added the curve $\rho_{\text{ne}} = \sqrt{\kappa/\bar{\gamma}}$ to the plot (black dashed line), which is the neck radius attained by tubular surfaces with $L_0/\rho_0 \gg 1$.

surfaces correspond to stationary shapes of the Helfrich energy F_H given in Eq. (2.7).

To parametrise the Helfrich energy, we approximate surface shapes by two inverted spherical caps that are connected by a cylindrical neck (Fig. 2.7 a). For fixed total length L_0 and enclosed volume $V = \pi L_0 \rho_0^2$, the radius of the connecting cylinder – the neck radius ρ_{ne} – is the only free parameter of this geometry. Note that for given L_0 , the fixed volume V defines the initial cylinder radius ρ_0 , which is the parameter we use from now on. Equilibrium shapes and corresponding neck radii can then be found from

$$\left. \frac{\partial F_H}{\partial \rho_{\text{ne}}} \right|_{\rho_0, L_0} = 0, \quad (2.59)$$

with F_H given in Eq. (2.7) evaluated for shapes that are parametrised as just described. For the discussion here, it is useful to consider the expansion of the corresponding Helfrich energy F_H up to second order in the neck radius, which reads (Appendix D.5)

$$F_H \approx F_0 + A\rho_{\text{ne}} + \frac{B}{\rho_{\text{ne}}} + C\rho_{\text{ne}}^2. \quad (2.60)$$

Here, the coefficients F_0 , A , B and C depend on L_0 , ρ_0 , $\bar{\gamma}$ and κ and are given in the appendix Eqs. (D.96)–(D.99).

In the next step, we determine stationary neck radii from the full nonlinear description of

tubular surfaces with a fixed aspect ratio and varying bending rigidity. For simplicity, we only consider the transient homogeneous steady states to extract numerical values of neck radii. Accordingly, we use $\bar{\gamma} = \gamma + \xi f(c_0)$ as approximation for the effective homogeneous tension in the toy model when comparing it to neck radii these numerical values. The neck radius scaling as a function of the bending rigidity (Fig. 2.7 c) can be understood by first considering the limit of large aspect ratios: $L_0/\rho_0 \gg 1$. In this limit, neck radius-dependent contributions of the spherical caps to the energy are negligible and we find from Eq. (2.60) to leading order in L_0/ρ_0 :

$$F_H - F_0 = 2\pi L_0 \left(\bar{\gamma} \rho_{\text{ne}} + \frac{\kappa}{\rho_{\text{ne}}} \right), \quad (2.61)$$

Here, we have used the corresponding limits of the coefficients A, B and C given in Appendix D.5. From Eq. (2.61), we see that the equilibrium neck radius in this limit takes the value $\sqrt{\kappa/\bar{\gamma}}$ (black dashed line in Fig. 2.7 c). However, if the aspect ratio L_0/ρ_0 becomes finite, a new relevant quadratic term in the expansion of F_H , Eq. (2.60), appears. This term can be traced back to the conservation of the enclosed volume: tubes, which form a small neck, gain relevant energetic contributions from surface regions that have to bulge out elsewhere. In our toy model these bulged out surface regions are represented by the spherical caps. The important observation is that the lowest order contribution that describes this effect in Eq. (2.60) is negative ($C < 0$). Hence, the quadratic term $C\rho_{\text{ne}}^2$ acts effectively as an elastic spring that penalises small neck radii.¹ The minima of Eq. (2.60) then yield equilibrium neck radii with $\rho_{\text{ne}} > \sqrt{\kappa/\bar{\gamma}}$ (blue dashed line in Fig. 2.7 c). Neck radii that follow from Eq. (2.59) for the general parametrisation of F_H in terms of the toy model geometry are depicted as solid blue line in Fig. 2.7 c (see Appendix D.5). Numerically obtained neck radii are depicted by red crosses.

2.5 Discussion

In this chapter, we presented a simple but general model for the mechano-chemical self-organisation of surface geometry. Active stresses in the surface are regulated by a diffusible and advected molecular species. Gradients of active stress induce surface flows and shape changes, which in turn influence the distribution of the stress regulator. As a consequence, shape changes, shape oscillations and spontaneous surface flows can be generated via mechano-chemical instabilities. In contrast to mechano-chemical instabilities that have been previously studied on fixed geometries [117, 120, 124, 136], we described here new phenomena that give rise to shape changes and crucially depend on the shape changes that occur.

To solve the dynamic equations for the shape, flows and concentration fields, we developed

¹The energy is still bound for large radii because the neck radius is geometrically constraint to $\rho_{\text{ne}} \leq \rho_0$.

a numerical approach based on an integral representation of axisymmetric surfaces (Section 2.2). We introduced a time-dependent coordinate transformation, which allowed us to obtain the shape dynamics in an implicit surface representation. Explicit coordinates of surface points can be calculated independently. This implicit representation drastically simplifies the numerical scheme to solve vector-valued partial differential equations on the deforming surface. Such a simplification would not be available, for example, when level-set methods are used [137]. The latter methods provide on the other hand a more flexible way to represent non-axisymmetric, deforming surfaces and their topological changes [132]. However, the discretisation of vector-valued partial differential equations within a level-set framework requires additional operations to extend vector fields into the embedding space [138, 139], which is not the case for the method developed here.

Using our approach, we identified a mechano-chemical shape instability of a sphere (Section 2.3). Beyond a critical value α_s^* of the contractility parameter, this instability leads to concentration and flow patterns with a polar asymmetry, and to an axisymmetric oblate shape with broken mirror symmetry. In addition, we note that shape changes associated with the unstable polar mode do not change the curvature to linear order. As a result, the critical contractility parameter α_s^* is independent of the bending rigidity.

We then studied periodic tubular surfaces (Section 2.4). We found contractility-induced instabilities of cylindrical surfaces beyond a critical value α_c^* , and a Plateau-Rayleigh instability for contractility parameters smaller than α_c^* . The Plateau-Rayleigh instability occurs when the aspect ratio of the cylinder surface reaches 2π [133]. Beyond α_c^* , we find that the cylinder becomes unstable already at aspect ratios smaller than 2π . Near the point that separates the two regimes, we found that the contractile instability is oscillatory. This could result from a competition between a weak contractile instability and the stability of the cylinder with respect to the Plateau-Rayleigh criterion in this parameter region.

On tubular surfaces for which a small neck radius is stabilised at long times, we described a pearling instability [140], which is followed by the emergent formation of directed surface flows via spontaneous symmetry breaking. In a reference frame, where the average of the surface velocity vanishes, this results in a propagating surface constriction that resembles the dynamics of a peristaltic wave. A toy model, which incorporates the conservation of the enclosed volume, can quantitatively account for neck radii that are obtained from numerical solutions of the full nonlinear problem. Interestingly, propagating pearling instabilities have been previously studied experimentally and theoretically in passive tubular vesicles [140–142]. For these systems, it was shown that a local laser-induced modification of surface tension can trigger peristaltic surface motion, qualitatively similar to those described here on a self-organised active surface.

We focused here on the shape dynamics of axisymmetric surfaces and materials that are isotropic in the surface plane. The generalisation of our approach to non-axisymmetric sur-

faces was beyond the scope of this thesis. However, it represents an important task to be tackled in the future, especially because many biological systems generate shapes that are not axisymmetric. For example, many dynamic processes in cells and tissues break the axisymmetry, including cell migration or gastrulation events [32, 79, 95, 143, 144]. Additionally, active surfaces in natural biological systems or generated *in-vitro* are often anisotropic. Examples are given by the planar polarity in epithelial tissues [72] or the polar and nematic anisotropies in cytoskeletal systems [108]. Studying the shape dynamics of active nematic vesicles containing topological defects [145, 146] also requires a representation of non-axisymmetric deforming surface, which provides important challenges for future work.

Chapter 3

Symmetry breaking on an active fluid surfaces in viscous environments

In this chapter, we study the mechano-chemical self-organisation of an isotropic active fluid film on a sphere. In contrast to the previous chapter, we consider the general, non-axisymmetric dynamics on a fixed surface. Additionally, we take external shear stresses from a surrounding passive fluid into account.

The chapter is organised as follows. In Section 3.1, we introduce the constitutive relations of a self-organised active fluid on a fixed surface. Furthermore, we derive the explicit form of shear stresses from a passive fluid in which the active surface is embedded. Additionally, a closed solution for the full nonlinear system is presented. We then consider two scenarios of mechano-chemical self-organisation that this model can represent. First, in Section 3.2, we study the mechano-chemical patterning processes on the active surface, and we investigate how they are affected by shear stresses from an interior¹ passive fluid. We find that the symmetry of the homogeneous state can be spontaneously broken, and mechano-chemical patterns with polar and nematic asymmetries emerge. This description can represent, for example, the dynamics of the cellular cortex that is in contact with the cytoplasmic fluid. Second, in Section 3.3, we focus on interactions with an exterior passive fluid. This represents a squirmer model, in which spontaneously emerging active surface flows can lead to a force-free, translational motion of the surface. We characterise the bifurcation associated with the spontaneous onset of motion by performing a weakly nonlinear analysis for this system. We conclude with a summary and discussion of the main results in Section 3.4.

¹We refer to the domain that is enclosed by the surface as *interior* and to the domain outside as *exterior*. Note that this is distinct from *internal* and *external*, which we use to distinguish, for example, internal forces and moments within the surface (described by the tension and moment tensors) and external forces acting on it.

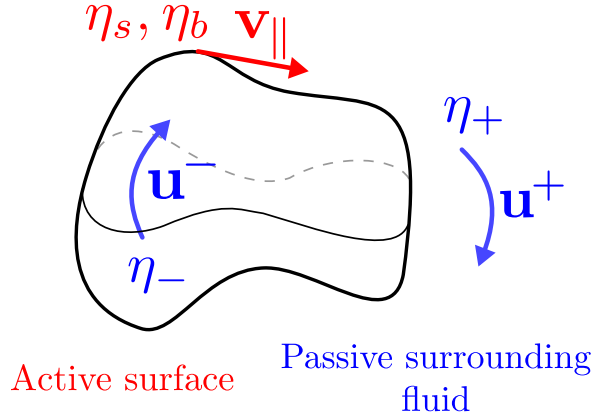


Figure 3.1: Sketch of the model that is discussed in this chapter. Quantities related to the active surface are shown in red, quantities related to the passive surrounding fluid are shown in blue. We consider flows \mathbf{v}_{\parallel} on a closed and fixed active fluid surface with shear and bulk viscosities η_s and η_b , respectively. This surface is surrounded by a passive incompressible fluid, where the viscosity of the fluid enclosed by the surface is denoted by η_- , the viscosity of the fluid outside the surface by η_+ . The flow fields in each domain are accordingly denoted by \mathbf{u}^- and \mathbf{u}^+ . Active surface flows can set the passive fluid into motion, which leads to shear stresses that can feed back on the surface flows.

3.1 Self-organised active fluid surface in a viscous environment

In this section, we introduce the description of an active self-organised fluid surface that is embedded in a passive fluid. We derive a closed solution of the nonlinear problem for the case in which the active surface is a sphere. The results presented in this section provide the basis for a detailed characterisation of the mechano-chemical self-organisation and symmetry breaking that occurs in this model and which will be discussed further in Sections 3.2 and 3.3.

3.1.1 Constitutive relations and governing equations for the active surface

We consider an isotropic viscous thin film on a fixed surface $\bar{\Gamma}$ with constitutive relation

$$t_{ij} = 2\eta_s \left(v_{ij} - \frac{1}{2} v_k^k g_{ij} \right) + \eta_b v_k^k g_{ij} + t_{ij}^a, \quad (3.1)$$

where

$$v_{ij} = \frac{1}{2} (\nabla_i v_j + \nabla_j v_i) \quad (3.2)$$

is the symmetric strain rate tensor on a fixed surface.¹ Here, v_i denotes components of the tangential flow field $\mathbf{v}_{\parallel} = v^i \mathbf{e}_i$, and η_s and η_b denote shear and bulk viscosities of the surface, respectively. As for the deforming surfaces discussed in Chapter 2, we consider an isotropic

¹In the interest of a simple notation, we consider here the strain rate tensor defined in Eq. (2.10) restricted to a fixed surface and therefore do not introduce a new symbol. We exclusively study fixed surfaces in this chapter, such that this should not lead to any confusion.

active tension

$$t_{ij}^a = \xi f(c) g_{ij}, \quad (3.3)$$

where the contractility ξ is modulated by the concentration field c of a stress-regulating chemical species. The function $f(c)$ is specified together with the concrete problems studied in Sections 3.2 and 3.3. The dynamics of the concentration field c is determined by the advection-diffusion-reaction equation

$$\partial_t c = -\nabla_i (c v^i) + D \Delta_{\bar{\Gamma}} c + R(c). \quad (3.4)$$

Here, $\Delta_{\bar{\Gamma}}$ denotes the Laplace-Beltrami operator, D is the diffusion constant and $R(c)$ represents reactions that describe the turnover of stress regulator. Neglecting inertial forces, the force balance equation reads

$$\nabla_j t_i^j = -f_i^{\text{ext}}. \quad (3.5)$$

With t_{ij} given in Eq. (3.1), the force balance Eq. (3.5) determines surface flows v_i for a given distribution of active tension and external forces f_i^{ext} . In the present chapter, we are interested in the case where the latter result from interactions of active surface flows with a surrounding passive fluid. The explicit form of these external forces is derived in the next section.

3.1.2 Mechanical interactions of surfaces with a surrounding fluid

In the following, we derive the hydrodynamic stress that is exerted by a viscous fluid onto a curved surface. We first formulate this problem for a general surface with a prescribed surface flow velocity $\mathbf{v}_{\parallel} = v^i \mathbf{e}_i$. This surface flow sets the surrounding fluid into motion, which results in shear stresses that are acting back onto the surface. We then present an explicit solution for the case where the surface is given by a sphere. This is also the geometry that is considered throughout the remainder of the present chapter.

We consider a surface embedded in an incompressible Stokes fluid that is described by the constitutive relation

$$\boldsymbol{\sigma} = \eta \left(\nabla \mathbf{u} + (\nabla \mathbf{u})^T \right) - p \mathbb{I}. \quad (3.6)$$

Here, \mathbf{u} denotes the flow field of the Stokes fluid, η is its viscosity and p is the pressure that is determined by the incompressibility condition $\nabla \cdot \mathbf{u} = 0$. The superscript T in Eq. (3.6) denotes the transpose of the dyadic tensor $\nabla \mathbf{u}$. Equation (3.6) describes the fluid on the domain enclosed by (*interior*) and outside the surface (*exterior*). In the following, we denote fields and parameters on the interior (exterior) domain with an additional index ‘-’ (‘+’). Neglecting inertial terms, the force balance reads $\nabla \cdot \boldsymbol{\sigma}^{\pm} = 0$ and leads to the Stokes equation

$$\eta_{\pm} \Delta \mathbf{u}^{\pm} = \nabla p^{\pm}. \quad (3.7)$$

As boundary conditions for the Stokes flow, we consider impermeability and no-slip conditions on the surface:

$$\mathbf{u}^\pm \cdot \mathbf{n}|_\Gamma = 0 \quad (3.8)$$

$$\mathbf{u}^\pm \cdot \mathbf{e}_i|_\Gamma = v_i. \quad (3.9)$$

With this, the force that is exerted by the passive fluid onto the surface can be written as

$$\mathbf{f}^\eta = \mathbf{n} \cdot (\boldsymbol{\sigma}^+ - \boldsymbol{\sigma}^-)|_\Gamma, \quad (3.10)$$

where \mathbf{n} is the outward pointing surface normal and $\boldsymbol{\sigma}^\pm$ denote the stress tensor Eq. (3.6) evaluated for the corresponding flow fields \mathbf{u}^\pm and viscosities η_\pm in the interior and exterior domains.

To determine \mathbf{f}^η , we have to solve the Stokes Eq. (3.7) on the interior and exterior domains with boundary conditions Eqs. (3.8) and (3.9) and use this solution in Eq. (3.6). For a flow field that is prescribed on the surface of a sphere, this problem can be solved analytically (Appendix B.2). To provide the details that are most relevant for this chapter, we present this solution here briefly for a non-deforming surface of a sphere with radius R . We consider tangential flows $\mathbf{v}_\parallel(\theta, \varphi)$ on this sphere and expand their covariant components¹ $v_i(\theta, \varphi) = \mathbf{e}_i \cdot \mathbf{v}_\parallel$ as

$$v_i = \sum_{l,m} \left(v_{lm}^{(1)} \Psi_i^{(lm)} + v_{lm}^{(2)} \Phi_i^{(lm)} \right). \quad (3.11)$$

Here, $\sum_{l,m} = \sum_{l=0}^{\infty} \sum_{m=-l}^l$, and $\Psi_i^{(lm)}(\theta, \varphi) = \partial_i Y_{lm}$ and $\Phi_i^{(lm)}(\theta, \varphi) = \epsilon^j_i \Psi_j^{(lm)}$ are covariant components of vector spherical harmonics that are constructed from scalar spherical harmonics $Y_{lm}(\theta, \varphi)$ (Appendix B.1.2). In this general expansion, we take into account all harmonic modes, including the non-axisymmetric ones with $m \neq 0$. We then have for each l a set of $2l + 1$ modes labelled by $m \in \{-l, -l + 1, \dots, l - 1, l\}$. To determine a solution for the Stokes Eq. (3.7), we consider an ansatz for the pressure $p(r, \theta, \varphi) = \sum_{l,m} p_{lm}(r) Y_{lm}$ and an ansatz for the fluid flow $\mathbf{u}(r, \theta, \varphi)$ given by

$$\mathbf{u} = \sum_{l,m} \left(u_{lm}^r(r) \mathbf{Y}^{(lm)} + u_{lm}^{(1)}(r) \boldsymbol{\Psi}^{(lm)} + u_{lm}^{(2)}(r) \boldsymbol{\Phi}^{(lm)} \right), \quad (3.12)$$

where $\mathbf{Y}^{(lm)}(\theta, \varphi) = Y_{lm} \mathbf{n}$, $\boldsymbol{\Psi}^{(lm)} = \mathbf{e}^i \Psi_i^{(lm)}$ and $\boldsymbol{\Phi}^{(lm)} = \mathbf{e}^i \Phi_i^{(lm)}$. Using this ansatz in the Stokes Eq. (3.7), one finds a system of ordinary differential equations for the coefficient functions $p_{lm}(r)$, $u_{lm}^r(r)$, $u_{lm}^{(1)}(r)$ and $u_{lm}^{(2)}(r)$. This system can be solved by a power law ansatz in r and the integration constants are found using the boundary conditions Eqs. (3.8) and (3.9),

¹Note that we consider here the specific parametrisation of a unit sphere \mathcal{S} given by $\mathbf{X}(\theta, \varphi) = \bar{\mathbf{e}}_r$ (Appendix A.3.2), but keep the covariant component notation to describe vector fields on the surface for simplicity. For the basis vectors this implies $\mathbf{e}_1 = \bar{\mathbf{e}}_\theta$, $\mathbf{e}_2 = \sin \theta \bar{\mathbf{e}}_\varphi$, $\mathbf{n} = \bar{\mathbf{e}}_r$, where $\{\bar{\mathbf{e}}_r, \bar{\mathbf{e}}_\theta, \bar{\mathbf{e}}_\varphi\}$ is the orthonormal standard basis of spherical coordinates.

with v_i given in Eq. (3.11) (Appendix B.2.2). From this, we can determine the force Eq. (3.10) that arises from viscous shear stresses acting on the surface. For a fixed surface, only the tangential components $f_i^\eta = \mathbf{e}_i \cdot \mathbf{f}^\eta$ of this force are relevant and we find that they can be expressed as

$$f_i^\eta = \sum_{l,m} \left(f_{lm}^{\eta,(1)} \Psi_i^{(lm)} + f_{lm}^{\eta,(2)} \Phi_i^{(lm)} \right), \quad (3.13)$$

with

$$R f_{lm}^{\eta,(1)} = -(\eta_- + \eta_+) (1 + 2l) v_{lm}^{(1)} + \eta_+ v_{lm}^{(1)} \delta_{l,1} \quad (3.14)$$

$$R f_{lm}^{\eta,(2)} = -[\eta_- (-1 + l) + \eta_+ (2 + l)] v_{lm}^{(2)}. \quad (3.15)$$

Details of this derivation can be found in Appendix B.2. The important result here is that we can write the general non-axisymmetric expansion of external shear forces Eq. (3.13) in a covariant expansion of vector harmonics that compresses the solution of the Stokes boundary value problem into a set of simple coefficients given by Eqs. (3.14) and (3.15).

3.1.3 Closed solution of the nonlinear problem

In the following, we derive a closed solution for the dynamics of the self-organised fluid surface that interacts with a surrounding passive fluid as introduced in Sections 3.1.1 and 3.1.2.

The constitutive relations of the active fluid surface Eq. (3.1), as well as the external viscous forces derived in the previous section are linear in the surface flows v_i . Therefore, an analytic solution for v_i of the force balance Eq. (3.5) can be found for a given distribution of active tension $t_{ij}^a = \xi f(c) g_{ij}$, which we derive in the first part of this section. In the second part, we use this result to derive a closed solution for the nonlinear dynamic problem that is based on a harmonic projection of the nonlinear advection term in Eq. (3.4).

General solution of the force balance equation

The force balance Eq. (3.5) in terms of the constitutive relations Eq. (3.1) can be written as

$$\frac{\eta_s}{R^2} \left(\nabla_j \nabla^j v_i + v_i \right) + \frac{\eta_b}{R^2} \nabla_i \nabla_j v^j + \frac{\xi}{R} \partial_i f(c) = -f_i^{\text{ext}}, \quad (3.16)$$

where R is the radius of the sphere. Recall that vector components and covariant derivatives are defined here with respect to the parametrisation of the unit sphere. Hence, there are no length scales ‘hidden’ in the covariant derivative and in the basis vectors, such that we can simply factor out powers of R as done in Eq. (3.16). The form of the shear part in Eq. (3.16) follows from the Ricci identity Eq. (A.28), which takes into account the non-commutativity of the covariant derivative of vector fields on curved surfaces. Physically, this implies that a

fluid, which flows on a curved surface, can shear due to purely geometric effects.¹

Next, we expand the regulating function $f(c(\theta, \varphi))$ in terms of spherical harmonics Y_{lm} :

$$f(c) = \sum_{l,m} f_{lm} Y_{lm}. \quad (3.17)$$

Using Eq. (3.17), together with the expansion of the surface flow v_i given in Eq. (3.11), in the force balance Eq. (3.16), we find

$$\sum_{l,m} \left\{ \frac{\eta_s}{R^2} (1-l)(l+2) \left(v_{lm}^{(1)} \Psi_i^{(lm)} + v_{lm}^{(2)} \Phi_i^{(lm)} \right) - \frac{\eta_b}{R^2} l(l+1) v_{lm}^{(1)} \Psi_i^{(lm)} + \frac{\xi}{R} f_{lm} \Psi_i^{(lm)} \right\} = -f_i^{\text{ext}}. \quad (3.18)$$

Here, we have used the definition of the vector harmonic modes $\Psi_i^{(lm)} = \partial_i Y_{lm}$, as well as a set of identities given in the appendix (Eqs. (B.13)–(B.16)) to evaluate the covariant derivatives in Eq. (3.16). For the external forces, we consider interactions with a surrounding passive fluid $f_i^{\text{ext}} = f_i^\eta$, with f_i^η given explicitly in terms of the velocity modes $v_{lm}^{(1)}$ and $v_{lm}^{(2)}$ in Eq. (3.13). From the orthogonality of the vector spherical harmonics it then follows that $v_{lm}^{(2)} = 0$ and

$$v_{lm}^{(1)} = \frac{R\xi f_{lm}}{R(\eta_- + \eta_+)(1+2l) - R\eta_+ \delta_{l,1} + (\eta_b + \eta_s)l(l+1) - 2\eta_s}. \quad (3.19)$$

Recall that R denotes the radius of the sphere, ξ the active contractility, η_b and η_s the bulk and the shear viscosity of the surface and η_\pm the viscosity of the interior (–) and exterior (+) passive fluid. With the coefficients given in Eq. (3.19), the expansion of surface flows Eq. (3.11) into vector harmonics represents a general solution of the force balance Eq. (3.5) for an arbitrary distribution of active tension $t_{ij}^a = \xi f(c) g_{ij}$.

Dynamic equation for the concentration field

To express a solution of the general problem, where active flows redistribute the stress regulator dynamically, we expand the concentration field $c(\theta, \varphi)$ in terms of scalar spherical harmonics:

$$c = \sum_{l,m} c_{lm} Y_{lm}. \quad (3.20)$$

¹Another perspective can be taken by considering a translation of the sphere. One finds that the shear term $\nabla_j \nabla^j v_i + v_i$ in Eq. (3.16) vanishes for the tangential contributions of this translation. This shows that, only if the surface curvature is properly taken into account, the shear term is written such that translations do not contribute to shear on the surface.

Plugging this expansion into the dynamic equation of the concentration field Eq. (3.4) and considering a turnover dynamics in the form

$$R(c) = -k(c - c_0), \quad (3.21)$$

we find

$$\begin{aligned} \sum_{l,m} \frac{d}{dt} c_{lm} Y_{lm} &= k c_0 - \sum_{l,m} \left(\frac{D}{R^2} l(l+1) + k \right) c_{lm} Y_{lm} \\ &+ \sum_{l,m} \sum_{l',m'} c_{lm} \left(v_{l'm'}^{(1)} \Psi^{(lm)} \cdot \Psi^{(l'm')} - v_{l'm'}^{(1)} l'(l'+1) Y_{lm} Y_{l'm'} \right). \end{aligned} \quad (3.22)$$

Here, we have again used the definitions of the vector harmonics, as well as $v_{lm}^{(2)} = 0$. The nonlinear expression in the second line of Eq. (3.22) arises from the advection term in the dynamic equation of the concentration field. A projection of Eq. (3.22) on scalar spherical harmonics yields

$$\frac{d}{dt} c_{lm} = 2\sqrt{\pi} k c_0 \delta_{l,0} - \left(\frac{D}{R^2} l(l+1) + k \right) c_{lm} + A_{lm}. \quad (3.23)$$

The prefactor of the first term stems from the normalisation of the scalar spherical harmonics. The mode coefficients A_{lm} correspond to the projection of the advection term and read

$$A_{lm} = \frac{1}{2R} \sum_{l_1, m_1} \sum_{l_2, m_2} c_{l_1 m_1} v_{l_2 m_2}^{(1)} [l(l+1) + l_2(l_2+1) - l_1(l_1+1)] \int d\Omega Y_{l_1 m_1} Y_{l_2 m_2} Y_{lm}. \quad (3.24)$$

Here, we denote $d\Omega = \sin\theta d\theta d\varphi$. The derivation of Eq. (3.24) is given in Appendix B.3.1. The integrals over a product of three spherical harmonics are known as Gaunt-coefficients [147]. Apart from a potentially nonlinear regulation of active tension, $f(c)$, the advection term is the only nonlinear contribution in this model and, as such, couples the different harmonic modes.

For a given distribution of active tension $t_{ij}^a = \xi f(c) g_{ij}$ with $f(c)$ given in Eq. (3.17), Eqs. (3.19) and (3.23) provide a closed solution for the surface flows and the dynamics of the concentration modes c_{lm} .

Linearised dynamics

Finally, we linearise the general closed solution around the homogeneous stationary state. The stationary homogeneous state is given by $c = c_0$, $v_i = 0$ and $\mathbf{u}^\pm = 0$. The linearisation of the tension-regulating function $f(c)$ for small deviations of the concentration field $\delta c = c - c_0$ yields $f(c_0 + \delta c) - f(c_0) \approx \partial_c f(c_0) \delta c$. For $\delta c(\theta, \varphi)$ given in the form $\delta c = \sum_{l,m} \delta c_{lm} Y_{lm}$ the resulting surface flow $\delta v_i(\theta, \varphi)$ in the form $\delta v_i = \sum_{l,m} \delta v_{lm}^{(1)} \Psi_i^{(lm)}$ directly follows from

Eq. (3.19), with velocity modes given by

$$\delta v_{lm}^{(1)} = \frac{R\xi c_0 \partial_c f(c_0)}{R(\eta_- + \eta_+)(1 + 2l) - R\eta_+ \delta_{l,1} + (\eta_b + \eta_s)l(l + 1) - 2\eta_s} \delta c_{lm}. \quad (3.25)$$

From Eq. (3.23), we find a dynamic equation for δc_{lm} that is given to linear order by

$$\frac{d}{dt} \delta c_{lm} = - \left(\frac{D}{R^2} l(l + 1) + k \right) \delta c_{lm} - c_0 l(l + 1) \delta v_{lm}^{(1)}. \quad (3.26)$$

Using the velocity modes $\delta v_{lm}^{(1)}$ given in Eq. (3.25), the dynamic Eq. (3.26) is closed in the concentration modes δc_{lm} .

In the remainder of this chapter, we will refer several times to the general closed solution and the linearised solution just derived. In particular, these solutions will be used to approximate inhomogeneous steady-state solutions and to analyse the mechano-chemical stability properties of the active surface.

3.2 Mechano-chemical symmetry breaking in the cellular cortex

In this section, we show that mechanical interactions of the active fluid film with a passive surrounding fluid enable the spontaneous formation of patterns with different spatial symmetries. We consider for this analysis the active surface dynamics defined by Eqs. (3.1)–(3.5), where we focus on external forces from the interior passive fluid only and set $\eta_+ = 0$.¹ This represents a minimal model for the mechano-chemical self-organisation of the cellular actomyosin cortex whose dynamics can be affected by shear stresses from the cytoplasm.

In the following, we first perform a linear stability analysis of the homogeneous state, and we determine parameter regimes in which harmonic modes with different symmetries are unstable. We then analyse the general nonlinear dynamics using a numerical approach. In particular, we describe the spontaneous formation of a contractile ring from a mechano-chemical instability. Finally, we discuss the interaction of the observed patterning processes with an external anisotropic field that represents inhomogeneous signalling cues in a cell.

3.2.1 Linear stability analysis

Here, we determine the dispersion relation for perturbations of the homogeneous stationary state and analyse its linear stability properties. To this end, we note that the linearised

¹The patterning processes discussed here are qualitatively unchanged when an exterior fluid is additionally included. Because of this redundancy it suffices for the analysis of mechano-chemical surface patterning to consider interactions with the interior passive fluid alone.

dynamic Eq. (3.26) has the form $\frac{d}{dt}\delta c_{lm} = \lambda_l \delta c_{lm}$ with

$$\lambda_l = -l(l+1)\frac{D}{R^2} - k + \frac{l(l+1)\xi c_0 \partial_c f(c_0)}{(1+2l)R\eta_- + l(l+1)(\eta_b + \eta_s) - 2\eta_s}, \quad (3.27)$$

which can be solved by an ansatz $\delta c_{lm} = \delta c_{lm}^{(0)} \exp(\lambda_{lm} t)$. We can therefore identify $\lambda_{lm} = \lambda_l$ with λ_l given in Eq. (3.27) as the growth-rate of the l -th harmonic mode after a concentration perturbation of the homogeneous state.

To discuss the dispersion relation Eq. (3.27) further, we first note that two important time scales can be defined from the parameters of this model. The contractility time scale $\tau_c = \eta_b/\xi$ describes the advection-driven accumulation of stress regulator, and the time scale $\tau_D = R^2/D$ describes the diffusion of the stress regulator. The ratio

$$\text{Pe} = \frac{\tau_D}{\tau_c} = \frac{\xi R^2}{D\eta_b} \quad (3.28)$$

can be identified as the Péclet number [117, 120] that characterises the relative strength of advective and diffusive flows. For large Péclet numbers, the contractility-driven advection dominates over diffusive fluxes. With these definitions, we can rewrite the dispersion relation Eq. (3.27) as

$$\tau_D \lambda_l = -l(l+1) \left(1 + \frac{\tau_D k}{l(l+1)} - \frac{\text{Pe } c_0 \partial_c f(c_0)}{(1+2l)\nu R/L_h + l(l+1)(1+\nu) - 2\nu} \right), \quad (3.29)$$

where

$$\nu = \eta_s/\eta_b \quad (3.30)$$

is the surface viscosity ratio and we have introduced the hydrodynamic length scale

$$L_h = \frac{\eta_s}{\eta_-}. \quad (3.31)$$

As we will show, this hydrodynamic length scale plays a crucial role for the organisation mechano-chemical surface patterns.

Critical Péclet number for interactions with an interior fluid

In the following, we discuss the linear stability based on the dispersion relation Eq. (3.29). To this end, we use that the homogeneous state on the surface is unstable against perturbations with mode l if $\lambda_l > 0$, and stable if $\lambda_l < 0$.

In the regime $L_h \gg R$, where interactions with the interior fluid are negligible, λ_l is

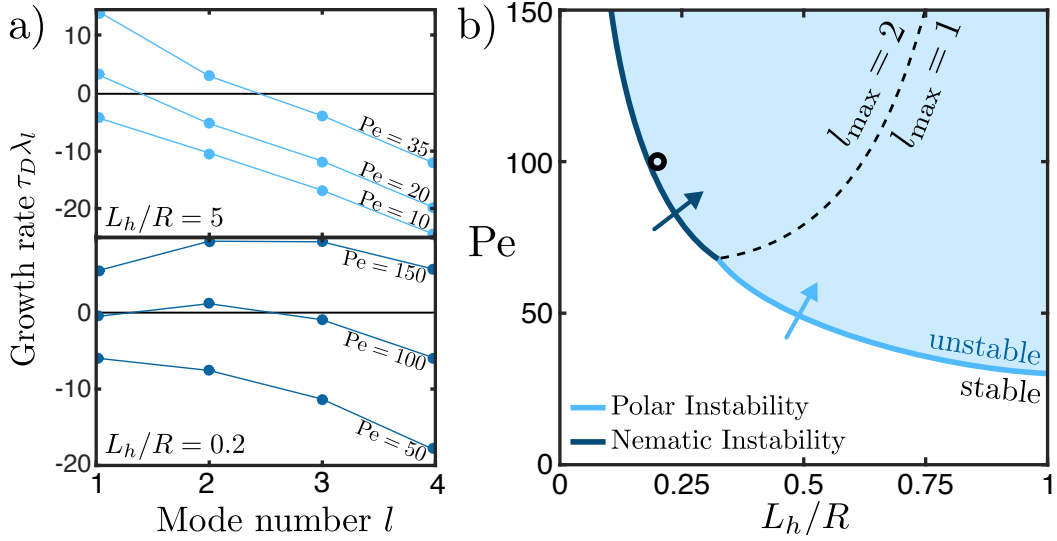


Figure 3.2: Dispersion relation and stability diagram for perturbations of the homogeneous state. **a)** Dispersion relation given in Eq. (3.29) for larger (top) and smaller (bottom) hydrodynamic length L_h/R , corresponding to small and large viscosities η_- of the interior passive fluid. Dots show the values of the growth rate and the connecting lines serve as guide to the eye. In each plot, we show growth rates for increasing Péclet number Pe defined in Eq. (3.28). For a large hydrodynamic length, the mode $l = 1$ becomes unstable first when Pe is increased (top). For a small hydrodynamic length, the mode $l = 2$ can become unstable first when Pe is increased (bottom). **b)** Representative stability diagram, where the homogeneous state is unstable in the bright blue region. The bright blue line indicates $Pe = Pe_-^*$ (Eq. (3.32)) and corresponds to a transition at which the polar mode $l = 1$ becomes unstable first. The dark blue line indicates a transition at which the nematic mode $l = 2$ becomes unstable first for an increasing Péclet number. The black circle depicts values for which we study the nonlinear dynamics in Section 3.2.2. The black dashed line separates parameter regions in which perturbations with the mode $l = 1$ or $l = 2$ have the larger growth rate: $l_{\max} = 1 : \lambda_1 > \lambda_2$ and $l_{\max} = 2 : \lambda_2 > \lambda_1$. Parameters: $k\tau_D = 10$, $\nu = 1$ and $c_0 \partial_c f(c_0) = 1$.

monotonically decreasing for $l \geq 1$. The polar mode¹ $l = 1$ always becomes unstable first when the Péclet number is increased up to $Pe = Pe_-^*$ with

$$Pe_-^* = \frac{1}{c_0 \partial_c f(c_0)} (2 + \tau_D k) \left(1 + \frac{3\nu R}{2L_h} \right). \quad (3.32)$$

If the viscosity of the interior fluid is negligible such that $L_h \rightarrow \infty$, Eq. (3.32) is formally equivalent to the instability threshold previously derived for the deforming spherical surface (Eq. (2.41)). Higher modes can also become unstable if Pe is increased further, but have always a smaller growth rate λ_l than the mode $l = 1$ (Fig. 3.2 a, top).

Further inspection of the dispersion relation Eq. (3.29) reveals that in the regime $L_h \approx R$,

¹Scalar and vector spherical harmonics with $l = 1$ correspond to fields with a polar asymmetry on the sphere. We refer to the corresponding mode coefficients simply as *polar mode*. Note that we already encountered an instability with this symmetry on the deforming spherical surface discussed in Section 2.3.2. Furthermore, we refer to coefficients with $l = 2$ simply as *nematic mode*, in correspondence with the symmetry of the respective spherical harmonics.

where shear stresses in the interior passive fluid are comparable with those in the surface, the dispersion relation can become non-monotonic. To see this, we use the dispersion relation λ_l given in Eq. (3.29) and evaluate the inequality $\lambda_2 > \lambda_1$. We find that this inequality can only be fulfilled if $L_h < R$, which provides a necessary condition for the nematic mode $l = 2$ to become unstable with the largest growth rate. If the turnover k is additionally finite, the nematic mode can become the only unstable mode in the system (Fig. 3.2 a, bottom).

Figure 3.2b shows a representative stability diagram that captures the two different regimes of smaller and larger hydrodynamic length. The homogeneous state is unstable in the blue-shaded region. The bright blue line indicates the transition towards an unstable polar mode $l = 1$. The nematic mode $l = 2$ can become unstable first for increasing Péclet numbers at a smaller hydrodynamic length L_h (dark blue line).

3.2.2 Spontaneous formation of a contractile ring

In the following, we numerically solve Eqs. (3.4) and (3.5) on the surface of a sphere to identify inhomogeneous steady states that emerge from the linear instabilities just discussed. The details of the numerical approach are presented in Appendix E.3.2.

First, we consider the case of a larger hydrodynamic length $L_h/R = 5$, which corresponds to a small viscosity of the interior fluid. Using a randomly perturbed concentration field as initial condition, a single patch of stress regulator spontaneously forms. A steady state emerges, which corresponds to a mechano-chemical surface pattern with global polar asymmetry (Fig. 3.3 a, top row). A cross section that contains the polar axis defined by this pattern reveals a backflow in the center (Fig. 3.3 b, top). This flow appears as a consequence of the incompressibility of the passive fluid and the topology of the active surface flows, which we have schematically depicted in Fig. 3.3 c (top).

In the next step, we analyse the nonlinear dynamics for a smaller hydrodynamic length $L_h/R = 0.2$, such that shear stresses from the interior passive fluid are comparable with those on the active surface. For reference, we have depicted the parameter values used for this analysis as a black circle in the stability diagram Fig. 3.2. In this case, a perturbation of the concentration field either leads to the formation of two patches of stress regulator at opposing poles of the surface, or to the formation of a contractile ring, both of which correspond to a surface pattern with a global nematic symmetry. In the bottom row of Fig. 3.3, we show the steady state in which the contractile ring has formed. The interior passive fluid flow is in this case given by two oppositely rotating, toroidal vortex tubes that are stacked orthogonal to the nematic axis defined by the surface pattern (Fig. 3.3 c, bottom).

Finally, we note that all steady states that have been observed in the numerical solutions are axially symmetric, even though the dispersion relation is degenerate in the azimuthal mode number m .

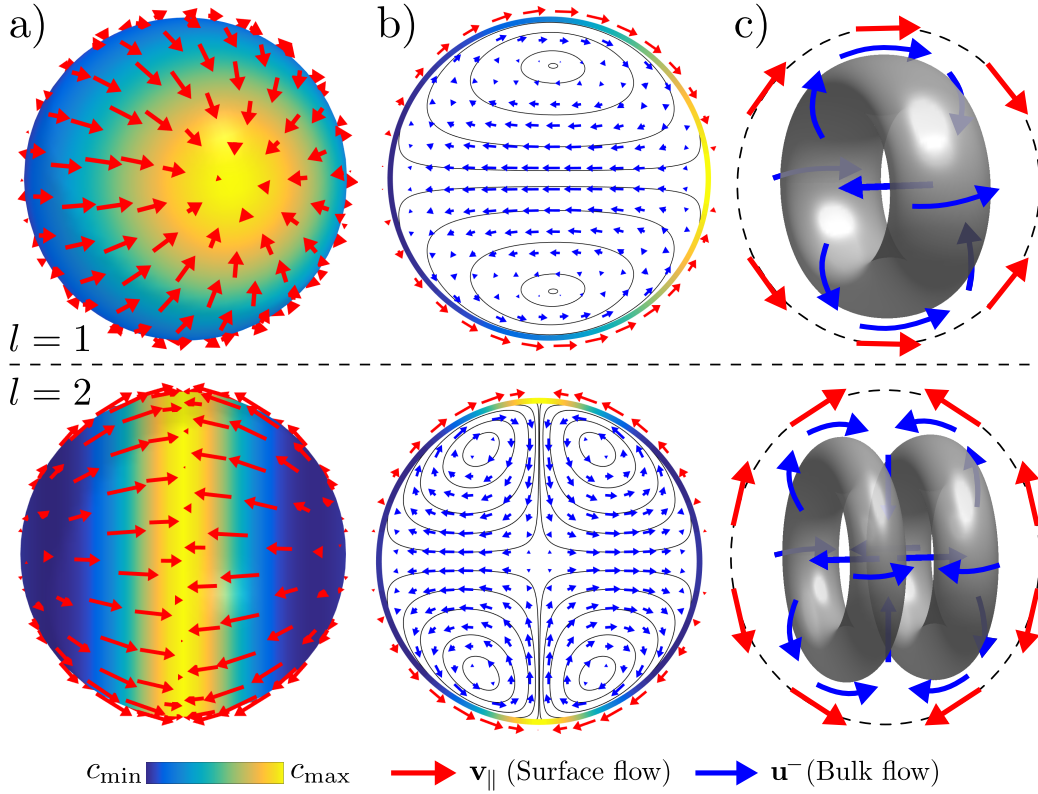


Figure 3.3: Spontaneously formed polar (top row) and nematic (bottom row) steady states. **a)** Surface view of tangential flows (red arrows) and concentration patterns. An instability of the mode $l = 1$ leads to a surface pattern with polar asymmetry (top). In regimes where the mode $l = 2$ is the only unstable mode, a contractile ring with nematic asymmetry can form (bottom). **b)** Central cross-sectional views that are parallel to the polar and nematic axis defined by the surface patterns. Blue arrows depict the local flow field of the interior passive fluid. Black lines depict streamlines. Note the central backflow in the $l = 1$ steady state (top), which occurs as a consequence of the incompressibility of the interior fluid. **c)** Schematic representation of the global flow topology. Grey tori depict vortex rings. In the $l = 1$ steady state, a single vortex ring is present in the flow field of the passive fluid. In the $l = 2$ steady state, two such vortex rings are stacked along the axis defined by the surface pattern, and rotate in opposite directions. Parameters: $k\tau_D = 10$, $\nu = 1$ (in both cases), as well as $Pe = 20$, $L_h/R = 5$ (top) and $Pe = 100$, $L_h/R = 0.2$ (bottom). Active tension is regulated by $f(c) = 2c^2/(c_0^2 + c^2)$, such that $c_0\partial_c f(c_0) = 1$.

3.2.3 Interactions of patterns with an inhomogeneous external cue

In this last part of Section 3.2, we study interaction of the self-organised formation of polar and nematic patterns with an inhomogeneous external cue. This analysis is inspired by the spatially nematic signalling cues that the spindle apparatus in a cell provides for the cortex during cell division.

To introduce an *external nematic cue*, we consider a reaction term in the dynamic equation of the concentration field Eq. (3.4) given by

$$R(c) = -k_{\text{off}} c + k_{\text{on}}(\mathbf{X}), \quad (3.33)$$

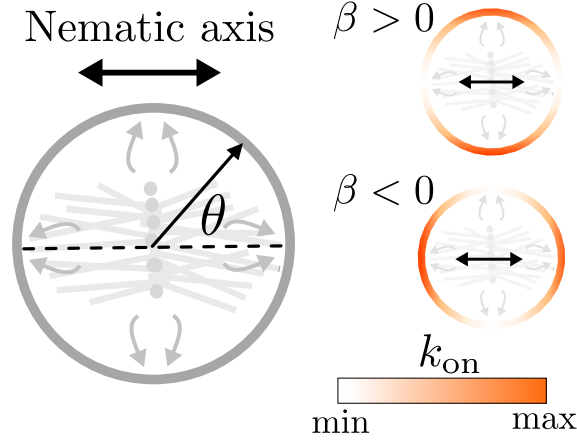


Figure 3.4: Introducing an external nematic cue in the form of an inhomogeneous on-rate k_{on} of stress regulator. The explicit expression used for k_{on} is given in Eq. (3.34). We depict the orientation of the nematic axis by a black left-right arrow. The spatial organisation of such a cue can be provided, for example, by the spindle apparatus in a cell that represents a nematic structure (left). The dimensionless coefficient β determines the strength and sign of the nematic cue (right). Qualitatively, there is a recruitment of stress regulator predominantly near the equator at $\theta = \pi/2$ if $\beta > 0$, and a recruitment of stress regulator predominantly near the poles at $\theta \in \{0, \pi\}$ if $\beta < 0$.

where

$$k_{\text{on}}(\mathbf{X}) = k_{\text{on}}^0 \left[1 + \beta \left(1 - 3 \cos^2 \theta \right) \right]. \quad (3.34)$$

The surface profile prescribed by $k_{\text{on}}(\mathbf{X})$ is shown in Fig. 3.4. The term $1 - 3 \cos^2 \theta$ in Eq. (3.34) is proportional to the scalar spherical harmonic $Y_{2,0}$ and describes an axisymmetric nematic pattern on the sphere. Hence, $k_{\text{on}}(\mathbf{X})$ represents an on-rate with a spatially nematic pattern if $k_{\text{on}}^0 \neq 0$ and $\beta \neq 0$. The coefficient β determines the strength and sign of the nematic cue and is chosen from the interval $[-1, 1/2]$, which ensures that $k_{\text{on}}(\mathbf{X}) \geq 0$ everywhere on the surface.¹ In the context of cytokinesis one has $\beta > 0$, such that there is a recruitment of stress regulator predominantly to the equator region around $\theta = \pi/2$. The case $\beta < 0$ represents the inverse scenario, where the stress regulator is preferably recruited to the pole region around $\theta \in \{0, \pi\}$. For $\beta = 0$, we recover with $k_{\text{on}}^0/k_{\text{off}} = c_0$ and $k_{\text{off}} = k$ the homogeneous turnover $R(c) = -k(c - c_0)$ discussed before. This minimal model can also be interpreted as choosing a preferred concentration $c_0(\mathbf{X}) = k_{\text{on}}(\mathbf{X})/k_{\text{off}}$ that varies across the surface.

¹The asymmetric interval is a consequence of choosing a purely nematic spatial pattern for the modulation of the on-rate. Using instead, for example, a modulation in the form $\beta \cos(2\theta)$ would allow choosing β from a symmetric interval, but also yields contributions to the mode $l = 0$ and therefore would affect the average concentration c_0 in a non-transparent way. This is avoided by choosing the purely nematic on-rate given in Eq. (3.34).

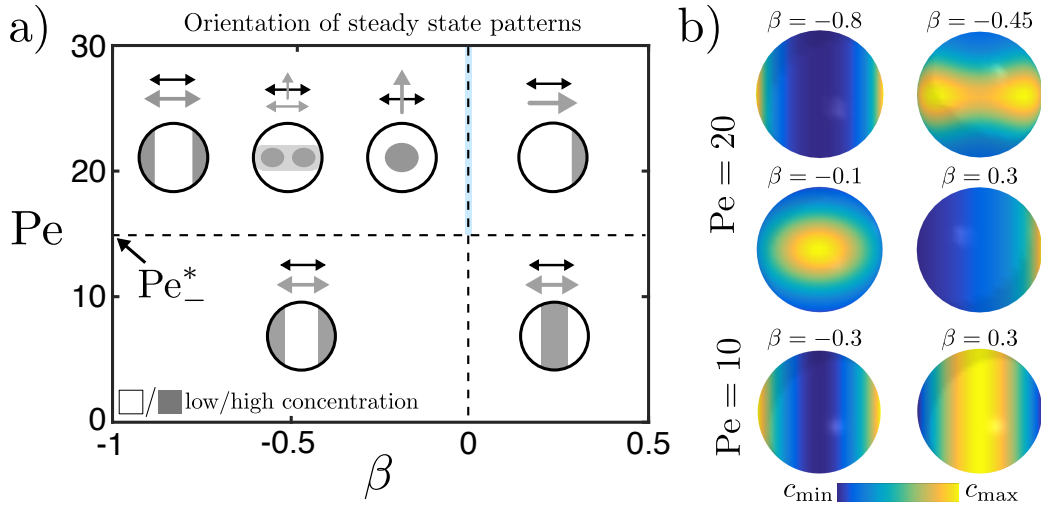


Figure 3.5: Orientation of surface patterns by an external nematic cue. **a)** Schematic representation of surface patterns and their orientation for varying Péclet number Pe (defined in Eq. (3.28)) and strength of the nematic cue β (cf. Eq. (3.34)). The black left-right arrow depicts the orientation of the external nematic cue, grey arrows depict the symmetry axis defined by the surface patterns. We chose parameters, for which the polar mode $l = 1$ becomes unstable first at $Pe = Pe_-^*$ if $\beta = 0$. This instability of the homogeneous state was derived in Section 3.2.1 and can be found in this graph along the bright blue line. For $Pe < Pe_-^*$ and $\beta \neq 0$, the steady state surface patterns are essentially imprinted by the nematic cue: At steady state, surface regions where the rate k_{on} is large (small) contain a high (low) concentration of stress regulator. For $Pe > Pe_-^*$ and $\beta \neq 0$, spontaneously forming patterns on the surface interact with the nematic cue. Depending on the strength of the nematic cue β , this leads to polar and nematic surface patterns that orient their axis with the one of the nematic cue. **b)** Representative steady-state patterns obtained from numerical solutions of the full problem. Parameters: $L_h/R = 5$, $\tau_D k_{\text{on}}^0 = 10$ and $\eta_s/\eta_b = 1$.

Orientation of polar surface patterns by an external nematic cue

In the following, we discuss the effect of the external nematic cue on the mechano-chemical surface patterning. We first consider the regime of a larger hydrodynamic length $L_h = \eta_s/\eta_-$, corresponding to a small viscosity of the interior fluid. We have derived in Section 3.2.1 that in this case, the polar mode $l = 1$ becomes unstable first when increasing the Péclet number Pe up to the critical value Pe_-^* given in Eq. (3.32). This stability property corresponds to the case $\beta = 0$ for the model discussed here and serves as our reference to develop an understanding of the observed patterns when the nematic cue is present.

When turning on the nematic cue, $\beta \neq 0$, we observe steady-state patterns as depicted in Fig. 3.5 a. Additionally, we indicate in this graph the orientation and symmetry of these patterns (grey arrows) relative to the axis defined by the nematic cue (black left-right arrows).

For $\beta \neq 0$ and $Pe < Pe_-^*$ (below the horizontal dashed line in Fig. 3.5 a), patterns are essentially imprinted by the spatially varying on-rate $k_{\text{on}}(\mathbf{X})$. This is consistent with the idea that the active surface is stable with respect to its contractile properties ($Pe < Pe_-^*$), but the external nematic cue generates an inhomogeneous concentration profile in a steady

state. Corresponding concentration patterns are depicted in Fig. 3.5 b ($Pe = 10$).

For $Pe > Pe_*$ (above the horizontal dashed line in Fig. 3.5 a), we find emerging patterns that appear as a ‘superposition’ of the external nematic cue and the intrinsic mechano-chemical instability of the polar mode on the active surface. For $\beta > 0$ (increased recruitment of stress regulator to the equator) a polar surface pattern forms, whose axis is oriented parallel to the axis of the nematic cue (Fig. 3.5 a, top right). For $\beta < 0$ (increased recruitment of stress regulator to the poles), we can qualitatively distinguish three regimes (Fig. 3.5 a, top left). If $|\beta|$ is small, a single contractile patch forms and defines a polar axis that is oriented orthogonal to the axis of the nematic cue. If $|\beta|$ is increased, two local concentration maxima appear. This steady state represents a pattern that somewhat contains a polar and a nematic asymmetry. Finally, if $|\beta|$ is increased even further, the nematic cue dominates and leads to two patches of stress regulator at opposing poles, defining an axis parallel to the axis of the nematic cue. In Fig. 3.5 ($Pe = 20$), we depict exemplary steady-state concentration patterns for the different cases just discussed.

Orientation of the contractile ring by an external nematic cue

We have just discussed the case of a larger hydrodynamic length $L_h = \eta_s/\eta_-$ in which the polar mode $l = 1$ becomes unstable first for $\beta = 0$ (no external cue). We then switched on the external cue and could interpret the resulting patterns as the ‘superposition’ of the cue and the mechano-chemical stability properties of the surface. An analogous analysis can be made in the regime of smaller hydrodynamic length, where the nematic mode $l = 2$ becomes unstable first for $\beta = 0$. We have studied the dynamics in this parameter regime and complemented the system by the external nematic cue given in Eq. (3.33). The essential insight of such an analysis is that the nematic axis defined by emerging contractile rings is always oriented parallel to the axis of the external nematic cue, independently of the initial condition. This is the key difference with the spontaneous formation of the contractile ring for $\beta = 0$ discussed in Section 3.2.2, where the nematic axis defined by the ring pattern can be oriented arbitrarily.

3.3 Spontaneous motion of an active surface swimmer

In the previous section, we have focused on mechanical interactions of the active surface with an interior passive fluid. In this section, we discuss the complementary case and study the active surface dynamics described by Eqs. (3.1)–(3.5) for external forces from an exterior passive fluid. We show that an instability on the active surface leads in this case to the spontaneous onset of force-free, translational motion through the exterior fluid. This represents a model for a *squirmers*, a small object that can propel itself in the absence of inertial forces through a viscous environment. Squirmer models have widespread applications in the study of artificial self-propelling particles and are used to describe key properties of biological

microswimmers, such as sperm cells or swimming algae [148, 149].

In the following, we first explain in detail how a mechano-chemical instability on the surface can be linked to a force-free translational motion relative to the laboratory frame. We then derive an analytic approximation of the steady-state propagation velocity of such an *active surface swimmer* and compare it to the general solution obtained numerically. Finally, we characterise the bifurcation that is associated with the spontaneous onset of motion.

3.3.1 Spontaneous onset of translational motion

In the following, we show that translational motion of the sphere through the exterior fluid can arise spontaneously via a mechano-chemical instability on the active surface. To this end, we first introduce a general relation between surface flows on the sphere and its force-free motion through an exterior fluid. We then show that the corresponding surface flows, and thus the onset of translational motion, can arise spontaneously from a mechano-chemical instability.

Force-free motion through a viscous fluid

The net force exerted by the surface on the surrounding fluid, $-\int \mathbf{f}^n dA$ with \mathbf{f}^n given in Eq. (3.10), must vanish in the absence of external body forces. We show in Appendix B.2.4 that this implies a relation between surface flows on the sphere given in terms of a harmonic expansion

$$v_i = \sum_{l,m} v_{lm}^{(1)} \Psi_i^{(lm)}, \quad (3.35)$$

and a translational motion relative to the laboratory frame with velocity \mathbf{u}_0 given by

$$\mathbf{u}_0 = \frac{1}{\sqrt{3\pi}} \left(v_{1,1}^{(1)} \bar{\mathbf{e}}_x + v_{1,-1}^{(1)} \bar{\mathbf{e}}_y - v_{1,0}^{(1)} \bar{\mathbf{e}}_z \right). \quad (3.36)$$

Briefly, Eq. (3.36) can be found as follows. First, the Stokes equation for the exterior fluid is solved as described in Section 3.1.2 with no-slip boundary condition on the sphere for surface flows given by Eq. (3.35). Additionally, we impose the boundary condition $\mathbf{u}(r \rightarrow \infty) = -\mathbf{u}_0$. Using this solution, the net force acting on the surface can be expressed as a function of surface flows v_i and the propagation velocity \mathbf{u}_0 . Imposing a vanishing net force yields Eq. (3.36). An essential conclusion from Eq. (3.36) is that only velocity modes with $l = 1$ are relevant to describe translational motion of the surface through the exterior fluid.

Critical Péclet number for interactions with an exterior fluid

We have seen in Section 3.2 that the self-organisation of the active surface can give rise to spontaneous surface flows from a mechano-chemical instability. In general, we expect similar instabilities to be present if mechanical interactions with an exterior fluid are considered. From Eq. (3.36) it then follows that any contribution of surface flows associated with an

instability of the mode $l = 1$ leads to a spontaneous onset of translational motion. In the following, we characterise the instability of the mode $l = 1$ for the case where the surface is embedded in an exterior fluid.¹ To this end, we solve the linearised dynamic Eq. (3.26) for vanishing interior viscosity, $\eta_- = 0$, with an exponential ansatz and identify the growth rate of the mode $l = 1$. From this, we find that the mode $l = 1$ becomes unstable for an increasing Péclet number $\text{Pe} = \xi R^2 / (D\eta_b)$ at $\text{Pe} = \text{Pe}_+^*$ with

$$\text{Pe}_+^* = \frac{1}{c_0 \partial_c f(c_0)} \left(2 + \frac{kR^2}{D} \right) \left(1 + \frac{R\eta_+}{\eta_b} \right). \quad (3.37)$$

Recall that R denotes the radius of the sphere, ξ the active contractility, η_b the bulk of the surface and η_+ the viscosity of the exterior passive fluid. The dynamics of modes with $l \geq 2$ does not lead to new effects compared to the case where mechanical interactions with an interior passive fluid are considered (Section 3.2). This is due to the fact that the general solution for the surface flows, Eq. (3.19), is for modes with $l \geq 2$ symmetric in the interior and exterior viscosity and therefore invariant under $\eta_+ \leftrightarrow \eta_-$.

Steady-state flow during translational motion

In the next step, we solve the general nonlinear problem defined by Eqs. (3.1)–(3.5) for external forces from an exterior passive fluid (see Section 3.1.2) using a numerical approach (Appendix E.3.2). Using a randomly perturbed concentration field as initial condition, we find for Péclet numbers $\text{Pe} = R^2 \xi / (\eta_b D)$ with $\text{Pe} > \text{Pe}_+^*$ and Pe_+^* given in Eq. (3.37) the emergence of a single patch of stress regulator. This pattern defines a polar asymmetry on the surface. The mechanical coupling of the active surface with the passive exterior fluid leads to a steady state at which the surface translates through the surrounding fluid. Cross sections of the corresponding steady-state flow profiles in the frame comoving with the surface and in the laboratory frame are shown in Figs. 3.6a and b, respectively. An interesting feature of the passive steady-state flow field is the stagnation point that trails the active surface swimmer in the laboratory frame (red circle in Fig. 3.6 b).

3.3.2 Analytic approximation of the propagation velocity

In the previous section, we have shown that force-free, translational motion can spontaneously arise from a mechano-chemical instability on the active surface. In the following, we derive an analytic approximation of the steady-state propagation velocity u_0 that emerges from this instability.

It is evident from Eq. (3.36) that determining an approximation for \mathbf{u}_0 is equivalent to determining an approximation of the steady-state solution for the velocity modes $v_{1,m}^{(1)}$. For this, we have to go beyond the linear regime and therefore use the general closed solution

¹The corresponding calculation is very similar to the derivation for the case of an interior fluid presented in Section 3.2.1 and therefore only described briefly here.

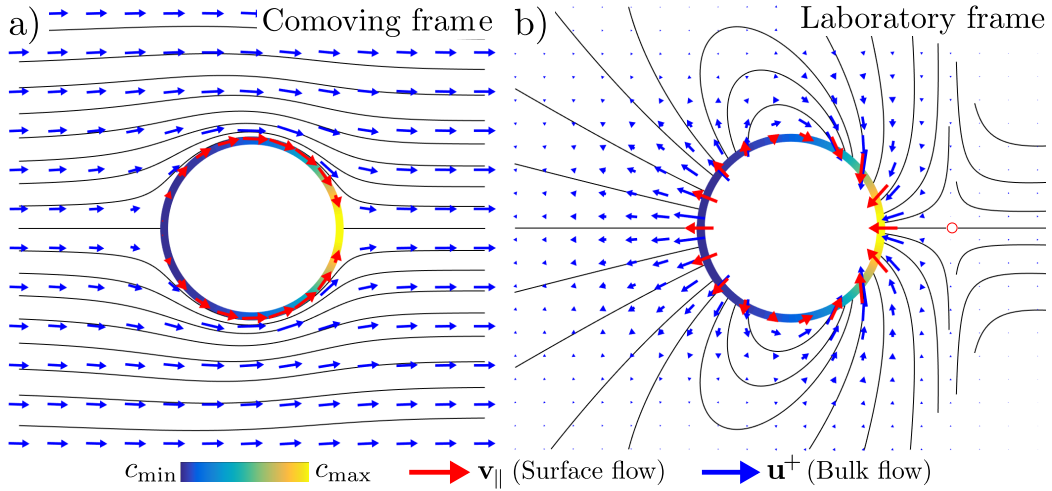


Figure 3.6: Central cross section through the steady-state flow profile of an active surface swimmer. Black lines depict stream lines of the surrounding flow field. **a)** The flow field depicted in the frame comoving with the surface. **b)** The flow field depicted in the laboratory frame. This flow field contains a stagnation point with $\mathbf{u}^+ = 0$ (red circle). This point trails the active surface swimmer and therefore indicates a microswimmer that can be characterised as a puller [150]. This can also be shown analytically based on the standard criteria for the classification of squirmers (see below and Appendix E.1.1).

of the nonlinear problem derived in Section 3.1.3 as a starting point. In the first step, we approximate the regulation of active tension in Eq. (3.3) by a linear function $f(c) = c/c_0$. Representing the concentration field by a harmonic expansion $c = \sum_{l,m} c_{lm} Y_{lm}$, the velocity modes of the surface flows as expanded in Eq. (3.35) are given by

$$v_{lm}^{(1)} = V_l \frac{c_{lm}}{c_0}, \quad (3.38)$$

(no summation) with constant coefficients

$$V_l = \frac{R\xi}{(1+2l)R\eta_+ - \delta_{l,1}R\eta_+ + l(l+1)(\eta_b + \eta_s) - 2\eta_s}, \quad (3.39)$$

which follows from Eq. (3.19) and is exact for a linear regulation of active tension.

In the next step, we take into account that we only observe axisymmetric steady states in numerically obtained solutions of the general surface dynamics.¹ We assume that this is a general property of the isotropic, self-organised active surface, such that the z -axis of the Cartesian coordinate system can always be aligned with the rotational symmetry axis that is defined by the final surface pattern. From Eqs. (3.36) and (3.38) it then follows that the

¹This holds true very generally in the presence or absence of mechanical interactions with a passive fluid in any of the domains, interior or exterior.

translational velocity of a steady-state solution can be expressed as $\mathbf{u}_0 = u_0 \bar{\mathbf{e}}_z$ with

$$u_0 = -\frac{V_1}{\sqrt{3\pi}} \frac{c_{1,0}}{c_0}. \quad (3.40)$$

In order to approximate the propagation velocity u_0 , it therefore suffices to consider axisymmetric solutions and determine an approximation of the concentration mode $c_{1,0}$ at steady state. Accordingly, we consider an ansatz for the concentration field in the form

$$c = c_0 + c_{1,0} Y_{1,0} + c_{2,0} Y_{2,0}. \quad (3.41)$$

Here, c_0 represents a given average concentration and $c_{1,0}$ and $c_{2,0}$ are unknown coefficients whose steady-state values are approximated in the following. To this end, we use the ansatz Eq. (3.41) in the general solution of the nonlinear problem Eq. (3.23), which yields

$$\frac{d}{dt} c_{1,0} = -2 \frac{D}{R^2} c_{1,0} - k c_{1,0} + \frac{2V_1 c_{1,0}}{R} + \frac{1}{\sqrt{5\pi}} \frac{c_{1,0} c_{2,0}}{R c_0} (3V_2 - V_1) \quad (3.42)$$

$$\frac{d}{dt} c_{2,0} = -6 \frac{D}{R^2} c_{2,0} - k c_{2,0} + \frac{3}{\sqrt{5\pi}} \frac{c_{1,0}^2 V_1}{c_0 R} + \frac{V_2 c_{2,0}}{R c_0} \left(6c_0 + \frac{3}{7} \sqrt{\frac{5}{\pi}} c_{2,0} \right) \quad (3.43)$$

with V_l for $l = 1$ and $l = 2$ given in Eq. (3.39). Here, we have also used Eq. (3.38) to eliminate the velocity modes in the general dynamic equation for the concentration modes (Eq. (3.23)). Note that Eqs. (3.42) and (3.43) are not a power-series expansion, but follow from truncating the general solution Eq. (3.23) in the space of spherical harmonics at $l = 2$. Including higher modes would in fact lead to further quadratic terms in the concentration modes.

Steady-state solutions for the concentration modes $c_{1,0}$ and $c_{2,0}$ can be found by setting $dc_{1,0}/dt = dc_{2,0}/dt = 0$ in Eqs. (3.42) and (3.43). The resulting quadratic system of equations for $c_{1,0}$ and $c_{2,0}$ has four solutions that can essentially be read off: a homogeneous solution $c_{1,0}^{hom} = c_{2,0}^{hom} = 0$, a solution $c_{1,0}^{nem} = 0$, $c_{2,0}^{nem} \neq 0$ that corresponds to a nematic state, as well as two solutions with $c_{1,0}^{pol} \neq 0$, $c_{2,0}^{pol} \neq 0$ that correspond to steady states for which, according to Eq. (3.40), the surface propagates through the exterior fluid. We present the explicit form of these solutions in Appendix E.1.1. In Fig. 3.7 a, we show the surface flow and concentration field determined from the steady-state solutions $c_{1,0}^{pol}$ and $c_{2,0}^{pol}$ using Eqs. (3.38) and (3.41), as well as numerically obtained steady-state solutions of the full problem.

Finally, the propagation velocity u_0 of the surface follows from Eq. (3.40) and is given by

$$u_0 = \pm \left[\frac{20}{3} \frac{V_1 - \frac{D}{R}}{V_1 - 3V_2} \left(\frac{DV_1}{R} - V_1 V_2 \left\{ 1 + \frac{5}{7} \frac{V_1 - \frac{D}{R}}{V_1 - 3V_2} \right\} \right) \right]^{1/2} \quad (3.44)$$

with V_l for $l = 1$ and $l = 2$ given in Eq. (3.39). Here, we have for simplicity neglected the turnover of the stress regulator ($k = 0$). In Fig. 3.7 b, we show the approximated propagation

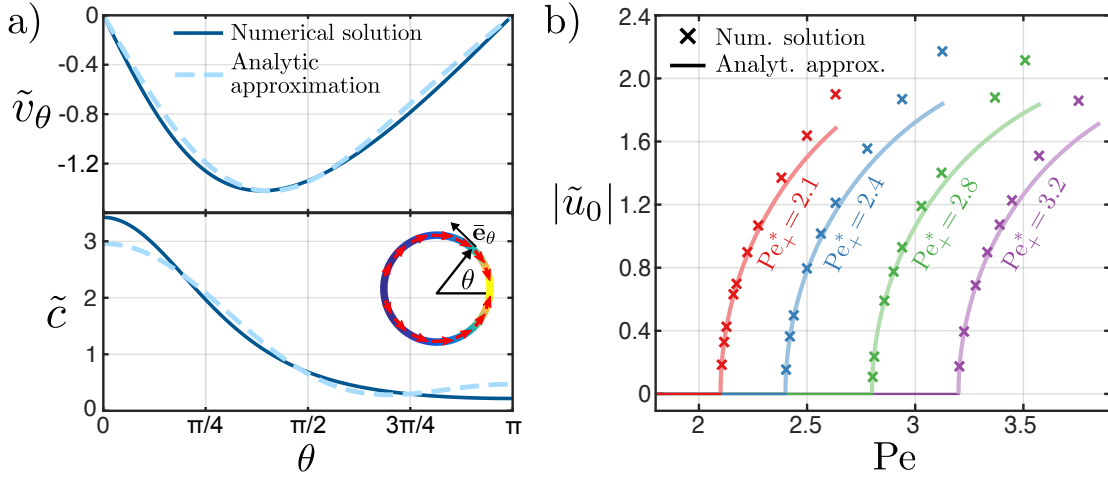


Figure 3.7: Comparison of numerical results and analytic approximations for steady-state solutions of an active surface embedded in an exterior passive fluid. **a)** Surface flows $\tilde{v}_\theta = \bar{\mathbf{e}}_\theta \cdot \mathbf{v}_\parallel / v_D$, where $v_D = R/\tau_D = D/R$ is the characteristic velocity, and concentration field of the stress regulator $\tilde{c} = c/c_0$ at steady state. Dashed lines depict analytic approximations determined using Eqs. (3.38), (3.42) and (3.43). Solid lines depict solutions that have been obtained numerically from the general problem defined by Eqs. (3.1)–(3.5). For details of the numerical approach see Appendix E.3.2. Parameters: $R\eta_+/\eta_b = 0.05$, $Pe = 2.2$. **b)** Propagation velocity $\tilde{u}_0 = u_0/v_D$ as function of the Péclet number $Pe = \xi R^2/(\eta_b D)$. Solid lines depict the approximation given in Eq. (3.44), crosses depict numerical solutions. Colours indicate different values of the dimensionless parameter $R\eta_+/\eta_b$, corresponding to different critical Péclet numbers Pe_+^* (Eq. (3.45)). For $Pe < Pe_+^*$ the steady state is homogeneous and $u_0 = 0$. Common parameters used for all results shown are $k = 0$, $\eta_b/\eta_s = 1$ and we have used $f(c) = c/c_0$ for the regulation of active tension Eq. (3.3).

velocity u_0 given in Eq. (3.44) as a function of the Péclet number $Pe = \xi R^2/(\eta_b D)$, for different values of the critical Péclet number Pe_+^* given in Eq. (3.37). The analytic approximation agrees particularly well with the full numerical solution closer to the onset of the instability. Furthermore, we find from Eq. (3.44) that $u_0 = 0$ for $Pe = Pe_+^*$.

Identifying the active surface swimmer as a puller

Microswimmers can be classified by the far-field of the surrounding fluid flow that is generated during their motion [151]. Because the motion is typically force-free, the first relevant contribution to the far-field corresponds to flows generated from a force-dipole. One then distinguishes two classes of swimmers based on the orientation of the forces within the dipole. In the case of a contractile force-dipole, point forces pointing towards each other, the swimmer represents a *puller*. In the case of an extensile force-dipole, the swimmer represents a *pusher* [149].¹ A simple way to identify this class for swimmers that are driven by surface flows, is to determine the sign of the velocity mode $v_{2,0}^{(1)}$ [149–151]. In our model, it suffices to

¹This terminology originates from biological microswimmers that ‘pull’ themselves through the fluid in a swimming stroke fashion to draw fluid along their body axis or, alternatively, *push* themselves by repelling fluid from the body along the axis of motion [151].

determine the sign of the concentration mode $c_{2,0}^{pol}$ during translational motion, which differ from the velocity modes $v_{2,0}^{(1)}$ only by a positive prefactor (cf. Eq. (3.39)). From the explicit expression for the concentration mode $c_{2,0}^{pol}$ given in Appendix E.1.1, it follows that the active surface swimmer introduced in this section belongs to the class of pullers. Note that the trailing stagnation point in the surrounding flow field (red circle in Fig. 3.6 b) had already revealed this fact: a trailing stagnation point is a known characteristic of pullers [150].

3.3.3 Bifurcation analysis at the spontaneous onset of motion

We conclude Section 3.3 by analysing the bifurcation that is associated with the spontaneous onset of translational motion just described. Recall that the onset of this motion occurs for increasing Péclet number Pe at the critical value Pe_+^* given in Eq. (3.37). For $Pe < Pe_+^*$, the homogeneous state is stable and there is no translational motion. We consider for the following analysis of this transition a linear regulation of active tension $f(c) = c/c_0$ in Eq. (3.3) and neglect turnover ($k = 0$), such that the critical Péclet number Pe_+^* simplifies to

$$\hat{Pe}_+^* = 2 \left(1 + \frac{R\eta_+}{\eta_b} \right). \quad (3.45)$$

Scaling of the propagation velocity near the instability

To analyse the behaviour of the propagation velocity u_0 near the spontaneous onset of motion, we first note that the approximation of u_0 given in Eq. (3.44) can be brought into the form

$$\frac{|u_0|}{v_D} = \left(\frac{Pe - \hat{Pe}_+^*}{\hat{Pe}_+^*} \right)^{1/2} (aPe + b)^{1/2}, \quad (3.46)$$

where $v_D = D/R$ is a fixed characteristic velocity. The coefficients a and b depend only on Pe_+^* and are given in Appendix E.1.2. Near the onset of the instability, we can introduce the relative deviation from the critical Péclet number

$$\Delta Pe = \frac{Pe - \hat{Pe}_+^*}{\hat{Pe}_+^*} \quad (3.47)$$

and find from Eq. (3.46)

$$\frac{|u_0|}{v_D} = (a\hat{Pe}_+^* + b)^{1/2} \Delta Pe^{1/2} + \mathcal{O}(\Delta Pe^{3/2}). \quad (3.48)$$

Note that $a\hat{Pe}_+^* + b > 0$, such that the prefactor of $\Delta Pe^{1/2}$ is always real (Appendix E.1.1). As a final verification of this result, we rescale the numerical data presented in Fig. 3.7 b according to Eq. (3.48), in which case they indeed collapse on a single curve (Fig. 3.8).

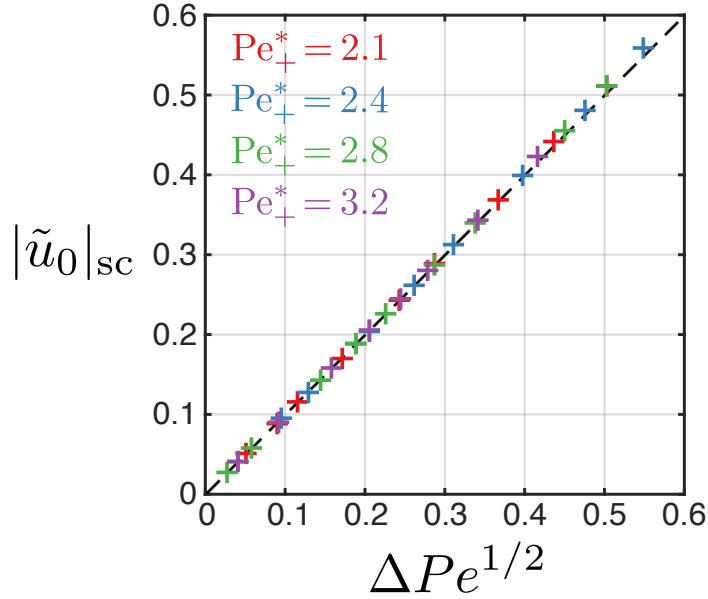


Figure 3.8: Scaling of the propagation velocity of an active surface swimmer. Crosses denote the same numerical steady-state solutions as shown in Fig. 3.7 b. Here we rescaled the data according to Eq. (3.48), where $\Delta\text{Pe} = (\text{Pe} - \hat{\text{Pe}}_+^*)/\hat{\text{Pe}}_+^*$ is the relative deviation of the Péclet number from the critical value $\hat{\text{Pe}}_+^*$ given in Eq. (3.37). Along the ordinate axis, we depict $|\tilde{u}_0|_{\text{sc}} = (a\hat{\text{Pe}}_+^* + b)^{-1/2}|u_0|/v_D$, where $v_D = D/R$ is held fixed and the coefficients a and b depend only on $\hat{\text{Pe}}_+^*$ (Appendix E.1.2). The black dashed line depicts a line with slope 1 for reference. Increasing deviations of the numerical values appear for larger values of ΔPe , when higher modes ($l \geq 3$) become relevant for the steady-state solution. The collapse of the numerically obtained solutions confirms the square-root scaling of the propagation velocity and the spontaneous onset of motion at the critical Péclet number $\hat{\text{Pe}}_+^*$.

Pitchfork bifurcation at the spontaneous onset of motion

The square-root scaling of the velocity amplitude $|u_0|$ and the invariance of the dynamic Eqs. (3.42) and (3.43) under $c_{1,0} \rightarrow -c_{1,0}$ are indications of a pitchfork bifurcation at the onset of translational motion [152, 153]. This can be corroborated by reducing the dynamical system near the point $(c_{1,0}, c_{2,0}) = (0, 0)$ to an equation for the slow degrees of freedom. The corresponding center-manifold reduction [152] can be performed analytically in our system (Appendix E.1.2). Briefly, we consider near the bifurcation an ansatz $c_{2,0} = \bar{a}c_{1,0}^2/c_0$ for the center-manifold. Taking the time derivative of this expression and using Eqs. (3.42) and (3.43), we can self-consistently determine the coefficient \bar{a} . From this, we find a ‘slow’ dynamic equation near $(c_{1,0}, c_{2,0}) = (0, 0)$ in the form

$$\tau_D \frac{d}{dt} \frac{c_{1,0}}{c_0} = 2\Delta\text{Pe} \frac{c_{1,0}}{c_0} + \bar{a} \left(\frac{c_{1,0}}{c_0} \right)^3, \quad (3.49)$$

where ΔPe is defined in Eq. (3.47) and the prefactor \bar{a} of the cubic term is given by

$$\bar{a} = \frac{1}{10\pi} \frac{R\eta_+ - 4\eta_s}{3R\eta_+ + 4\eta_b + 4\eta_s} \quad (3.50)$$

at the bifurcation $\text{Pe} = \hat{\text{Pe}}_+^* = 2(1 + R\eta_+/\eta_b)$. Equation (3.49) indeed corresponds to the dynamic equation of a pitchfork bifurcation at $\text{Pe} = \hat{\text{Pe}}_+^*$. Because the propagation velocity u_0 is directly proportional to the value of $c_{1,0}$ (Eq. (3.40)), the spontaneous onset of translational motion itself occurs via a pitchfork bifurcation.

The specific type of the pitchfork bifurcation is determined by the coefficient \bar{a} of the cubic term in Eq. (3.49), where $\bar{a} > 0$ ($\bar{a} < 0$) corresponds to a supercritical (subcritical) pitchfork bifurcation [152]. We see from Eq. (3.50) that formally both cases can occur, depending on the amplitude of the exterior viscosity. For $R\eta_+ < 4\eta_s$, the bifurcation is supercritical. All results discussed here belong to this supercritical regime. We also tried to collect numerical evidence for a potential transition to the subcritical regime by increasing the exterior viscosity up to $\eta_+ > 4\eta_s$. However, increasing values of η_+ also imply larger critical Péclet numbers Pe_+^* (Eq. (3.37)). Thus, a stronger contractile tension is required for the instability to occur, when larger values for η_+ are chosen. For values of η_+ that still corresponded to the supercritical regime ($R\eta_+ < 4\eta_s \Rightarrow \bar{a} < 0$), the numerical analysis then indicated the presence of singularities emerging from instabilities of the homogeneous state before the regime $R\eta_+ > 4\eta_s$ could be reached. These singularities likely appear due to the *unsaturated* linear regulation of active tension used here. Therefore, we could not conclude further about the properties of the bifurcation at larger exterior viscosities.

3.4 Discussion

In this chapter, we studied the mechano-chemical self-organisation of an isotropic active fluid on a sphere. Gradients of a diffusing stress regulator lead to surface flows, which in turn change the distribution of the stress regulator due to advection. In contrast to the previous chapter, we considered here the general, non-axisymmetric dynamics on the surface and took external shear stresses from a surrounding passive fluid into account. We identified a new mechanism that leads to a spontaneous polarisation on an active fluid surface, as well as to the formation of a contractile ring in a fully self-organised fashion. Our description also gives rise to a squirmer model, whose nonlinear properties we characterised in detail.

Throughout this chapter, we used the Péclet number $\text{Pe} = \xi R^2/(D\eta_b)$, with contractility ξ , sphere radius R , diffusion constant D , and surface viscosity η_b , to indicate the strength of active contractile stress in the system. It has been shown previously that the Péclet number can be used to characterise instabilities in self-organised active fluids [117].

We first derived a closed solution for the general nonlinear dynamics that served as the formal basis to develop the results presented in this chapter (Section 3.1). This solution builds on a covariant harmonic expansion of the hydrodynamic shear stresses acting on the surface.

In the first part of the analysis, we focused on interactions with an interior passive fluid (Section 3.2). This description is motivated by the dynamics of the cellular actomyosin

cortex, which interacts mechanically with the cytoplasm. Furthermore, it is of general importance for a cell to have access to different modes of spatial organisation, which can help to robustly guide polarisation and cell division [12, 35]. The corresponding spatial symmetries can directly be related to specific harmonic modes on the sphere.

We have identified a critical Péclet number Pe_-^* given in Eq. (3.32), beyond which the mode $l = 1$ is unstable and surface patterns with a polar asymmetry can spontaneously form from the homogeneous state. Note that for a vanishing interior viscosity, Pe_-^* is equivalent to the critical contractility α_s^* given in Eq. (2.41) that was derived for a deformable surface. The reason for this equivalence is that the instability of the mode $l = 1$ is driven solely by an isotropic in-plane compression that is to linear order the same on a fixed and on a deforming surface. Note in this context also that Pe_-^* does only depend on the bulk viscosity η_b , but not on the shear viscosity η_s .

For larger shear stresses from the interior fluid and a finite homogeneous turnover, the mode $l = 2$ can become unstable first for increasing Péclet numbers, leading to a situation in which a contractile ring with nematic symmetry spontaneously forms. This resembles the formation of a contractile ring in the cortex of a cell before cytokinesis [39]. Qualitatively, the appearance of a ring pattern can be understood by considering the hydrodynamic length scale $L_h = \eta_s/\eta_-$, where η_- is the viscosity of the interior passive fluid. This length scale represents a screening length for local contractile tension, similar to a hydrodynamic length scale that results from friction with a substrate [64, 117]. If L_h becomes smaller than the radius of the sphere R , patterns other than a single contractile patch can emerge. Note that an exterior fluid also introduces a hydrodynamic length scale, hence it can affect the mechano-chemical patterning processes in a similar way. Our description does not take various properties associated with an actual actomyosin cortex into account, such as anisotropies or a complex composition. Even without these ingredients, our minimal model of an isotropic one-component fluid that integrates a self-organised active stress is sufficient to generate the steady-state pattern of a contractile ring.

Inspired by the spatially nematic signalling cues that the spindle apparatus in a cell provides for the cortex, we additionally studied the surface dynamics in the background of a on-rate k_{on} with a spatially nematic profile on the surface. In parameter regimes for which the homogeneous state is stable, switching on the spatially dependent rate trivially imprints a corresponding pattern of stress regulator on the surface. This represents a scenario in which the organisation of the surface is fully guided by the external cue and the dynamics shows no signature of mechano-chemical self-organisation. In parameter regimes for which the homogeneous state is unstable, several different patterns form and are eventually oriented with the axis provided by the external nematic cue. For example, a contractile ring can spontaneously emerge and is eventually oriented in a well-defined way by the external cue. We considered here a spatially fixed cue, but we point out that its orientation could in principle depend on the surface dynamics. In the context of a spindle, for example, it is known that feedback

mechanisms exist between the spindle orientation and the stress distribution on the cellular cortex [154].

In the last part of this chapter, we focused on interactions of self-organised surface flows with an exterior passive fluid (Section 3.3). We found that this description gives rise to a squirmer model: the active surface swimmer. Surface patterns with polar asymmetry spontaneously form for Péclet numbers beyond a critical value Pe_+^* given in Eq. (3.37). The mechanical coupling with the surrounding passive fluid leads to a spontaneous onset of force-free motion relative to the laboratory frame. We obtained numerical solutions of the full problem and found a trailing stagnation point in the passive fluid flow around the active surface swimmer. A trailing stagnation point indicates that our swimmer belongs to the class of pullers [150], which we also confirmed analytically.

We used the general closed solution of the nonlinear problem to approximate the steady-state propagation velocity of the active surface swimmer, and found good agreement with solutions obtained numerically. We derived the normal form of the bifurcation associated with the spontaneous onset of translational motion. From this, we found that the onset of motion appears as a supercritical pitchfork bifurcation, and we identified the relative deviation from the critical Péclet number $\Delta Pe = (Pe - Pe_+^*)/Pe_+^*$ as the corresponding control parameter.

Finally, we note that for the special case of vanishing surface viscosity, $\eta_b = \eta_s = 0$, our model shares several features with descriptions previously used to study Marangoni flows [149, 155, 156]. These are flows that arise due to surface tension gradients on fluid-fluid interfaces, which can be used to generate spontaneously moving droplets [157]. It would be interesting to study whether the results presented here are applicable in systems where such Marangoni flows occur and *vice versa*.

Chapter 4

Self-organised contractility oscillations on an active viscoelastic surface

In this chapter, we analyse the dynamics of a self-organised active surface with viscoelastic properties. This is motivated by the fact that the cellular cortex and epithelial tissues typically show a viscoelastic response to applied stress [12, 72, 111]. To study this property in the context of the mechano-chemical self-organisation of surfaces, we extend the description developed in the previous chapter and consider here a Maxwell model to describe the response of the surface material to active stress. A Maxwell model is characterised by a time scale τ_M on which elastic stress in the material relaxes. Such a relaxation time leads to an elastic response at short times and a fluid-like response at long times if the material is deformed at a constant rate.

The chapter is organised as follows. In Section 4.1, we introduce covariant constitutive relations of an active viscoelastic surface. In Section 4.2, we perform a linear stability analysis of the material dynamics on a sphere. From this, we identify a critical Maxwell time τ_M^* that indicates the transition to an oscillatory instability. In Section 4.3, we study the full nonlinear dynamics of these oscillations using a numerical approach. We find steady states in which chemically regulated active stress oscillates between two opposite poles. In Section 4.4, we summarise and discuss the main results of this chapter.

4.1 Constitutive relation of an active viscoelastic surface

We consider in this chapter an isotropic viscoelastic material on a fixed surface $\bar{\Gamma}$ with constitutive relation

$$t_{ij} = t_{ij}^{\text{el}} + t_{ij}^{\text{a}}. \quad (4.1)$$

Here, t_{ij}^a is an active isotropic tension and t_{ij}^{el} is described by a Maxwell model, which we write as

$$\left(1 + \tau_M \frac{\bar{D}}{Dt}\right) t_i^{\text{el},j} = 2\eta_s \left(v_i^{\cdot j} - \frac{1}{2}v_k^k \delta_i^j\right) + \eta_b v_k^k \delta_i^j. \quad (4.2)$$

Here, τ_M is the Maxwell relaxation time and we have assumed for simplicity that its value is the same for shear deformations and isotropic deformations of the material. As in the previous chapter, $v_{ij} = (\nabla_i v_j + \nabla_j v_i)/2$ denotes the symmetric part of the strain rate tensor on the fixed surface. In Eq. (4.2), we use the covariant form of the convected corotational derivative \bar{D}/Dt (Jaumann derivative) given by

$$\frac{\bar{D}}{Dt} t_i^{\cdot j} = \partial_t t_i^{\cdot j} + v^k \nabla_k t_i^{\cdot j} + \omega_n \left(\epsilon_{ik} t^{kj} + \epsilon^{jk} t_{ik}\right), \quad (4.3)$$

where $\omega_n = \frac{1}{2}\epsilon^{ij}\nabla_i v_j$ denotes the in-plane vorticity of the flow field. Equation (4.3) represents the symmetrised form of a general Lagrangian derivative D/Dt on curved surfaces and is derived in Appendix E.2.1. There, we also show that the metric tensor g_{ij} does not commute with \bar{D}/Dt , even on a fixed surface. However, \bar{D}/Dt does commute with the Kronecker delta δ_i^j . Writing the Maxwell model Eq. (4.2) in terms of mixed coordinates therefore ensures that the traceless symmetric part of t_{ij}^{el} is related exclusively to shear deformations and the trace of t_{ij}^{el} is exclusively related to isotropic compressions and expansions of the material. For a more detailed discussion of these rather technical aspects, we refer to Appendix E.2.1.

We consider for the active contribution t_{ij}^a in Eq. (4.2) an isotropic tension $t_{ij}^a = \xi f(c) g_{ij}$ that depends on the concentration c of a stress regulator. The dynamic equation of the concentration field is given by

$$\partial_t c = -\nabla_i (c v^i) + D \Delta_{\bar{\Gamma}} c + R(c), \quad (4.4)$$

where D is the diffusion constant and $\Delta_{\bar{\Gamma}}$ is the Laplace-Beltrami operator. The reaction term in Eq. (4.4) is given by $R(c) = -k_{\text{off}}c + k_{\text{on}}$. We use the characteristic concentration $c_0 = k_{\text{on}}/k_{\text{off}}$ and the degradation rate $k = k_{\text{off}}$ as the two free parameters and write $R(c) = -k(c - c_0)$. The model is closed by the force balance equation

$$\nabla_i t^i_j = -f_j^{\text{ext}}, \quad (4.5)$$

where we neglect inertial effects. We study in the following sections the dynamics of the viscoelastic self-organised isotropic active surface as described by Eqs. (4.1)–(4.5) on a sphere. We also include external shear forces f_j^{ext} from an interior passive, incompressible fluid with viscosity η_- as introduced in Section 3.1.2.

4.2 Linear stability analysis

In the following, we present the linear stability analysis of the homogeneous steady state for the active viscoelastic surface model on a sphere. First, we derive the Jacobian of this system using tensor spherical harmonics to represent the elastic tension tensor t_{ij}^{el} . The general problem contains at each point on the surface four degrees of freedom: the concentration field c and three degrees of freedom described by the symmetric tensor t_{ij}^{el} . We show here that this problem can be reduced to two independent degrees of freedom by using a suitable transformation. From this, we determine a critical Maxwell time τ_M^* that indicates the presence of oscillatory instabilities in the system if the Maxwell relaxation time τ_M becomes larger than τ_M^* .

4.2.1 Derivation of the Jacobian

Here, we derive the Jacobian for perturbations of the homogeneous state $c = c_0$, $v_i = 0$ and $t_{ij}^{\text{el}} = 0$ on a sphere of radius R . Note that as in Chapter 3, we consider the specific parametrisation of a unit sphere to represent tensor components and covariant derivatives (Appendix A.3.2), but keep the covariant component notation general to simplify the calculations. In contrast to the purely viscous surface, the tension tensor $t_{ij}^{\text{el}}(\theta, \varphi)$ is now an independent dynamic variable. We expand perturbations around $t_{ij}^{\text{el}} = 0$ as

$$\delta t_{ij}^{\text{el}} = \sum_{l,m} \left(\delta t_{lm}^{(0)} \eta_{ij}^{(lm)} + \delta t_{lm}^{(1)} \Psi_{ij}^{(lm)} + \delta t_{lm}^{(2)} \Phi_{ij}^{(lm)} \right). \quad (4.6)$$

Here, the time-dependent mode coefficients $\{\delta t_{lm}^{(0)}, \delta t_{lm}^{(1)}, \delta t_{lm}^{(2)}\}$ represent the three local degrees of freedom of $\delta t_{ij}^{\text{el}}$ and $\{\eta_{ij}^{(lm)}(\theta, \varphi), \Psi_{ij}^{(lm)}(\theta, \varphi), \Phi_{ij}^{(lm)}(\theta, \varphi)\}$ denote tensor spherical harmonics [158]. Briefly, $\eta_{ij}^{(lm)}$ denotes modes of the isotropic part of a tensor on a sphere, while $\Psi_{ij}^{(lm)}$ and $\Phi_{ij}^{(lm)}$ represent modes associated with the two degrees of freedom of a traceless symmetric tensor on a sphere. Tensor spherical harmonics obey eigenvalue equations with the Laplace-Beltrami operator on a sphere and are therefore orthogonal with respect to a suitably defined scalar product. Furthermore, covariant divergences of tensor harmonics can be expressed in terms of vector harmonics, such that Eq. (4.6) can be combined with expansions of other quantities in terms of vector and scalar spherical harmonics. Explicit representations of tensor spherical harmonics together with an overview of their relevant properties are given in Appendix B.1.3.

Small perturbations of the surface flow $\delta v_i(\theta, \varphi)$ and concentration field $\delta c(\theta, \varphi)$ are ex-

panded as

$$\delta v_i = \sum_{l,m} \left(\delta v_{lm}^{(1)} \Psi_i^{lm} + \delta v_{lm}^{(2)} \Phi_i^{lm} \right) \quad (4.7)$$

$$\delta c = \sum_{l,m} \delta c_{lm} Y_{lm}, \quad (4.8)$$

where we use scalar and vector spherical harmonics, $Y_{lm}(\theta, \varphi)$ and $\{\Psi_i^{(lm)}(\theta, \varphi), \Phi_i^{(lm)}(\theta, \varphi)\}$, respectively (Appendix B).

With the expansions Eqs. (4.6) and (4.7), we first derive a linearised form of the Maxwell constitutive relation Eq. (4.2). To this end, we note that the right-hand side of Eq. (4.2) can be written with Eq. (4.7) as

$$2\eta_s \left(\delta v_{ij} - \frac{1}{2} \delta v_k^k g_{ij} \right) + \eta_b \delta v_k^k g_{ij} = \frac{1}{R} \sum_{l,m} \left[\delta v_{lm}^{(1)} \left(2\eta_s \Psi_{ij}^{(lm)} - \eta_b l(l+1) \eta_{ij}^{(lm)} \right) + 2\delta v_{lm}^{(2)} \eta_s \Phi_{ij}^{(lm)} \right], \quad (4.9)$$

where we have used the definitions of vector and tensor spherical harmonics (Appendix B.3.2). Inserting Eqs. (4.6) and (4.9) in the constitutive relation Eq. (4.2), and using the orthogonality of tensor spherical harmonics, we find

$$\frac{d}{dt} \delta t_{lm}^{(0)} = -\frac{1}{\tau_M} \delta t_{lm}^{(0)} - l(l+1) \frac{\eta_b}{\tau_M R} \delta v_{lm}^{(1)} \quad (4.10)$$

$$\frac{d}{dt} \delta t_{lm}^{(1)} = -\frac{1}{\tau_M} \delta t_{lm}^{(1)} + \frac{2\eta_s}{\tau_M R} \delta v_{lm}^{(1)} \quad (4.11)$$

$$\frac{d}{dt} \delta t_{lm}^{(2)} = -\frac{1}{\tau_M} \delta t_{lm}^{(2)} + \frac{2\eta_s}{\tau_M R} \delta v_{lm}^{(2)}, \quad (4.12)$$

where we have additionally used $\bar{D}/Dt \approx \partial_t$ to linear order. This system can be simplified by introducing a new set of coefficients $\{\tilde{\delta t}_{lm}^{(0)}, \tilde{\delta t}_{lm}^{(1)}\}$ defined by

$$\tilde{\delta t}_{lm}^{(0)} = \delta t_{lm}^{(0)} + l(l+1) \frac{\eta_b}{2\eta_s} \delta t_{lm}^{(1)} \quad (4.13)$$

$$\tilde{\delta t}_{lm}^{(1)} = \delta t_{lm}^{(1)} + \left(1 - \frac{l(l+1)}{2} \right) \delta t_{lm}^{(1)}. \quad (4.14)$$

With this transformation, Eqs. (4.10) and (4.11) yield

$$\frac{d}{dt} \tilde{\delta t}_{lm}^{(0)} = -\frac{1}{\tau_M} \tilde{\delta t}_{lm}^{(0)} \quad (4.15)$$

$$\frac{d}{dt} \tilde{\delta t}_{lm}^{(1)} = -\frac{1}{\tau_M} \tilde{\delta t}_{lm}^{(1)} + \frac{\eta_s [2 - l(l+1)] - \eta_b l(l+1)}{\tau_M R} \delta v_{lm}^{(1)}, \quad (4.16)$$

which implies that a stable degree of freedom described by $\delta\tilde{t}_{lm}^{(0)}$ drops out of the problem.¹

In the next step, we use the force balance to determine the flow field δv_i . For $\delta t_{ij} = \delta t_{ij}^{\text{el}} + \delta t_{ij}^a$ with $\delta t_{ij}^{\text{el}}$ given in Eq. (4.6) and $\delta t_{ij}^a = \xi c_0 \partial_c f(c_0) \delta c g_{ij}$ the force balance Eq. (4.5) yields

$$\sum_{l,m} \left\{ \left(\delta\tilde{t}_{lm}^{(1)} + \xi \partial_c f(c_0) \delta c_{lm} \right) \Psi_i^{(lm)} + \left[1 - \frac{l(l+1)}{2} \right] \delta t_{lm}^{(2)} \Phi_i^{(lm)} \right\} = -R \delta f_i^{\text{ext}}. \quad (4.17)$$

We consider here external forces δf_j^{ext} from an interior passive fluid as introduced in Section 3.1.2. We recall that this force can be expressed as

$$\delta f_i^{\text{ext}} = \sum_{l,m} \left(\delta f_{lm}^{(1)} \Psi_i^{(lm)} + \delta f_{lm}^{(2)} \Phi_i^{(lm)} \right), \quad (4.18)$$

with

$$\delta f_{lm}^{(1)} = -\frac{\eta_-}{R} (2l+1) \delta v_{lm}^{(1)} \quad (4.19)$$

$$\delta f_{lm}^{(2)} = -\frac{\eta_-}{R} (l-1) \delta v_{lm}^{(2)}, \quad (4.20)$$

where η_- denotes the viscosity of the interior fluid. Note that the velocity modes $\delta v_{lm}^{(2)}$ for $l=1$ represent full body rotation that are not relevant for this problem and can be set to zero. Furthermore, the special case $\eta_- = 0$ yields $\delta f_i^{\text{ext}} = 0$, such that the force balance Eq. (4.17) implies $\delta t_{lm}^{(2)} = 0$ and $\delta\tilde{t}_{lm}^{(1)} \sim \delta c_{lm}$. Hence, for $\eta_- = 0$ only the concentration mode δc_{lm} remains as an independent degree of freedom and we find a dispersion relation similar to the case already studied in Section 3.2. In the following, we therefore focus on the case $\eta_- > 0$.

Using Eqs. (4.19) and (4.20) in Eq. (4.17), the velocity modes are determined as

$$\delta v_{lm}^{(1)} = \frac{\left(\delta\tilde{t}_{lm}^{(1)} + \xi \partial_c f(c_0) \delta c_{lm} \right)}{\eta_- (1+2l)} \quad (4.21)$$

$$\delta v_{lm}^{(2)} = -\frac{[l(l+1)-2]}{2\eta_- (l-1)} \delta\tilde{t}_{lm}^{(2)}. \quad (4.22)$$

From Eqs. (4.12) and Eq. (4.22), we find that the stationary state is always stable against perturbations described by the mode coefficients $\delta t_{lm}^{(2)}$. Using Eq. (4.21) to eliminate the

¹The physical meaning of the coefficients $\delta\tilde{t}_{lm}^{(0)}$ can be understood as follows. Equation (4.15) implies that at long times $\delta\tilde{t}_{lm}^{(0)} \rightarrow 0$. Hence, the mode coefficients $\delta t_{lm}^{(0)}$ and $\delta t_{lm}^{(1)}$, which respectively describe isotropic and anisotropic tension, become linearly dependent according to Eq. (4.13) and their relative amplitude is essentially set by the surface viscosity ratio η_b/η_s at long times. Only at short times, the modes $\delta t_{lm}^{(0)}$ and $\delta t_{lm}^{(1)}$ describe independent degrees of freedom that correspond to elastic responses with effective moduli $E_b = \eta_b/\tau_M$ and $E_s = \eta_s/\tau_M$.

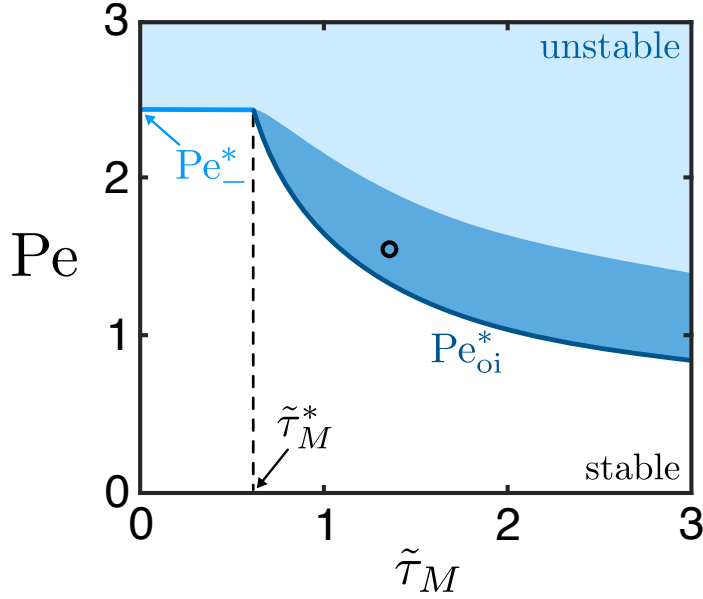


Figure 4.1: Representative stability diagram of the homogeneous state on a self-organised viscoelastic active surface. The Péclet number and dimensionless Maxwell time are defined by $Pe = \xi R^2 / (\eta_b D)$ and $\tilde{\tau}_M = \tau_M / \tau_D$, respectively. Here, $\tau_D = D / R^2$ is the time scale of diffusion that is held fixed in this stability diagram. The homogeneous state is unstable in the blue shaded region. The eigenvalues of the Jacobian \mathbf{J}_{el}^l described by Eqs. (4.23) and (4.24) are complex in the region shaded in dark blue, indicating oscillatory instabilities. For $\tau_M \rightarrow 0$, we recover the stability properties of the purely viscous surface studied in Chapter 3. The critical Péclet number Pe_* is given in Eq. (3.32). For Maxwell times $\tau_M > \tau_M^*$ (τ_M^* is given in Eq. (4.25)) instabilities occur at $Pe = Pe_{\text{oi}}^*$ (Pe_{oi}^* is given in Eq. (4.26)). In the stability diagram, we have annotated the dimensionless critical Maxwell time: $\tilde{\tau}_M^* = \tau_M^* / \tau_D$. The black circle depicts parameter values for which we representatively discuss the full nonlinear dynamics in Section 4.3. Parameters: $k = 0$, $\eta_s / \eta_b = 1$, $R\eta_- / \eta_b = 0.15$, $c_0 \partial_c f(c_0) = 1$.

velocity modes in the dynamic Eq. (4.16) leads finally to

$$\frac{d}{dt} \delta \tilde{t}_{lm}^{(1)} = -\frac{1}{\tau_M} \delta \tilde{t}_{lm}^{(1)} + \frac{\eta_s [2 - l(l+1)] - \eta_b l(l+1)}{R\tau_M \eta_- (1+2l)} \left(\delta \tilde{t}_{lm}^{(1)} + \xi \partial_c f(c_0) \delta c_{lm} \right). \quad (4.23)$$

Hence, only a single relevant degree of freedom of the tension tensor remains after the linearisation of the force balance equation. The dynamics of the corresponding modes is described by Eq. (4.23). The system is closed by the linearisation of the dynamic equation for the concentration field Eq. (4.4), which reads

$$\frac{d}{dt} \delta c_{lm} = \frac{l(l+1)}{\eta_- (1+2l)} \frac{c_0}{R} \delta \tilde{t}_{lm}^{(1)} - \left[\frac{D}{R^2} l(l+1) + k - \frac{l(l+1)}{\eta_- (1+2l)} \frac{c_0}{R} \xi \partial_c f(c_0) \right] \delta c_{lm}. \quad (4.24)$$

Here, we have used Eqs. (3.26) and (4.21). Equations (4.23) and (4.24) define the final Jacobian \mathbf{J}_{el}^l for the dynamics of the modes $\delta \tilde{t}_{lm}^{(1)}$ and δc_{lm} . We write \mathbf{J}_{el}^l explicitly in Appendix E.2.2. The eigenvalues of \mathbf{J}_{el}^l indicate the stability of the homogeneous state, which we analyse in the next part.

4.2.2 Critical Maxwell time

In the limit $\tau_M \rightarrow 0$, the Jacobian \mathbf{J}_{el}^l defined by the linear system Eqs. (4.23) and (4.24) leads to a dispersion relation that is equivalent to the dispersion relation derived in Section 3.2.1 for a purely viscous fluid surface.¹ There, we have discussed that *stationary instabilities*² can occur on a viscous surface for increasing Péclet numbers $\text{Pe} = \xi R^2 / (\eta_b D)$ at a critical value Pe_* . In the regime $\tau_M > 0$ for the viscoelastic surface studied here, we can additionally identify a critical Maxwell time given by

$$\tau_M^* = \frac{1 + \frac{3}{2} \frac{R\eta_-}{\eta_b}}{\frac{2D}{R^2} + k} \quad (4.25)$$

from the Jacobian \mathbf{J}_{el}^l (see Appendix E.2.2 for details). For $\tau_M > \tau_M^*$, *oscillatory instabilities* can occur. In particular, for increasing Péclet numbers the mode $l = 1$ becomes unstable at $\text{Pe} = \text{Pe}_{\text{oi}}^*$ with

$$\text{Pe}_{\text{oi}}^* = \frac{3R\eta_-}{2\eta_b c_0 \partial_c f(c_0)} \left[2 + \frac{kR^2}{D} + \frac{R^2}{\tau_M D} \left(1 + \frac{2\eta_b}{3R\eta_-} \right) \right]. \quad (4.26)$$

A representative stability diagram is shown in Fig. 4.1. The homogeneous state is unstable in the blue shaded region. Parameter regimes with complex eigenvalues of the underlying Jacobian \mathbf{J}_{el}^l are shaded in dark blue. For Maxwell times $\tau_M < \tau_M^*$ with τ_M^* given in Eq. (4.25), the homogeneous state undergoes a stationary instability for increasing Péclet number at $\text{Pe} = \text{Pe}_*$, with Pe_* given in Eq. (3.32). For $\tau_M > \tau_M^*$, oscillatory instabilities occur. In this regime, the critical Péclet number depends on the Maxwell time τ_M and is given in Eq. (4.26).

4.3 Nonlinear dynamics of contractility oscillations

In the final section of this chapter, we study the full nonlinear dynamics of the self-organised viscoelastic active surface on a sphere. For this purpose, we have developed a spectral numerical approach that enables us to solve nonlinear tensor-valued differential equations on the surface of a sphere. The details of this method are introduced in Appendix E.3.3. Finally, we present an explicit expression for the frequencies of the steady-state oscillations and compare them to numerical results.

In the following, we use our numerical approach to analyse the nonlinear dynamics in parameter regimes for which the stability analysis presented in Section 4.2 indicates oscillatory instabilities. Using a randomly perturbed concentration field as initial condition, we find the formation of steady states in which a single contractile region appears and disappears

¹This is shown explicitly in Appendix E.2.2.

²Stationary instabilities correspond to unstable modes with a real-valued growth rate. If the mode becomes unstable and the growth rate has an imaginary part, an *oscillatory instability* is present [135].

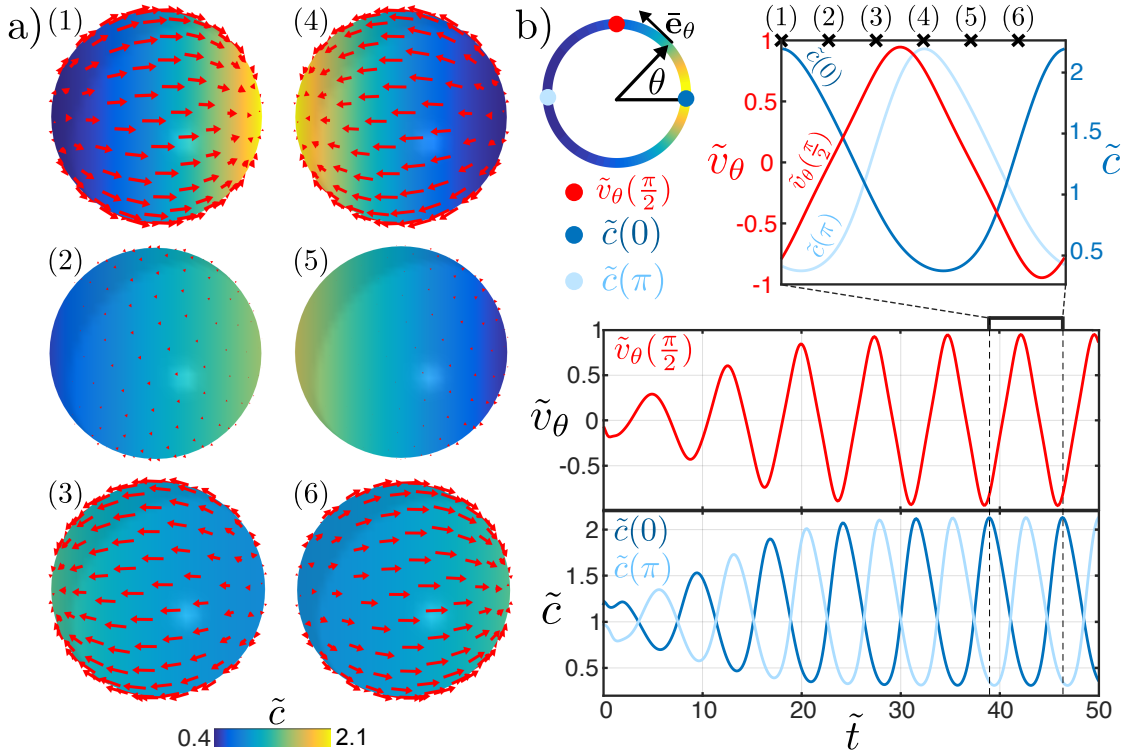


Figure 4.2: Characterisation of steady-state oscillations on a viscoelastic active surface. **a)** Surface view of the concentration field $\tilde{c} = c/c_0$ and the flow velocity \mathbf{v}_{\parallel} (red arrows) over one period of an oscillation cycle. Snapshots are shown for six equidistant time points enumerated from (1) to (6). During one cycle, a region of large contractile tension (high concentration) appears and disappears on two opposite poles in an axisymmetric fashion. **b)** Quantitative details of the oscillations starting from a random initial condition. Scales for nondimensionalisation are given by the time scale of diffusion $\tau_D = R^2/D$ and the characteristic velocity $v_D = R/\tau_D$, where R denotes the radius of the sphere. We depict over time $\tilde{t} = t/\tau_D$ the only non-vanishing component of the flow velocity, $\tilde{v}_{\theta} = \bar{\mathbf{e}}_{\theta} \cdot \mathbf{v}_{\parallel}/v_D$, at the equator $\theta = \pi/2$, and the values of the concentration field at the poles $\theta \in \{0, \pi\}$. The position of the poles is defined by the axis of the oscillating pattern at steady state. On the bottom, we plot the fields starting from the initial condition. Nonlinearities eventually saturate the oscillation amplitudes. In the upper graph, we show a close-up view of over one oscillation cycle at steady state. The time points of the surface images shown in a) are indicated by black crosses. The accumulation of stress regulator is preceded by the large tangential flow with a small phase shift. Parameters: $k = 0$, $\eta_s/\eta_b = 1$, $R\eta_-/\eta_b = 0.15$, $\tau_M/\tau_D = 1.3$, and $\text{Pe} = 1.5$ (Black circle in the stability diagram Fig. 4.1). Active tension is regulated by $f(c) = 2c^2/(c_0^2 + c^2)$, such that $c_0 \partial_c f(c_0) = 1$.

alternately on opposite surface poles. In Fig. 4.2a, we show a time series of concentration patterns and flow profiles that occur during one period of the corresponding steady-state oscillations. There, we use $k = 0$ (no turnover), $\text{Pe} = 1.5$ and $\tilde{\tau}_M = 1.3$. For reference, these parameters are denoted by a black circle in the stability diagram Fig. 4.1. The steady states observed in the numerical solutions are always axisymmetric, even if the initial conditions are chosen non-axisymmetric. Hence, the final axis of the pole-to-pole oscillations remains fixed over time. The surface views in Fig. 4.2a are accordingly orthogonal to the axis defined

by the pole-to-pole oscillations.

In Fig. 4.2 b, we give a more quantitative overview of the oscillations. For this, we orient the z -axis parallel to the axis defined by the steady-state oscillations and plot the time course of the concentration field and velocity on characteristic points on the surface. In particular, we show the concentration field at the poles at $\theta \in \{0, \pi\}$ and the amplitude of the tangential velocity at the equator $\theta = \pi/2$.¹ In the time course shown in Fig. 4.2 b (bottom), we see that the nonlinearities saturate the amplitudes of the oscillations. During oscillations, the concentration values at the opposite poles, $\tilde{c}(0)$ and $\tilde{c}(\pi)$, cross at the conserved average concentration value of $\tilde{c} = c/c_0 = 1$.

In the graph at the top of Fig. 4.2 b, we depict a close-up view of the time course over exactly one oscillation period at steady state. The black crosses depict the time points of the surface snapshots shown in Fig. 4.2 a. To ‘read’ this graph, note that a positive value of the tangential flow field at the equator, $\tilde{v}_\theta(\pi/2) > 0$, corresponds to tangential flows and a corresponding advection of stress regulator towards the pole at $\theta = \pi$. Negative values $\tilde{v}_\theta(\pi/2) < 0$ accordingly correspond to flows towards the pole at $\theta = 0$. If we focus at the pole at $\theta = \pi$, we recognise that the appearance of a concentration maximum $\tilde{c}(\pi)$ is preceded by the maximum of the flow amplitude towards this pole. Furthermore, we can identify a more subtle phase shift between the appearance of minimum-maximum pairs on opposite poles. This can be seen particularly well by comparing the curves for $\tilde{c}(0)$ and $\tilde{c}(\pi)$ in the close-up view of the oscillation dynamics (Fig. 4.2 b, top).

Oscillation frequencies

The Jacobian \mathbf{J}_{el}^l , defined by the linear system Eqs. (4.23) and (4.24), also contains information about the oscillation frequency ω associated with the oscillatory instability. At the critical Péclet number Pe_{oi}^* given in Eq. (4.26), this frequency (squared) is given by the determinant of the Jacobian [135]. From this, we find

$$\omega^2 = \frac{2\eta_b}{3R\eta_-} \left(\frac{2D}{R^2} + k \right) \left(1 - \frac{\tau_M^*}{\tau_M} \right) \frac{1}{\tau_M}, \quad (4.27)$$

with the critical Maxwell time τ_M^* given in Eq. (4.25). It follows from Eq. (4.27) that the oscillation frequency is maximal at $\tau_M = 2\tau_M^*$.

Finally, we have verified the expression for ω given in Eq. (4.27) by comparing it to oscillation frequencies that we obtained from solving the full nonlinear problem numerically. In particular, we varied $\tau_M \geq \tau_M^*$, then calculated the critical Péclet number Pe_{oi}^* from Eq. (4.26) and obtained numerical solutions for $\text{Pe} = \text{Pe}_{\text{oi}}^* + 0.01$. In Fig. 4.3, we show the curve described by Eq. (4.27) (solid line) against the oscillation frequencies obtained from the numerical solutions (crosses). Numerical results agree well with the analytic expression,

¹By symmetry, the velocity of an axisymmetric flow profile vanishes at the poles. Hence, the velocity field at the equator is the natural choice for depicting the kinetics of the oscillations.

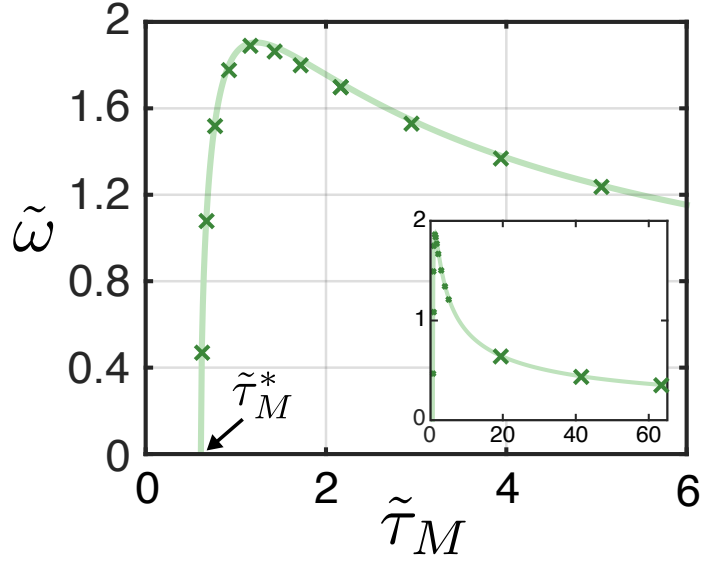


Figure 4.3: Comparison of the analytic prediction for the oscillation frequencies Eq. (4.27) with numerical solutions. We depict here dimensionless frequencies $\tilde{\omega} = \omega\tau_D$ against $\tilde{\tau}_M = \tau_M/\tau_D$ for a diffusion time scale $\tau_D = R^2/D$ that is held fixed. The dimensionless critical Maxwell time reads $\tilde{\tau}_M^* = \tau_M^*/\tau_D$ with τ_M^* given in Eq. (4.25). The solid lines follows from Eq. (4.27). Crosses depict oscillation frequencies obtained from numerical solution. The inset shows the same quantities over a larger range of Maxwell times. Parameters: $k = 0$, $\eta_s/\eta_b = 1$, and $R\eta_-/\eta_b = 0.15$. Active tension is regulated by $f(c) = 2c^2/(c_0^2 + c^2)$, such that $c_0\partial_c f(c_0) = 1$.

indicating that the observed oscillatory dynamics on the surface can be understood from a linear instability of the homogeneous state.

4.4 Discussion

In this chapter, we studied the effects of viscoelasticity on the mechano-chemical self-organisation of an active surface. To describe the response of the viscoelastic surface to active stress, we introduced a covariant Maxwell model with a relaxation time τ_M . To analyse the active viscoelastic surface, we considered the non-axisymmetric dynamics on a sphere and included external shear stresses from an interior passive fluid. As in the previous chapter, we characterised mechano-chemical instabilities using the Péclet number $Pe = \xi R^2/(\eta_b D)$, and we used a one-component description for the active surface. For a viscoelastic material, this description implies that we effectively neglected permeation effects, which can arise from friction of the viscoelastic gel with a solvent. Permeation could be included into our model by using a multi-component description in which the gel and the solvent are treated explicitly [5, 109, 110]. In general, a one-component description captures many characteristic features of active viscoelastic gels [5, 108, 159], but its quantitative validity for experimental comparisons certainly depends on the concrete system to which it is applied.

To analyse the linear stability properties of the viscoelastic surface, we first derived the general Jacobian for perturbations of the homogeneous state (Section 4.2). To this end, we introduced a transformation to reduce the problem from originally four local degrees of freedom to only two in the linear analysis. This allowed for a detailed analytic characterisation of the Jacobian. As a key result, we found a critical Maxwell time τ_M^* given in Eq. (4.25), which indicates the presence of oscillatory instabilities for sufficiently large Péclet numbers. For relaxation times smaller than τ_M^* , the homogeneous state becomes unstable when the Péclet number is increased up to $\text{Pe} = \text{Pe}_-^*$. The critical value Pe_-^* does not depend on τ_M and is the same as already found for the purely viscous surface (Eq. (3.32)). Hence, the mechano-chemical stability properties of the viscous and the viscoelastic active surface are equivalent for $\tau_M < \tau_M^*$. For $\tau_M \rightarrow 0$, we recover exactly the purely viscous surface studied in Chapter 3. In the regime $\tau_M > \tau_M^*$, we identified an oscillatory instability that appears for an increasing Péclet number at $\text{Pe} = \text{Pe}_{\text{oi}}^*$. The critical Péclet number Pe_{oi}^* associated with this instability depends on τ_M and is given in Eq. (4.26).

For simplicity, we have focused here on parameter regimes for which the mode $l = 1$ becomes unstable first when the Péclet number is increased. However, in regimes of larger interior viscosity η_- , other modes can also become unstable first, which is similar to the case of a purely viscous surface (Section 3.2.2). The critical Maxwell time τ_M^* and Péclet number Pe_{oi}^* can be generalised to these situations, in which case they indicate oscillatory instabilities of higher modes (Appendix E.2.2).

To analyse the full nonlinear dynamics, we developed a spectral approach, which enabled us to numerically solve tensor-valued, non-linear differential equations on the surface of a sphere (Appendix E.3.3). An alternative application of our approach could be the study of nematic surfaces. For example, the actomyosin cortex shares properties with an active nematic fluid [33,101] and active nematic shells have been successfully constituted *in-vitro* [145]. Continuum theories of nematic surfaces can also be formulated as tensor-valued, non-linear differential equations [160], and therefore impose very similar constraints on a numerical solution scheme as the viscoelastic surface dynamics studied here.

Using our numerical approach, we then verified the results of the linear stability analysis, and we studied non-trivial steady states emerging from instabilities of the homogeneous state (Section 4.3). In the regime of Maxwell times with $\tau_M < \tau_M^*$, the mechano-chemical stability properties and steady states of the active viscoelastic surface are essentially the same as for a purely viscous active surface. The existence of such a regime could be one reason why the cellular cortex can often be sufficiently well described by taking only its viscous properties into account [31–33, 120], even though the cortex is in general viscoelastic [13]. In the regime $\tau_M > \tau_M^*$, and for an increasing Péclet number, oscillatory steady states start emerging at $\text{Pe} = \text{Pe}_{\text{oi}}^*$, which is in agreement with the linear stability analysis. These steady states are characterised by a single contractile region that appears and disappears alternately on opposite surface poles. At steady state, the corresponding pole-to-pole oscillations are

axisymmetric, even if a non-axisymmetric initial condition is chosen.

To develop a qualitative understanding of these oscillatory steady states, we recall that they emerge from an instability of the mode $l = 1$. In the unstable regime, the active surface tends to generate mechano-chemical patterns with a polar asymmetry, which appear in the form of a single contractile patch. If the delay between the formation of this patch due to contractile flows and the relaxation of associated elastic tension becomes sufficiently large ($\tau_M > \tau_M^*$), the polar surface pattern starts to oscillate between opposite poles. Interestingly, pole-to-pole oscillations of contractile tension have been observed experimentally during cell size oscillations [131]. These results were explained theoretically by introducing a ‘cytoplasmic elasticity’, which summarised elastic contributions from the cytoplasm and the cortex into an effective parameter. We demonstrated here that the mechano-chemical self-organisation of a viscoelastic surface provides an alternative mechanism that also leads to the spontaneous emergence of pole-to-pole oscillations of contractile tension.

Chapter 5

Conclusion and Outlook

In this thesis, we identified and characterised various processes related to the self-organisation of active surfaces. In particular, we studied mechano-chemical processes on these surfaces, as well as their interaction with the surface shape and external forces. To this end, we used the hydrodynamic theory of active surfaces, and we explored minimal models that reflect key principles of the mechano-chemical self-organisation observed in biological systems. In this concluding chapter, we summarise the key results and point out possible directions for future work.

In Chapter 2, we presented a simple but general model for the mechano-chemical self-organisation of the geometry of an isotropic active surface. In our description, active isotropic tension in the surface is regulated by a diffusible and advected molecular species. Gradients of active tension induce surface flows and shape changes, which in turn influence the distribution of the regulator. To solve the nonlinear dynamic equations for the shape, the flows and the concentration of the regulator species, we developed a novel numerical approach based on an integral representation of axisymmetric surfaces and a dynamic coordinate transformation.

Using this framework, we found that a sphere becomes unstable for increasing contractility. Shape perturbations of an unstable sphere lead to concentration and flow patterns with polar asymmetry, and to axisymmetric oblate shapes with broken mirror symmetry. Cylindrical surfaces become unstable at a critical aspect ratio of 2π if the contractility is small, which corresponds to a Plateau-Rayleigh instability [133]. We also found a critical contractility, beyond which the cylinder becomes unstable at aspect ratios smaller than 2π . In this regime, instabilities are induced by the active contractility. In contrast to mechano-chemical instabilities that have been previously studied on fixed geometries [117, 120, 124, 136], we described here new phenomena that give rise to shape changes and crucially depend on the shape changes that occur.

On tubular surfaces for which a small neck radius is stabilised at long times, we have additionally described the emergent formation of directed surface flows via spontaneous symmetry breaking. In a reference frame, where the average of the surface velocity vanishes, this results

in a propagating surface constriction that resembles the dynamics of a peristaltic wave. Interestingly, we found that directed surface flows occur independently of the mechanism with which neck radii are stabilised. Hence, the spontaneous symmetry breaking seems to be a generic feature of a self-organised active fluid that prescribes a deforming tubular surface.

Our general framework provides the basis to explore a large variety of alternative constitutive relations of active materials on axisymmetric surfaces. An important future challenge is certainly the generalisation of the numerical approach so that it enables also to study non-axisymmetric surface shapes and deformations.

In Chapter 3, we studied the mechano-chemical self-organisation of an isotropic active fluid on a sphere. In contrast to the analysis of the deforming surface, we considered here the general, non-axisymmetric dynamics of a self-organised stress regulator on the surface and took external shear stresses from a surrounding passive fluid into account.

We identified a new mechanism that leads to the spontaneous formation of surface patterns with polar asymmetry and to the formation of a contractile ring in a fully self-organised fashion. The formation of polar patterns appears generally for small viscosities of the surrounding fluid. For larger external viscosities and finite homogeneous turnover, a contractile ring with nematic symmetry can spontaneously emerge from an instability of the homogeneous state. This resembles the formation of a contractile ring in the cortex of a cell before cytokinesis [39]. We showed that this ring pattern, as well as patterns with polar asymmetry, can be oriented by an external nematic cue. An interesting question for future investigations is whether a similar minimal model can describe the emergence of asymmetrically positioned contractile rings, which appears during asymmetric cell divisions [57, 64].

Our description of an active surface embedded in a passive fluid also gives rise to a squirmer model that we characterised in detail. We used the general closed solution of the nonlinear problem to approximate the steady-state propagation velocity of this active surface swimmer, and we found good agreement with solutions obtained numerically. We studied the spontaneous onset of translational motion and derived the normal form of the associated bifurcation. From this, we found that the onset of motion appears as a supercritical pitchfork bifurcation.

In Chapter 4, we studied the effects of viscoelasticity on the mechano-chemical self-organisation of an active surface. To describe the response of the viscoelastic surface to active stress, we introduced a covariant Maxwell model. To characterise linear stability properties of the active viscoelastic surface, we derived the fully general Jacobian for perturbations of the homogeneous state. To this end, we used tensor spherical harmonics [158], which provide a powerful tool to conveniently expand tensor fields on a sphere. From the Jacobian, we identified a minimal time scale for the relaxation of elastic stress, beyond which spatio-temporal oscillations of active stress can spontaneously emerge. These steady-state

oscillations are characterised by a single contractile region that appears and disappears alternately on opposite surface poles. At steady state, the corresponding pole-to-pole oscillations are axisymmetric, even if a non-axisymmetric initial condition is chosen.

To analyse the full nonlinear dynamics of this system, we developed a spectral approach, which enabled us to numerically solve tensor-valued, non-linear differential equations on the surface of a sphere. Our numerical approach could also be used to study nematic surfaces, which are described by continuum theories that impose very similar constraints on a numerical solution scheme as the viscoelastic surface dynamics.

For our description of the viscoelastic surface, we chose for simplicity a one-component description and therefore effectively neglected permeation effects. These can arise from friction of the viscoelastic gel with a solvent. In order to develop a more complete picture, it would be interesting to include permeation into our framework by treating the gel and the solvent explicitly in a multi-component description [5, 109, 110].

Not only for the viscoelastic surface, but throughout the thesis, we used minimal models with a single chemical species to regulate active stress. This enabled us to reveal generic features of the mechano-chemical feedback acting on surfaces. Our formulations on fixed and deforming surfaces can easily be extended to more complex chemical schemes, involving several chemical species [84]. Such extended models could represent, for example, the actin dynamics present in the cell cortex and its biochemical regulators [58, 120], or the behaviour of sets of morphogens spreading in epithelial tissues [73, 98]. The description can be generalised further by explicitly treating a potential mass exchange of the surface with the environment, as well as height changes of the surface.

Furthermore, our work exclusively focussed on materials that are isotropic in the surface plane. However, the numerical tools we developed could also be used to explore constitutive relations of surface materials that generate anisotropic or chiral active tension in the plane [36, 80, 112]. Finally, we note that a future challenge of particular interest is to further develop these numerical tools so that they enable to combine the deformation dynamics of self-organised active surfaces with mechanical interactions of material surrounding this surface.

Appendices

Appendix A

Differential geometry of embedded surfaces

Here, we present an overview of the mathematical framework used in this thesis to describe the differential geometry of surfaces embedded in Euclidean space. Section A.1 is devoted to an introduction of the basic definitions of a surface parametrisation, invariants of tensor fields and covariant derivatives on curved surfaces. These elements provide the mathematical language to construct models of complex materials on surfaces and to formulate conservation laws in the form of differential equations on them. In Section A.2, we introduce the description of surface deformations of parametrised surfaces. To this end, we first present the variations of surface quantities under small shape perturbations. Furthermore, we state general dynamic equation of a surface for a prescribed deformation field. In Section A.3, we present explicit parametrisations of axisymmetric surfaces that are relevant for this thesis.

A.1 Definitions and basic identities

A.1.1 Parametrisation of an embedded surface

Consider a two-dimensional surface Γ that is embedded in Euclidean space and parametrised by a vector field $\mathbf{X}(s^1, s^2) \subset \mathbb{R}^3$. Tangential basis vectors are defined as derivatives with respect to the surface parameters s^1 and s^2 :

$$\mathbf{e}_i = \partial_i \mathbf{X}, \quad (\text{A.1})$$

where $i = 1, 2$ and we use the notation $\partial_i := \partial/\partial s^i$. The surface normal is given by

$$\mathbf{n} = \frac{\mathbf{e}_1 \times \mathbf{e}_2}{|\mathbf{e}_1 \times \mathbf{e}_2|}. \quad (\text{A.2})$$

The metric tensor is given by

$$g_{ij} = \mathbf{e}_i \cdot \mathbf{e}_j, \quad (\text{A.3})$$

where the dot denotes the scalar product in Euclidean space. The inverse metric tensor $g^{ij} = (g_{ij})^{-1}$ obeys

$$g^{ik}g_{kj} = \delta_j^i \quad (\text{A.4})$$

The metric tensor relates covariant and contravariant components by

$$v_i = g_{ij}v^j, \quad (\text{A.5})$$

such that scalar products in the tangent space of Γ can be expressed as

$$\mathbf{v}_{\parallel} \cdot \mathbf{w}_{\parallel} = g_{ij}v^i w^j = v^i w_i. \quad (\text{A.6})$$

Here, we have introduced the decomposition

$$\mathbf{v} = \mathbf{v}_{\parallel} + \mathbf{v}_{\perp} \quad (\text{A.7})$$

with tangential and normal parts of a vector field, $\mathbf{v}_{\parallel} = v^i \mathbf{e}_i$ and $\mathbf{v}_{\perp} = v_n \mathbf{n}$, respectively. The covariant antisymmetric Levi-Civita tensor ϵ_{ij} is defined by

$$\mathbf{e}_i \times \mathbf{e}_j = \epsilon_{ij} \mathbf{n}, \quad (\text{A.8})$$

which implies additionally

$$\mathbf{n} \times \mathbf{e}_i = \epsilon_i^j \mathbf{e}_j. \quad (\text{A.9})$$

Derivatives of the basis vectors are determined by the Gauss-Weingarten relations [128]

$$\partial_i \mathbf{e}_j = -C_{ij} \mathbf{n} + \Gamma_{ij}^k \mathbf{e}_k \quad (\text{A.10})$$

$$\partial_i \mathbf{n} = C_i^j \mathbf{e}_j, \quad (\text{A.11})$$

which define the curvature tensor

$$C_{ij} = -\mathbf{n} \cdot \partial_i \partial_j \mathbf{X}, \quad (\text{A.12})$$

and Christoffel symbols

$$\begin{aligned} \Gamma_{ij}^k &= \mathbf{e}^k \cdot \partial_i \partial_j \mathbf{X} \\ &= \frac{1}{2} g^{kl} (\partial_i g_{jk} + \partial_j g_{ik} - \partial_k g_{ij}). \end{aligned} \quad (\text{A.13})$$

A.1.2 Invariants of surface tensors

The parametrisation-invariant trace of a tensor field is computed by $T_k^k = g^{ij} T_{ij}$. The trace of the metric tensor on a two-dimensional surface therefore yields $g^{ij} g_{ij} = \delta_k^k = 2$. The trace

of the curvature tensor C_{ij} defines the mean curvature H by

$$H = \frac{1}{2} C^k_k. \quad (\text{A.14})$$

Any tensor field T_{ij} can be decomposed into

$$T_{ij} = \tilde{T}_{ij} + \frac{1}{2} T^k_k g_{ij} + \frac{1}{2} T_{kl} \epsilon^{kl} \epsilon_{ij}, \quad (\text{A.15})$$

where

$$\tilde{T}_{ij} = \frac{1}{2} (T_{ij} + T_{ji} - T^k_k g_{ij}) \quad (\text{A.16})$$

is the symmetric, traceless part of the tensor T_{ij} . The second and third term on the right hand side of Eq. (A.15) correspond to the trace and the antisymmetric part of T_{ij} , respectively.

For any tensor field T_{ij} , we can define a *parametrisation-invariant* determinant by

$$\det(T^i_j) = \frac{1}{2} \epsilon_{ij} \epsilon^{kl} T^i_k T^j_l. \quad (\text{A.17})$$

The parametrisation-invariant determinant of the metric tensor on any two-dimensional surface is meaningfully determined from Eq. (A.17) as $\det(g^i_j) = \det(\delta^i_j) = 1$. The determinant of the curvature tensor C_{ij} defines the Gaussian curvature K (intrinsic curvature)

$$K = \det(C^i_j). \quad (\text{A.18})$$

Importantly, definition Eq. (A.17) is distinct from what is typically referred to as the *determinant of the metric* given by

$$g = \det(g_{ij}) = g_{11}g_{22} - g_{12}g_{21}, \quad (\text{A.19})$$

from which one can construct the surface area element

$$dA = \sqrt{g} ds^1 ds^2. \quad (\text{A.20})$$

The field g is calculated from the covariant metric tensor components only and therefore *parametrisation-dependent*. This is also evident from Eq. (A.20): The surface area dA should not depend on the parametrisation, such that \sqrt{g} must have a different form for different choices of parameters s^1 and s^2 .

A useful relation between the trace and the determinant of a tensor field T_{ij} on a two-dimensional surface is given by [112]

$$T^k_i T_{kj} = T^k_k T_{ij} - g_{ij} \det(T^k_l). \quad (\text{A.21})$$

This implies a relation between mean curvature and Gaussian curvature:

$$C_{ik}C_j^k = 2HC_{ij} - Kg_{ij}. \quad (\text{A.22})$$

A.1.3 Differentiation on curved surfaces

Definition and properties of the covariant derivative

The covariant derivative of vector field in the tangent space is defined by $\nabla_i v^j = \mathbf{e}^j \cdot \partial_i \mathbf{v}_{\parallel}$, which yields

$$\nabla_i v^j = \partial_i v^j + \Gamma_{ik}^j v^k. \quad (\text{A.23})$$

For a tensor $\mathbf{t} = t^{ij} \mathbf{e}_i \mathbf{e}_j$, we define $\nabla_i t^{jk} = \mathbf{e}^j \cdot \partial_i \mathbf{t} \cdot \mathbf{e}^k$, which yields

$$\nabla_i t^{jk} = \partial_i t^{jk} + \Gamma_{il}^j t^{lk} + \Gamma_{il}^k t^{jl}. \quad (\text{A.24})$$

These definitions, together with the requirement that the covariant derivative on a scalar field has to be equivalent to a partial derivative, also determine the action of ∇_i on covariant vector and tensor components v_i and t_{ij} :

$$\nabla_i v_j = \partial_i v_j - \Gamma_{ij}^k v_k \quad (\text{A.25})$$

$$\nabla_i t_{jk} = \partial_i t_{jk} - \Gamma_{ij}^l t_{lk} - \Gamma_{ik}^l t_{jl}. \quad (\text{A.26})$$

The Laplace-Beltrami operator is defined as

$$\Delta_{\Gamma} f = g^{ij} \nabla_i \nabla_j f. \quad (\text{A.27})$$

Additional properties of the covariant derivative that are relevant for this thesis are briefly introduced in the following. First, note that $\nabla_i g_{jk} = \nabla_i \epsilon_{jk} = 0$, such that the metric tensor and the Levi-Civita tensor commute with the covariant derivative. Furthermore, we have $\nabla_i \nabla_j f = \nabla_j \nabla_i f$, but the covariant derivative does not commute when acting on vector and tensor fields. Instead, it obeys Ricci identities given by [158]

$$\nabla_i \nabla_j v^k - \nabla_j \nabla_i v^k = R_{lij}^k v^l, \quad (\text{A.28})$$

$$\nabla_i \nabla_j t^{km} - \nabla_j \nabla_i t^{km} = R_{lij}^k t^{lm} + R_{lij}^m t^{kl}, \quad (\text{A.29})$$

where R_{ijkl}^i is the Riemann tensor that describes intrinsic geometric properties of curved spaces. For two-dimensional spaces R_{ijkl}^i only depends on the Gaussian curvature K and can be expressed as [128]

$$R_{ijkl}^i = K \left(\delta_k^i g_{jl} - \delta_l^i g_{jk} \right). \quad (\text{A.30})$$

Equations (A.28) and (A.30) have important consequences for the force balance equation of two-dimensional fluid surfaces, particularly for contributions from shear flows. The latter

are described by the traceless symmetric part of the strain rate tensor, which is given on a fixed surface by $(\nabla_i v_j + \nabla_j v_i - \nabla_k v^k g_{ij})/2$. The force balance of the surface includes the divergence of this tensor, which reads

$$\begin{aligned} \frac{1}{2} \nabla_i (\nabla^i v_j + \nabla_j v^i - \nabla_k v^k \delta_j^i) &= \frac{1}{2} (\nabla_i \nabla^i v_j + \nabla_i \nabla_j v^i - \nabla_j \nabla_i v^i) \\ &= \frac{1}{2} (\nabla_i \nabla^i v_j + K v_j), \end{aligned} \quad (\text{A.31})$$

where we have used Eqs. (A.28) and (A.30). Equation (A.31) gives rise to the additional term in the shear part given in Eq. (3.16), where we have used $K = 1/R^2$ on a sphere of radius R .

Furthermore, the curvature tensor obeys the Mainardi-Codazzi equation [128]

$$\nabla_i C_{jk} = \nabla_j C_{ik}. \quad (\text{A.32})$$

The covariant derivative can also be used to formulate the Stokes integral theorem [112]

$$\int_{\Gamma} \nabla_i v^i dA = \int_{\partial\Gamma} \nu_i v^i ds. \quad (\text{A.33})$$

Here, $\nu = \nu^i \mathbf{e}_i$ is a tangential unit vector that is orthogonal to the curve prescribed by the surface boundary $\partial\Gamma$ and points away from the surface.

Definition of the surface vector gradient

The surface vector gradient operator is defined by

$$\nabla_{\Gamma} f = \mathbf{e}^i \partial_i f. \quad (\text{A.34})$$

The in-plane divergence of a tangential vector field obeys

$$\nabla_{\Gamma} \cdot \mathbf{v}_{\parallel} = \nabla_i v^i. \quad (\text{A.35})$$

The Laplace-Beltrami operator defined in Eq. (A.27) can accordingly be written as

$$\Delta_{\Gamma} f = \nabla_{\Gamma} \cdot \nabla_{\Gamma} f. \quad (\text{A.36})$$

A.2 Geometric surface variation under small deformations

In the following, we consider a small variation of the surface shape given by

$$\mathbf{X}'(s^1, s^2) - \mathbf{X}(s^1, s^2) = \delta X_n \mathbf{n}. \quad (\text{A.37})$$

From the definitions Eqs. (A.1), (A.2), (A.3), (A.8), (A.12) and (A.13) of surface quantities as a function of the parametrisation $\mathbf{X}(s^1, s^2)$, it follows to linear order that

$$\delta \mathbf{n} = -\mathbf{e}^i \nabla_i \delta X_n \quad (\text{A.38})$$

$$\delta \mathbf{e}_i = \mathbf{e}_j C^j_i \delta X_n + \mathbf{n} \nabla_i \delta X_n \quad (\text{A.39})$$

$$\delta g_{ij} = 2C_{ij} \delta X_n \quad (\text{A.40})$$

$$\delta \epsilon_{ij} = \left(\epsilon_{ik} C^k_j - \epsilon_{jk} C^k_i \right) \delta X_n \quad (\text{A.41})$$

$$\delta C_{ij} = -\nabla_i \nabla_j \delta X_n + C_{ik} C^k_j \delta X_n \quad (\text{A.42})$$

$$\delta \Gamma_{ij}^k = C^k_i \nabla_j \delta X_n + C^k_j \nabla_i \delta X_n + C_{ij} \nabla^k \delta X_n + \delta X_n \nabla_i C^k_j. \quad (\text{A.43})$$

Variations of g^{ij} follow from Eq. (A.4) and read

$$\delta g^{ij} = -2C^{ij} \delta X_n. \quad (\text{A.44})$$

Using Eqs. (A.5) and (A.44), the variations of contravariant vector and tensor components can be determined from Eqs. (A.39), (A.41), and (A.42) as

$$\delta \mathbf{e}^i = -\mathbf{e}_j C^{ij} \delta X_n + \mathbf{n} \nabla^i \delta X_n \quad (\text{A.45})$$

$$\delta \epsilon^i_j = \left(\epsilon^{ik} C_{kj} + \epsilon_{jk} C^{ki} \right) \delta X_n \quad (\text{A.46})$$

$$\delta C^i_j = -\nabla^i \nabla_j \delta X_n - C^{ik} C_{kj} \delta X_n. \quad (\text{A.47})$$

Variations of the mean curvature follow from Eqs. (A.14) and (A.47) and read

$$\delta H = \left(K - 2H^2 \right) \delta X_n - \frac{1}{2} \Delta_\Gamma \delta X_n. \quad (\text{A.48})$$

The variation of the Gaussian curvature then follows from Eq. (A.22) and Eq. (A.48) as

$$\delta K = -2H \left(K \delta X_n + \Delta_\Gamma \delta X_n \right) + C^{ij} \nabla_i \nabla_j \delta X_n. \quad (\text{A.49})$$

A.2.1 Dynamic equations of geometric surface properties

Dynamic equations of any geometric surface property described in an Eulerian parametrisation can be found by using the variational expressions derived above and considering $\delta X_n = v_n dt$.

Dynamic equations that are relevant for this thesis are given by

$$\partial_t g_{ij} = 2C_{ij} v_n \quad (\text{A.50})$$

$$\partial_t C_{ij} = -\nabla_i \nabla_j v_n + C_{ik} C^k_j v_n \quad (\text{A.51})$$

$$\partial_t \Gamma_{ij}^k = C^k_i \nabla_j v_n + C^k_j \nabla_i v_n + C_{ij} \nabla^k v_n + v_n \nabla_i C^k_j, \quad (\text{A.52})$$

as well as

$$\partial_t \mathbf{e}_i = \mathbf{e}_j C_i^j v_n + \mathbf{n} \nabla_i v_n \quad (\text{A.53})$$

$$\partial_t \mathbf{e}^i = -\mathbf{e}_j C^{ij} v_n + \mathbf{n} \nabla^i v_n. \quad (\text{A.54})$$

A.3 Parametrisation of axisymmetric surfaces

In this section, we define a general parametrisation for surfaces with axial symmetry. We explain how particular choices for the parametrisation are linked by a coordinate transformation and introduce the special case of an arc length parametrisation. Finally, we collect the explicit expressions of metric tensor, curvature tensor and Christoffel symbols for these parametrisations using the definitions introduced in Section A.1.1.

A.3.1 Arc length surface parametrisation

A general parametrisation of an axisymmetric surface can be written as

$$\mathbf{X}(\varphi, u) = \rho(u) \bar{\mathbf{e}}_\rho + z(u) \bar{\mathbf{e}}_z, \quad (\text{A.55})$$

where $\{\bar{\mathbf{e}}_\rho, \bar{\mathbf{e}}_\varphi, \bar{\mathbf{e}}_z\}$ is the normalised standard basis $\bar{\mathbf{e}}_\alpha \cdot \bar{\mathbf{e}}_\beta = \delta_{\alpha\beta}$ with $\alpha, \beta \in \{\rho, \varphi, z\}$ in cylindrical coordinates and u is a parameter that runs along the meridional outline of the surface. In the following, we will use the coordinates $i \in \{\varphi, u\}$ as explicit tensor indices. The basis vectors $\mathbf{e}_i = \partial_i \mathbf{X}$ and $\mathbf{n} = \mathbf{e}_\varphi \times \mathbf{e}_u / |\mathbf{e}_\varphi \times \mathbf{e}_u|$ read:

$$\mathbf{e}_\varphi = \partial_\varphi \mathbf{X} = \rho \bar{\mathbf{e}}_\varphi \quad (\text{A.56})$$

$$\mathbf{e}_u = \partial_u \mathbf{X} = \partial_u \rho \bar{\mathbf{e}}_\rho + \partial_u z \bar{\mathbf{e}}_z \quad (\text{A.57})$$

$$\mathbf{n} = \frac{\partial_u z \bar{\mathbf{e}}_\rho - \partial_u \rho \bar{\mathbf{e}}_z}{\sqrt{(\partial_u z)^2 + (\partial_u \rho)^2}}. \quad (\text{A.58})$$

Alternative parametrisations are related to Eq. (A.55) by coordinate transformations. In the following, we consider a coordinate transformation of u to a new coordinate s that is described by a scale factor¹

$$h(u) = \frac{ds}{du}. \quad (\text{A.59})$$

This represents a standard coordinate transformation that can be used interchangeably in its explicit forms $s(u)$ and $u(s)$. With this, Eq. (A.55) leads to define a new parametrisation given by $\mathbf{X}(\varphi, s) = \mathbf{X}(\varphi, u(s))$. The tangent vectors along the meridional outline for each parametrisation are related by: $\mathbf{e}_u = \frac{\partial s}{\partial u} \mathbf{e}_s = h \mathbf{e}_s$. A particularly useful choice for a parametrisation is defined by imposing $|\mathbf{e}_s| = 1$, in which case $\mathbf{X}(\varphi, s)$ is the well-known *arc*

¹This refers to the fact that such a coordinate transformation corresponds to a (potentially inhomogeneous) *scaling* of the coordinates along a single curvilinear coordinate axis.

length parametrisation [161]. Of the basis vectors given above, the form of \mathbf{e}_φ is unchanged and we have

$$\mathbf{e}_s = \partial_s \rho \bar{\mathbf{e}}_\rho + \partial_s z \bar{\mathbf{e}}_z \quad (\text{A.60})$$

$$\mathbf{n} = \partial_s z \bar{\mathbf{e}}_\rho - \partial_s \rho \bar{\mathbf{e}}_z. \quad (\text{A.61})$$

Here, we have used $\partial_u = h\partial_s$ and the expression for \mathbf{n} simplifies because the normalisation of \mathbf{e}_s implies $(\partial_s \rho)^2 + (\partial_s z)^2 = 1$. The latter relation motivates the definition of an angle $\psi(s)$ by $(\partial_s \rho, \partial_s z) = (\cos \psi, \sin \psi)$, which can be identified as the tangent angle along the meridional outline [161].

The non-vanishing components of the metric tensor and curvature tensor for each parametrisation follow from Eqs. (A.3) and (A.12). For both parametrisations, we have $g_{\varphi\varphi} = \rho^2$, the meridional metric tensor components are given by $g_{ss} = 1$ for the arc length parametrisation and $g_{uu} = h^2$ for the parametrisation with the parameter u . Furthermore, we have

$$C_s^s = C_u^u = \partial_s \psi(s) = \frac{1}{h} \partial_u \psi[s(u)] \quad (\text{A.62})$$

$$C_\varphi^\varphi = \frac{\sin \psi}{\rho}. \quad (\text{A.63})$$

The relevant Christoffel symbols of the two parametrisations follow from Eq. (A.13) and read:

$$\begin{aligned} \Gamma_{s\varphi}^\varphi &= \frac{1}{2} g^{\varphi\varphi} \partial_s g_{\varphi\varphi} = \frac{\cos \psi}{\rho} \\ &= \frac{1}{2h} g^{\varphi\varphi} \partial_u g_{\varphi\varphi} = \frac{1}{h} \Gamma_{u\varphi}^\varphi \end{aligned} \quad (\text{A.64})$$

$$\begin{aligned} \Gamma_{\varphi\varphi}^s &= -\frac{1}{2} g^{ss} \partial_s g_{\varphi\varphi} = -\rho \cos \psi \\ &= -\frac{1}{2} h^2 g^{uu} \frac{1}{h} \partial_u g_{\varphi\varphi} = h \Gamma_{\varphi\varphi}^u. \end{aligned} \quad (\text{A.65})$$

The Levi-Civita tensor follows from Eq. (A.8) is given by

$$\epsilon_{\varphi s} = \rho \quad (\text{A.66})$$

$$= \frac{1}{h} \epsilon_{\varphi u}. \quad (\text{A.67})$$

A.3.2 Parametrisation of the unit sphere

The surface of a unit sphere, denoted in this thesis by $\bar{\mathcal{S}}$, is parametrised by

$$\mathbf{X}(\theta, \varphi) = \bar{\mathbf{e}}_r, \quad (\text{A.68})$$

where $\{\bar{\mathbf{e}}_r, \bar{\mathbf{e}}_\theta, \bar{\mathbf{e}}_\varphi\}$ is the normalised standard basis $\bar{\mathbf{e}}_\alpha \cdot \bar{\mathbf{e}}_\beta = \delta_{\alpha\beta}$ with $\alpha, \beta \in \{r, \theta, \varphi\}$ in spherical coordinates. The parametrisation Eq. (A.68) defines basis vectors

$$\mathbf{e}_\theta = \bar{\mathbf{e}}_\theta \tag{A.69}$$

$$\mathbf{e}_\varphi = \sin \theta \bar{\mathbf{e}}_\varphi \tag{A.70}$$

$$\mathbf{n} = \bar{\mathbf{e}}_r \tag{A.71}$$

and a diagonal metric tensor with $g_{\theta\theta} = 1$, $g_{\varphi\varphi} = \sin^2 \theta$. Furthermore, $\epsilon_{\theta\varphi} = -\epsilon_{\varphi\theta} = \sin \theta$ and the only non-vanishing Christoffel symbols are given by $\Gamma_{\theta\varphi}^\varphi = \cot \theta$ and $\Gamma_{\varphi\varphi}^\theta = -\sin \theta \cos \theta$. Finally, note that the curvature of a spherical surface is isotropic, such that the curvature tensor C_{ij} has the same components as the metric tensor on the unit sphere and we can use $C_{ij} = g_{ij}$ in equations that concern fixed¹ spherical surfaces.

From the definitions Eqs. (A.34) and (A.27), vector gradient and Laplace operator on the unit sphere $\bar{\mathcal{S}}$ are given by

$$\nabla_{\bar{\mathcal{S}}} f = \left(\bar{\mathbf{e}}_\theta \partial_\theta + \bar{\mathbf{e}}_\varphi \frac{1}{\sin \theta} \partial_\varphi \right) f \tag{A.72}$$

$$\Delta_{\bar{\mathcal{S}}} f = \left(\partial_\theta^2 + \cot \theta \partial_\theta + \frac{1}{\sin^2 \theta} \partial_\varphi^2 \right) f. \tag{A.73}$$

¹For example, $\delta g_{ij} \neq \delta C_{ij}$ under deformations of the surface of a sphere, which can be seen by comparing the right hand side of Eqs. (A.40) and (A.42).

Appendix B

Definitions and applications of scalar, vector and tensor spherical harmonics

In this chapter, we systematically introduce scalar, vector and tensor spherical harmonics. Additionally, we present details of calculations involving spherical harmonics that have only been explained briefly in the main part of this thesis.

In Section B.1, we first introduce the form of scalar spherical harmonics used in this thesis and present the construction of vector and tensor spherical harmonics from them. Then, in Section B.2, we present a detailed derivation the hydrodynamic stress on the surface of a sphere that we have used in Chapters 3 and 4. For this, we present the general solution of the Stokes equation and show how forces resulting from viscous shear stress on the surface can be compactly expressed in terms of covariant vector harmonics. Finally, in Section B.3, we derive additional relations used in this thesis that are based on harmonic expansions in terms of vector and tensor harmonics.

B.1 Definitions and basic identities

B.1.1 Scalar spherical harmonics

Scalar spherical harmonics can be defined as eigenfunctions of the Laplace-Beltrami operator on the unit sphere \mathcal{S}

$$\Delta_{\mathcal{S}} Y_{lm} = -l(l+1)Y_{lm}, \quad (\text{B.1})$$

where the explicit form of $\Delta_{\mathcal{S}}$ is given in Eq. (A.73). Throughout this thesis, we use real spherical harmonics given by [162]

$$Y_{lm}(\theta, \varphi) = \sqrt{\frac{2l+1}{4\pi} \frac{(n-|m|)!}{(n+|m|)!}} P_l^{|m|}(\cos\theta) N_m(\varphi), \quad (\text{B.2})$$

where

$$N_m(\varphi) = \begin{cases} \sqrt{2} \cos(m\varphi) & \text{if } m > 0 \\ 1 & \text{if } m = 0 \\ \sqrt{2} \sin \theta (|m|\varphi) & \text{if } m < 0 \end{cases}. \quad (\text{B.3})$$

The mode numbers $l \geq 0$ are integers and we have for each l a set of $2l + 1$ modes labelled by $m \in \{-l, -l + 1, \dots, l - 1, l\}$. The prefactor in Eq. (B.2) ensures that the functions Y_{lm} are orthonormal, i.e. they obey

$$\int Y_{lm} Y_{l'm'} d\Omega = \delta_{ll'} \delta_{mm'}, \quad (\text{B.4})$$

where $d\Omega = \sin \theta d\varphi d\theta$ denotes the differential solid angle.

B.1.2 Vector spherical harmonics

Vector harmonics are defined as [158]

$$\Psi_i^{(lm)} = \partial_i Y_{lm} \quad (\text{B.5})$$

$$\Phi_i^{(lm)} = \epsilon^j{}_i \partial_j Y_{lm}, \quad (\text{B.6})$$

which can be used to represent any vector field in the tangent space of the surface of a sphere. The vector harmonics Eqs. (B.5) and (B.6) are orthogonal with

$$\int g^{ij} \Psi_i^{(lm)} \Psi_j^{(l'm')} d\Omega = \int g^{ij} \Phi_i^{(lm)} \Phi_j^{(l'm')} d\Omega = l(l+1) \delta_{l,l'} \delta_{m,m'} \quad (\text{B.7})$$

$$\int g^{ij} \Psi_i^{(lm)} \Phi_j^{(l'm')} d\Omega = 0. \quad (\text{B.8})$$

The first relation implies that vector harmonics are non-vanishing only for $l \geq 1$. The components of the vector harmonics with respect to the basis vectors Eqs. (A.69) and (A.70) defined by the parametrisation of the unit sphere¹ read

$$\Psi_\theta^{(lm)} = \partial_\theta Y_{lm} \quad (\text{B.9})$$

$$\Psi_\varphi^{(lm)} = \partial_\varphi Y_{lm} \quad (\text{B.10})$$

$$\Phi_\theta^{(lm)} = -\frac{1}{\sin \theta} \partial_\varphi Y_{lm} \quad (\text{B.11})$$

$$\Phi_\varphi^{(lm)} = \sin \theta \partial_\theta Y_{lm}. \quad (\text{B.12})$$

¹Note that the corresponding azimuthal basis vector \mathbf{e}_φ of this parametrisation that is not normalised. We intentionally keep it this way, such that we treat the parametrisation of the sphere as a general parametrisation $\mathbf{X}(s^1, s^2)$. This way, we can use the fully covariant calculus with abstract index notation to performing computations on the sphere and can write the final identities in terms of the harmonic vector components given here.

Vector harmonics obey an eigenvalue equation [158]

$$\nabla_j \nabla^j \Psi_i^{(lm)} = [1 - l(l+1)] \Psi_i^{(lm)} \quad (\text{B.13})$$

$$\nabla_j \nabla^j \Phi_i^{(lm)} = [1 - l(l+1)] \Phi_i^{(lm)}. \quad (\text{B.14})$$

Furthermore, it follows from their definition that

$$\nabla^i \Psi_i^{(lm)} = -l(l+1) Y_{lm} \quad (\text{B.15})$$

$$\nabla^i \Phi_i^{(lm)} = 0. \quad (\text{B.16})$$

The definitions (B.5) and (B.6) are equivalent to

$$\mathbf{\Psi}^{(lm)} = \nabla_{\bar{S}} Y_{lm} \quad (\text{B.17})$$

$$\mathbf{\Phi}^{(lm)} = \bar{\mathbf{e}}_r \times \mathbf{\Psi}^{(lm)}, \quad (\text{B.18})$$

which is the form that is more commonly found in the literature. To perform computations in the tangent space of the spherical surface, it is convenient to work with the covariant components of the vector harmonics Eqs. (B.5) and (B.6). The two representations are related by $\Psi_i^{(lm)} = \mathbf{e}_i \cdot \mathbf{\Psi}^{(lm)}$ and $\Phi_i^{(lm)} = \mathbf{e}_i \cdot \mathbf{\Phi}^{(lm)}$, as can be verified by determining their explicit representations. Additionally, one defines a radial vector harmonic by

$$\mathbf{Y}^{(lm)} = Y_{lm} \bar{\mathbf{e}}_r. \quad (\text{B.19})$$

From the definition of the vector spherical harmonics, Eqs. (B.17) and (B.19), it follows that

$$\bar{\mathbf{e}}_x = -\sqrt{\frac{4\pi}{3}} \left(\mathbf{Y}^{(11)} + \mathbf{\Psi}^{(11)} \right) \quad (\text{B.20})$$

$$\bar{\mathbf{e}}_y = -\sqrt{\frac{4\pi}{3}} \left(\mathbf{Y}^{(1,-1)} + \mathbf{\Psi}^{(1,-1)} \right) \quad (\text{B.21})$$

$$\bar{\mathbf{e}}_z = \sqrt{\frac{4\pi}{3}} \left(\mathbf{Y}^{(10)} + \mathbf{\Psi}^{(10)} \right), \quad (\text{B.22})$$

which are useful relations to derive identities that connect representations of vector fields in spherical and Cartesian coordinates (see Section B.2.4).

Note that $\mathbf{\Psi}^{(lm)}$, $\mathbf{\Phi}^{(lm)}$ and $\mathbf{Y}^{(lm)}$ are not eigenfunctions of the Laplace-Beltrami operator. To see this, consider on a general curved surface Γ the identities

$$\Delta_{\Gamma} \mathbf{v}_{\parallel} = \mathbf{e}_i \nabla_j \nabla^j v^i - 2\mathbf{n} C^i_j \nabla_i v^j - \mathbf{e}_k v^i C^j_i C^k_j \quad (\text{B.23})$$

$$\Delta_{\Gamma} \mathbf{v}_{\perp} = \mathbf{n} \Delta_{\Gamma} v_n + 2\mathbf{e}_i C^{ij} \nabla_j v_n - \mathbf{n} C^i_j C^j_i v_n, \quad (\text{B.24})$$

which can be derived by several times applying the Gauss-Weingarten relation Eq. (A.10). Using Eqs. (B.23) and (B.24) for $C_{ij} = g_{ij}$ and $\mathbf{n} = \bar{\mathbf{e}}_r$ on the surface of the unit sphere \bar{S}

implies

$$\Delta_{\bar{S}} \Psi^{(lm)} = -l(l+1) \Psi^{(lm)} + 2l(l+1) \mathbf{Y}^{(lm)} \quad (\text{B.25})$$

$$\Delta_{\bar{S}} \Phi^{(lm)} = -l(l+1) \Phi^{(lm)} \quad (\text{B.26})$$

$$\Delta_{\bar{S}} \mathbf{Y}^{(lm)} = -[2 + l(l+1)] \mathbf{Y}^{(lm)} + 2\Psi^{(lm)}, \quad (\text{B.27})$$

where $\Delta_{\bar{S}}$ is the Laplace-Beltrami operator on the unit sphere Eq. (A.73). From $\nabla_{\Gamma} \cdot \mathbf{v}_{\perp} = C_i^i v_n$ and $\nabla_{\Gamma} \cdot \mathbf{v}_{\parallel} = \nabla_i v^i$ on a general surface, it follows additionally that

$$\nabla_{\bar{S}} \cdot \Psi^{(lm)} = -l(l+1) Y_{lm} \quad (\text{B.28})$$

$$\nabla_{\bar{S}} \cdot \Phi^{(lm)} = 0 \quad (\text{B.29})$$

$$\nabla_{\bar{S}} \cdot \mathbf{Y}^{(lm)} = 2Y_{lm}. \quad (\text{B.30})$$

Equations (B.25)–(B.30) can be used to solve the Stokes equation using an ansatz for the flow field in terms of vector harmonics (see Section B.2).

B.1.3 Tensor spherical harmonics

Tensor harmonics are defined as [158]

$$\eta_{ij}^{(lm)} = Y_{lm} g_{ij} \quad (\text{B.31})$$

$$\chi_{ij}^{(lm)} = Y_{lm} \epsilon_{ij} \quad (\text{B.32})$$

$$\Psi_{ij}^{(lm)} = \nabla_i \Psi_j^{(lm)} + \frac{1}{2} l(l+1) Y_{lm} g_{ij} \quad (\text{B.33})$$

$$\Phi_{ij}^{(lm)} = \frac{1}{2} \left(\nabla_i \Phi_j^{(lm)} + \nabla_j \Phi_i^{(lm)} \right). \quad (\text{B.34})$$

Tensor spherical harmonics can be used to decompose tensor fields on the sphere into isotropic ($\eta_{ij}^{(lm)}$), fully antisymmetric ($\chi_{ij}^{(lm)}$) and traceless¹, symmetric modes ($\Psi_{ij}^{(lm)}$ and $\Phi_{ij}^{(lm)}$). Tensor spherical harmonics are orthogonal with

$$\int g^{ik} g^{jl} \eta_{ij}^{(lm)} \eta_{kl}^{(l'm')} d\Omega = \int g^{ik} g^{jl} \chi_{ij}^{(lm)} \chi_{kl}^{(l'm')} d\Omega = 2\delta_{l,l'} \delta_{m,m'} \quad (\text{B.35})$$

$$\int g^{ik} g^{jl} \Psi_{ij}^{(lm)} \Psi_{kl}^{(l'm')} d\Omega = \int g^{ik} g^{jl} \Phi_{ij}^{(lm)} \Phi_{kl}^{(l'm')} d\Omega = l(l+1) \left(\frac{1}{2} l(l+1) - 1 \right) \delta_{l,l'} \delta_{m,m'}, \quad (\text{B.36})$$

all other pairwise integrals vanish. This implies that isotropic and fully antisymmetric tensors can contain contributions from modes with $l \geq 0$, traceless symmetric tensor fields only for $l \geq 2$. The components of the traceless symmetric tensor harmonics with respect to the

¹This follows from Eqs. (B.15) and (B.16).

basis Eqs. (A.69) and (A.70) are given and related by

$$\Psi_{\theta\theta}^{(lm)} = -\frac{1}{\sin^2\theta}\Psi_{\varphi\varphi}^{(lm)} = \frac{1}{\sin\theta}\Phi_{\varphi\theta}^{(lm)} = \partial_\theta^2 Y_{lm} + \frac{1}{2}l(l+1)Y_{lm} \quad (\text{B.37})$$

$$\Psi_{\theta\varphi}^{(lm)} = (\partial_\varphi\partial_\theta - \cot\theta\partial_\varphi)Y_{lm} \quad (\text{B.38})$$

$$\Phi_{\theta\theta}^{(lm)} = -\frac{1}{\sin^2\theta}\Phi_{\varphi\varphi}^{(lm)} = -\frac{1}{\sin\theta}\Psi_{\theta\varphi}^{(lm)}. \quad (\text{B.39})$$

Tensor spherical harmonics obey eigenvalue equations [158]

$$\nabla_k\nabla^k\eta_{ij}^{(lm)} = -l(l+1)\eta_{ij}^{(lm)} \quad (\text{B.40})$$

$$\nabla_k\nabla^k\chi_{ij}^{(lm)} = -l(l+1)\chi_{ij}^{(lm)} \quad (\text{B.41})$$

$$\nabla_k\nabla^k\Psi_{ij}^{(lm)} = [4 - l(l+1)]\Psi_{ij}^{(lm)} \quad (\text{B.42})$$

$$\nabla_k\nabla^k\Phi_{ij}^{(lm)} = [4 - l(l+1)]\Phi_{ij}^{(lm)}, \quad (\text{B.43})$$

which follows from their definition and using the Ricci identity Eq. (A.29), together with Eq. (A.30) and $K = 1$ on the unit sphere. Divergences of the tensor harmonics are given by

$$\nabla^i\eta_{ij}^{(lm)} = \Psi_j^{(lm)} \quad (\text{B.44})$$

$$\nabla^i\chi_{ij}^{(lm)} = \Phi_j^{(lm)} \quad (\text{B.45})$$

for isotropic and antisymmetric harmonic tensor fields and

$$\nabla^i\Psi_{ij}^{(lm)} = \left(1 - \frac{1}{2}l(l+1)\right)\Psi_j^{(lm)} \quad (\text{B.46})$$

$$\nabla^i\Phi_{ij}^{(lm)} = \left(1 - \frac{1}{2}l(l+1)\right)\Phi_j^{(lm)} \quad (\text{B.47})$$

for the traceless, symmetric harmonic tensor fields.

B.2 Solution of the Stokes equation in terms of vector spherical harmonics

In the following, we derive the hydrodynamic stress exerted by a passive incompressible fluid onto the deforming surface of a sphere. To this end, we first have to solve the Stokes equation

$$\eta\Delta\mathbf{u} = \nabla p \quad (\text{B.48})$$

with boundary conditions given by flows and deformations on and of the spherical surface. The pressure p is determined by the incompressibility constraint

$$\nabla \cdot \mathbf{u} = 0. \quad (\text{B.49})$$

Here, ∇ denotes the vector gradient in \mathbb{R}^3 and Δ the Laplace operator in \mathbb{R}^3 . They are related to the corresponding operators on a unit sphere, given in Eqs. (A.72) and (A.73), by

$$\nabla = \bar{\mathbf{e}}_r \partial_r + \frac{1}{r} \nabla_{\bar{\mathcal{S}}} \quad (\text{B.50})$$

$$\Delta = \partial_r^2 + \frac{2}{r} \partial_r + \frac{1}{r^2} \Delta_{\bar{\mathcal{S}}}. \quad (\text{B.51})$$

B.2.1 General solution

We make an ansatz for the flow field and the pressure in the form

$$\mathbf{u} = \sum_{l=0}^{\infty} \sum_{m=-l}^l \left(u_{lm}^r(r) \mathbf{Y}^{(lm)} + u_{lm}^{(1)}(r) \mathbf{\Psi}^{(lm)} + u_{lm}^{(2)}(r) \mathbf{\Phi}^{(lm)} \right), \quad (\text{B.52})$$

and

$$p = \sum_{l=0}^{\infty} \sum_{m=-l}^l p_{lm}(r) Y_{lm}. \quad (\text{B.53})$$

This ansatz is plugged into Eqs. (B.48) and (B.49) and the differential operators in the form Eqs. (B.50) and (B.51) can be conveniently evaluated using the identities given in Eqs. (B.25)–(B.30). From the orthogonality of the vector harmonics, one then finds a system of ordinary differential equations for the coefficient functions $u_{lm}^{(1)}(r)$, $u_{lm}^{(2)}(r)$, $u_{lm}^r(r)$ and $p_{lm}(r)$. With a power law ansatz, the solution can be determined as

$$u_{lm}^r(r) = A_{lm}^{(1)} r^{l+1} + A_{lm}^{(2)} r^{l-1} + A_{lm}^{(3)} r^{-l} + A_{lm}^{(4)} r^{-l-2} \quad (\text{B.54})$$

$$u_{lm}^{(1)}(r) = \frac{1}{l(l+1)} \left((l+3)A_{lm}^{(1)} r^{l+1} + (l+1)A_{lm}^{(2)} r^{l-1} - (l-2)A_{lm}^{(3)} r^{-l} - lA_{lm}^{(4)} r^{-l-2} \right) \quad (\text{B.55})$$

$$u_{lm}^{(2)}(r) = B_{lm}^{(1)} r^l + B_{lm}^{(2)} r^{-l-1} \quad (\text{B.56})$$

$$p_{lm}(r) = \eta \left(\frac{4l+6}{l} A_{lm}^{(1)} r^l + \frac{4l-2}{l+1} A_{lm}^{(3)} r^{-l-1} \right), \quad (\text{B.57})$$

where $A_{lm}^{(1)}$, $A_{lm}^{(2)}$, $B_{lm}^{(1)}$, $A_{lm}^{(3)}$, $A_{lm}^{(4)}$, $B_{lm}^{(2)}$ are integration constants that need to be determined from boundary conditions. The first (last) three coefficients yield solutions that are finite at $r=0$ ($r \rightarrow \infty$), which are denoted in this thesis by \mathbf{u}^- , p^- (\mathbf{u}^+ , p^+) and referred to as *interior* (–) and *exterior* (+). The modes $A_{1,m}^{(2)}$ describe three degrees of translation, the modes $B_{1,m}^{(1)}$ describe rotations around three axis. This solution is equivalent to the result given in [163], where the Laplace operator in Eq. (B.48) was replaced with $\Delta \mathbf{u} = \nabla(\nabla \cdot \mathbf{u}) - \nabla \times (\nabla \times \mathbf{u})$ and computation rules for the curl operator on vector harmonics have been employed [164].

B.2.2 Solution of the boundary value problem

In the following, we determine the integration constants in Eqs. (B.54)–(B.57) from boundary conditions on a spherical surface. To this end, we consider the flow and deformation of a

spherical surface with radius R given by

$$\mathbf{v} = \sum_{l=0}^{\infty} \sum_{m=-l}^l \left(v_{lm}^r \mathbf{Y}^{(lm)} + v_{lm}^{(1)} \mathbf{\Psi}^{(lm)} + v_{lm}^{(2)} \mathbf{\Phi}^{(lm)} \right). \quad (\text{B.58})$$

Impermeability of the surface and no-slip boundary conditions for a deforming spherical surface implies $u_{lm}^{(1)}(R) = v_{lm}^{(1)}$, $u_{lm}^{(2)}(R) = v_{lm}^{(2)}$, and $u_{lm}^r(R) = v_{lm}^r$, which leads to an interior solution given by

$$A_{lm}^{(1)} = \frac{1}{2}(1+l) \left(l v_{lm}^{(1)} - v_{lm}^r \right) \quad (\text{B.59})$$

$$A_{lm}^{(2)} = \frac{1}{2} \left(-l(l+1)v_{lm}^{(1)} + (l+3)v_{lm}^r \right) \quad (\text{B.60})$$

$$B_{lm}^{(1)} = v_{lm}^{(2)} \quad (\text{B.61})$$

and an exterior solution given by

$$A_{lm}^{(3)} = \frac{1}{2}l \left((l+1)v_{lm}^{(1)} + v_{lm}^r \right) - \frac{3}{2}A_{lm}^{(2)}\delta_{l,1} \quad (\text{B.62})$$

$$A_{lm}^{(4)} = \frac{1}{2} \left(-l(l+1)v_{lm}^{(1)} + (2-l)v_{lm}^r \right) + \frac{1}{2}A_{lm}^{(2)}\delta_{l,1} \quad (\text{B.63})$$

$$B_{lm}^{(2)} = v_{lm}^{(2)}. \quad (\text{B.64})$$

Here, we have redefined the integration constants with appropriate powers of R , $A_{lm}^{(1)'} = R^{l+1}A_{lm}^{(1)}$, $A_{lm}^{(2)'} = R^{l-1}A_{lm}^{(2)}$, $A_{lm}^{(3)'} = R^{-l}A_{lm}^{(3)}$, $A_{lm}^{(4)'} = R^{-l-2}A_{lm}^{(4)}$, $B_{lm}^{(1)'} = R^l B_{lm}^{(1)}$, and $B_{lm}^{(2)'} = R^{-l-1}B_{lm}^{(2)}$, and dropped the $'$ again for brevity. We additionally kept the coefficient $A_{1m}^{(2)}$, which describes translations and is determined in Section (B.2.4).

B.2.3 The hydrodynamic stress on a spherical surface

In order to find the hydrodynamic stress on a spherical surface in terms of vector spherical harmonics, we consider first the general form of the hydrodynamic stress tensor

$$\boldsymbol{\sigma} = \eta \left(\nabla \mathbf{u} + (\nabla \mathbf{u})^T \right) - p\mathbb{I}, \quad (\text{B.65})$$

where the superscript T denotes the transpose of the dyadic tensor $\nabla \mathbf{u}$. The force (per area) \mathbf{f} on a surface with normal \mathbf{n} is in general given by $\mathbf{f} = \mathbf{n} \cdot \boldsymbol{\sigma}$, which yields for a sphere with radius r and $\mathbf{n} = \bar{\mathbf{e}}_r$ the expression

$$\begin{aligned} \mathbf{f} &= \bar{\mathbf{e}}_r \cdot \boldsymbol{\sigma} \\ &= \eta \left(\partial_r \mathbf{u} + \bar{\mathbf{e}}_r \cdot \nabla \mathbf{u} \right) - p\bar{\mathbf{e}}_r \\ &= \eta \left(\partial_r \mathbf{u} + \nabla u_r - \frac{1}{r} \mathbf{P}_{\bar{\mathcal{S}}} \mathbf{u} \right) - p\bar{\mathbf{e}}_r, \end{aligned} \quad (\text{B.66})$$

Here, we performed a partial integration, introduced $u_r = \mathbf{u} \cdot \bar{\mathbf{e}}_r$, and defined the tangential projection operator on the unit sphere

$$\begin{aligned} \mathbf{P}_{\bar{\mathcal{S}}} &= r \nabla \bar{\mathbf{e}}_r \\ &= \mathbb{I} - \bar{\mathbf{e}}_r \bar{\mathbf{e}}_r \\ &= \bar{\mathbf{e}}_\theta \bar{\mathbf{e}}_\theta + \bar{\mathbf{e}}_\varphi \bar{\mathbf{e}}_\varphi. \end{aligned} \quad (\text{B.67})$$

This follows from $\bar{\mathbf{e}}_r = \mathbf{r}/r$ and standard rules of vector calculus: $\nabla \mathbf{r} = \mathbb{I}$ and $\nabla r = \bar{\mathbf{e}}_r$. From Eqs. (B.52) and (B.66), we find

$$\mathbf{f} = \sum_{l=0}^{\infty} \sum_{m=-l}^{m=l} \left(f_{lm}^r(r) \mathbf{Y}^{(lm)} + f_{lm}^{(1)}(r) \mathbf{\Psi}^{(lm)} + f_{lm}^{(2)}(r) \mathbf{\Phi}^{(lm)} \right), \quad (\text{B.68})$$

where

$$f_{lm}^r(r) = 2\eta \frac{du_{lm}^r(r)}{dr} - p_{lm}(r) \quad (\text{B.69})$$

$$f_{lm}^{(1)}(r) = \eta \left(\frac{du_{lm}^{(1)}(r)}{dr} - \frac{u_{lm}^{(1)}(r)}{r} + \frac{u_{lm}^r(r)}{r} \right) \quad (\text{B.70})$$

$$f_{lm}^{(2)}(r) = \eta \left(\frac{du_{lm}^{(2)}(r)}{dr} - \frac{u_{lm}^{(2)}(r)}{r} \right). \quad (\text{B.71})$$

Interior and exterior passive fluid flow \mathbf{u}^\pm contribute shear forces on the surface in the form

$$\mathbf{f}^- = -\bar{\mathbf{e}}_r \cdot \boldsymbol{\sigma}^- \Big|_{r=R} \quad (\text{B.72})$$

$$\mathbf{f}^+ = \bar{\mathbf{e}}_r \cdot \boldsymbol{\sigma}^+ \Big|_{r=R}, \quad (\text{B.73})$$

respectively, to the total viscous surface force $\mathbf{f}^\eta = \mathbf{f}^- + \mathbf{f}^+$. From Eqs. (B.54)–(B.57), (B.59)–(B.64), and (B.68)–(B.71) we eventually find its representation in the form

$$\mathbf{f}^\eta = \sum_{l=0}^{\infty} \sum_{m=-l}^{m=l} \left(f_{lm}^{\eta,r} \mathbf{Y}^{(lm)} + f_{lm}^{\eta,(1)} \mathbf{\Psi}^{(lm)} + f_{lm}^{\eta,(2)} \mathbf{\Phi}^{(lm)} \right), \quad (\text{B.74})$$

where

$$\begin{aligned} Rf_{lm}^{\eta,r} &= 3[\eta_-(l+1) + \eta_+l] v_{lm}^{(1)} \\ &\quad - \left[(\eta_- + \eta_+) (4 + 3l + 2l^2) l + 3\eta_- \right] \frac{v_{lm}^r}{l(l+1)} + \eta_+ \frac{3}{2} A_{lm}^{(2)} \delta_{l,1} \end{aligned} \quad (\text{B.75})$$

$$Rf_{lm}^{\eta,(1)} = -(\eta_- + \eta_+) (1 + 2l) v_{lm}^{(1)} + 3[\eta_-(l+1) + \eta_+l] \frac{v_{lm}^r}{l(l+1)} + \eta_+ \frac{3}{2} A_{lm}^{(2)} \delta_{l,1} \quad (\text{B.76})$$

$$Rf_{lm}^{\eta,(2)} = -[\eta_-(l-1) + \eta_+(l+2)] v_{lm}^{(2)}. \quad (\text{B.77})$$

The coefficients $A_{1m}^{(2)}$, which are related to translational motion, are determined in the next section.

B.2.4 Generalised Stokes drag

In the following, we determine a general expression for the *viscous net force* that is exerted by the passive fluid onto the spherical surface and discuss the implications of a force-free surface dynamics. In the absence of external body forces acting on the interior fluid or directly on the surface, the viscous net force is fully determined by interactions with the exterior fluid and we denote it accordingly as $\mathbf{F}^+ = \int_{\Gamma} \mathbf{f}^+ dA$. Its components can be determined from

$$\begin{aligned} \frac{F_{\alpha}^+}{R^2\eta_+} &= \frac{1}{\eta_+} \int_{\bar{S}} \bar{\mathbf{e}}_r \cdot \boldsymbol{\sigma}^+ \cdot \bar{\mathbf{e}}_{\alpha} d\Omega \\ &= \sum_{l,m} \left(2 \frac{du_{lm}^r(r)}{dr} - \frac{p(r)_{lm}}{\eta_+} \right) \Big|_{r=R} \int_{\bar{S}} Y_{lm} \bar{\mathbf{e}}_r \cdot \bar{\mathbf{e}}_{\alpha} d\Omega \\ &\quad + \sum_{l,m} \left(\frac{du_{lm}^{(1)}(r)}{dr} - \frac{u_{lm}^{(1)}(r)}{r} + \frac{u_{lm}^r(r)}{r} \right) \Big|_{r=R} \int_{\bar{S}} \boldsymbol{\Psi}^{(lm)} \cdot \bar{\mathbf{e}}_{\alpha} d\Omega. \end{aligned} \quad (\text{B.78})$$

To evaluate the integrals, we note that from the definitions of the scalar spherical harmonics Eq. (B.2), it follows that $\bar{\mathbf{e}}_r \cdot \bar{\mathbf{e}}_x = -\sqrt{4\pi/3} Y_{11}$, $\bar{\mathbf{e}}_r \cdot \bar{\mathbf{e}}_y = -\sqrt{4\pi/3} Y_{1,-1}$ and $\bar{\mathbf{e}}_r \cdot \bar{\mathbf{e}}_z = \sqrt{4\pi/3} Y_{10}$. From the orthogonality of the scalar and vector spherical harmonics and Eqs. (B.20)–(B.22), we can then evaluate the integrals in Eq. (B.78). Using additionally Eqs. (B.54)–(B.57), we find that the viscous net force acting on the surface is related to the integration constants of the Stokes problem by

$$\frac{F_x^+}{R^2\eta_+} = \sqrt{12\pi} A_{1,1}^{(3)} \quad (\text{B.79})$$

$$\frac{F_y^+}{R^2\eta_+} = \sqrt{12\pi} A_{1,-1}^{(3)} \quad (\text{B.80})$$

$$\frac{F_z^+}{R^2\eta_+} = -\sqrt{12\pi} A_{1,0}^{(3)}. \quad (\text{B.81})$$

As can be seen from Eqs. (B.54) and (B.55), these coefficients describe contributions to the passive fluid flow that decay with $1/r$, which indeed corresponds to the far field of a force monopole.

To relate the force \mathbf{F}^+ to flows on the spherical surface and translational motion, we first note that one can express a constant flow $\mathbf{u}(r \rightarrow \infty) = -\mathbf{u}_0$ of the passive fluid using the integration constants $A_{1m}^{(2)}$ defined by

$$-\mathbf{u}_0 = \sqrt{\frac{3}{4\pi}} \left(-A_{1,1}^{(2)} \bar{\mathbf{e}}_x - A_{1,-1}^{(2)} \bar{\mathbf{e}}_y + A_{1,0}^{(2)} \bar{\mathbf{e}}_z \right). \quad (\text{B.82})$$

This follows from Eqs. (B.54) and (B.55), together with Eqs. (B.20)–(B.22). The velocity

$-\mathbf{u}_0$ is ‘measured’ relative to the surface, such that the boundary condition $\mathbf{u}(r \rightarrow \infty) = -\mathbf{u}_0$ corresponds to a motion of the surface through the fluid with velocity $+\mathbf{u}_0$ relative to the laboratory frame.¹ Using the solution of the boundary value problem Eq. (B.62) together with Eqs. (B.79)–(B.82), the viscous force exerted by the passive fluid onto the surface can be determined as

$$\frac{\mathbf{F}^+}{R^2\eta_+} = -6\pi\mathbf{u}_0 + \sqrt{3\pi} \sum_{m=-1,0,1} s_m \left(2v_{1m}^{(1)} + v_{1m}^r\right) \bar{\mathbf{e}}_{\alpha_m}, \quad (\text{B.83})$$

where we have introduced the sign-vector $s_1 = s_{-1} = -s_0 = 1$, as well as indices $\alpha_1 = x$, $\alpha_{-1} = y$, $\alpha_0 = z$. Equation (B.83) generalises the Stokes drag to situations, where flows and deformations on and of the spherical surface additionally interact with the surrounding fluid.

Force free surface dynamics

To discuss the *total net force* $\mathbf{F}^{\text{ext}} = \int_{\Gamma} \mathbf{f}^{\text{ext}} dA$ acting on the surface, we note that on a closed surface we have in general

$$\nabla_i \mathbf{t}^i = -\mathbf{f}^{\text{ext}} \Rightarrow \mathbf{F}^{\text{ext}} = - \int_{\Gamma} \nabla_i \mathbf{t}^i dA = 0, \quad (\text{B.84})$$

where the last step follows from the Stokes integral theorem Eq. (A.33). In the models that are discussed in this thesis, the external forces are given by the viscous stress alone, such that $\mathbf{F}^{\text{ext}} = \mathbf{F}^+$. In this case, Eq. (B.84) states that a solution of the force balance equations also implies $\mathbf{F}^+ = 0$. From Eq. (B.83) it then follows that

$$\mathbf{u}_0 = \sqrt{\frac{1}{12\pi}} \sum_{m=-1,0,1} s_m \left(2v_{1m}^{(1)} + v_{1m}^r\right) \bar{\mathbf{e}}_{\alpha_m}, \quad (\text{B.85})$$

where the coefficients $v_{1,m}^r$ and $v_{1,m}^{(1)}$ have to be determined from the force balance equations of the surface. Whenever the right-hand side of Eq. (B.85) is non-zero, flows and deformations on and of the surface lead to a force-free, translational motion relative to the laboratory frame.

Solving the linearised force balance equations of a deforming spherical surface, Eqs. (D.61) and (D.63), one finds $2v_{1m}^{(1)} + v_{1m}^r = 0$. Hence, there is no translational motion associated with the onset of the deformation.

On the surface of a non-deforming sphere we have $v_{1m}^r = 0$. In this case, any contribution to surface flows with modes $v_{1m}^{(1)}$ leads to a force-free translational motion relative to the laboratory frame. The propagation speed can be determined from Eqs. (B.85). This result was used in Section 3.3 to describe the spontaneous onset of motion due to self-organised

¹The Stokes equation is invariant under $\mathbf{u} \rightarrow \mathbf{u} + \mathbf{u}_0$. Additionally, the force balance equations on the surface considered in this thesis are invariant under $\mathbf{v} \rightarrow \mathbf{v} + \mathbf{u}_0$, such that boundary conditions on the surface are still satisfied.

active surface flows.

Certainly, the surface dynamics does not have to be force-free with respect to the external viscous net forces. In general, additional body forces \mathbf{F}_b from, for example, gravity, magnetic or electric fields may act on the interior fluid or directly on the surface. We then have $\mathbf{F}^{\text{ext}} = \mathbf{F}_b + \mathbf{F}^+$ and it follows from Eq. (B.84) that $\mathbf{F}^+ = -\mathbf{F}_b$, which then has to be used in the more general relation Eq. (B.83) to determine the propagation velocity \mathbf{u}_0 .

Finally, note that the aspects presented in Sections B.2.3 and B.2.4 can be analogously discussed for the *viscous net torque* $\mathbf{T}^+ = \int_{\bar{S}} \bar{\mathbf{e}}_r \times \bar{\mathbf{e}}_r \cdot \boldsymbol{\sigma}^+ d\Omega$ acting on the surface. In this case, the coefficients that represent full body rotations of the surrounding fluid, $B_{1,m}^{(1)}$ in Eq. (B.56) of the general solution of the Stokes problem, have to be included into the exterior flow solution and rotations relative to the laboratory frame can be discussed.

B.3 Further relations used in this thesis

B.3.1 Harmonic projection of the nonlinear advection term

In the following, we determine the projections

$$A_{lm} = \int \nabla_i (c v^i) Y_{lm} d\Omega \quad (\text{B.86})$$

in terms of scalar harmonics only, which we have used in Section 3.1 to derive a closed analytic solution and in Section 3.3 to approximate nonlinear steady-states. For harmonic expansions of the concentration field $c = \sum_{l,m} c_{lm} Y_{lm}$ and the flow velocity $v_i = \sum_{l,m} v_{lm}^{(1)} \Psi_i^{(lm)}$, we have by the chain rule

$$\nabla_i (c v^i) = \sum_{l,l',m,m'} c_{lm} v_{l'm'}^{(1)} \left(\Psi_i^{(lm)} \Psi^{i,(l'm')} - l'(l'+1) Y_{lm} Y_{l'm'} \right), \quad (\text{B.87})$$

where we used Eqs. (B.5) and (B.15). The harmonic projection of the first term follows from integration by parts:

$$\begin{aligned} & \int \Psi_i^{(lm)} \Psi^{i,(l'm')} Y_{\bar{l}\bar{m}} d\Omega \\ &= \int (\nabla_i Y_{lm}) (\nabla^i Y_{l'm'}) Y_{\bar{l}\bar{m}} d\Omega \\ &= - \int Y_{lm} \nabla_i \left((\nabla^i Y_{l'm'}) Y_{\bar{l}\bar{m}} \right) d\Omega \\ &= l'(l'+1) \int Y_{lm} Y_{l'm'} Y_{\bar{l}\bar{m}} d\Omega - \int Y_{lm} (\nabla_i Y_{l'm'}) (\nabla^i Y_{\bar{l}\bar{m}}) \\ &= [l'(l'+1) - \bar{l}(\bar{l}+1)] \int Y_{lm} Y_{l'm'} Y_{\bar{l}\bar{m}} d\Omega + \int Y_{l'm'} (\nabla_i Y_{\bar{l}\bar{m}}) (\nabla^i Y_{lm}) d\Omega \\ &= [l(l+1) + l'(l'+1) - \bar{l}(\bar{l}+1)] \int Y_{lm} Y_{l'm'} Y_{\bar{l}\bar{m}} d\Omega - \int \Psi_i^{(lm)} \Psi^{i,(l'm')} Y_{\bar{l}\bar{m}} d\Omega. \end{aligned}$$

Combining the first and the last expression we eventually find

$$\int \Psi_i^{(lm)} \Psi^{i,(l'm')} Y_{\bar{l}\bar{m}} d\Omega = \frac{1}{2} [l(l+1) + l'(l'+1) - \bar{l}(\bar{l}+1)] \int Y_{lm} Y_{l'm'} Y_{\bar{l}\bar{m}} d\Omega. \quad (\text{B.88})$$

Using equations (B.87) and (B.88) and relabelling of the modes yields

$$A_{lm} = \frac{1}{2} \sum_{l_1, l_2, m_1, m_2} c_{l_1 m_1} v_{l_2 m_2}^{(1)} [l(l+1) + l_2(l_2+1) - l_1(l_1+1)] \int d\Omega Y_{l_1 m_1} Y_{l_2 m_2} Y_{lm}, \quad (\text{B.89})$$

where the integrals over three spherical harmonics is known as Gaunt coefficients or 3- jm symbols [162]. Note that $A_{00} = 0$, which is consistent with the fact that the advection term does not contribute to changes in the total number of molecules $\partial_t c_{00}$ in Eq. (3.23).

B.3.2 Harmonic decomposition of the surface strain rate tensor

The harmonic fields introduced in Section B.1 are particularly convenient to treat problems that require to simultaneously describe scalar, vector and tensor fields on the surface of a sphere. This becomes evident when analysing different representations of the in-plane strain rate tensor $\nabla_i v_j$ using vector and tensor spherical harmonics. Decomposing this tensor according to Eq. (A.15), the trace can be associated with the compression rate, the antisymmetric part $\omega_n = \epsilon^{ij} \nabla_i v_j / 2$ describes the in-plane vorticity and

$$\tilde{v}_{ij} = \frac{1}{2} \left(\nabla_i v_j + \nabla_j v_i - \nabla_k v^k g_{ij} \right) \quad (\text{B.90})$$

describes pure shear in the moving fluid surface. For a general flow field expressed in terms of vector spherical harmonics

$$v_i = \sum_{l,m} \left(v_{lm}^{(1)} \Psi_i^{(lm)} + v_{lm}^{(2)} \Phi_i^{(lm)} \right) \quad (\text{B.91})$$

we find

$$\tilde{v}_{ij} = \frac{1}{2} \sum_{l,m} \left[v_{lm}^{(1)} \left(2\nabla_i \Psi_j^{(lm)} + l(l+1) Y^{(lm)} g_{ij} \right) + v_{lm}^{(2)} \left(\nabla_i \Phi_j^{(lm)} + \nabla_j \Phi_i^{(lm)} \right) \right] \quad (\text{B.92})$$

$$= \sum_{l,m} \left(v_{lm}^{(1)} \Psi_{ij}^{(lm)} + v_{lm}^{(2)} \Phi_{ij}^{(lm)} \right), \quad (\text{B.93})$$

such that the mode coefficients associated with distinct set of modes at the vector level are also independently linked to distinct set of modes at the tensorial level. The trace and antisymmetric part of the in-plane strain rate tensor $\nabla_i v_j$ can be expressed in terms of the

tensor harmonics Eqs. (B.31) and (B.32) as

$$\frac{1}{2}\nabla_k v^k g_{ij} = -\frac{1}{2}\sum_{l,m} v_{lm}^{(1)} l(l+1) \eta_{ij}^{(lm)} \quad (\text{B.94})$$

$$\frac{1}{2}\epsilon^{kl}\nabla_k v_l \epsilon_{ij} = -\frac{1}{2}\sum_{l,m} v_{lm}^{(2)} l(l+1) \chi_{ij}^{(lm)}. \quad (\text{B.95})$$

Equations (B.93)–(B.95) illustrate the different physical contributions of the mode coefficients $v_{lm}^{(1)}$ and $v_{lm}^{(2)}$ to the total surface shear rate. Note that for brevity, we have written expansions here on a unit sphere with radius $R = 1$. On a sphere with arbitrary radius, Eqs. (B.93)–(B.95) must be supplemented by a prefactor $1/R$.

Appendix C

Strain rate tensor and viscous stress in deforming thin films

Here, we derive and discuss the three-dimensional strain rate tensor $\partial_\alpha v_\beta$ in curved and deforming fluid films. From this, effective constitutive relations for two-dimensional viscous fluid surfaces can be derived in the thin film limit.

First, in Section C.1, we derive a representation of $\partial_\alpha v_\beta$ on the midplane of a curved and deforming fluid film. This derivation requires geometric assumptions about the flows on and near the midplane, which we introduce in detail. In Section C.2, we discuss the symmetric part of $\partial_\alpha v_\beta$. Based on its representation on the midplane of the fluid film, we determine a thin film limit and identify constitutive relation of a viscous fluid surface. Finally, in Section C.3, we discuss the antisymmetric part of $\partial_\alpha v_\beta$, which is related to rotational flows in the fluid film.

C.1 General expression for the strain rate tensor in a thin film

The three-dimensional strain rate tensor on the material midplane of a fluid film can be generically computed by [112]

$$\begin{aligned}(\nabla \mathbf{v})_{\alpha\beta} &= \partial_\alpha v_\beta \\ &= (\partial_i v_\beta) (\mathbf{e}^i)_\alpha + (\partial_n v_\beta) n_\alpha,\end{aligned}\tag{C.1}$$

where ∂_n denotes the derivative along the direction normal to the midplane. In this appendix, Greek indices represent Cartesian coordinates $\alpha, \beta \in \{x, y, z\}$ and we denote dyadic products interchangeably as

$$(\mathbf{vw})_{\alpha\beta} = v_\alpha w_\beta.\tag{C.2}$$

The first term in the in Eq. (C.1) corresponds to the dyadic product $\mathbf{e}^i \partial_i \mathbf{v}$. The vector $\partial_i \mathbf{v}$ can be further split into tangential and normal part such that we can express Eq. (C.1) in

terms of the local basis as

$$\nabla \mathbf{v} = \mathbf{e}_j \cdot \partial_i \mathbf{v} \mathbf{e}^i \mathbf{e}^j + \mathbf{n} \cdot \partial_i \mathbf{v} \mathbf{e}^i \mathbf{n} + \mathbf{n} \partial_n \mathbf{v}. \quad (\text{C.3})$$

To determine an expression for the normal derivative $\partial_n \mathbf{v}$, we generalise an approach that has been described in [112]. The derivation is based on the geometric assumption that points on a straight line along the normal of the initial surface, remain along a straight line along the normal of the deformed surface. In analogy to the thin shell assumption in elastic shells [115,165], we refer to this geometric constraint in the following as *thin film assumption*. As will be discussed below, an additional assumption is required about flows parallel to the midplane that are not associated with midplane deformations.

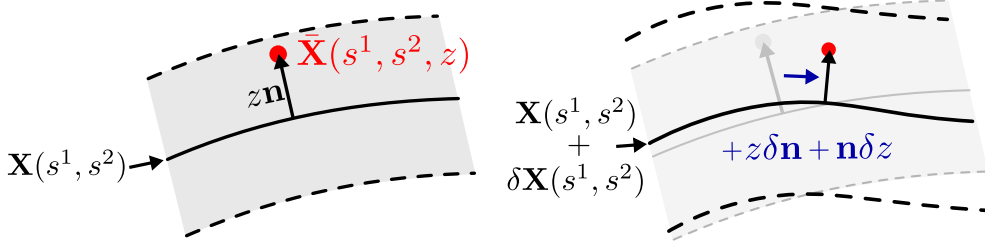


Figure C.1: Parametrisation of the thin film. Material points in the vicinity of the midplane are described by a parametrisation $\bar{\mathbf{X}}(s^1, s^2, z) = \mathbf{X}(s^1, s^2) + z\mathbf{n}$. During deformations, a material point (red dot) away from the midplane moves with the changing surface normal ($z\delta\mathbf{n}$) and it can change its distance to the midplane by moving along the normal ($\mathbf{n}\delta z$).

The starting point for the derivation of an expression for ∂_n is a parametrisation of the material points around the midplane of the surface given by $\bar{\mathbf{X}}(s^1, s^2, z) = \mathbf{X}(s^1, s^2) + z\mathbf{n}$. We then consider a material deformation that is determined by a variation of the midplane $\delta\mathbf{X} = \delta X^i \mathbf{e}_i + \delta X_n \mathbf{n}$, and motion of material along the surface normal $\mathbf{n}\delta z$ (Fig. C.1). The corresponding variation of the material points on and around the midplane reads

$$\delta\bar{\mathbf{X}}(s^1, s^2, z) = \delta\mathbf{X}(s^1, s^2) + z\delta\mathbf{n} + \mathbf{n}\delta z \quad (\text{C.4})$$

The variation of the surface normal is given by $\delta\mathbf{n} = -(\mathbf{n} \cdot \partial_i \delta\mathbf{X}) \mathbf{e}^i$, which follows from $\mathbf{n} \cdot \delta\mathbf{n} = 0$ and $\mathbf{e}_i \cdot \delta\mathbf{n} = -\mathbf{n} \cdot \delta\mathbf{e}_i$. Furthermore, we can formally expand the motion of material points in z -direction near the surface to linear order as $\delta z \approx z\partial_n \delta X_n$. The zeroth order contribution of this expansion is already contained in $\delta\mathbf{X}$. Because of the thin film assumption, we can identify $\partial_z \delta\bar{\mathbf{X}}$ with $\partial_n \delta\mathbf{X}$ and evaluate the resulting relation for $\delta\mathbf{X} = \mathbf{v}dt$, where we denote $\partial_n \delta X_n = dt\partial_n v_n$. Altogether, we then have

$$\partial_n \mathbf{v} = -(\mathbf{n} \cdot \partial_i \mathbf{v}) \mathbf{e}^i + \partial_n v_n \mathbf{n}. \quad (\text{C.5})$$

Using Eqs. (C.2), (C.3) and (C.5), the three-dimensional strain rate tensor given in Eq. (C.1)

can be therefore be expressed in the local basis on the midplane surface as

$$\nabla \mathbf{v} = \mathbf{e}_j \cdot \partial_i \mathbf{v} \mathbf{e}^i \mathbf{e}^j + \mathbf{n} \cdot \partial_i \mathbf{v} (\mathbf{e}^i \mathbf{n} - \mathbf{n} \mathbf{e}^i) + \partial_n v_n \mathbf{nn}. \quad (\text{C.6})$$

The explicit form of $\partial_n v_n$ follows from an additional assumption about flows near the midplane that are not associated with deformations. If we consider for simplicity a non-deforming, flat fluid film with $\delta X_n = 0$ and $\delta \mathbf{n} = 0$, we see from Eq. (C.4) that the choice $\partial_n v_n = 0 \Leftrightarrow \delta z = 0$ corresponds to the assumption that material points move along the fluid film independently of z , i.e. parallel to the midplane. The form of the strain rate tensor in the limit $\partial_n v_n = 0$ will be discussed in Section C.2.1. Alternatively, an expression for $\partial_n v_n$ can be derived by imposing incompressibility of the three-dimensional fluid film, which we discuss in Section C.2.2.

C.2 Discussion of the symmetric part

The symmetric part of $(\nabla \mathbf{v})_{\alpha\beta}$ corresponds to the symmetric strain rate tensor $v_{\alpha\beta} = (\partial_\alpha v_\beta + \partial_\beta v_\alpha) / 2$. According to Eq. (C.6), it can be written as

$$\frac{1}{2} (\nabla \mathbf{v} + (\nabla \mathbf{v})^T) = \frac{1}{2} (\mathbf{e}_j \cdot \partial_i \mathbf{v} + \mathbf{e}_i \cdot \partial_j \mathbf{v}) \mathbf{e}^i \mathbf{e}^j + \partial_n v_n \mathbf{nn}. \quad (\text{C.7})$$

Here, we have used the transposition property of dyadic products: $(\mathbf{vw})^T = \mathbf{vw}$.

Note that as a consequence of the thin film assumption, the symmetric strain rate tensor in Eq. (C.7) has no contribution from the dyadic products $\mathbf{n} \mathbf{e}_i$ and $\mathbf{e}_i \mathbf{n}$, or equivalently: $v_{\alpha\beta} (\mathbf{e}_i)_\alpha n_\beta = 0$. This corresponds to the absence of transverse shear in the fluid film, which is generally at the heart of the thin film assumption.

From Eq. (C.7), we can define a two-dimensional strain rate tensor by

$$v_{ij} = v_{\alpha\beta} (\mathbf{e}_i)_\alpha (\mathbf{e}_j)_\beta, \quad (\text{C.8})$$

which is the in-plane part of the three-dimensional strain rate tensor. We have

$$\begin{aligned} v_{ij} &= \frac{1}{2} (\mathbf{e}_j \cdot \partial_i \mathbf{v} + \mathbf{e}_i \cdot \partial_j \mathbf{v}) \\ &= \frac{1}{2} (\nabla_i v_j + \nabla_j v_i) + C_{ij} v_n. \end{aligned} \quad (\text{C.9})$$

Here, we have used $\mathbf{v} = v^i \mathbf{e}_i + v_n \mathbf{n}$ to explicitly evaluate $\partial_i \mathbf{v}$. The strain rate tensor v_{ij} is defined on the midplane of the curved and deforming thin film. Note that for $\partial_n v_n = 0$, we even have $v_{\alpha\beta} = v^{ij} (\mathbf{e}_i)_\alpha (\mathbf{e}_j)_\beta$, such that in this case the two-dimensional tensor v_{ij} contains the full information about shear and compression ($\nabla \cdot \mathbf{v} = v^k_k$) in the three dimensional fluid film.

C.2.1 Viscous stress in compressible thin films

We now consider the viscous stress in the fluid film given by (see Eq. (1.14))

$$\sigma_{\alpha\beta}^{\eta} = 2\bar{\eta}_s \left(v_{\alpha\beta} - \frac{1}{3} v_{\gamma\gamma} \delta_{\alpha\beta} \right) + \bar{\eta}_b v_{\gamma\gamma} \delta_{\alpha\beta}. \quad (\text{C.10})$$

We chose $\partial_n v_n = 0$ and determine the effective tension tensor t_{ij}^{η} that is defined by Eq. (C.10) in the thin film limit. For this, we write the projected stress tensor $\sigma_{ij}^{\eta} = \sigma_{\alpha\beta}^{\eta} (\mathbf{e}_i)_{\alpha} (\mathbf{e}_j)_{\beta}$ with the help of Eq. (C.8) as

$$\begin{aligned} \sigma_{ij}^{\eta} &= 2\bar{\eta}_s \left(v_{ij} - \frac{1}{3} v_{kk}^k g_{ij} \right) + \bar{\eta}_b v_{kk}^k g_{ij} \\ &= 2\bar{\eta}_s \left(v_{ij} - \frac{1}{2} v_{kk}^k g_{ij} \right) + \left(\bar{\eta}_b + \frac{1}{3} \bar{\eta}_s \right) v_{kk}^k g_{ij}, \end{aligned} \quad (\text{C.11})$$

where we have restored the separation into traceless part and trace of the surface strain rate tensor in the second line. In the thin film limit, we find a tension tensor $t_{ij}^{\eta} \approx h \sigma_{ij}^{\eta}$, where h is the height of the film. Furthermore, we can identify effective shear and bulk viscosities for the corresponding fluid surface as

$$\eta_s = h \bar{\eta}_s \quad (\text{C.12})$$

$$\eta_b = h \left(\bar{\eta}_b + \frac{1}{3} \bar{\eta}_s \right), \quad (\text{C.13})$$

which follows from the comparison of Eq. (C.11) with Eq. (2.11).

C.2.2 Viscous stress in incompressible thin films

So far, we have discussed the thin film description for $\partial_n v_n = 0$ in Eq. (C.7). In this case, the three-dimensional incompressibility of the thin film is equivalent with the incompressibility of the midplane, i.e. $\partial_{\gamma} v_{\gamma} = 0 \Leftrightarrow v_{kk}^k = 0$. We now consider an alternative flow field of the fluid film, which is incompressible in three-dimensions but can have a non-vanishing normal derivative. To distinguish this case from the previous section, we denote this flow field by \mathbf{u} . We allow in general $\partial_n u_n \neq 0$ and derive an expression for $\partial_n u_n$ from the three-dimensional incompressibility $\partial_{\gamma} u_{\gamma} = 0$. From Eq. (C.7), it directly follows that

$$\partial_n u_n = -u_{kk}^k, \quad (\text{C.14})$$

where u_{ij} has the same form as v_{ij} in Eq. (C.9) and the symmetric part of the three-dimensional strain rate tensor $u_{\alpha\beta}$ of the thin film reads

$$\frac{1}{2} \left(\nabla \mathbf{u} + (\nabla \mathbf{u})^T \right) = u_{ij} \mathbf{e}^i \mathbf{e}^j - u_{kk}^k \mathbf{nn}. \quad (\text{C.15})$$

To find a closed description of the effective thin film properties represented on the midplane

surface, further assumptions are required. We consider for the three-dimensional thin film an incompressible fluid described by

$$\sigma_{\alpha\beta}^u = 2\bar{\eta}u_{\alpha\beta} - P\delta_{\alpha\beta}, \quad (\text{C.16})$$

where the pressure P is determined by the incompressibility. In the next step, we inspect the stress tensor component σ_{nn}^u defined by

$$\sigma_{nn}^u = \sigma_{\alpha\beta}^u n_\alpha n_\beta \quad (\text{C.17})$$

$$= -2\bar{\eta}u_k^k - P. \quad (\text{C.18})$$

We follow [36] and assume that σ_{nn}^u is approximately constant across the film height and balanced by an external force density f_n^{ext} . From this, we find from Eq. (C.18) that $-P = f_n^{\text{ext}} + 2\bar{\eta}u_k^k$. Using this relation to eliminate the pressure in Eq. (C.16), we find a closed expression of the projected thin film stress $\sigma_{ij}^u = \sigma_{\alpha\beta}^u (\mathbf{e}_i)_\alpha (\mathbf{e}_j)_\beta$ given by

$$\sigma_{ij}^u = 2\bar{\eta} \left(u_{ij} + u_k^k g_{ij} \right) + f_n^{\text{ext}} g_{ij} \quad (\text{C.19})$$

$$= 2\bar{\eta} \left(u_{ij} - \frac{1}{2} u_k^k g_{ij} \right) + 3\bar{\eta} u_k^k + f_n^{\text{ext}} g_{ij}. \quad (\text{C.20})$$

This shows that the corresponding two dimensional fluid surface is compressible, where the effective surface viscosities are given by

$$\eta_s = h\bar{\eta} \quad (\text{C.21})$$

$$\eta_b = 3h\bar{\eta}. \quad (\text{C.22})$$

Here, h is the thin film height and we have compared Eq. (C.20) with Eq. (2.11) to read off effective surface viscosities.

Importantly, we note that within a thin film that is incompressible in three dimensions there cannot exist an independent three-dimensional isotropic active stress. However, it is possible that active stresses, which are anisotropic in the three-dimensional film, yield effectively isotropic contributions in the two-dimensional thin film limit [36, 41].

C.3 Discussion of the antisymmetric part

For completeness, we finally discuss the antisymmetric part of the three-dimensional strain rate tensor $\nabla \mathbf{v}$. Note that this component is in a tensorial sense orthogonal to the symmetric part and can therefore be discussed independently of the aspects described in Section C.2.

From Eq. (C.6), we find that the antisymmetric part of $\nabla \mathbf{v}$ is given by

$$\mathbf{\Omega} = \frac{1}{2} \left(\nabla \mathbf{v} - (\nabla \mathbf{v})^T \right) \quad (\text{C.23})$$

$$= \frac{1}{2} \mathbf{e}_j \cdot \partial_i \mathbf{v} \left(\mathbf{e}^i \mathbf{e}^j - \mathbf{e}^j \mathbf{e}^i \right) + \mathbf{n} \cdot \partial_i \mathbf{v} \left(\mathbf{e}^i \mathbf{n} - \mathbf{n} \mathbf{e}^i \right). \quad (\text{C.24})$$

The antisymmetric Cartesian tensor $\mathbf{\Omega}$ has three independent degrees of freedom, which can be conveniently represented using the vorticity $\boldsymbol{\omega}$ of the flow defined by $\omega_\alpha = \frac{1}{2} \epsilon_{\alpha\beta\gamma} \Omega_{\beta\gamma}$. Note that this definition is equivalent to $\boldsymbol{\omega} = (\nabla \times \mathbf{v})/2$. We realise that contracting Eq. (C.23) with the Cartesian Levi-Civita tensor $\epsilon_{\alpha\beta\gamma}$ corresponds to calculating the cross-products between the vectors that form the dyadic tensors. These cross-products can be evaluated using Eqs. (A.8) and (A.9), which yields

$$\boldsymbol{\omega} = \frac{1}{2} \epsilon^{ij} \mathbf{e}_j \cdot \partial_i \mathbf{v} \mathbf{n} - \epsilon^{ij} \mathbf{n} \cdot \partial_i \mathbf{v} \mathbf{e}_j \quad (\text{C.25})$$

$$= \omega_n \mathbf{n} + \omega^i \mathbf{e}_i, \quad (\text{C.26})$$

where

$$\omega_n = \frac{1}{2} \epsilon^{ij} \nabla_i v_j \quad (\text{C.27})$$

$$\omega^i = \epsilon^{ij} \left(\partial_j v_n - C_{jk} v^k \right). \quad (\text{C.28})$$

Hence, under the thin film assumption, we find an expression $\omega_\alpha = \omega^i (\mathbf{e}_i)_\alpha + \omega_n n_\alpha$ on the midplane that contains the full information about the antisymmetric part of the three-dimensional strain rate tensor $\partial_\alpha v_\beta$ of the thin film. Note that the normal component ω_n is equal to the antisymmetric part of the surface strain rate tensor v_{ij} given in Eq. (C.9).

The vorticity vector describes an axis around which the fluid film locally rotates. Therefore, ω_n describes in-plane rotations and ω^i describes rotations out of the plane. The gradient of vorticity $\mathbf{n} \cdot \partial_i \boldsymbol{\omega}$ has been identified as a conjugate thermodynamic flux in the entropy production of active surfaces, where it is associated with the dissipative cost of gradients of rotations [112].

Appendix D

Active fluid dynamics on deforming surfaces

In this appendix, we present the formal details and derivations underlying the results presented in Chapter 2.

First, in Section D.1, we derive the dynamic equations to evolve the geometry of a deforming axisymmetric surface for a given deformation field. This deformation field is in our description given by the solution of the force balance equations of the active fluid surface. The explicit formulation of the latter on an axisymmetric surface is presented in Section D.2. The boundary conditions and global constraints, we have used to solve these equations, are introduced in Section D.3. In Section D.4, we derive the linearisation of the surface dynamics for the active fluid surface around homogeneous states of a sphere and a cylindrical surface, from which the linear stability analysis presented in Sections 2.3.1 and 2.4.1 follows. In Section D.5, we derive a toy model to quantitatively understand the scaling of neck radii of tubular surfaces with bending rigidity. Finally, in Section D.6, we present details of the numerical discretisation scheme and validation results of the implementation with which we have obtained numerical solutions of the full nonlinear surface dynamics.

D.1 Dynamic representation of deforming axisymmetric surfaces

In the following, we derive the dynamic equations for geometric surface properties of a deforming axisymmetric surface that have been presented in Sections 2.3 and 2.4. The corresponding fields, the curvature tensor and Christoffel symbols, are required to represent the surface implicitly and to formulate covariant differential equations on the surface that determine its dynamics.

In this section, we interchangeably use the two parametrisations introduced in Section 2.2.1 and described in full detail in Section A.3.1: an arc length surface parametrisation and a fixed Eulerian parametrisation for which the meridional outline of the axisymmetric surface is respectively described by an arc length parameter $s \in [0, L(t)]$ and an Eulerian coor-

dinate $u \in [0, L_0]$. The two parametrisations are related via a time-dependent coordinate transformation $h(u, t)$ introduced in Section 2.2.2, for which we recall the dynamic equation

$$\partial_t h(u, t) = h C_s^s v_n. \quad (\text{D.1})$$

Spatial derivatives with respect to the arc length parameter s can be written as

$$\partial_s = \frac{1}{h} \partial_u, \quad (\text{D.2})$$

which we make use of several times in the following derivations.

Time-dependence of the tangent angle

First, we derive a dynamic equation for the tangent angle ψ . For this, we take the time derivative of both sides of the identity $\sin \psi = \mathbf{e}_u \cdot \bar{\mathbf{e}}_z / h$ (see Section A.3.1), which yields

$$\begin{aligned} \cos \psi \partial_t \psi &= \bar{\mathbf{e}}_z \cdot \left(-\mathbf{e}_u \frac{\partial_t h}{h^2} + \frac{1}{h} \partial_t \mathbf{e}_u \right) \\ &= \bar{\mathbf{e}}_z \cdot (-\mathbf{e}_s C_s^s v_n + \mathbf{n} \partial_s v_n + v_n C_s^s \mathbf{e}_s) \\ &= \bar{\mathbf{e}}_z \cdot \mathbf{n} \partial_s v_n \\ \Rightarrow \partial_t \psi &= -\partial_s v_n, \end{aligned} \quad (\text{D.3})$$

where we have used Eq. (A.53) in the third step and $\bar{\mathbf{e}}_z \cdot \mathbf{n} = -\cos \psi$ in the last step. Although this derivation is only valid for $\psi \neq n + \pi/2$, $n \in \mathbb{Z}$, the same calculation starting with $\cos \psi = \mathbf{e}_u \cdot \bar{\mathbf{e}}_\rho / h$ shows that Eq. (D.3) is indeed valid for all ψ .

Time-dependence of the curvature tensor

From its definition Eq. (A.62), we find for the meridional curvature

$$\begin{aligned} \partial_t C_s^s &= \partial_t \left(\frac{1}{h} \partial_u \psi \right) \\ &= -\frac{\partial_t h}{h^2} \partial_u \psi + \partial_s \partial_t \psi \\ &= -C_s^s v_n \partial_s \psi - \partial_s^2 v_n. \end{aligned} \quad (\text{D.4})$$

where we have used Eqs (D.1), and (D.3). Similarly, from the definition of the azimuthal curvature given in Eqs. (A.63), we find

$$\begin{aligned}
 \partial_t C_\varphi^\varphi &= \partial_t \frac{\sin \psi}{\rho} \\
 &= -\frac{\sin \psi}{\rho^2} \partial_t \rho + \frac{\cos \psi}{\rho} \partial_t \psi \\
 &= -\left(\frac{\sin \psi}{\rho}\right)^2 v_n - \frac{\cos \psi}{\rho} \partial_s v_n.
 \end{aligned} \tag{D.5}$$

Here, we have additionally used

$$\partial_t \rho = v_n \sin \psi, \tag{D.6}$$

which follows from the dynamic equation for the metric tensor Eq. (A.50) and $g_{\varphi\varphi} = \rho^2$.

Time-dependence of the Christoffel symbols

For the Christoffel symbol $\Gamma_{\varphi u}^\varphi$ defined in Eqs. (A.64), we have

$$\begin{aligned}
 \partial_t \Gamma_{\varphi u}^\varphi &= \partial_t \left(h \Gamma_{\varphi s}^\varphi \right) \\
 &= v_n C_s^\varphi \Gamma_{\varphi u}^\varphi + h \left(\frac{\sin \psi}{\rho} \partial_s v_n - \frac{\cos \psi \sin \psi}{\rho^2} v_n \right) \\
 &= v_n C_s^\varphi \Gamma_{\varphi u}^\varphi + C_\varphi^\varphi \partial_u v_n + h v_n \left(\partial_s \frac{\sin \psi}{\rho} - \frac{\cos \psi}{\rho} \partial_s \psi \right) \\
 &= \partial_u \left(C_\varphi^\varphi v_n \right).
 \end{aligned} \tag{D.7}$$

In the second step, we have used Eqs. (D.1), (D.3), and (D.6). In the last two steps, we used $\partial_s \rho = \cos \psi$ and the explicit components of the curvature tensor given in Eqs. (A.62) and (A.63). Similarly, starting with Eq. (A.65), we find:

$$\begin{aligned}
 \partial_t \Gamma_{\varphi\varphi}^u &= \partial_t \left(\frac{1}{h} \Gamma_{\varphi\varphi}^s \right) \\
 &= -\frac{v_n C_s^s}{h} \Gamma_{\varphi\varphi}^s - \frac{1}{h} (\rho \sin \psi \partial_s v_n + \cos \psi \sin \psi v_n)
 \end{aligned} \tag{D.8}$$

$$\begin{aligned}
 &= -\frac{v_n C_s^s}{h} \Gamma_{\varphi\varphi}^s - \frac{\rho^2}{h} \left[\frac{\sin \psi}{\rho} \partial_s v_n - v_n \left(\partial_s \frac{\sin \psi}{\rho} - \frac{\cos \psi}{\rho} \partial_s \psi \right) \right] \\
 &= \frac{g_{\varphi\varphi}}{h^2} \left(v_n \partial_u C_\varphi^\varphi - C_\varphi^\varphi \partial_u v_n \right).
 \end{aligned} \tag{D.9}$$

This relation is not used in this thesis, but given here for completeness.

To determine the time dependent initial points of the integral surface reconstruction for the examples presented in this work, we used Eqs. (D.3), (D.6), and $\partial_t z = -v_n \cos \psi$ at $s = u = 0$. The latter relation follows from $\partial_t \mathbf{X} = v_n \mathbf{n}$, Eqs. (A.55) and (D.6).

Finally, note that as a consistency check, Eqs. (D.4)–(D.9) can also be found by expressing the general covariant dynamic equations for tensor fields, Eqs. (A.50)–(A.52) in terms of the arc length parametrisation introduced in Section A.3.1.

D.2 Governing equations for axisymmetric active fluid surfaces

In this section, we provide explicit expressions for the force balance equations and for the dynamic equation of the concentration field used in Chapter 2. These governing equations have been used to determine numerical solutions of the deformation field, in-plane flows and concentration dynamics on an axisymmetric active fluid surface. Furthermore, we derive the analytic limits of these equations at the parametric poles of spherical surfaces, where axisymmetric parametrisations contains spurious divergences.

D.2.1 Force and torque balance equations

The bending moment tensor m_{ij}^H used in this work is purely antisymmetric, such that the normal moment-balance Eq. (2.6) with $m_n^i = 0$ implies that the tension tensor has no anti-symmetric contribution, i.e. $\epsilon_{ij}t^{ij} = 0$. Using $\epsilon_{ik}\epsilon^{kj} = -\delta_i^j$, the in-plane moment balance, Eq. (2.5), implies:

$$t_{i,n} = 2\kappa\partial_i C_k^k. \quad (\text{D.10})$$

The remaining force balance Eqs. (2.3) and (2.4) for an axisymmetric surface in terms of an arc length parametrisation read:

$$\partial_s t_s^s + \Gamma_{\varphi s}^\varphi (t_s^s - t_\varphi^\varphi) + C_s^s t_n^s = -f_s^{\text{ext}} \quad (\text{D.11})$$

$$\partial_s t_\varphi^s - \Gamma_{\varphi\varphi}^s t_\varphi^\varphi + C_\varphi^\varphi t_n^\varphi = -f_\varphi^{\text{ext}} \quad (\text{D.12})$$

$$\partial_s t_n^s + \Gamma_{\varphi s}^\varphi (t_n^s + t_n^\varphi) - C_s^s t_s^s - C_\varphi^\varphi t_\varphi^\varphi = -f_n^{\text{ext}}, \quad (\text{D.13})$$

which can be found using Eqs. (A.23) and (A.24). Here, we have assumed that all fields are axisymmetric, such that they only depend on the arc length parameter s . The components of the tension tensor $t_{ij} = t_{ij}^d + t_{ij}^H$ thus read

$$t_s^s = (\eta_s + \eta_b)v_s^s + (\eta_b - \eta_s)v_\varphi^\varphi + \xi f(c) + \gamma + \kappa C_k^k (C_\varphi^\varphi - C_s^s) \quad (\text{D.14})$$

$$t_\varphi^\varphi = (\eta_s + \eta_b)v_\varphi^\varphi + (\eta_b - \eta_s)v_s^s + \xi f(c) + \gamma - \kappa C_k^k (C_\varphi^\varphi - C_s^s) \quad (\text{D.15})$$

$$t_\varphi^s = \rho^2 t^{s\varphi} = 2\eta_s v_\varphi^s. \quad (\text{D.16})$$

The components of the symmetrised strain-rate tensor v_{ij} , defined in Eq. (C.9), read:

$$v^s_s = \partial_s v^s + C^s_s v_n \quad (\text{D.17})$$

$$v^\varphi_\varphi = \Gamma^\varphi_{\varphi s} v^s + C^\varphi_\varphi v_n \quad (\text{D.18})$$

$$v^s_\varphi = \frac{\rho^2}{2} \partial_s v^\varphi. \quad (\text{D.19})$$

In our examples, we have f_φ^{ext} and $t_n^\varphi = 0$, such that Eq. (D.12) together with Eq. (D.19) yields:

$$\partial_s \left(\rho^2 \partial_s v^\varphi \right) + \rho \cos \psi \partial_s v^\varphi = 0. \quad (\text{D.20})$$

This equation is solved by

$$v^\varphi(s) = A \int_0^s \frac{1}{\rho^3} ds' + v_0^\varphi, \quad (\text{D.21})$$

with integration constants A and v_0^φ . The latter corresponds to rigid-body rotations about the symmetry axis, which appear because we did not include any external friction forces in our description and we can arbitrarily choose $v_0^\varphi = 0$. On spherical surfaces, as well as on tubular surfaces with periodic or no-flux boundary conditions, the form of Eq. (D.21) implies $A = 0$. Under the assumptions made in this work, Eq. (D.12) therefore implies $v^\varphi = 0$. Using the explicit form of the tension tensor components Eqs. (D.14) and (D.15) in Eqs. (D.11) and (D.13), one finds the final parametric form of the force balance equations

$$(\eta_s + \eta_b) \partial_s v^s_s + (\eta_b - \eta_s) \partial_s v^\varphi_\varphi + 2\eta_s \Gamma^\varphi_{\varphi s} (v^s_s - v^\varphi_\varphi) + \xi \partial_s f(c) = 0 \quad (\text{D.22})$$

$$\begin{aligned} (\eta_s + \eta_b) \left(C^s_s v^s_s + C^\varphi_\varphi v^\varphi_\varphi \right) + (\eta_b - \eta_s) \left(C^s_s v^\varphi_\varphi + C^\varphi_\varphi v^s_s \right) + (\xi f(c) + \gamma) C^k_k \\ - \kappa C^k_k \left(C^s_s - C^\varphi_\varphi \right)^2 - 2\kappa \left(\partial_s^2 C^k_k + \Gamma^\varphi_{\varphi s} \partial_s C^k_k \right) = p. \end{aligned} \quad (\text{D.23})$$

Equations (D.22) and (D.23) form a closed system of ordinary differential equations, which are – for a given geometry – linear in the unknown flow fields v_s , v_n , and the pressure $f_n^{\text{ext}} = p$. These effectively linear equations contain inhomogeneities arising from active contractility ξ , passive surface tension γ , and bending rigidity κ . At the poles of a spherical surface, where $\Gamma^\varphi_{\varphi s}$ diverges, Eq. (D.22) vanishes identically by symmetry, and Eq. (D.23) yields a non-trivial analytic limit, which is derived below. The following helpful identities avoid the numerical approximation of certain derivatives that appear in those equations:

$$\begin{aligned} \partial_s C^\varphi_\varphi &= \Gamma^\varphi_{\varphi s} \left(C^s_s - C^\varphi_\varphi \right) \\ \partial_s \Gamma^\varphi_{\varphi s} &= -C^\varphi_\varphi C^s_s - \left(\Gamma^\varphi_{\varphi s} \right)^2. \end{aligned}$$

This directly follows from the explicit form of these fields given in Eqs (A.63) and (A.64).

D.2.2 Dynamic equation for the concentration field

The dynamic equation for the concentration field reads:

$$\partial_t c = -\partial_s (c v_s) - \Gamma_{s\varphi}^\varphi c v_s - c v_n C_k^k + D \left(\partial_s^2 c + \Gamma_{s\varphi}^\varphi \partial_s c \right) - k (c - c_0). \quad (\text{D.24})$$

D.2.3 Analytic limits at the poles of axisymmetric spherical surfaces

In the following, we derive analytic limits of the governing Eqs. (D.22), (D.23) and (D.24) at the poles of axisymmetric spherical surfaces where $r \rightarrow 0$ and the Christoffel symbol $\Gamma_{s\varphi}^\varphi = \frac{1}{r} \cos \psi$ diverges. These spurious singularities arise due to the axisymmetric surface parametrisation of a spherical surface. The limits we derive here are required to determine a complete numerical solution of the force balance equations and the dynamic equation for the concentration field, including the points on the poles of spherical surfaces.

From the Taylor theorem, it follows that for any function $g(s) \in C^2(\mathbb{R})$ with $g(u) = 0$ we have

$$\lim_{s \rightarrow u} \frac{g(s)}{s - u} = \left. \frac{dg}{ds} \right|_u. \quad (\text{D.25})$$

Furthermore, smooth axisymmetric vector fields must vanish at the poles of a spherical surface. This implies for any scalar function $G(s)$: $\partial_s G|_{0,L} = 0$. Most importantly, such scalars include the mean curvature $H = C_k^k/2$, as well as v_n . With Eq. (D.25), we therefore find the analytic limits

$$\Gamma_{s\varphi}^\varphi v_s \rightarrow \partial_s v_s \quad (\text{D.26})$$

$$\Gamma_{s\varphi}^\varphi \partial_s C_k^k \rightarrow \partial_s^2 C_k^k \quad (\text{D.27})$$

at the parametric poles. Additionally, we have for the principal curvatures $C_\varphi^\varphi|_{0,L} = C_s^s|_{0,L}$, because the curvature must be isotropic at the pole of an axisymmetric surface. This allows us to evaluate $C_\varphi^\varphi = \frac{1}{r} \sin \psi$ at the poles as follows: Near the pole at $s = 0$, we have $\psi(\delta s) = \mathcal{O}(\delta s)$ and therefore, using Eq. (21),

$$r(\delta s) = \int_0^{\delta s} \cos \psi(s') ds' = \delta s + \mathcal{O}(\delta s^3). \quad (\text{D.28})$$

Using Eq. (D.25), the explicit form of the azimuthal curvature in Eq. (18) therefore implies

$$\lim_{\delta s \rightarrow 0} C_\varphi^\varphi(\delta s) = \lim_{\delta s \rightarrow 0} \frac{\sin \psi}{\delta s} = \partial_s \psi|_{s=0} = C_s^s(0). \quad (\text{D.29})$$

Similarly, it can be shown that $C_\varphi^\varphi(L) = \partial_s \psi|_L$ on a spherical surface.

Using Eqs. (D.26)–(D.27), it follows that the tangential force balance Eq. (D.22) vanishes

identically at $s = \{0, L\}$, and the normal force balance Eq. (D.23) reads:

$$4\eta_b C_s^s (\partial_s v_s + C_s^s v_n) + 2(\xi f(c) + \gamma) C_s^s - 8\kappa \partial_s^2 C_s^s = p \quad (\text{D.30})$$

at the poles. This is the final form we use in our numerical scheme to solve the force balance equations at $s = \{0, L\}$. This analysis also implies that the equations derived for the time evolution of the curvature tensor components in Eq. (D.4) and (D.5) are equivalent at the poles, such that $C_\varphi^\varphi|_{0,L} = C_s^s|_{0,L}$ is consistently conserved during deformations. Using similar arguments, we find of the dynamic equation for the concentration field at the poles of a spherical surface:

$$\partial_t c = 2 \left(-\partial_s (c v_s) - c v_n C_s^s + D \partial_s^2 c \right) - k(c - c_0). \quad (\text{D.31})$$

D.3 Boundary conditions and global constraints

Here, we present details on the boundary conditions and global constraints, we have used to determine solutions of the force balance equations and the surface dynamics. Fields on axisymmetric spherical surfaces must have specific symmetries at the poles so that their global smoothness is ensured. These *closure conditions* effectively define boundary conditions for solutions of the force balance equations, which we discuss in the first part of this section. In the second part, we derive a condition on the deformation field v_n that ensures conservation of the volume enclosed by the surface during deformations. The corresponding Lagrange multiplier defines a pressure that we have used as an external force in the numerical solutions. In the last part, we discuss the translational invariance of the governing equations and explain how specific reference frames have been chosen in this work to determine unique solutions for the flow field \mathbf{v} .

D.3.1 Closure conditions on spherical axisymmetric surfaces

On spherical, axially symmetric surfaces, there exist generic constraints at the parametric poles $s \in \{0, L\}$ that ensure global regularity of the fields and smooth poles throughout the deformation process.

To ensure global regularity of, we require at the poles of an axisymmetric spherical surface

$$\mathbf{v}_\parallel|_{s=0,L} = 0 \quad (\text{D.32})$$

$$\partial_s c|_{s=0,L} = 0. \quad (\text{D.33})$$

Smoothness of the surface at the poles requires $\psi|_{s=0} = 0$ and $\psi|_{s=L} = \pi$. We see from Eq. (D.3) that this can be ensured during deformations by the condition

$$\partial_s v_n|_{s=0,L} = 0. \quad (\text{D.34})$$

For initial conditions with smooth poles, the constraint Eq. (D.34) additionally ensures that the integral representation of a spherical surface is well-defined. This can be seen from Eq. (D.6), which indeed implies $\partial_t \rho|_{s=0,L} = 0$ if $\psi|_{s=0} = 0$ and $\psi|_{s=L} = \pi$. Even though the surface is constructed from an integral along the azimuthal outline that can change its length and local curvature, the local constraint given by Eq. (D.34) is sufficient for the endpoint of this integral curve ($\rho|_{s=L} = 0$) to remain on the symmetry-axis.

Equations (D.32) and (D.34) are formally imposed as boundary conditions when solving the force balance Eqs. (D.22) and (D.23) for the in-plane velocity v_s and the deformation field v_n on a spherical surface. Eq. (D.33) only needs to be fulfilled by the initial condition for c , because on an axisymmetric surface the dynamic equation for the concentration field Eq (D.24) implies $\partial_t(\partial_s c)|_{s=0,L} = 0$.

On tubular surfaces, we use Eqs. (D.3) and (D.6) to keep track of $\psi(t)|_{s=0}$ and $\rho(t)|_{s=0}$, respectively, which is required to reconstruct tubular surfaces using Eqs. (2.22)–(2.24). The coordinate $z(t)|_{s=0}$ can be chosen arbitrarily due to the translational invariance discussed below.

D.3.2 Conservation of the enclosed volume

For our numerical results, we have considered the case where the volume enclosed by the surface is conserved throughout the deformation process. Here, we briefly explain how this constraint was implemented into our framework. The volume enclosed by an axisymmetric surface can be expressed in our parametrisation as

$$V = \pi \int_{z(u_a)}^{z(u_b)} \rho^2 dz = \pi \int_{u_a}^{u_b} \rho^2 \sin \psi h du. \quad (\text{D.35})$$

For a deformation velocity v_n , volume changes are therefore given by

$$\begin{aligned} \partial_t V &= \pi \int_{s(u_a,t)}^{s(u_b,t)} \left(2\rho v_n \sin^2 \psi - \rho^2 \cos \psi \partial_s v_n + \rho^2 v_n C_s^s \sin \psi \right) ds \\ &= 2\pi \int_{u_a}^{u_b} v_n \sqrt{g} du - \pi \rho^2 \cos \psi v_n \Big|_{s(u_a,t)}^{s(u_b,t)}. \end{aligned} \quad (\text{D.36})$$

Here, we have used Eqs. (A.62), (D.1), (D.3), and (D.6) and $\sqrt{g(u)} = \rho h$. Equation (D.36) is valid for spherical surfaces, as well as for open surfaces ($\rho|_{s=0,L} \neq 0$) with $v_s|_{s=0,L} = 0$ and for tubular surfaces with periodic boundary conditions. On spherical surfaces and on tubular surfaces with periodic boundary conditions, the boundary term in Eq. (D.36) vanishes. For the examples in this thesis, we use the integral expression in Eq. (D.36) as a constraint on the deformation velocity v_n in order to impose $\partial_t V = 0$ and introduce an internal pressure $p = f_n^{\text{ext}}$ as the corresponding Lagrange multiplier.

D.3.3 Translational invariance and choice of reference frame

The governing equations for the deforming active fluid surface introduced in Section 2.1 are translational invariant, such that solutions are only defined up to a constant velocity vector. When solving the force balance equations on axisymmetric surfaces, we have eliminated this degeneracy by choosing specific reference frames, which is explained here in more detail.

For an axisymmetric parametrisation, only translations along the z -axis with a constant vector $\mathbf{v}_0 = v_0 \bar{\mathbf{e}}_z$ are relevant. In the local basis of an axisymmetric surface, a constant vector can be expressed as

$$\mathbf{v}_0 = v_0 (\sin \psi \mathbf{e}_s - \cos \psi \mathbf{n}). \quad (\text{D.37})$$

We write a translation for the purpose of this discussion as $\mathbf{v} = \mathbf{v}' - \mathbf{v}_0$, where \mathbf{v}' and $c'(s', t)$ is an arbitrary solution of the force balance equations and the dynamic equation of the concentration field. Using $v_s^0 = v_0 \sin \psi$ and $v_n^0 = -v_0 \cos \psi$, one can verify explicitly that the force balance Eqs. (D.22) and (D.23) are unchanged and the dynamic equation of the concentration field is invariant under $\mathbf{v}' \rightarrow \mathbf{v} + \mathbf{v}_0$ and $c'(s', t) \rightarrow c(s - v_s^0 t, t)$. In the following, we briefly explain which reference frame we have chosen in the different examples shown in Chapter 2 and how these choices fix v_0 in a way that \mathbf{v} is uniquely determined.

To fix v_0 on spherical surfaces discussed in Section 2.3, we have chosen the reference frame where $\mathbf{v}|_{s=0} = -\mathbf{v}|_{s=L} \Rightarrow v_n|_{s=0} = v_n|_{s=L}$, which implies $v_0 = (v_n'|_{s=L} - v_n'|_{s=0})/2$. This choice ensures that $v_n = 0$ everywhere, if the geometry of the surfaces shape is stationary.

On periodic tubular surfaces discussed in Section 2.4, we have imposed $\int_0^L v_s ds = 0$ when determining the flow fields using our numerical approach. This implicitly fixes $v_0 = \int_0^L v_s' ds / L_0$ (where $L_0 = L|_{t=0}$) and was used to determine the flow fields shown in Fig. 2.5. To determine the in-plane flow field in the reference frame of the stationary constriction shown in Fig. 2.6, we have used that the surface geometry does not change in the final steady state. Therefore, the normal flow field must be of the form $v_n' = -v_0' \cos \psi$. We then chose $v_0 = v_0'$, for which $\mathbf{v} = \mathbf{v}' - \mathbf{v}_0$ yields a flow field with $v_n = 0$, such that the constriction does not move. The corresponding tangential flow in this reference frame is shown in Figs. 2.6 a and b.

D.4 Linearisation of the dynamics of deforming active fluid surfaces

Here, we present a detailed derivation of the linearisation of shape perturbations used in this thesis. The brute-force approach to perform linearisations of vector- and tensor-valued problems along with surface shape changes would be using the specific parameterisation of the reference shape from the start. This requires expressing all covariant (differential) equations and their perturbations component by component, including Christoffel symbols and the

components of all tensor fields that are relevant for the problem. However, this procedure is not only fairly tedious, but can also make it difficult to identify potentially more compact and instructive forms of the final linearised equations. To avoid these technicalities, we follow a different approach and first rewrite in Section D.4.1 the force balance equations for an arbitrary surface presented in a *coordinate-free*¹ form. To compute linearised equations of spherical and tubular surfaces in Sections D.4.2 and D.4.3, it is then sufficient to specify the effect of shape perturbations on the mean curvature and the Gaussian curvature of the reference geometry and calculations on the level parameterisation-dependent components are avoided.

D.4.1 Coordinate-free form of the governing equations

Force balance equations

As a preparatory step for the linearisations, we first determine the coordinate-free representation of the force balance equations for the viscous part of the tension tensor

$$t_{ij}^\eta = 2\eta_s \left(v_{ij} - \frac{1}{2} v_k^k g_{ij} \right) + \eta_b v_k^k g_{ij}, \quad (\text{D.38})$$

with the symmetric strain rate tensor v_{ij} given in Eq. (2.10). Additionally, we introduce the decomposition

$$t_{ij}^\eta = t_{\parallel,ij}^\eta + t_{\perp,ij}^\eta, \quad (\text{D.39})$$

where $t_{\parallel,ij}^\eta$ and $t_{\perp,ij}^\eta$, respectively, contain the contributions from tangential flow fields v_i and the deformation field v_n . To determine a coordinate-free representation of $t_{\parallel,ij}^\eta$, we first note that

$$\begin{aligned} \nabla_i t_{\parallel,j}^{\eta,i} &= \eta_s \left(\nabla_i \nabla^i v_j + \nabla_i \nabla_j v^i - \nabla_j \nabla_i v^i \right) \\ &= \eta_s \left(\nabla_i \nabla^i v_j + K v_j \right) \\ &= \eta_s \left(\mathbf{e}_j \cdot \Delta_\Gamma \mathbf{v}_\parallel + 2HC_{ij} v^i \right). \end{aligned} \quad (\text{D.40})$$

In the first step, we have used the Ricci-identity for a two-dimensional surface Eq. (A.28). In the second step, we have used the tangential projection of Eq. (B.24)

$$\nabla_i \nabla^i v_j = \mathbf{e}_j \cdot \Delta_\Gamma \mathbf{v}_\parallel + C_{ij} C^i_k v^k, \quad (\text{D.41})$$

as well as Eq. (A.22). From Eq. (D.40) it then follows that the tangential force balance for in-plane flows can be equivalently expressed in the embedding Euclidean space as

$$\mathbf{e}^j \nabla_i \nabla_i t_{\parallel,j}^{\eta,i} = \eta_s \left(\mathbf{P}_\Gamma \cdot \Delta_\Gamma \mathbf{v}_\parallel + 2HC \cdot \mathbf{v}_\parallel \right). \quad (\text{D.42})$$

¹Here, we mean coordinate-free in the sense that no explicit vector or tensor components appear in the expression. Effectively, this amounts to expressing all equations in the embedding Euclidean space.

Here, we have introduced the general tangential projection operator

$$\mathbf{P}_\Gamma = \mathbf{e}_i \mathbf{e}^i, \quad (\text{D.43})$$

as well as the representation of the curvature $\mathbf{C} = C_{ij} \mathbf{e}^i \mathbf{e}^j = \nabla_\Gamma \mathbf{n}$ as a 3×3 matrix, where we recall that $\nabla_\Gamma = \mathbf{e}^i \nabla_i$. Contributions of the deformation field v_n to the tangential force balance can be written as

$$\begin{aligned} \mathbf{e}^j \nabla_i t_{\perp,ij}^\eta &= 2\eta_s \mathbf{e}^j \nabla_i \left(C^i_j v_n - \frac{1}{2} C^k_k \delta^i_j v_n \right) + \eta_b \mathbf{e}^j \nabla_j C^k_k v_n \\ &= 2\eta_s (v_n \nabla_\Gamma H - H \nabla_\Gamma v_n + \mathbf{C} \cdot \nabla_\Gamma v_n) + 2\eta_b \nabla_\Gamma (H v_n), \end{aligned} \quad (\text{D.44})$$

where we have used Eq. (A.32).

To rewrite the normal force balance, one proceeds in a similar fashion using Eq. (A.22). From this and Eqs. (D.42) and (D.44) it follows that the force balance Eqs. (2.3) and (2.4) for an active fluid surface can be written as

$$\begin{aligned} \eta_s \left[\mathbf{P}_\Gamma \cdot \Delta_\Gamma \mathbf{v}_\parallel + 2H \mathbf{C} \cdot \mathbf{v}_\parallel + 2(v_n \nabla_\Gamma H - H \nabla_\Gamma v_n + \mathbf{C} \cdot \nabla_\Gamma v_n) \right] \\ + \eta_b \nabla_\Gamma \left(\nabla_\Gamma \cdot \mathbf{v}_\parallel + 2H v_n \right) + \mathbf{T}_\parallel = -\mathbf{f}_\parallel^{\text{ext}} \end{aligned} \quad (\text{D.45})$$

$$\begin{aligned} 2\eta_s \left[\nabla_\Gamma \cdot (\mathbf{C} \cdot \mathbf{v}_\parallel) - 2 \mathbf{v}_\parallel \cdot \nabla_\Gamma H - H \nabla_\Gamma \cdot \mathbf{v}_\parallel + 2(H^2 - K) v_n \right] \\ + 2\eta_b H \left(\nabla_\Gamma \cdot \mathbf{v}_\parallel + 2H v_n \right) + T_H = f_{(n)}^{\text{ext}}. \end{aligned} \quad (\text{D.46})$$

Here, $\mathbf{T}_\parallel = \nabla_\Gamma \xi_a$ denotes contributions from the isotropic active tension, and $\mathbf{f}_\parallel^{\text{ext}} = \mathbf{P}_\Gamma \cdot \mathbf{f}^{\text{ext}}$ and $f_{(n)}^{\text{ext}} = \mathbf{n} \cdot \mathbf{f}^{\text{ext}}$ denote tangential and normal contributions from external forces. We have additionally included a term T_H in Eq. (D.46), which comprises the remaining passive terms that are used in this thesis and which are derived from the Helfrich energy

$$F_H = \int \gamma + \kappa \left(C^k_k - 2C_0 \right)^2 dA. \quad (\text{D.47})$$

In Chapter 2, we have considered the case of a vanishing spontaneous curvature $C_0 = 0$. In the more general form given in Eq. (D.47), the Helfrich energy corresponds to tension and moments in the surface given by [112, 129]

$$t_H^{ij} = \gamma g_{ij} + \kappa \left(C^k_k - 2C_0 \right) \left(\left(C^k_k - 2C_0 \right) g^{ij} - 2C^{ij} \right) \quad (\text{D.48})$$

$$m_H^{ij} = 2\kappa \left(C^k_k - 2C_0 \right) \epsilon^{ij}. \quad (\text{D.49})$$

Because m_H^{ij} is antisymmetric, the normal torque balance Eq. (2.6) is satisfied with $t_{ij} \epsilon^{ij} = 0$ in the absence of external torques. The in-plane torque balance Eq. (2.5) yields $t_{n,H}^i = 2\kappa \nabla^i C^k_k$. Using this and t_H^{ij} , the tangential force balance Eq. (2.3) yields $\nabla_i t_H^{ij} + C^j_i t_{n,H}^i = 0$, such that there are no additional terms to Eq. (D.45). The contributions to the normal force

balance Eq. (D.46) read

$$T_H = 2\gamma H + 4\kappa \left[2K(H - C_0) - 2H^3 + 2HC_0^2 - \Delta_\Gamma H \right], \quad (\text{D.50})$$

which, in the absence of flows and active stresses, yields the well-known shape equation for surfaces with bending rigidity [129].

Equations (D.45) and (D.46) are valid for any surface and will be the starting point for the linearisations derived in the following Section D.4.2. Note that these equations can also be used in numerical approaches that compute differential operators in the embedding space, as is done for example in level set methods [137]. Solving Eqs. (D.45), (D.46) in such a framework corresponds to determining the dynamics of an active fluid surface whose covariant constitutive equations for the tension and moment tensor are given by Eqs. (2.12) and (2.13).

Dynamic equation of the concentration field

The dynamic equation of the concentration field Eq. (3.4) can be written as

$$\partial_t c + \nabla_\Gamma \cdot (c\mathbf{v}_\parallel) + 2Hcv_n = D\Delta_\Gamma c - k(c - c_0), \quad (\text{D.51})$$

where we have used Eqs. (A.35) and the definition of the mean curvature Eq. (A.14).

D.4.2 Linearisation on spherical surfaces

In the following, we present the linearisation of the active surface dynamics on spherical geometries used in Section 2.3. Using the formal preparations derived in Section D.4.1, in particular Eqs. (D.45), (D.46), and (D.51), the linearisation procedure now reduces essentially to specifying perturbations of mean and Gaussian curvature, as well as to finding a convenient representation of the curvature tensor $\mathbf{C} = C_{ij}\mathbf{e}^i\mathbf{e}^j$. The latter is only needed to zeroth order, as it appears always in products with the flow field, which we expand around $\mathbf{v} = 0$. On the surface of a sphere with radius R_0 , the curvature is isotropic and can be written as

$$C_{ij}^{(0)} = \frac{1}{R_0} g_{ij}. \quad (\text{D.52})$$

This implies the matrix form

$$C_{ij}^{(0)}\mathbf{e}^i\mathbf{e}^j = \frac{1}{R_0}\mathbf{P}_S, \quad (\text{D.53})$$

where the projection onto the unit sphere \mathbf{P}_S is defined in Eq. (B.67). Perturbations of mean and Gaussian curvature for a shape variation $\delta X_n = \delta R$ are given by

$$\delta H = -\frac{\delta R}{R_0^2} - \frac{1}{2}\Delta_S\delta R \quad (\text{D.54})$$

$$\delta K = -2\frac{\delta R}{R_0^3} - \frac{1}{R_0}\Delta_S\delta R, \quad (\text{D.55})$$

where we have used Eqs. (A.48) and (A.49). Furthermore, it follows from the dynamic equation of the surface $\partial_t \mathbf{X} = v_n \mathbf{n}$ and $\delta \mathbf{X} = \delta R \mathbf{n}$ that

$$\begin{aligned} \delta v_n &= \mathbf{n} \cdot \partial_t \delta \mathbf{X} \\ &= \partial_t \delta R, \end{aligned} \quad (\text{D.56})$$

where we have additionally used $\partial_t \mathbf{n} \sim \mathbf{e}_i$ due to the normalisation of \mathbf{n} . We consider an expansion of flows, deformations and concentration perturbations in the form¹

$$\delta c = \sum_{l,m} \delta c_{lm} Y_{lm} \quad (\text{D.57})$$

$$\delta R = \sum_{l,m} \delta R_{lm} Y_{lm} \quad (\text{D.58})$$

$$\delta \mathbf{v}_{\parallel} = \sum_{l,m} \left(\delta v_{lm}^{(1)} \Psi^{(lm)} + \delta v_{lm}^{(2)} \Phi^{(lm)} \right), \quad (\text{D.59})$$

and general external forces given by

$$\delta \mathbf{f}^{\text{ext}} = \sum_{l,m} \left(f_{lm}^{e,r}(r) \mathbf{Y}^{(lm)} + f_{lm}^{e,(1)}(r) \Psi^{(lm)} + f_{lm}^{e,(2)}(r) \Phi^{(lm)} \right), \quad (\text{D.60})$$

where $\sum_{l,m} = \sum_{l=-\infty}^{\infty} \sum_{m=-l}^l$. We then collect terms to linear order from Eqs. (D.45), (D.46) and find from the orthogonality of scalar and vector harmonics the general linearised force balance equations for perturbations of a sphere:

$$\frac{\eta_s}{R_0^2} (1-l)(l+2) \delta v_{lm}^{(1)} + \left[\frac{\eta_b}{R_0^2} \left(2\delta \dot{R}_{lm} - l(l+1) \delta v_{lm}^{(1)} \right) + \frac{\xi}{R_0} \partial_c f \delta c_{lm} \right] = -\delta f_{lm}^{e,(1)} \quad (\text{D.61})$$

$$\frac{\eta_s}{R_0^2} (1-l)(l+2) \delta v_{lm}^{(2)} = -\delta f_{lm}^{e,(2)} \quad (\text{D.62})$$

$$\begin{aligned} & \frac{2\eta_b}{R_0^2} \left(2\delta \dot{R}_{lm} - l(l+1) \delta v_{lm}^{(1)} \right) + \frac{2\xi}{R_0} \partial_c f(c_0) \delta c_{lm} \\ & + \left[\frac{2\kappa}{R_0^4} \{l(l+1) - 4C_0 R_0\} + \frac{\gamma + 4\kappa C_0^2 + \xi f(c_0)}{R_0^2} \right] (l-1)(l+2) \delta R_{lm} = \delta f_{lm}^{e,r}, \end{aligned} \quad (\text{D.63})$$

where $\delta \dot{R}_{lm} = \frac{d}{dt} \delta R_{lm}$ and the differentiation of the vector harmonics was performed using Eqs. (B.25), (B.26), (B.28), and (B.29). Furthermore, we have used Eqs. (D.54) and (D.55) together with the eigenfunction property of scalar harmonics Eq. (B.1). For external forces that result from hydrodynamic stresses of a passive surrounding fluid, the expansion coefficients $\delta f_{lm}^{e,r}$, $\delta f_{lm}^{e,(1)}$ and $\delta f_{lm}^{e,(2)}$ are given in Eqs. (B.75)–(B.77). The linearised dynamic

¹Note that in Chapter 2, we have discussed axisymmetric perturbations with $m = 0$ and presented numerical solutions of the axisymmetric nonlinear problem. We keep the expansion here general, to demonstrate that the linear dynamics described by the dispersion relation is degenerate in m .

equation of the concentration field (D.51) reads

$$\delta\dot{c}_{lm} + \frac{c_0}{R_0} \left(2\delta\dot{R}_{lm} - l(l+1)\delta v_{lm}^{(1)} \right) + \left(\frac{D}{R_0^2} l(l+1) + k \right) \delta c_{lm} = 0. \quad (\text{D.64})$$

For each mode number l , Eqs. (D.61)–(D.64) yield a closed system of equations for the coefficients $\{\delta v_{lm}^{(1)}, \delta v_{lm}^{(2)}, \delta R_{lm}, \delta c_{lm}\}$. Note that there is a $2l+1$ -fold degeneracy for each l in these equations. The force balance equations can be used to eliminate $\delta v_{lm}^{(1)}$ and $\delta v_{lm}^{(2)}$ from this system, which leads to a two-dimensional Jacobian for the dynamics of the modes δR_{lm} and δc_{lm} .

D.4.3 Linearisation on tubular surfaces

In the following, we present the linearisation of the active surface dynamics on tubular geometries used in Section 2.4. We use cylindrical coordinates $\{\rho, \varphi, z\}$ with the normalised standard basis $\{\bar{\mathbf{e}}_\rho, \bar{\mathbf{e}}_\varphi, \bar{\mathbf{e}}_z\}$. For reference, we present the linearisation of perturbations of a cylindrical surface also for the fully general case of non-axisymmetric perturbations. The stationary state around which we linearise is given by a cylindrical surface \mathcal{C} of radius ρ_0 and length L_0 , where $\mathbf{v}_\parallel = 0$ and a concentration $c = c_0$ is homogeneous. The expansions of concentration, shape, and flow perturbations read

$$\delta c = \sum_{n,q} \delta c_{nq} y_{nq}(z, \varphi) \quad (\text{D.65})$$

$$\delta \rho = \sum_{n,q} \delta \rho_{nq} y_{nq}(z, \varphi) \quad (\text{D.66})$$

$$\delta \mathbf{v}_\parallel = \sum_{n,q} \left(\delta v_{nq}^z \bar{\mathbf{e}}_z + \delta v_{nq}^\varphi \bar{\mathbf{e}}_\varphi \right) y_{nq}(z, \varphi) \quad (\text{D.67})$$

and general external forces are written as

$$\delta \mathbf{f}^{\text{ext}} = \sum_{m,q} \left(\delta f_{nq}^\rho \bar{\mathbf{e}}_\rho + \delta f_{nq}^z \bar{\mathbf{e}}_z + \delta f_{nq}^\varphi \bar{\mathbf{e}}_\varphi \right) y_{nq}(z, \varphi) \quad (\text{D.68})$$

with summation $\sum_{n,q} = \sum_{n=-\infty}^{\infty} \sum_{q=-\infty}^{\infty}$. Here, we have defined

$$y_{nq}(z, \varphi) = \exp[i(k_n z + q\varphi)], \quad (\text{D.69})$$

where $k_n = b\pi n/L$ are the wave numbers with $b = 2$ ($b = 1$) for periodic (no-flux) boundary conditions. These definitions imply

$$\Delta_{\mathcal{C}} y_{nq} = -\lambda_{nq} y_{nq} / \rho_0^2 \quad (\text{D.70})$$

where $\lambda_{nq} = k_n^2 \rho_0^2 + q^2$ and

$$\nabla_{\mathcal{C}} \cdot \delta \mathbf{v}_{\parallel} = i \sum_{n,q} \left(\delta v_{nq}^z k_n + \delta v_{nq}^{\varphi} \frac{q}{\rho_0} \right) y_{nq} \quad (\text{D.71})$$

$$\Delta_{\mathcal{C}} \delta \mathbf{v}_{\parallel} = -\frac{\lambda_{nq}}{\rho_0^2} \delta \mathbf{v}_{\parallel} - \sum_{n,q} \frac{\delta v_{nq}^{\varphi}}{\rho_0^2} y_{nq} (2iq \bar{\mathbf{e}}_{\rho} + \bar{\mathbf{e}}_{\varphi}). \quad (\text{D.72})$$

Here, $\nabla_{\mathcal{C}}$ and $\Delta_{\mathcal{C}}$ are the vector gradient and Laplace-Beltrami operator defined in Eqs. (A.27) and (A.34) on a surface parametrised by $\mathbf{X}(\varphi, z) = \rho_0 \bar{\mathbf{e}}_{\rho} + z \bar{\mathbf{e}}_z$.

The curvature tensor of a cylindrical surface can be expressed in matrix form as

$$C_{ij}^{(0)} \mathbf{e}^i \mathbf{e}^j = \frac{1}{\rho_0} \bar{\mathbf{e}}_{\varphi} \bar{\mathbf{e}}_{\varphi}, \quad (\text{D.73})$$

which acts as an anisotropic projection operator on the cylindrical surface. From Eqs. (A.48) and (A.49) it follows for $\delta X_n = \delta \rho$ that

$$\delta H = -\frac{\delta \rho}{2\rho_0^2} - \frac{1}{2} \Delta_{\mathcal{C}} \delta \rho \quad (\text{D.74})$$

$$\delta K = -\frac{\partial_z^2 \delta \rho}{\rho_0}. \quad (\text{D.75})$$

Furthermore, note that in an Eulerian representation we have

$$\begin{aligned} \delta v_n &= \mathbf{n} \cdot \partial_t \delta \mathbf{X} \\ &= \partial_t \delta \rho, \end{aligned} \quad (\text{D.76})$$

which follows from the same arguments as Eq. (D.56). For an expansion of flows, deformations and concentration perturbations given in Eqs. (D.65)–(D.67), we can then directly collect terms to linear order from Eqs. (D.45), (D.46), and (D.51) and from which we find the general linearised force balance equations for perturbations of a cylindrical surface

$$-\eta_s \left(\lambda_{nq} \frac{\delta v_{nq}^z}{\rho_0^2} + \frac{ik_n}{\rho_0} \delta \dot{\rho}_{nq} \right) + k_n \left[\eta_b \left(-q \frac{\delta v_{nq}^{\varphi}}{\rho_0} - k_n \delta v_{nq}^z + i \frac{\delta \dot{\rho}_{nq}}{\rho_0} \right) + i \xi \partial_c f(c_0) \delta c_{nq} \right] = -\delta f_{nq}^z \quad (\text{D.77})$$

$$\eta_s \left(-\lambda_{nq} \frac{\delta v_{nq}^{\varphi}}{\rho_0^2} + iq \frac{\delta \dot{\rho}_{nq}}{\rho_0^2} \right) + \frac{q}{\rho_0} \left[\eta_b \left(-q \frac{\delta v_{nq}^{\varphi}}{\rho_0} - k_n \delta v_{nq}^z + i \frac{\delta \dot{\rho}_{nq}}{\rho_0} \right) + i \xi \partial_c f(c_0) \delta c_{nq} \right] = -\delta f_{nq}^{\varphi} \quad (\text{D.78})$$

$$\begin{aligned} &\frac{\eta_s}{\rho_0} \left(iq \frac{\delta v_{nq}^{\varphi}}{\rho_0} - ik_n \delta v_{nq}^z + \frac{\delta \dot{\rho}_{nq}}{\rho_0} \right) + \frac{\eta_b}{\rho_0} \left(iq \frac{\delta v_{nq}^{\varphi}}{\rho_0} + ik_n \delta v_{nq}^z + \frac{\delta \dot{\rho}_{nq}}{\rho_0} \right) + \frac{\xi}{\rho_0} \partial_c f(c_0) \delta c_{nq} \\ &+ \left[4\kappa \frac{k_n^2}{\rho_0^2} (1 - 2C_0 \rho_0) + \frac{\kappa}{\rho_0^4} (\lambda_{nq} - 1) (2\lambda_{nq} - 3) + \frac{\gamma + 4\kappa C_0^2 + \xi f(c_0)}{\rho_0^2} (\lambda_{nq} - 1) \right] \delta \rho_{nq} = \delta f_{nq}^{\rho} \end{aligned} \quad (\text{D.79})$$

of the force balance equations in z , φ and ρ -direction, respectively. For external forces that result from hydrodynamic stresses of a passive surrounding fluid, the expansion coefficients

δf_{nq}^ρ , δf_{nq}^z and δf_{nq}^φ can be determined in terms of Bessel-functions [166,167]. The linearised dynamic equation for the concentration field

$$\delta \dot{c}_{nq} + c_0 \left(iq \frac{\delta v_{nq}^\varphi}{\rho_0} + ik_n \delta v_{nq}^z + \frac{\delta \dot{\rho}_{nq}}{\rho_0} \right) + \left(\frac{D}{\rho_0^2} \lambda_{nq} + k \right) \delta c_{nq} = 0, \quad (\text{D.80})$$

where $\delta \dot{\rho}_{nq} = \frac{d}{dt} \delta \rho_{nq}$ and Eqs. (D.71)–(D.75) have been repeatedly used.

Linearised dynamic equations for the constitutive relations studied in Section 2.4 on axisymmetric tubular surfaces can be obtained for $q = 0$. We can then use Eqs. (D.77) and (D.79) to eliminate the modes $\delta v_{n,0}^z = \delta v_n^z$. Together with Eq. (D.80), we find

$$\frac{d}{dt} \frac{\delta \rho_n}{\rho_0} = \frac{\eta_s + \eta_b}{4\eta_s \eta_b} \left\{ -\kappa B_\kappa(k_n \rho_0) + [\gamma + \xi f(c_0)] (1 - k_n^2 \rho_0^2) \right\} \frac{\delta \rho_n}{\rho_0} - \frac{\xi c_0 \partial_c f(c_0)}{2\eta_b} \frac{\delta c_n}{c_0} \quad (\text{D.81})$$

$$\frac{d}{dt} \frac{\delta c_n}{c_0} = \frac{1}{2\eta_b} \left\{ \kappa B_c(k_n r_0) - [\gamma + \xi f(c_0)] (1 - k_n^2 r_0^2) \right\} \frac{\delta \rho_n}{\rho_0} + \left(\frac{\xi c_0 \partial_c f(c_0)}{\eta_b} - D k_n^2 - k \right) \frac{\delta c_n}{c_0}, \quad (\text{D.82})$$

where all terms related to the bending rigidity have been collected into

$$B_\kappa(k_n \rho_0) = 4 \frac{k_n^2}{\rho_0^2} + \frac{1}{\rho_0^4} (2k_n^2 \rho_0^2 - 3) (\rho_n^2 \rho_0^2 - 1) \quad (\text{D.83})$$

and we dropped the $q = 0$ subscripts for brevity. Equations (2.50) and (2.51) follow from Eqs. (D.81) and (D.82) for $\kappa = 0$. Evaluating the Jacobian defined by this system numerically reveals that that critical contractility α_c^* used in Section 2.4 depends in general on κ .

D.5 Neck radius scaling of tubular surfaces with bending rigidity

In the following, we present a geometric toy model to analyse the neck radius of tubular surface shapes discussed in Section 2.4.4. In this toy model, we ignore for simplicity tension inhomogeneities due to flows and contractility. Force-balanced surface shapes then correspond to minima of the energy

$$F_H(L_0, V) = \bar{\gamma} A + 4\kappa \int H^2 dA, \quad (\text{D.84})$$

where $\bar{\gamma}$ is an effective surface tension, κ is the bending rigidity and H is the mean curvature. According to the constraints used in the numerical simulations, the total length of the initial cylinder L_0 , as well as its volume V are fixed.

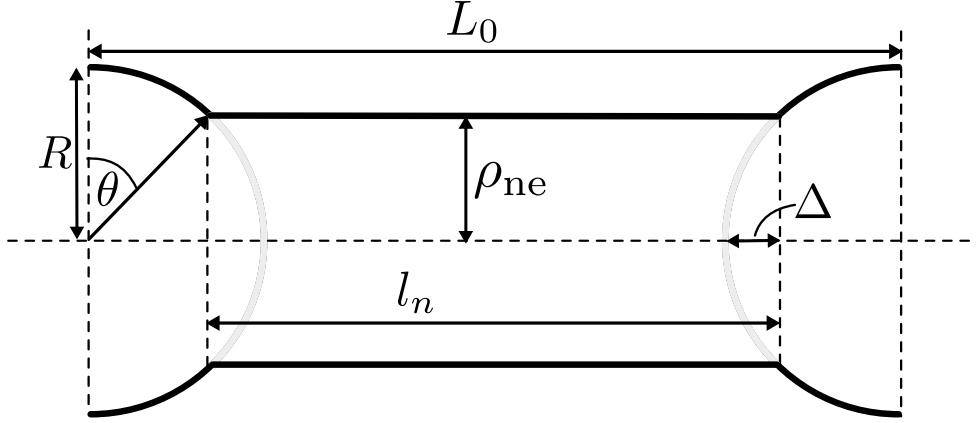


Figure D.1: Overview of the geometric parameters used to derive a simplified shape parameterisation of a constricting tubular surface with bending rigidity. Surface shapes are parametrised by inverted spherical caps with radius R at the boundaries, which are connected by a cylindrical neck of length l_n and radius ρ_{ne} . For fixed enclosed volume V and total length L_0 , the neck radius ρ_{ne} is the only free parameter to uniquely describe this toy model geometry. The length Δ is a dummy variable that is required for the geometric calculations.

We parametrise surface shapes as inverted spherical caps with radius R at the boundaries that are connected by a cylindrical neck of length l_n and radius ρ_{ne} . We denote surface areas and volumes of the spherical caps by A_s and V_s , those of the neck forming cylindrical surface by A_n and V_n . The total surface area is then given by $A_{\text{tot}} = 2A_2 + A_n$. The mean curvatures of each domain read $H_s = 1/R$ on the spherical caps and $H_n = 1/(2\rho_{ne})$ in the neck region. The Helfrich energy Eq. (D.84) can be expressed in terms of this shape parameterisation as

$$\frac{F_H}{2\pi} = \bar{\gamma} \left(\rho_{ne} l_n + 2R^2 \sin \theta \right) + \kappa \left(\frac{l_n}{\rho_{ne}} + 8 \sin \theta \right). \quad (\text{D.85})$$

In the following, we use the geometric relations imposed by fixing L_0 and V and express Eq. (D.85) as $F(\rho_{ne}, L_0, V)$. First, we derive two geometric relations that are needed later. To this end, we note that the total length can be expressed as

$$L_0 = l_n + 2\sqrt{R^2 - \rho_{ne}^2}. \quad (\text{D.86})$$

Therefore, we can write

$$R^2 = \frac{1}{4} (L_0 - l_n)^2 + \rho_{ne}^2 \quad (\text{D.87})$$

$$\sqrt{R^2 - \rho_{ne}^2} = \frac{1}{2} (L_0 - l_n). \quad (\text{D.88})$$

The total volume can be written as

$$V = \pi l_n \rho_{ne}^2 + \frac{2\pi}{3} \left[2R^3 - \Delta^2 (3R - \Delta) \right]. \quad (\text{D.89})$$

The last term corrects the over estimation of volume due to the spherical cap penetrating with depth Δ into the neck cylinder volume. Using the geometric consistency relation $\Delta = R - \sqrt{R^2 - \rho_{\text{ne}}^2}$, this simplifies to

$$V = \pi l_n \rho_{\text{ne}}^2 + \frac{2\pi}{3} \sqrt{R^2 - \rho_{\text{ne}}^2} (2R^2 + \rho_{\text{ne}}^2). \quad (\text{D.90})$$

We can then use Eqs. (D.87) and (D.88) in Eq. (D.90) and find¹

$$l_n = L_0 - 6^{1/3} \left(\frac{V}{\pi} - L_0 \rho_{\text{ne}}^2 \right)^{1/3}. \quad (\text{D.91})$$

As a consistency check of this relation, we consider two limiting cases. First, we assume the volume is given by $\pi L_0 \rho_{\text{ne}}^2$. In this case we find $l_n = L_0$, which is consistent with the fact that the ‘neck’ takes up all the available volume and the geometry is given simply by a cylindrical surface. For $V = 4\pi R^3/3$ and $\rho_{\text{ne}} = 0$, we find $l_n = L_0 - 2R$ because two fully closed spherical caps contribute with $2R$ to the total length and the remaining part belongs to the neck.

Using Eqs. (D.87) and (D.91), we find

$$R^2 = \frac{6^{2/3}}{4} \left(\frac{V}{\pi} - L_0 \rho_{\text{ne}}^2 \right)^{2/3} + \rho_{\text{ne}}^2. \quad (\text{D.92})$$

Finally, we use $\sin \theta = \sqrt{R^2 - \rho_{\text{ne}}^2}/R$, Eqs. (D.88), (D.91) and (D.92) to write

$$\sin \theta = \frac{6^{1/3} \left(\frac{V}{\pi} - L_0 \rho_{\text{ne}}^2 \right)^{1/3}}{\sqrt{6^{2/3} \left(\frac{V}{\pi} - L_0 \rho_{\text{ne}}^2 \right)^{2/3} + 4\rho_{\text{ne}}^2}}. \quad (\text{D.93})$$

With Eqs. (D.91), (D.92) and (D.93) we can fully parametrise the energy Eq. (D.85) in terms of the fixed quantities L_0 and V , as well as the neck radius ρ_{ne} . We parametrise the volume in terms of the radius of the initial cylindrical surface ρ_0 as $V = \pi L_0 \rho_0^2$ and define the dimensionless neck radius $\tilde{\rho}_{\text{ne}} = \rho_{\text{ne}}/\rho_0$, the aspect ratio $\tilde{L}_0 = L_0/\rho_0$ and bending rigidity $\tilde{\kappa} = \kappa/(\tilde{\gamma}\rho_0^2)$. Altogether, we can write the free energy given in Eq. (D.84) for this

¹The resulting third order polynomial has only one physical solution

geometry as

$$\begin{aligned} \frac{F_H}{2\pi\bar{\gamma}\rho_0^2} &= \left[\tilde{\rho}_{\text{ne}}\tilde{L}_0 + (6\tilde{L}_0)^{1/3} (1 - \tilde{\rho}_{\text{ne}}^2)^{1/3} \left\{ \frac{1}{2} \left((6\tilde{L}_0)^{2/3} (1 - \tilde{\rho}_{\text{ne}}^2)^{2/3} + 4\tilde{\rho}_{\text{ne}}^2 \right)^{1/2} - \tilde{\rho}_{\text{ne}} \right\} \right] \\ &+ \tilde{\kappa} \left[\frac{\tilde{L}_0}{\tilde{\rho}_{\text{ne}}} + (6\tilde{L}_0)^{1/3} (1 - \tilde{\rho}_{\text{ne}}^2)^{1/3} \left(\frac{8}{\sqrt{(6\tilde{L}_0)^{2/3} (1 - \tilde{\rho}_{\text{ne}}^2)^{2/3} + 4\tilde{\rho}_{\text{ne}}^2}} - \frac{1}{\tilde{\rho}_{\text{ne}}} \right) \right] \end{aligned} \quad (\text{D.94})$$

$$\begin{aligned} &= \tilde{F}_0 + \tilde{L}_0 \left[\left(1 - \frac{6^{1/3}}{\tilde{L}_0^{2/3}} \right) \left(\tilde{\rho}_{\text{ne}} + \frac{\tilde{\kappa}}{\tilde{\rho}_{\text{ne}}} \right) + 2\tilde{\kappa} \frac{1}{(6\tilde{L}_0)^{2/3} \tilde{\rho}_{\text{ne}}} \right] \\ &+ \tilde{L}_0 \left[\left(\frac{1}{\tilde{L}_0} - 2 \frac{1}{(6\tilde{L}_0)^{1/3}} - \tilde{\kappa} \frac{8}{3} \frac{6^{1/3}}{\tilde{L}_0^{5/3}} \right) \tilde{\rho}_{\text{ne}}^2 + \mathcal{O}(\tilde{\rho}_{\text{ne}}^3, \tilde{L}_0^{-2/3}) \right]. \end{aligned} \quad (\text{D.95})$$

If the volume constraint is dropped, we have $\rho_0 = \rho_{\text{ne}} \Rightarrow \tilde{\rho}_{\text{ne}} = 1$ in Eq. (D.94) and only the leading terms in squared brackets remain, predicting from $\partial F/\partial \tilde{\rho}_{\text{ne}} = 0$ a neck radius $\sqrt{\kappa/\bar{\gamma}}$. As discussed in Section 2.4.4, these are also the terms that remain to leading order in $\tilde{L}_0 \gg 1$. This can be seen more easily from the way we have written Eq. (D.95). From this equation, we can essentially read off the coefficients used in Eq. (2.60):

$$F_0 = \pi\bar{\gamma}(6L_0)^{2/3} \rho_0^{4/3} + 16\pi\kappa \quad (\text{D.96})$$

$$A = 2\pi L_0 \left[\bar{\gamma} \left(1 - 6^{1/3} \frac{\rho_0^{2/3}}{L_0^{2/3}} \right) + \kappa \frac{2}{6^{2/3}} \frac{1}{L_0^{2/3} \rho_0^{4/3}} \right] \quad (\text{D.97})$$

$$B = 2\pi L_0 \kappa \left(1 - 6^{1/3} \frac{\rho_0^{2/3}}{L_0^{2/3}} \right) \quad (\text{D.98})$$

$$C = 2\pi \left[\bar{\gamma} \left(1 - \frac{2}{6^{1/3}} \frac{L_0^{2/3}}{\rho_0^{2/3}} \right) - \kappa 6^{1/3} \frac{8}{3} \frac{1}{L_0^{5/3} \rho_0^{1/3}} \right]. \quad (\text{D.99})$$

The increase in neck radii discussed in Section 2.4.4 compared to $\sqrt{\kappa/\bar{\gamma}}$ follows from $C < 0$. This inequality can be seen from Eq. (D.99) as follows. We note that the relations derived above only describe F_H correctly for all neck radii $\rho_{\text{ne}} \in [0, \rho_0]$ only if $6^{-1/3} L_0^{2/3} \rho_0^{-2/3} > 1$, or equivalently $L_0/\rho_0 > \sqrt{6} \approx 2.4$.¹ All the cases we have studied in this thesis obey this threshold. This implies that all terms that appear in Eq. (D.99) are negative and hence $C < 0$.

D.6 Details of the numerical approach

In the following, we present a detailed description of the numerical discretisation method we have used to solve the differential equations introduced above. We present validation results of this implementation and list the parameters we have used to obtain the numerical solutions presented in this work.

¹If this condition is not fulfilled, the spherical caps permeate each other for a neck radius $\rho_{\text{ne}} > 0$ and the geometric description would need to be changed.

D.6.1 Numerical discretisation

We discretise Eqs. (D.22) and (D.23) on the initial arc length domain $\mathcal{S}|_{t=0} = \mathcal{S}_0 = [0, L_0]$ by N equally spaced collocation points at coordinates $u_{(i)}$, $i = 1, 2, \dots, N$. Each point carries the local differential geometric information of the initial shape, given by the extrinsic curvature and the Christoffel symbols, as well as other problem-specific quantities, such as concentration fields. For brevity, we collectively refer to all fields stored on collocation points $u_{(i)} \in \mathcal{S}_0$ as $\{\Phi_{(i)}\}$. On this grid, we express the derivative operators of the force balance Eqs. (D.22) and (D.23) using centred fourth-order finite difference operators [168] and solve the resulting linear system of equations for the flow field components $(v_n, \mathbf{v}_{\parallel})$ and the internal pressure p . The latter follows from conservation of the enclosed volume, which is imposed using the integral constraint Eq. (D.36) using Simpson integration weights [168]. Then, we use the dynamic equations for the intrinsic and extrinsic geometry, Eqs. (D.1), (D.6), and Eqs. (D.4)–(D.7), as well as the dynamic equation for the concentration field Eq. (D.24) to update the set $\{\Phi_{(i)}\}$ using explicit Euler time stepping with step size δt . In subsequent time steps, the coordinate transformation h is used to express all equations in the reference space \mathcal{S}_0 , which allows solving the force-balance equations and evolving the set $\{\Phi_{(i)}\}$ on the same equidistant grid.

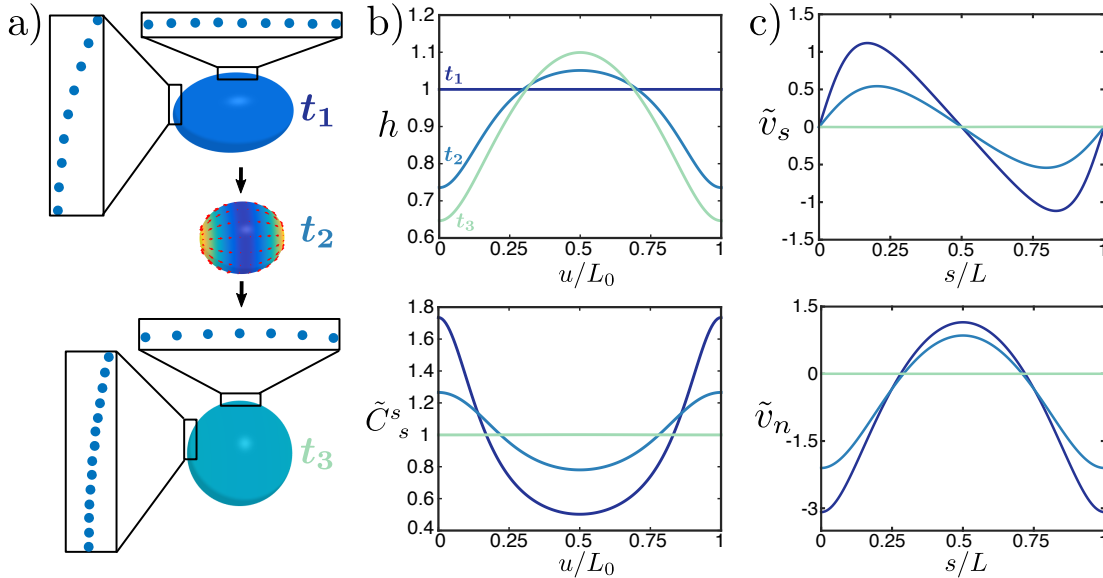


Figure D.2: Exemplary dynamics of collocation points and the geometric fields required to reconstruct and iterate axisymmetric surface shapes. (shown for the surface relaxation discussed in Section 2.3.2). **a)** Collocation points in physical space are initially homogeneously spaced ($h = 1$) and become inhomogeneously distributed during shape changes. **b)** Dynamic coordinate transformation h and dimensionless meridional curvature $\tilde{C}_s^s = R_0 C_s^s$ in the reference space $\mathcal{S}_0 = [0, L_0]$. Note the compression (dilation) of collocation points in **a)** in regions with $h < 1$ ($h > 1$). **c)** In-plane flow field $\tilde{v}_s = \mathbf{e}_s \cdot \mathbf{v}\tau/R_0$ and deformation velocity $\tilde{v}_n = v_n\tau/R_0$, where $\tau = \eta_b/\gamma$. The parameter values used are given in Table D.1.

Figure D.2 shows an example of the typical dynamics of collocation points in the physical space, as well as a time series of the different fields that are required to reconstruct and iterate the surface shape. The expected error convergence behaviour $\mathcal{O}(N^{-4}, \delta t)$ is verified in the following section, using a range of numerical tests.

D.6.2 Grid convergence analysis and simulation code validation

We validate the spatial discretisation of \mathcal{S}_0 by inverting the force balance Eqs. (D.22) and (D.23) on a spheroidal surface for increasing numbers N of collocation points. Figure D.2a shows the maximum error norm with respect to the numerical solution computed for $N = 3201$ collocation points for the flow-field components v_n and v_s , confirming fourth-order convergence.

Next, we validate the temporal convergence using a similar numerical experiment as shown in Fig. D.2, gradually increasing the number of time steps N_t used to reach a fixed final time point (Fig. D.2b). As expected from using explicit Euler time stepping, the geometric fields converge with $\sim N_t^{-1}$.

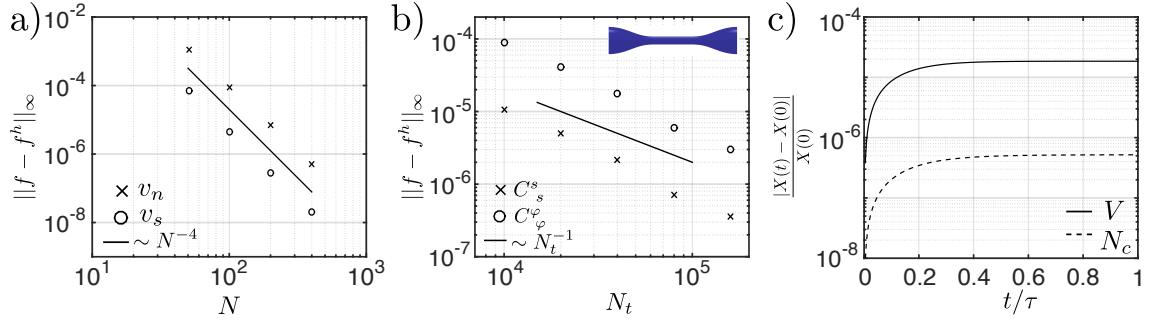


Figure D.3: Validation of convergence behaviour and conservation properties. **a)** Grid convergence of the spatial discretisation: Numerical solutions f^h of Eqs. (D.22) and (D.23) for single time step on a prolate spheroid with eccentricity 0.6 and homogeneous surface concentration compared with the high-resolution solution f for $N = 3201$ in the maximum error norm $\|\cdot\|_\infty$. **b)** Grid convergence of the temporal discretisation: Principle curvatures of a passive tubular surface ($\xi = 0$) after convergence to non-trivial stationary shape (inset) compared with the solution for $N_t = 3.2 \times 10^5$ in the maximum error norm $\|\cdot\|_\infty$. **c)** Relative numerical error of the conservation of the enclosed volume and the total number of molecules: Relaxation of an active, spheroidal surface with initial eccentricity 0.6. A complete overview of the parameters used for the corresponding simulations is given in Table D.1.

Finally, we test the conservation of enclosed volume and total molecule number, for which we consider a shape relaxation as presented in Fig. 2.3b. The volume is determined by integrating the surface shape via Eqs. (2.22)–(2.24) and using

$$V = \pi \int_{z(0)}^{z(L)} \rho^2 dz. \quad (\text{D.100})$$

This is an important validation of the constraint imposed by Eq. (D.36), which enforces vol-

ume conservation using intrinsic fields on the surface, while Eq. (D.100) determines the volume using the surface representation in the embedding space. The total number of molecules is given by

$$N_c = \int_{\Gamma} c dA. \quad (\text{D.101})$$

Even though the concentration field c and the surface area are changing in space and time in this test case, N_c should be constant when there is no degradation $k = 0$. In this case only diffusion and advection on the surface, as well as surface-area changes are modulating the local concentration. This validation therefore demonstrates that our reparametrisation approach faithfully evolves the metric properties of the surface. The behaviour of the relative numerical errors for V and N_c over time are depicted in Fig. D.2 c.

D.6.3 Parameters used for numerical results

	$L_0/(2\pi\rho_0)$	ξ/γ	$\kappa/(\gamma l_c^2)$	$D\tau/l_c^2$	$k\tau$
Fig. 2.3 b / Fig. D.2	–	15	0	8	0
Fig. 2.3 c	–	10	0	0.3	0
Fig. 2.5 a	0.82	6	0	0.05	1.95
Fig. 2.5 b	0.95	6	0	0.05	1.95
Fig. 2.6 a	1.1	6	0.25	0.05	1.95
Fig. 2.6 c	2.5 / 1.1 / 2.5	6	0.25 / 0.25 / 0.8	0.05	1.95
Fig. D.3 a	–	5	0	–	–
Fig. D.3 b	2.5	–	0.15	–	–
Fig. D.3 c	–	2	0	4	0

Table D.1: Overview of parameters used for the numerical results presented in Chapter 2. The characteristic length for the sphere is its radius $l_c = R_0$, for the tubular surface the radius of the azimuthal cross-section $l_c = \rho_0$. The characteristic time-scale is given by $\tau = \eta_b/\gamma$. The triplet values are given with respect to the positions ‘top/middle/bottom’ of the images shown in Fig. 2.6 c. The enclosed volume spherical surfaces was set in all simulations to $V/R_0^3 = 4\pi/3$. On tubular surfaces the volume is implicitly fixed by fixing the aspect ratio L_0/ρ_0 . The Hill-coefficient m in Eq. (2.16) was in all simulations set to $m = 2$, such that $f(c_0) = c_0\partial_c f(c_0) = 1/2$. The surface viscosity ratio was in all simulations set to $\eta_s/\eta_b = 1$.

Appendix E

Active fluid dynamics on a sphere

In this appendix, we present additional information about the theoretical analysis of the self-organised active fluid dynamics on a sphere, which we have studied in Chapters 3 and 4.

First, in Section E.1, we introduce a range of intermediate results that were obtained during the nonlinear analysis of the active surface swimmer studied in Section 3.3. Then, in Section E.2, we provide supporting information for the analysis of the viscoelastic surface discussed in Chapter 4. In particular, we review general Lagrangian derivatives on curved surfaces and derive the covariant Jaumann derivative used to formulate viscoelastic constitutive relations in Section 4.1. Additionally, we present formal details of the analytic characterisation of the Jacobian derived in Section 4.2. Finally, in Section E.3, we develop spectral approaches used to obtain numerical solutions of the nonlinear tensor-valued differential equations that arose in Chapters 3 and 4.

E.1 Active surface swimmer

In this section, we provide further details related to the analysis of the active surface swimmer model discussed in Section 3.3.

In Section E.1.1, we present the explicit steady-state solutions used to approximate the propagation velocity of the swimmer. In Section E.1.2, we detail the center-manifold reduction that we have performed to identify the bifurcation class for the onset of spontaneous motion.

E.1.1 Steady-state solutions

Here, we present explicit steady-state solutions of the dynamic system Eqs. (3.42) and (3.43) for the concentration modes $c_{1,0}$ and $c_{2,0}$ together with the resulting propagation velocity u_0 introduced in Section 3.3.2. For convenience, we recall here the coefficients

$$V_l = \frac{R\xi}{(1 + 2l)R\eta_+ - \delta_{l,1}R\eta_+ + l(l + 1)(\eta_b + \eta_s) - 2\eta_s}, \quad (\text{E.1})$$

which we have introduced in Section 3.3.2 as proportionality factors between concentration modes c_{lm} and velocity modes $v_{lm}^{(1)} = V_l c_{lm}/c_0$ (no summation). The steady state with polar asymmetry can be found by first dividing Eqs. (3.42) by $c_{1,0}$, which yields

$$\frac{c_{2,0}^{pol}}{c_0} = \sqrt{5\pi} \frac{2\frac{D}{R} - 2V_1 + Rk}{3V_2 - V_1}. \quad (\text{E.2})$$

The coefficients V_l are given in Eq. (E.1). Rearranging Eq. (3.43), one finds

$$\frac{c_{1,0}^{pol}}{c_0} = \pm \left(\frac{\sqrt{5\pi}R}{3V_1 c_0} \right)^{1/2} \left(6\frac{D}{R^2} c_{2,0}^{pol} - \frac{V_2 c_{2,0}^{pol}}{R c_0} \left(6c_0 + \frac{3}{7} \sqrt{\frac{5}{\pi}} c_{2,0}^{pol} \right) + k c_{2,0}^{pol} \right)^{1/2}, \quad (\text{E.3})$$

which, together with $c_{2,0}^{pol}$ given in Eq. (E.2), provides a closed steady-state solution for $c_{1,0}^{pol}$.

Note that additional steady-state solutions exist for the dynamic system Eqs. (3.42) and (3.43). Besides the the trivial homogeneous solutions $c_{1,0}^{hom} = c_{2,0}^{hom} = 0$, we also have a nematic steady state for which $c_{1,0}^{nem} = 0$ and

$$\frac{c_{2,0}^{nem}}{c_0} = \frac{7}{3} \sqrt{\frac{\pi}{5}} \frac{6\frac{D}{R} - 6V_2 + Rk}{V_2}, \quad (\text{E.4})$$

which directly follows from Eq. (3.43).

Propagation velocity

Using the proportionality of the concentration mode $c_{1,0}$ with the propagation velocity u_0 of the active surface swimmer, Eq. (3.40), one finds from Eqs. (E.2) and (E.3) the expression for u_0 given in Eq. (3.44), which we recall here for completeness:

$$\frac{|u_0|}{v_D} = \left(\frac{\text{Pe}}{\hat{\text{Pe}}_+^*} - 1 \right)^{1/2} (a\text{Pe} + b)^{1/2}. \quad (\text{E.5})$$

In this expression, $v_D = D/R$ represents a fixed characteristic velocity, $\text{Pe} = \xi R^2/(\eta_b D)$ is the Péclet number and $\hat{\text{Pe}}_+^* = 2(1 + R\eta_+/ \eta_b)$ is the critical Péclet number at which the mode $l = 1$ becomes unstable. The coefficients a and b are given by

$$a = -\frac{20}{3\alpha'} \frac{1}{1 + 4\nu + \frac{5}{2}\hat{\text{Pe}}_+^*} \left(1 + \frac{5}{7\alpha'} \right) \quad (\text{E.6})$$

$$b = \frac{20}{3\alpha'} \left(1 + \frac{5}{7\alpha'} \frac{\hat{\text{Pe}}_+^*}{1 + 4\nu + \frac{5}{2}\hat{\text{Pe}}_+^*} \right), \quad (\text{E.7})$$

where

$$\alpha' = 1 - 3 \frac{\hat{\text{Pe}}_+^*}{1 + 4\nu + \frac{5}{2}\hat{\text{Pe}}_+^*}. \quad (\text{E.8})$$

The parameter $\nu = \eta_s/\eta_b$ denotes the surface viscosity ratio.

Identifying the active surface swimmer as a puller

As briefly explained at the end of Section 3.3.2, microswimmers can be characterised as pullers and pushers based on the sign of the velocity mode $v_{2,0}^{(1)} > 0$. This velocity mode in turn is related to the concentration mode simply by $v_{2,0}^{(1)} = V_2 c_{2,0}/c_0$, where V_2 is just a positive prefactor given by Eq. (E.1) for $l = 2$. It therefore suffices to determine the sign of $c_{2,0}$ during steady-state motion. The corresponding solution $c_{2,0}^{pol}$ is given in Eq. (E.2). For the regime of external viscosities considered in Section 3.3, $R\eta_+ < 4\eta_s$, we have $3V_2 - V_1 < 0$. Parameters with which the mode $l = 1$ is unstable and translational motion spontaneously emerges, correspond to $D/R - V_1 < 0$. Hence, we see from Eq. (E.2) that $c_{2,0}^{pol} > 0$. This implies $v_{2,0}^{(1)} > 0$ and shows that the active surface swimmer introduced in this thesis indeed behaves as a puller [149]. Note that in the regime $R\eta_+ > 4\eta_s \Rightarrow 3V_2 - V_1 > 0$, for which the swimmer would have been characterised as a pusher, our numerical analysis does not yield physical steady states if the homogeneous state is unstable. This is due the singularities discussed at the end of Section 3.3.2 that likely arise from the unsaturated linear regulation of active tension.

E.1.2 Characterisation of the spontaneous onset of motion

Here, we describe the bifurcation analysis performed for the active surface swimmer in Section 3.3.3 in more detail. Recall that in this model, we identified a mechano-chemical instability on the surface of a sphere, where the harmonic mode $l = 1$ becomes unstable for an increasing Péclet number $Pe = \xi R^2/(\eta_b D)$ at the critical value \hat{Pe}_+ given in Eq. (3.37). Surface flows associated with this instability have a polar asymmetry and the mechanical interaction with a surrounding passive fluid leads to translational motion with steady-state propagation velocity u_0 relative to the laboratory frame.

Center-manifold

In order to extract the slow dynamics near the equilibrium point $(c_{1,0}, c_{2,0}) = (0, 0)$ of the dynamic system of Eqs. (3.42) and (3.43), we have to perform a center-manifold reduction [152]. In our system, this can be done analytically as follows.

First, we note that the polar and nematic mode coefficients $c_{1,0}$ and $c_{2,0}$ couple only according to their symmetry: Eq. (3.42), which describes the dynamics for the mode $l = 1$, only contains the ‘odd’ terms proportional to $c_{1,0}$ and to $c_{1,0}c_{2,0}$; Eq. (3.43) for the mode $l = 2$ contains only ‘even’ terms proportional to $c_{2,0}$ and $c_{1,0}^2$. Hence, we consider an ansatz for the center-manifold near $(c_{1,0}, c_{2,0}) = (0, 0)$ in the form

$$c_{2,0} = \bar{\alpha} \frac{c_{1,0}^2}{c_0}, \quad (\text{E.9})$$

where $\bar{\alpha}$ is coefficient that is determined in the next step. To this end, we take the time derivative of the ansatz Eq. (E.9) and use the dynamic Eqs. (3.42) and (3.43) to replace the time derivatives of $c_{1,0}$ and $c_{2,0}$. From this, we find a new equation

$$-6 \frac{D}{R^2} c_{2,0} - k c_{2,0} + \frac{3}{\sqrt{5\pi}} \frac{c_{1,0}^2 V_1}{c_0 R} + \frac{V_2 c_{2,0}}{R c_0} \left(6c_0 + \frac{3}{7} \sqrt{\frac{5}{\pi}} c_{2,0} \right) = 2\bar{\alpha} \frac{c_{1,0}}{c_0} \left(-2 \frac{D}{R^2} c_{1,0} - k c_{1,0} + \frac{2V_1 c_{1,0}}{R} + \frac{1}{\sqrt{5\pi}} \frac{c_{1,0} c_{2,0}}{R c_0} (3V_2 - V_1) \right). \quad (\text{E.10})$$

Eliminating $c_{2,0}$ by the ansatz Eq. (E.9) and neglecting terms $c_{1,0}^4$, we find

$$\bar{\alpha} = \frac{1}{\sqrt{5\pi}} \frac{3V_1}{2 \frac{D}{R} - kR + 4V_1 - 6V_2}. \quad (\text{E.11})$$

In the absence of turnover ($k = 0$), which was the case discussed in Section 3.3.3, we find for the concentration mode $c_{1,0}$ a closed dynamic equation near the point $(c_{1,0}, c_{2,0}) = (0, 0)$ in the form

$$\frac{d}{dt} \frac{c_{1,0}}{c_0} = 2 \left(\frac{V_1}{R} - \frac{D}{R^2} \right) \frac{c_{1,0}}{c_0} + \frac{1}{5\pi R} \frac{3V_1 (3V_2 - V_1)}{2 \frac{D}{R} + 4V_1 - 6V_2} \left(\frac{c_{1,0}}{c_0} \right)^3. \quad (\text{E.12})$$

Here, we have used the ansatz Eq. (E.9) with the explicit form of the coefficient Eq. (E.11) directly in the dynamic Eq. (3.42) for the concentration mode $c_{1,0}$. Equation (E.12) describes a pitchfork bifurcation. The coefficient of the cubic term evaluated at the critical Péclet number $\text{Pe} = \hat{\text{Pe}}_+^*$ yields the expression for $\bar{\alpha}$ given in Eq. (3.50), where we have used $\text{Pe} = \xi R^2 / (\eta_b D)$, $\hat{\text{Pe}}_+^* = 2(1 + R\eta_+ / \eta_b)$, $\nu = \eta_s / \eta_b$ and the coefficients V_l given in Eq. (E.1).

E.2 Active viscoelastic surface theory

In this section, we provide further details and derivations related to the viscoelastic active surface model studied in Chapter 4.

First, in Section E.2.1, we derive the general Lagrangian derivative D/Dt of vector and tensor fields on curved surfaces. The corresponding derivation cannot be found readily in the literature and is therefore presented and discussed in greater detail. We also show that the metric tensor does not commute with D/Dt , which gives rise to ambiguities when defining constitutive relations for viscoelastic materials. In Section E.2.2, we provide details about the analytic characterisation of the Jacobian \mathbf{J}_{el}^l derived in Section 4.2.1. In particular, we derive the critical Maxwell time τ_M^* presented Section 4.2.2 and we verify that the dispersion relation for a viscous surface can be recovered from the Jacobian in the limit $\tau_M \rightarrow 0$.

E.2.1 Lagrangian derivative on curved surfaces

In this section, we introduce the Lagrangian derivative on curved and deforming surfaces. We first explain how this derivative can be determined for geometric quantities that are defined

by the surface parametrisation. We then define the Lagrangian derivative for a general tensor field. From this definition, we derive explicit representations of Lagrangian derivatives on curved and deforming surfaces and show that they are equivalent to the Oldroyd formula [169] even if the surface is deforming. Finally, we show that the covariant Jaumann derivative, used in Section 4.1 to formulate constitutive equations of a viscoelastic surface, corresponds to a symmetrised Lagrangian derivative.

Lagrangian derivatives of geometric quantities

We first introduce the Lagrangian derivative D/Dt of geometric quantities that are defined by a surface parametrisation $\mathbf{X}(s^1, s^2, t)$, such as the metric tensor, the curvature tensor or basis vectors.

In the first step, one has to compute the variation of the corresponding vector or tensor field under a general shape variation $\delta\mathbf{X} = \delta X^i \mathbf{e}_i + \delta X_n \mathbf{n}$. An explicit expression for D/Dt is then given for $\delta\mathbf{X} = \mathbf{v}dt$, where \mathbf{v} is the local velocity of surface area elements. For example, from $\delta\mathbf{e}_i = \nabla_i \delta\mathbf{X}$ it then follows that the Lagrangian derivative of a covariant basis vector is given by

$$\frac{D}{Dt} \mathbf{e}_i = \left(\nabla_i v^j + C_i^j v_n \right) \mathbf{e}_j + \left(\nabla_i v_n - C_{ij} v^j \right) \mathbf{n}. \quad (\text{E.13})$$

Applying the same procedure to the metric tensor g^{ij} and to the curvature tensor C_i^j , we find

$$\frac{D}{Dt} g^{jk} = - \left(\nabla^j v^k + \nabla^k v^j + 2C^{jk} v_n \right) \quad (\text{E.14})$$

$$\frac{D}{Dt} C_i^j = - \nabla_i \nabla^j v_n - C_{ik} C^{kj} v_n + v^k \nabla_k C_i^j + C_k^j \nabla_i v^k - C_i^k \nabla_k v^j, \quad (\text{E.15})$$

which are two additional relations that are required in the following derivations. Equation (E.14) implies that the metric tensor does not commute with the Lagrangian derivative. This gives rise to an ambiguity when defining constitutive relations using D/Dt , which is discussed in Section E.2.1.

Lagrangian derivative of general vector and tensor fields

The component representation of the Lagrangian derivative of a general tangential vector field $\mathbf{p}_{\parallel} = p_i \mathbf{e}^i$ is determined by

$$\begin{aligned} \frac{D}{Dt} p_i &= \frac{D}{Dt} \left(\mathbf{p}_{\parallel} \cdot \mathbf{e}_i \right) \\ &= \mathbf{e}_i \cdot \frac{D}{Dt} \mathbf{p}_{\parallel} + \mathbf{p}_{\parallel} \cdot \frac{D}{Dt} \mathbf{e}_i. \end{aligned} \quad (\text{E.16})$$

To evaluate the first term of Eq. (E.16), we use the Lagrangian derivative of a scalar field – the classical *convected time derivative* – given by

$$\frac{D}{Dt}c = \partial_t c + v^k \nabla_k c, \quad (\text{E.17})$$

which yields

$$\begin{aligned} \frac{D}{Dt}\mathbf{P}_{\parallel} &= \partial_t \mathbf{P}_{\parallel} + v^k \nabla_k \mathbf{P}_{\parallel} \\ &= \mathbf{e}^i \partial_t p_i - p_i (\mathbf{e}_j C^{ij} v_n + \mathbf{n} \nabla^i v_n) + v^k (\mathbf{e}^i \nabla_k p_i - p_i C_k^i \mathbf{n}). \end{aligned} \quad (\text{E.18})$$

Here, we have additionally used Eq. (A.54) to evaluate the partial derivative $\partial_t \mathbf{e}^i$. To evaluate the second term in Eq. (E.16), we use Eq. (E.13). Taking everything together, we find

$$\frac{D}{Dt}p_i = \partial_t p_i + v^k \nabla_k p_i + p_j \nabla_i v^j. \quad (\text{E.19})$$

This is the general Lagrangian derivative of a vector field. Note that Eq. (E.19) does not contain explicit contributions from surface deformations v_n .

For a tensor field with $\mathbf{t} = t_{ij} \mathbf{e}^i \mathbf{e}^j$, a similar calculation yields

$$\begin{aligned} \frac{D}{Dt}t_{ij} &= \frac{D}{Dt}(\mathbf{e}_i \cdot \mathbf{t} \cdot \mathbf{e}_j) \\ &= \partial_t t_{ij} + v^k \nabla_k t_{ij} + t_{kj} \nabla_i v^k + t_{ik} \nabla_j v^k. \end{aligned} \quad (\text{E.20})$$

From this result, we can also determine the Lagrangian derivative of a tensor in mixed coordinates

$$\begin{aligned} \frac{D}{Dt}t_i^j &= t_{ik} \frac{D}{Dt}g^{jk} + g^{jk} \frac{D}{Dt}t_{ik} \\ &= \partial_t t_i^j + v^k \nabla_k t_i^j + t_k^j \nabla_i v^k - t_i^k \nabla_k v^j, \end{aligned} \quad (\text{E.21})$$

where we have used Eq. (E.14), as well as the relation $g^{jk} \partial_t t_{ik} = \partial_t t_i^j + 2t_{ik} C^{jk} v_n$ that follows from Eq. (A.44) with $\delta X_n = v_n dt$. Similarly, we find

$$\frac{D}{Dt}t^{ij} = \partial_t t^{ij} + v^k \nabla_k t^{ij} - t^{kj} \nabla_k v^i - t^{ik} \nabla_k v^j. \quad (\text{E.22})$$

Equations (E.20) and (E.22) in Euclidean space¹ correspond to the *lower and upper convected derivatives* [114]. The derivation shown here can be easily generalised to higher order tensors. In this case, one recovers the Oldroyd formula [169], even though the derivation here is more general in that it allows for the surface to change its shape. As a consistency check one can

¹None of the steps in this derivation depend on the dimensionality of the underlying space. We can therefore also consider a parametrisation $\mathbf{X}_{3D}(x, y, z) = x\mathbf{e}_x + y\mathbf{e}_y + z\mathbf{e}_z$ and would formally arrive at the same results as given in Eqs. (E.20)-(E.22) with $i, j, k \rightarrow \alpha, \beta, \gamma$.

verify that for $t_i^j = C_i^j$, Eq. (E.21) is equivalent to Eq. (E.15), where the latter was derived from explicitly varying the curvature tensor.

Determining the convected corotational derivative

The property of Lagrangian derivatives to evaluate dynamic changes in a comoving frame is used to formulate constitutive relations for a viscoelastic material, where it ensures that the relaxation of elastic stresses is described in the material reference frame.

To recover the covariant form of the Jaumann derivative \bar{D}/Dt given in Eq. (4.3) from a general Lagrangian derivative D/Dt , we use the latter for tensors in mixed coordinates Eq. (E.21). This particular choice over Eqs. (E.20) and (E.22) is motivated below. Equation (E.21) can be written as

$$\begin{aligned} \frac{D}{Dt}t_i^j &= \partial_t t_i^j + v^k \nabla_k t_i^j + \omega_n \left(\epsilon_{ik} t^{s,jk} + \epsilon^{jk} t_{ik}^s \right) \\ &+ \frac{1}{2} \epsilon^{lm} t_{lm} \left(\epsilon_{ki} v_{\parallel}^{jk} + \epsilon^{kj} v_{\parallel,ik} \right) + \epsilon^j_i \epsilon^l_m t_{lk}^s v_{\parallel}^{km}. \end{aligned} \quad (\text{E.23})$$

Here, we have used the vorticity ω_n defined in Eq. (C.27) and introduced the symmetric part of the in-plane strain rate tensor $v_{\parallel,ij} = (\nabla_i v_j + \nabla_j v_i)/2$, as well as the symmetrised tensor $t_{ij}^s = (t_{ij} + t_{ji})/2$. In general, it can be shown that rotational invariance of the system only fixes the vorticity terms in Eq. (E.23) [114], leading to the covariant form of the Jaumann derivative used in Chapter 4. The most general form of the Lagrangian derivative derived here also contains contributions from the antisymmetric part of the tensor t_{ij} , as well as a purely antisymmetric term (first and second term in the second line of Eq. (E.23), respectively). Because we do not consider chiral surfaces, we have $\epsilon^{lm} t_{lm} = 0$. Interestingly, the purely antisymmetric term in Eq. (E.23) cannot be excluded based on first principles. The covariant form of the Jaumann derivative used in Chapter 4 therefore corresponds to the symmetric part of the Lagrangian derivative given in Eq. (E.21), which can be written as

$$\frac{\bar{D}}{Dt}t_i^j = \frac{1}{2} \left(\delta_i^k \frac{D}{Dt}t_k^j + \delta_k^j \frac{D}{Dt}t_i^k \right). \quad (\text{E.24})$$

Why did we choose the Lagrangian derivative D/Dt for mixed tensors Eq. (E.21)? Constitutive relation defined for t_{ij} using Eq. (E.20) or defined in terms of t_i^j using Eq. (E.21) are in general not equivalent, because the metric tensor g_{ij} does not commute with the Lagrangian derivative D/Dt .¹ This was already noted by *Oldroyd* in 1950, who pointed out that this gives rise to a family of possible constitutive relations for Maxwell- and Kelvin-Voigt-type viscoelastic materials [169]. The choice of Eq. (E.21) is motivated by the trace-conserving property of this Lagrangian derivative. Taking the trace of the constitutive relation for the

¹Note that for this discussion it is not relevant if we consider symmetrised forms of Lagrangian derivatives or not.

elastic tension given in Eq. (4.2) and using $\frac{D}{Dt}\delta_i^j = 0$, which follows from Eq. (E.21), we find

$$\left(1 + \tau_M \frac{\bar{D}}{Dt}\right) t_k^k = 2\eta_b v_k^k, \quad (\text{E.25})$$

where we have dropped the superscript ‘el’ on the tension tensor used in Chapter 4 for brevity. Subtracting Eq. (E.25) from Eq. (4.2) leads to

$$\left(1 + \tau_M \frac{\bar{D}}{Dt}\right) \left(t_i^j - \frac{1}{2} t_k^k \delta_i^j\right) = 2\eta_s v_i^j. \quad (\text{E.26})$$

Hence, in this formulation the traceless symmetric part of t_{ij} is exclusively connected to the shear deformations of the surface. This is not the case for a constitutive relation in terms of ‘lower indices’ $\left(1 + \tau_M \frac{D}{Dt}\right) t'_{ij} = 2\eta_s(v_{ij} - v_k^k g_{ij}/2) + \eta_b v_k^k g_{ij}$: Taking the trace of this expression leads according to Eqs. (E.14) to

$$\left(1 + \tau_M \frac{D}{Dt}\right) t'^k_k = 2 \left(\eta_b v_k^k + \tau_M t'_{ij} \nabla^i v^j\right). \quad (\text{E.27})$$

In this scalar valued equation, isotropic and anisotropic contributions of the tension tensor are now getting mixed and hence are no longer independent.

E.2.2 Analysis of the Jacobian

Here, we provide a more detailed analysis of the Jacobian \mathbf{J}_{el}^l derived in Section 4.2, which we have used to analyse the linear stability of the homogeneous state on an isotropic, viscoelastic active surface.

The explicit form of \mathbf{J}_{el}^l can be read off from Eqs. (4.23) and (4.24), which yields

$$\mathbf{J}_{\text{el}}^l = \begin{pmatrix} -\frac{1}{\tau_M} + \frac{1}{R\tau_M} \frac{\eta_s[2-l(l+1)] - \eta_b l(l+1)}{\eta_-(1+2l)} & \frac{1}{R\tau_M} \frac{\eta_s[2-l(l+1)] - \eta_b l(l+1)}{\eta_-(1+2l)} \xi \partial_c f(c_0) \\ \frac{l(l+1)}{\eta_-(1+2l)} \frac{c_0}{R} & -\frac{D}{R^2} l(l+1) - k + \frac{l(l+1)}{\eta_-(1+2l)} \frac{c_0}{R} \xi \partial_c f(c_0) \end{pmatrix}. \quad (\text{E.28})$$

We see from Eq. (E.28), that the eigenvalues of \mathbf{J}_{el}^l are smaller than zero for $\xi = 0$. Hence, the homogeneous state is stable in the absence of active stress.

To study the case $\xi > 0$, it is convenient to first non-dimensionalise the linear system Eqs. (4.23) and (4.24). For this, we chose a characteristic time scale τ_D , and a characteristic tension η_b/τ_D and concentration c_0 . The Jacobian Eq. (E.28) then takes the form

$$\tilde{\mathbf{J}}_{\text{el}}^l = \begin{pmatrix} -\frac{1}{\tilde{\tau}_M} [1 + \Pi_1(l)] & -\frac{1}{\tilde{\tau}_M} \Pi_1(l) \text{Pe } c_0 \partial_c f(c_0) \\ \Pi_2(l) & -l(l+1) - \tilde{k} + \Pi_2(l) \text{Pe } c_0 \partial_c f(c_0) \end{pmatrix}, \quad (\text{E.29})$$

where $\text{Pe} = R^2\xi/(\eta_b D)$ is the Péclet number and we have defined

$$\Pi_1(l) = \tilde{L}_h \frac{\nu [l(l+1) - 2] + l(l+1)}{1 + 2l} \quad (\text{E.30})$$

$$\Pi_2(l) = \tilde{L}_h \frac{l(l+1)}{1 + 2l}, \quad (\text{E.31})$$

and introduced dimensionless parameters: the Maxwell relaxation time $\tilde{\tau}_M = \tau_M/\tau_D$ ($\tau_D = R^2/D$), the turnover rate $\tilde{k} = \tau_D k$, the surface viscosity ratio $\nu = \eta_s/\eta_b$, and the hydrodynamic length $\tilde{L}_h = \eta_s/(R\eta - \nu)$.

Linear stability analysis and derivation of the critical Maxwell time

In order to derive the critical Maxwell τ_M^* presented in Section 4.2.2 from the Jacobian Eq. (E.29), we analyse its determinant and trace following [135]. From Eq. (E.29), we can read off:

$$\tilde{\tau}_M \det(\tilde{\mathbf{J}}_{\text{el}}^l) = [1 + \Pi_1(l)] (l(l+1) + \tilde{k}) - \Pi_2(l) \text{Pe } c_0 \partial_c f(c_0) \quad (\text{E.32})$$

$$\text{tr}(\tilde{\mathbf{J}}_{\text{el}}^l) = -\frac{1}{\tilde{\tau}_M} [1 + \Pi_1(l)] - l(l+1) - \tilde{k} + \Pi_2(l) \text{Pe } c_0 \partial_c f(c_0). \quad (\text{E.33})$$

We first determine the scaling of eigenvalues of $\tilde{\mathbf{J}}_{\text{el}}^l$ for $l \rightarrow \infty$ to ensure the one-component description used in Chapter 4 is well-defined for the cases studied in this thesis. We have from their definitions, Eqs. (E.30) and (E.31), the scaling $\Pi_1(l), \Pi_2(l) \sim l$. Therefore, determinant and trace scale as $\det(\tilde{\mathbf{J}}_{\text{el}}^l) \sim l^3$ and $\text{tr}(\tilde{\mathbf{J}}_{\text{el}}^l) \sim -l^2$ for $l \rightarrow \infty$. This implies that the eigenvalues of $\tilde{\mathbf{J}}_{\text{el}}^l$ have negative real part $l \rightarrow \infty$ [135] and small wavelengths are always stable.

We now derive the detailed stability properties presented in Section 4.2.2. For parameters at which the determinant becomes negative with a negative trace, a stationary instability occurs [135]. For the Jacobian \mathbf{J}_{el}^l this implies the following. From Eq. (E.32), we find that the determinant vanishes at

$$\text{Pe}_l^{\text{si}} = \frac{1 + \Pi_1(l)}{\Pi_2(l) c_0 \partial_c f(c_0)} (l(l+1) + \tilde{k}) \quad (\text{E.34})$$

and is negative for $\text{Pe} > \text{Pe}_l^{\text{si}}$. We study this model in the regime where the mode $l = 1$ becomes unstable first, when the Péclet number Pe is increased up to a critical value. Evaluating the right-hand side of Eq. (E.34) for $l = 1$ with $\Pi_1(l)$ and $\Pi_2(l)$ defined in Eqs. (E.30) and (E.31), respectively, we find $\text{Pe}_1^{\text{si}} = \text{Pe}_-^*$, where Pe_-^* is the critical Péclet number found previously for the viscous active surface (Eq. (3.32)). The trace Eq. (E.33) is smaller than zero at the Péclet number given in Eq. (E.34) if

$$\tilde{\tau}_M < \frac{1 + \Pi_1(l)}{\Pi_1(l) [l(l+1) + \tilde{k}]}. \quad (\text{E.35})$$

In this regime (the determinant becoming negative at a negative trace), the homogeneous state undergoes a stationary instability [135] for increasing Péclet number at $\text{Pe} = \text{Pe}_1^{\text{si}} = \text{Pe}_-^*$. The expression on the right-hand side of Eq. (E.35) defines for each mode l a critical Maxwell time

$$\tau_{M,l}^* = \frac{\frac{R\eta_-(2l+1)}{\eta_s[2-l(l+1)]+\eta_b l(l+1)} + 1}{l(l+1)\frac{D}{R^2} + k}, \quad (\text{E.36})$$

which yields for $l = 1$ the critical Maxwell time $\tau_{M,1}^* = \tau_M^*$ discussed in Section 4.2.2 and given by

$$\tau_M^* = \frac{\frac{3}{2}\frac{R\eta_-}{\eta_b} + 1}{2\frac{D}{R^2} + k}. \quad (\text{E.37})$$

For parameters at which the trace becomes positive with a positive determinant, the homogeneous state undergoes an oscillatory instability [135]. To identify the regime in which such a transition can take place on the viscoelastic active surface, we first note that the trace Eq. (E.33) vanishes for

$$\text{Pe}_l^{\text{oi}} = \frac{1}{\Pi_2(l)c_0\partial_c f(c_0)} \left(l(l+1) + \tilde{k} + \frac{1}{\tilde{\tau}_M} [1 + \Pi_1(l)] \right) \quad (\text{E.38})$$

and it is positive for $\text{Pe} > \text{Pe}_l^{\text{oi}}$. Furthermore, the determinant is positive at $\text{Pe} = \text{Pe}_l^{\text{oi}}$ if $\tau_M > \tau_M^*$ with τ_M^* given in Eq. (E.37). In the regime, where the mode $l = 1$ becomes unstable first, the relevant critical Péclet number is Pe_1^{oi} , which we denoted as Pe_{oi}^* in Chapter 4 (Eq. (4.26)). For Maxwell times with $\tau_M > \tau_M^*$, it follows that an oscillatory instability occurs for increasing Péclet numbers at $\text{Pe} = \text{Pe}_{\text{oi}}^*$. This transition of a stable homogeneous state to an oscillatory unstable one is depicted by the dark blue line in the stability diagram Fig. 4.1.

Dispersion relation in the limit $\tau_M \rightarrow 0$

As an additional consistency check, we can verify that in the limit $\tau_M \rightarrow 0$ the Jacobian Eq. (E.29), or equivalently the linear dynamic system Eqs. (4.23) and (4.24), can be mapped to the dispersion relation found for a purely viscous surface. In the viscous limit, we have $\tau_M \frac{d}{dt} \delta \tilde{t}_{lm}^{(1)} = 0$, such that the dynamic equation for $\delta \tilde{t}_{lm}^{(1)}$, Eq. (4.23), implies

$$\frac{\tau_D}{\eta_b} \delta \tilde{t}_{lm}^{(1)} = -\frac{\Pi_1(l)}{1 + \Pi_1(l)} \text{Pe} c_0 \partial_c f(c_0) \frac{\delta c_{lm}}{c_0}, \quad (\text{E.39})$$

where $\Pi_1(l)$ has been defined in Eq. (E.30). This can be plugged into the dynamic equation for the concentration modes, Eq. (4.24), which yields

$$\begin{aligned} \tau_D \frac{d}{dt} \delta c_{lm} &= \left[-l(l+1) - \tau_D k + \Pi_2(l) \left(1 - \frac{\Pi_1(l)}{1 + \Pi_1(l)} \right) \text{Pe} c_0 \partial_c f(c_0) \right] \delta c_{lm} \\ &= \left[-l(l+1) - \tau_D k + \frac{l(l+1) \text{Pe} c_0 \partial_c f(c_0)}{(1+2l)R\eta_-/\eta_b + l(l+1)(1+\nu) - 2} \right] \delta c_{lm}. \end{aligned} \quad (\text{E.40})$$

The expression in square brackets is indeed equivalent to the dispersion relation Eq. (3.27) derived for the viscous active surface.

E.3 Details of the numerical approach

In this section, we introduce the framework that we have developed to determine the non-linear dynamics of the active surface models analysed in Chapters 3 and 4. Our numerical approach builds on the corresponding linearised solutions, for which we had used expansions of the relevant variables in terms of scalar, vector and tensor spherical harmonics. Here, we explain how the remaining nonlinear terms can be projected onto the corresponding harmonics as well, which takes care of all spatial dependencies in the problem. This provides us with a spectral solution of the full nonlinear dynamics, in which we only have to solve a set of ordinary differential equations for the mode coefficients of the harmonic expansions. An additional advantage of this approach is that the interaction with shear forces from the external passive fluid can readily be included by using the analytic solution derived in Section B.2.

To introduce the framework, we proceed as follows. In Section E.3.1, we present a least-square procedure to project scalar functions onto harmonic modes and extend this idea to the case of tensor-valued fields on the sphere. This projection represents a key element that underlies our numerical approach to solve tensor-valued partial differential equations on the surface of a sphere. In Sections E.3.2 and E.3.3, we explain how this method is used to treat the nonlinearities in the models of the self-organised viscous and viscoelastic fluid on the sphere, respectively.

E.3.1 Least-square fitting of scalar and tensor spherical harmonics

Here, we introduce the basic ‘workhorse’ that underlies the numerical approach we have developed: A least square fitting framework that allows efficiently switching between the representation of tensor components on a sphere in real space and in the space of tensor spherical harmonics. This concept extends the least square approach that has been previously developed for scalar functions on a sphere [170]. Both, the scalar and the tensorial method, are explained in the following.

Harmonic projection of scalar fields

We consider a function $G(\xi_k)$ given at a number N_k of points $\xi_k = (\theta_k, \varphi_k)$ on the surface of a sphere. The goal is to find an expansion of $G(\xi_k)$ in terms of a finite number of scalar spherical harmonics as

$$G = \sum_{l=0}^{l_{\max}} \sum_{m=-l}^l g_{lm} Y_{lm} \quad (\text{E.41})$$

up to the mode number l_{\max} , which amounts to a total number of

$$N_l = (l_{\max} + 1)^2 \quad (\text{E.42})$$

harmonics modes. Finding the coefficients g_{lm} in this expansion can be generally formulated as a least-square minimisation problem [170]:

$$\min_{g_{lm} \in \mathbb{R}} \sum_{k=1}^{N_k} \left(G(\xi_k) - \sum_{l=0}^{l_{\max}} \sum_{m=-l}^l g_{lm} Y_{lm}(\xi_k) \right)^2. \quad (\text{E.43})$$

Taking the derivative of this expression with respect to the coefficients g_{lm} and setting it to zero yields a (typically under-determined) linear system

$$\sum_{l=0}^{l_{\max}} \sum_{m=-l}^l \sum_{k=1}^{N_k} Y_{lm}(\xi_k) Y_{l'm'}(\xi_k) g_{lm} = \sum_{k=1}^{N_k} Y_{l'm'}(\xi_k) G(\xi_k). \quad (\text{E.44})$$

The right-hand side of Eq. (E.44) defines a column vector \mathbf{G} of length N_l . We denote the column vector of the harmonic coefficients as $\mathbf{g} = \{g_{lm}\}^T$. Furthermore, we define a $N_k \times N_l$ matrix $(\mathbf{Y})_{k,(lm)} = Y_{lm}(\xi_k)$, such that the solution of Eq. (E.44) can be compactly written as

$$\mathbf{g} = \left[(\mathbf{Y}^T \cdot \mathbf{Y})^{-1} \cdot \mathbf{Y}^T \right] \cdot \mathbf{G}. \quad (\text{E.45})$$

The operator in squared brackets represents the pseudo-inverse of \mathbf{Y} , which only needs to be calculated once for a given set of points $\xi_k = (\theta_k, \varphi_k)$ and maximum mode number l_{\max} . Both have been held fixed for the simulation results discussed in this thesis.

Harmonic projection of tensor valued fields

We now generalise the least-square fitting of a scalar function to tensor valued functions on the sphere. For this, we consider tensor components of a traceless symmetric tensor $\tilde{Q}_{ij}(\xi_k)$ in covariant coordinates with respect to the parametrisation of the unit sphere (Section A.3.2). The values of $\tilde{Q}_{ij}(\xi_k)$ are given at the points $\xi_k = (\theta_k, \varphi_k)$ on the sphere. The goal is to determine coefficients $\{q_{lm}^{(1)}, q_{lm}^{(2)}\}$ in an expansion

$$\tilde{Q}_{ij} = \sum_{l=0}^{l_{\max}} \sum_{m=-l}^l \left(q_{lm}^{(1)} \Psi_{ij}^{(lm)} + q_{lm}^{(2)} \Phi_{ij}^{(lm)} \right), \quad (\text{E.46})$$

where $\Psi_{ij}^{(lm)}$ and $\Phi_{ij}^{(lm)}$ denote tensor spherical harmonics (Section B.1.3). The corresponding least-square minimisation problem can be written as

$$\min_{q_{lm}^{(1)}, q_{lm}^{(2)} \in \mathbb{R}} \left\{ \sum_k \left[\tilde{Q}_{ij}(\xi_k) - \sum_{l=0}^{l_{\max}} \sum_{m=-l}^l \left(q_{lm}^{(1)} \Psi_{ij}^{(lm)}(\xi_k) + q_{lm}^{(2)} \Phi_{ij}^{(lm)}(\xi_k) \right) \right] \right. \\ \left. \times \left[\tilde{Q}^{ij}(\xi_k) - \sum_{l=0}^{l_{\max}} \sum_{m=-l}^l \left(q_{lm}^{(1)} \Psi^{(lm),ij}(\xi_k) + q_{lm}^{(2)} \Phi^{(lm),ij}(\xi_k) \right) \right] \right\}, \quad (\text{E.47})$$

where the covariant contractions ensure that the product is always positive. Taking the derivative of this expression with respect to the expansion coefficients $q_{lm}^{(1)}$ and $q_{lm}^{(2)}$, we find

$$\sum_{k=1}^{N_k} \Psi^{(l'm'),ij}(\xi_k) \sum_{l=0}^{l_{\max}} \sum_{m=-l}^l \left(q_{lm}^{(1)} \Psi_{ij}^{(lm)}(\xi_k) + q_{lm}^{(2)} \Phi_{ij}^{(lm)}(\xi_k) \right) = \sum_{k=1}^{N_k} \Psi^{(l'm'),ij}(\xi_k) Q_{ij}(\xi_k) \quad (\text{E.48})$$

$$\sum_{k=1}^{N_k} \Phi^{(l'm'),ij}(\xi_k) \sum_{l=0}^{l_{\max}} \sum_{m=-l}^l \left(q_{lm}^{(1)} \Psi_{ij}^{(lm)}(\xi_k) + q_{lm}^{(2)} \Phi_{ij}^{(lm)}(\xi_k) \right) = \sum_{k=1}^{N_k} \Phi^{(l'm'),ij}(\xi_k) Q_{ij}(\xi_k). \quad (\text{E.49})$$

To avoid difficulties at the parametric poles $\theta_k \in \{0, \pi\}$, where some of the components $\Psi^{(lm),\theta\varphi}$ and $\Phi^{(lm),\theta\varphi}$ diverge, we simply omit values of \tilde{Q}_{ij} given at the pole coordinates from the least square approximation.¹

The right hand side of the system of equations (E.48) and (E.49) represents a column vector \mathbf{Q} of length $2(l_{\max} + 1)^2$, where l_{\max} is the maximum mode number we take into account for the numerical approximation. We then define the column vector of unknown coefficients $\mathbf{q} = \left(q_{lm}^{(1)}, q_{lm}^{(2)} \right)^T$, as well as a $2(l_{\max} + 1)^2 \times 2(l_{\max} + 1)^2$ matrix \mathbf{M} given by

$$\mathbf{M} = \begin{pmatrix} M_{\Psi} & M_{\Psi,\Phi} \\ M_{\Psi,\Phi}^T & M_{\Phi} \end{pmatrix}, \quad (\text{E.50})$$

¹The divergences are spurious artefacts of the parametrisation of the unit sphere, for which \mathbf{e}_φ vanishes and \mathbf{e}^φ becomes singular at the poles (see Eq (A.70)). Because of the latter, $\tilde{Q}_{\theta\varphi}$ vanishes at the poles. The potentially finite limit of the product $\tilde{Q}_{\theta\varphi} \mathcal{V}^{\theta\varphi,(lm)}$ would need to be determined by an additional interpolation step at the poles, if this point is included on the right-hand side of Eqs. (E.48) and (E.49). In fact, using simply all points away from the pole for the least-square procedure and determining the harmonic expansion of \tilde{Q}_{ij} , is itself sufficient to calculate the values of $\tilde{Q}_{\theta\varphi} \mathcal{V}^{(lm),\theta\varphi}$ at the poles, if needed.

with

$$\begin{aligned}
 (M_{\Psi})_{(l,m)(l',m')} &= \sum_{k=1}^{N_k} \Psi^{(l'm'),ij}(\xi_k) \Psi_{ij}^{(lm)}(\xi_k) \\
 &= 2 \sum_{k=1}^{N_k} \left(\Psi_{\theta\theta}^{(l'm')}(\xi_k) \Psi_{\theta\theta}^{(lm)}(\xi_k) + \Phi_{\theta\theta}^{(l'm')}(\xi_k) \Phi_{\theta\theta}^{(lm)}(\xi_k) \right) \quad (\text{E.51})
 \end{aligned}$$

$$\begin{aligned}
 (M_{\Phi})_{(l,m)(l',m')} &= \sum_{k=1}^{N_k} \Phi^{(l'm'),ij}(\xi_k) \Phi_{ij}^{(lm)}(\xi_k) \\
 &= (M_{\Psi})_{(l,m)(l',m')} \quad (\text{E.52})
 \end{aligned}$$

$$\begin{aligned}
 (M_{\Psi,\Phi})_{(l,m)(l',m')} &= \sum_{k=1}^{N_k} \Phi^{(l'm'),ij}(\xi_k) \Psi_{ij}^{(lm)}(\xi_k) \\
 &= 2 \sum_{k=1}^{N_k} \left(\Phi_{\theta\theta}^{(l'm')}(\xi_k) \Psi_{\theta\theta}^{(lm)}(\xi_k) - \Psi_{\theta\theta}^{(l'm')}(\xi_k) \Phi_{\theta\theta}^{(lm)}(\xi_k) \right). \quad (\text{E.53})
 \end{aligned}$$

With this, the expansion coefficients $\mathbf{q} = \left(q_{lm}^{(1)}, q_{lm}^{(2)} \right)^T$ can be determined from Eqs. (E.48) and (E.49) as

$$\mathbf{q} = \mathbf{M}^{-1} \cdot \mathbf{Q}. \quad (\text{E.54})$$

Similar to the pseudo-inverse of \mathbf{Y} used for scalar harmonic expansion (Eq. (E.45)), the matrix \mathbf{M}^{-1} only needs to be calculated once for a given set of points $\xi_k = (\theta_k, \varphi_k)$ and maximum mode number l_{\max} .

E.3.2 Viscous surface dynamics

In the following, we describe in detail how the numerical results presented in Sections 3.2 and 3.3 have been obtained. In both models, the concentration field c is the only dynamic variable and we have to solve the system of ordinary differential equations given in (3.23) for the harmonic concentration modes. To this end, the harmonic expansion coefficients of the advection term A_{lm} have to be computed, which is done as follows. For a given concentration field c , we first determine the coefficients f_{lm} for the stress-regulating function $f(c)$ defined in the harmonic expansion Eq. (3.17) using the least-square projection described in Sec. E.3.1. Analytic solutions for the resulting surface flows have been derived in Section 3.1.3 in terms of the harmonic expansion

$$v_i = \sum_{l,m} v_{lm}^{(1)} \Psi_i^{(lm)}, \quad (\text{E.55})$$

where $v_{lm}^{(1)}$ is given in Eq. (3.19). This solution also determines the solution of the interior and exterior passive fluid flow problem via Eqs. (B.54)–(B.57) for coefficients given in Eqs. (B.59)–(B.64) with $v_{lm}^{(2)} = v_{lm}^r = 0$.

In the next step, a representation of the nonlinear advection term in the space of spherical

harmonics is obtained from

$$\nabla_{\bar{S}} \cdot (c\mathbf{v}_{\parallel}) = \mathbf{v}_{\parallel} \cdot \nabla_{\bar{S}} c + c \nabla_{\bar{S}} \cdot \mathbf{v}_{\parallel}, \quad (\text{E.56})$$

where the derivatives on the right-hand side can be computed spectrally from

$$\nabla_{\bar{S}} c = \sum_{l,m} c_{lm} \Psi^{(lm)} \quad (\text{E.57})$$

$$\nabla_{\bar{S}} \cdot \mathbf{v}_{\parallel} = - \sum_{l,m} v_{lm}^{(1)} l(l+1) Y_{lm}. \quad (\text{E.58})$$

These identities follow directly from Eqs. (B.17), (B.28), and (B.29). This determines $\nabla_{\bar{S}} \cdot (c\mathbf{v}_{\parallel})$ via the simple chain rule Eq. (E.56). Finally, we compute the projection

$$A_{lm} = \frac{1}{R} \int_{\bar{S}} \nabla_{\bar{S}} \cdot (c\mathbf{v}_{\parallel}) Y_{lm} d\Omega, \quad (\text{E.59})$$

using the least-square procedure introduced in Section E.3.1. The dynamic equation of the stress regulator Eq. (3.23) can then be solved, for which we use the explicit Runge-Kutta (4,5) formula as implemented in Matlab [171].

E.3.3 Viscoelastic surface dynamics

In the following, we describe how the numerical results presented in Section 4.3 have been obtained. The dynamic equation of the concentration field, Eq. (4.4), is solved numerically in the same way as described Section E.3.2. The analytic solution for the surface flows needed for this approach is on the viscoelastic surface with an interior passive fluid given by

$$v_i = \sum_{l,m} v_{lm}^{(1)} \Psi_i^{(lm)} + v_{lm}^{(2)} \Phi_i^{(lm)} \quad (\text{E.60})$$

with

$$v_{lm}^{(1)} = \frac{t_{lm}^{(0)} + [2 - l(l+1)] t_{lm}^{(1)} + \xi f_{lm}}{2\eta_-(2l+1)} \quad (\text{E.61})$$

$$v_{lm}^{(2)} = \frac{[2 - l(l+1)] t_{lm}^{(2)}}{2\eta_-(l-1)}. \quad (\text{E.62})$$

The coefficients f_{lm} are defined as previously by a harmonic expansion of the stress-regulating function $f(c) = \sum_{l,m} f_{lm} Y_{lm}$. The velocity modes $v_{1,m}^{(2)}$ correspond to full body rotations and are set to zero.

The nonlinear dynamics of the viscoelastic tension tensor can be obtained as follows. We

represent the general viscoelastic tension tensor in terms of tensor spherical harmonics¹

$$t_{ij}^{\text{el}} = \sum_{l,m} \left(t_{lm}^{(0)} \eta_{ij}^{(lm)} + t_{lm}^{(1)} \Psi_{ij}^{(lm)} + t_{lm}^{(2)} \Phi_{ij}^{(lm)} \right). \quad (\text{E.63})$$

The general dynamics of the expansion coefficients in Eq. (E.63) is determined by

$$\frac{d}{dt} t_{lm}^{(0)} = -\frac{1}{\tau_M} t_{lm}^{(0)} - l(l+1) \frac{\eta_b}{\tau_M R} v_{lm}^{(1)} - D_{lm}^{(0)} \quad l \geq 0 \quad (\text{E.64})$$

$$\frac{d}{dt} t_{lm}^{(1)} = -\frac{1}{\tau_M} t_{lm}^{(1)} + \frac{2\eta_s}{\tau_M R} v_{lm}^{(1)} - D_{lm}^{(1)} \quad l \geq 2 \quad (\text{E.65})$$

$$\frac{d}{dt} t_{lm}^{(2)} = -\frac{1}{\tau_M} t_{lm}^{(2)} + \frac{2\eta_s}{\tau_M R} v_{lm}^{(2)} - D_{lm}^{(2)} \quad l \geq 2. \quad (\text{E.66})$$

The coefficients $D_{lm}^{(0)}$, $D_{lm}^{(1)}$ and $D_{lm}^{(2)}$ denote contributions from the nonlinear convected, corotational derivative and are defined by

$$D_{ij} = v^k \nabla_k t_{ij}^{\text{el}} + \omega_i^k t_{kj}^{\text{el}} + \omega_j^k t_{ki}^{\text{el}} \quad (\text{E.67})$$

$$= \sum_{l,m} \left(D_{lm}^{(0)} \eta_{ij}^{(lm)} + D_{lm}^{(1)} \Psi_{ij}^{(lm)} + D_{lm}^{(2)} \Phi_{ij}^{(lm)} \right). \quad (\text{E.68})$$

The remaining terms in Eqs. (E.64)–(E.66) are equivalent to the linearised expressions determined in Section 4.2.1.

The coefficients $D_{lm}^{(0)}$, required in Eq. (E.64) to determine the dynamics of $t_{lm}^{(0)}$, are related to the trace of D_{ij} . Taking the trace of Eq. (E.67), we see that the latter can be determined from

$$D_i^i = v^k \nabla_k t_i^{\text{el},i} = 2 \sum_{l,m} t_{lm}^{(0)} \mathbf{v}_{\parallel} \cdot \Psi^{(lm)}, \quad (\text{E.69})$$

where we have used $g^{ij} \eta_{ij}^{(lm)} = 2Y_{lm}$, $\Psi_i^{(lm)} = \partial_i Y_{lm}$ and $v^k \Psi_k^{(lm)} = \mathbf{v}_{\parallel} \cdot \Psi^{(lm)}$. The coefficients $D_{lm}^{(0)}$ are then given by

$$D_{lm}^{(0)} = \frac{1}{2} \int D_i^i Y_{lm} d\Omega, \quad (\text{E.70})$$

which is computed using the least-square approach introduced in Section E.3.1.

The coefficients $D_{lm}^{(1)}$ and $D_{lm}^{(2)}$ in Eq. (E.68) are related to the traceless symmetric part of D_{ij} and have contributions from the convected derivative and from corotational terms. In the following, we show how to determine $D_{lm}^{(1)}$ and $D_{lm}^{(2)}$ in our framework.

Contributions from the convected derivative to the coefficients $D_{lm}^{(1)}$ and $D_{lm}^{(2)}$

We now require the traceless part of the Maxwell tension tensor given by

$$\tilde{t}_{ij}^{\text{el}} = t_{ij}^{\text{el}} - \frac{1}{2} t_k^{\text{el},k} g_{ij} \quad (\text{E.71})$$

¹Tensor spherical harmonics are defined in Appendix B.1.3.

and first discuss contributions from $v^k \nabla_k \tilde{t}_{ij}^{\text{el}}$. To express them in terms of $t_{lm}^{(1)}$ and $t_{lm}^{(2)}$, we consider a representation of $\tilde{t}_{ij}^{\text{el}}$ in the embedding Euclidean space in the form $\tilde{\mathbf{t}}^{\text{el}} = \tilde{t}_{ij}^{\text{el}} \mathbf{e}^i \mathbf{e}^j$, which is given on the unit sphere by

$$\begin{aligned}
 \tilde{\mathbf{t}}^{\text{el}} &= \tilde{t}_{ij}^{\text{el}} \mathbf{e}^i \mathbf{e}^j \\
 &= \tilde{t}_{\theta\theta}^{\text{el}} \mathbf{e}^\theta \mathbf{e}^\theta + \tilde{t}_{\varphi\varphi}^M \mathbf{e}^\varphi \mathbf{e}^\varphi + \tilde{t}_{\theta\varphi}^{\text{el}} (\mathbf{e}^\theta \mathbf{e}^\varphi + \mathbf{e}^\varphi \mathbf{e}^\theta) \\
 &= \tilde{t}_{\theta\theta}^{\text{el}} \bar{\mathbf{e}}_\theta \bar{\mathbf{e}}_\theta + \tilde{t}_{\varphi\varphi}^{\text{el}} \bar{\mathbf{e}}_\varphi \bar{\mathbf{e}}_\varphi + \frac{\tilde{t}_{\theta\varphi}^{\text{el}}}{\sin \theta} (\bar{\mathbf{e}}_\theta \bar{\mathbf{e}}_\varphi + \bar{\mathbf{e}}_\varphi \bar{\mathbf{e}}_\theta) \\
 &= \tilde{t}_{\theta\theta}^{\text{el}} (\bar{\mathbf{e}}_\theta \bar{\mathbf{e}}_\theta - \bar{\mathbf{e}}_\varphi \bar{\mathbf{e}}_\varphi) + \frac{\tilde{t}_{\theta\varphi}^{\text{el}}}{\sin \theta} (\bar{\mathbf{e}}_\theta \bar{\mathbf{e}}_\varphi + \bar{\mathbf{e}}_\varphi \bar{\mathbf{e}}_\theta), \tag{E.72}
 \end{aligned}$$

where we have used $\mathbf{e}^\theta = \mathbf{e}_\theta = \bar{\mathbf{e}}_\theta$, $\mathbf{e}_\varphi = \sin \theta \bar{\mathbf{e}}_\varphi$ and $\{\bar{\mathbf{e}}_\theta, \bar{\mathbf{e}}_\varphi\}$ represents the tangential normalised standard basis of spherical coordinates. The prefactor in the second term is given by

$$\frac{\tilde{t}_{\theta\varphi}^{\text{el}}}{\sin \theta} = \sum_{l,m} \left(-t_{lm}^{(1)} \Phi_{\theta\theta}^{(lm)} + t_{lm}^{(2)} \Psi_{\theta\theta}^{(lm)} \right), \tag{E.73}$$

which follows from Eqs. (B.37) and (B.39). With this, we can compute $\tilde{\mathbf{t}}^{\text{el}}$ given by Eq. (E.72) as a 3x3 matrix in a Cartesian basis with components

$$\tilde{t}_{\alpha\beta}^{\text{el}} = \bar{\mathbf{e}}_\alpha \cdot \tilde{\mathbf{t}}^{\text{el}} \cdot \bar{\mathbf{e}}_\beta, \tag{E.74}$$

where $\alpha, \beta \in \{x, y, z\}$. Because Eq. (E.74) yields components of $\tilde{\mathbf{t}}^{\text{el}}$ with respect to the fixed Cartesian basis, the complete angular dependence of this tensor must be contained in the scalar coefficients $t_{\alpha\beta}(\theta, \varphi)$. Hence, we can represent $\tilde{\mathbf{t}}^{\text{el}}$ in terms of scalar spherical harmonics by

$$\tilde{\mathbf{t}}^{\text{el}} = \sum_{\alpha,\beta} \sum_{l,m} \bar{\mathbf{e}}_\alpha \bar{\mathbf{e}}_\beta t_{\alpha\beta}^{(lm)} Y_{lm}, \tag{E.75}$$

where the coefficients $t_{\alpha\beta}^{(lm)}$ are defined by the harmonic expansions of $t_{\alpha\beta}(\theta, \varphi)$ and determined using the least-square harmonic projection (Section E.3.1). Finally, we use the general definition of the covariant derivative of a tensor given by

$$\nabla_i t_{ij} = \mathbf{e}_i \cdot \partial_k \mathbf{t} \cdot \mathbf{e}_j. \tag{E.76}$$

For $\mathbf{t} = \tilde{\mathbf{t}}^{\text{el}}$ in the form Eq. (E.75), the partial derivative can be easily evaluated using $\partial_k Y_{lm} = \Psi_k^{(lm)}$. Therefore, we find for the convected derivative the representation

$$\begin{aligned} v^k \nabla_k \tilde{t}_{ij}^{\text{el}} &= \sum_{l,m} \left\{ t_{xx}^{(lm)} (\mathbf{e}_i)_x (\mathbf{e}_j)_x + t_{yy}^{(lm)} (\mathbf{e}_i)_y (\mathbf{e}_j)_y + t_{zz}^{(lm)} (\mathbf{e}_i)_z (\mathbf{e}_j)_z \right. \\ &\quad + t_{xy}^{(lm)} \left[(\mathbf{e}_i)_x (\mathbf{e}_j)_y + (\mathbf{e}_i)_y (\mathbf{e}_j)_x \right] \\ &\quad + t_{xz}^{(lm)} \left[(\mathbf{e}_i)_x (\mathbf{e}_j)_z + (\mathbf{e}_i)_z (\mathbf{e}_j)_x \right] \\ &\quad \left. + t_{yz}^{(lm)} \left[(\mathbf{e}_i)_y (\mathbf{e}_j)_z + (\mathbf{e}_i)_z (\mathbf{e}_j)_y \right] \right\} \mathbf{v}_{\parallel} \cdot \Psi^{(lm)}. \end{aligned} \quad (\text{E.77})$$

Here, we have used that $t_{\alpha\beta} = t_{\beta\alpha}$ by definition Eq. (E.72) and $(\mathbf{e}_i)_\alpha$ denotes the Cartesian components of the basis vectors on the sphere: $\mathbf{e}_\theta = \bar{\mathbf{e}}_\theta$ and $\mathbf{e}_\varphi = \sin\theta \bar{\mathbf{e}}_\varphi$. From Eqs. (E.72)–(E.77), we can obtain the covariant components of $v^k \nabla_k \tilde{t}_{ij}^{\text{el}}$ from the knowledge of the coefficients $t_{lm}^{(1)}$ and $t_{lm}^{(2)}$ without the need to evaluate explicit spatial derivatives on the surface.

Contributions from the corotational terms to the coefficients $D_{lm}^{(1)}$ and $D_{lm}^{(2)}$

Contributions of the corotational terms $\omega_i^k t_{kj}^{\text{el}} + \omega_j^k t_{ki}^{\text{el}}$ to \tilde{D}_{ij} are obtained as follows. Using the explicit form of the antisymmetric part of the strain rate tensor, $\omega_{ij} = (\nabla_i v_j - \nabla_j v_i)/2$, we first note that

$$\begin{aligned} \int \chi_{ij}^{(lm)} \omega^{ij} d\Omega &= \sum_{l',m'} \int Y_{lm} v_{l'm'}^{(2)} \epsilon^{ij} \nabla_i \Phi_j^{(l'm')} d\Omega \\ &= \sum_{l',m'} \int Y_{lm} v_{l'm'}^{(2)} \epsilon^{ij} \epsilon_j^k \nabla_i \nabla_k Y_{l'm'} d\Omega \\ &= \sum_{l',m'} \int Y_{lm} v_{l'm'}^{(2)} g^{ik} \nabla_i \nabla_k Y_{l'm'} d\Omega \\ &= -l(l+1) v_{(lm)}^{(2)}, \end{aligned} \quad (\text{E.78})$$

which corresponds to the projection of ω_{ij} onto the antisymmetric tensor harmonics $\chi_{ij}^{(lm)} = Y_{lm} \epsilon_{ij}$. We can therefore write $\omega_{ij} = \omega_n \epsilon_{ij}$ with

$$\omega_n = -\frac{1}{2} \sum_{lm} l(l+1) v_{(lm)}^{(2)} Y_{lm}. \quad (\text{E.79})$$

The factor 1/2 appears because $\chi_{ij}^{(lm)}$ is not normalised (see Eq. B.35). The remaining task is to determine the independent components of the contractions $\epsilon_i^k \tilde{t}_{kj}^{\text{el}}$. For the ‘ $\theta\theta$ ’ component,

we find

$$\begin{aligned}
 \left(\omega_i^k t_{kj}^{\text{el}} + \omega_j^k t_{ki}^{\text{el}} \right)_{\theta\theta} &= 2\omega_n \epsilon_\theta^\varphi \tilde{t}_{\varphi\theta}^{\text{el}} \\
 &= \frac{2\omega_n}{\sin\theta} \sum_{l,m} \left(t_{(lm)}^{(1)} \Psi_{\varphi\theta}^{(lm)} + t_{(lm)}^{(2)} \Phi_{\varphi\theta}^{(lm)} \right) \\
 &= \omega_n \sum_{l,m} \left(-2t_{(lm)}^{(1)} \Phi_{\theta\theta}^{(lm)} + 2t_{(lm)}^{(2)} \Psi_{\theta\theta}^{(lm)} \right) \tag{E.80}
 \end{aligned}$$

and the ‘ $\theta\varphi$ ’ component is given by

$$\begin{aligned}
 \left(\omega_i^k \tilde{t}_{kj}^{\text{el}} + \omega_j^k \tilde{t}_{ki}^{\text{el}} \right)_{\theta\varphi} &= \omega_n \epsilon_\theta^\varphi \tilde{t}_{\varphi\varphi}^{\text{el}} + \omega_n \epsilon_\varphi^{\theta} \tilde{t}_{\theta\theta}^{\text{el}} \\
 &= \sum_{l,m} \omega_n \left(-2t_{(lm)}^{(1)} \Phi_{\theta\varphi}^{(lm)} + 2t_{(lm)}^{(2)} \Psi_{\theta\varphi}^{(lm)} \right), \tag{E.81}
 \end{aligned}$$

where we have used $\epsilon_{\theta\varphi} = \sin\theta$, $\epsilon_\theta^\varphi = 1/\sin\theta$ and Eqs. (B.37)–(B.39). From Eqs. (E.79)–(E.81), we can numerically obtain the components of the corotational terms from the current knowledge of the coefficients $t_{lm}^{(1)}$ and $t_{lm}^{(2)}$ ($v_{lm}^{(2)}$ needed in Eq. (E.79) is given in Eq. (E.62)).

Therefore, we have completely determined D_{ij} given in Eq. (E.67). Finally, we use the least square projection for tensor spherical harmonics described in Section E.3.1 to compute $D_{lm}^{(1)}$ and $D_{lm}^{(2)}$, which are required to determine the dynamics of the coefficients $t_{lm}^{(1)}$ and $t_{lm}^{(2)}$ in Eqs. (E.65) and (E.66).

With this, we have determined all terms on the right-hand side of the dynamic Eqs. (E.64)–(E.66) for the tension tensor modes. These are solved together with the dynamic equation of the stress regulator Eq. (3.23) using the explicit Runge-Kutta (4,5) formula as implemented in Matlab [171].

Bibliography

- [1] D. W. Thompson. *On Growth and Form*. Cambridge University Press (1992)
- [2] A. M. Turing. The Chemical Basis of Morphogenesis. *Philos. Trans. Royal Soc. B*, **237**(641): 37–72 (1952)
- [3] M. C. Marchetti, J. F. Joanny, S. Ramaswamy, T. B. Liverpool, J. Prost, M. Rao, and R. A. Simha. Hydrodynamics of soft active matter. *Rev. Mod. Phys.*, **85**: 1143–1189 (2013)
- [4] J. Prost, F. Jülicher, and J.-F. Joanny. Active gel physics. *Nat. Phys.*, **11**(2): 111–117 (2015)
- [5] F. Jülicher, S. W. Grill, and G. Salbreux. Hydrodynamic theory of active matter. *Rep. Prog. Phys.*, **81**(7) (2018)
- [6] D. A. Fletcher and P. L. Geissler. Active Biological Materials. *Annu. Rev. Phys. Chem.*, **60**: 469–486 (2009)
- [7] R. S. Fischer and V. M. Fowler. Thematic Minireview Series: The State of the Cytoskeleton in 2015. *J. Biol. Chem.*, **290**(28): 17133–17136 (2015)
- [8] P. Chugh, A. G. Clark, M. B. Smith, D. A. D. Cassani, K. Dierkes, A. Ragab, P. P. Roux, G. Charras, G. Salbreux, and E. K. Paluch. Actin cortex architecture regulates cell surface tension. *Nat. Cell Biol.*, **19**(6): 689–697 (2017)
- [9] B. Alberts, A. Johnson, J. Lewis, M. Raff, K. Roberts, and P. Walter. *Molecular Biology of the Cell*. Garland Science (2007)
- [10] M. J. Footer, J. W. J. Kerssemakers, J. A. Theriot, and M. Dogterom. Direct measurement of force generation by actin filament polymerization using an optical trap. *Proc. Natl. Acad. Sci. U.S.A.*, **104**(7): 2181–2186 (2007)
- [11] T. D. Pollard and G. G. Borisy. Cellular motility driven by assembly and disassembly of actin filaments. *Cell*, **112**(4): 453 – 465 (2003)
- [12] G. Salbreux, G. Charras, and E. Paluch. Actin cortex mechanics and cellular morphogenesis. *Trend. Cell. Biol.*, **22**(10): 536–545 (2012)
- [13] A. Saha, M. Nishikawa, M. Behrndt, C.-P. Heisenberg, F. Jülicher, and S. W. Grill. Determining Physical Properties of the Cell Cortex. *Biophys. J.*, **110**(6): 1421–1429 (2016)
- [14] K. Murthy and P. Wadsworth. Myosin-ii-dependent localization and dynamics of f-actin during cytokinesis. *Curr. Biol.*, **15**(8): 724 – 731 (2005)
- [15] M. Guha, M. Zhou, and Y.-l. Wang. Cortical Actin Turnover during Cytokinesis Requires Myosin II. *Curr. Biol.*, **15**(8): 732–736 (2005)
- [16] E. M. Reichl, Y. Ren, M. K. Morphew, M. Delannoy, J. C. Effler, K. D. Girard, S. Divi, P. A. Iglesias, S. C. Kuo, and D. N. Robinson. Interactions between myosin and actin crosslinkers control cytokinesis contractility dynamics and mechanics. *Curr. Biol.*, **18**(7): 471–480 (2008)
- [17] B. Fabry, G. N. Maksym, J. P. Butler, M. Glogauer, D. Navajas, and J. J. Fredberg. Scaling the microrheology of living cells. *Phys. Rev. Lett.*, **87**: 148102 (2001)
- [18] M. Balland, N. Desprat, D. Icard, S. Féréol, A. Asnacios, J. Browaeys, S. Hénon, and F. m. c. Gallet. Power laws in microrheology experiments on living cells: Comparative analysis and modeling. *Phys. Rev. E*, **74**: 021911 (2006)
- [19] D. Humphrey, C. Duggan, D. Saha, D. Smith, and J. Käs. Active fluidization of polymer networks through molecular motors. *Nature*, **416**(6879): 413–416 (2002)
- [20] L. Le Goff, F. m. c. Amblard, and E. M. Furst. Motor-driven dynamics in actin-myosin networks. *Phys. Rev. Lett.*, **88**: 018101 (2001)

- [21] D. Needleman and Z. Dogic. Active matter at the interface between materials science and cell biology. *Nat. Rev. Mater.*, **2**(9): 17048 (2017)
- [22] M. Murrell, P. W. Oakes, M. Lenz, and M. L. Gardel. Forcing cells into shape: the mechanics of actomyosin contractility. *Nat. Rev. Mol. Cell Biol.*, **16**(8): 486–498 (2015)
- [23] F. Jülicher, A. Ajdari, and J. Prost. Modeling molecular motors. *Rev. Mod. Phys.*, **69**: 1269–1282 (1997)
- [24] J. Howard. *Mechanics of Motor Proteins and the Cytoskeleton*. Sinauer Associates, Publishers (2001)
- [25] P. M. Bendix, G. H. Koenderink, D. Cuvelier, Z. Dogic, B. N. Koeleman, W. M. Briehner, C. M. Field, L. Mahadevan, and D. A. Weitz. A Quantitative Analysis of Contractility in Active Cytoskeletal Protein Networks. *Biophys. J.*, **94**(8): 3126–3136 (2008)
- [26] S. K. Vogel, Z. Petrasek, F. Heinemann, and P. Schwille. Myosin motors fragment and compact membrane-bound actin filaments. *eLife*, **2**: e00116 (2013)
- [27] A. Kumar, A. Maitra, M. Sumit, S. Ramaswamy, and G. V. Shivashankar. Actomyosin contractility rotates the cell nucleus. *Sci. Rep.*, **4**(1): 41 (2014)
- [28] H. Ennomani, G. Letort, C. Guérin, J.-L. Martiel, W. Cao, F. Nédélec, E. M. De La Cruz, M. Théry, and L. Blanchoin. Architecture and Connectivity Govern Actin Network Contractility. *Curr. Biol.*, **26**(5): 616–626 (2016)
- [29] M. Nishikawa, S. R. Naganathan, F. Jülicher, and S. W. Grill. Controlling contractile instabilities in the actomyosin cortex. *eLife*, **6**: e19595 (2017)
- [30] T. Hiraiwa and G. Salbreux. Role of turnover in active stress generation in a filament network. *Phys. Rev. Lett.*, **116**: 188101 (2016)
- [31] M. Mayer, M. Depken, J. S. Bois, F. Jülicher, and S. W. Grill. Anisotropies in cortical tension reveal the physical basis of polarizing cortical flows. *Nature*, **467**(7315): 617–621 (2010)
- [32] M. Bergert, A. Erzberger, R. A. Desai, I. M. Aspalter, A. C. Oates, G. Charras, G. Salbreux, and E. K. Paluch. Force transmission during adhesion-independent migration. *Nat. Cell Biol.*, **17**(4): 524–529 (2015)
- [33] A.-C. Reymann, F. Staniscia, A. Erzberger, G. Salbreux, and S. W. Grill. Cortical flow aligns actin filaments to form a furrow. *eLife*, **5**: e17807 (2016)
- [34] D. Bray and J. G. White. Cortical flow in animal cells. *Science*, **239**(4842): 883–888 (1988)
- [35] N. W. Goehring, P. K. Trong, J. S. Bois, D. Chowdhury, E. M. Nicola, A. A. Hyman, and S. W. Grill. Polarization of PAR Proteins by Advective Triggering of a Pattern-Forming System. *Science*, **334**(6059): 1137–1141 (2011)
- [36] S. R. Naganathan, S. Fürthauer, M. Nishikawa, F. Jülicher, and S. W. Grill. Active torque generation by the actomyosin cell cortex drives left-right symmetry breaking. *eLife*, **3**: e04165 (2014)
- [37] A. C. Callan-Jones, V. Ruprecht, S. Wieser, C. P. Heisenberg, and R. Voituriez. Cortical flow-driven shapes of nonadherent cells. *Phys. Rev. Lett.*, **116**: 028102 (2016)
- [38] R. Weinberg. *The Biology of Cancer*. Garland science (2013)
- [39] R. A. Green, E. Paluch, and K. Oegema. Cytokinesis in animal cells. *Annu. Rev. Cell Dev. Biol.*, **28**(1): 29–58 (2012)
- [40] A. G. Clark, O. Wartlick, G. Salbreux, and E. K. Paluch. Stresses at the Cell Surface during Animal Cell Morphogenesis. *Curr. Biol.*, **24**(10): R484–R494 (2014)
- [41] H. Turlier, B. Audoly, J. Prost, and J.-F. Joanny. Furrow constriction in animal cell cytokinesis. *Biophys. J.*, **106**(1): 114 – 123 (2014)
- [42] M. Stewart, J. Helenius, Y. Toyoda, S. Ramanathan, D. Muller, and A. Hyman. Hydrostatic pressure and the actomyosin cortex drive mitotic cell rounding. *Nature*, **469**(7329): 226–230 (2011)

- [43] O. M. Lancaster, M. Le Berre, A. Dimitracopoulos, D. Bonazzi, E. Zlotek-Zlotkiewicz, R. Picone, T. Duke, M. Piel, and B. Baum. Mitotic Rounding Alters Cell Geometry to Ensure Efficient Bipolar Spindle Formation. *Dev. Cell*, **25**(3): 270–283 (2013)
- [44] E. Fischer-Friedrich, A. A. Hyman, F. Julicher, D. J. Muller, and J. Helenius. Quantification of surface tension and internal pressure generated by single mitotic cells. *Sci. Rep.*, **4**(1): 137 (2014)
- [45] M. Théry and M. Bornens. Cell shape and cell division. *Curr. Opin. Cell Biol.*, **18**(6): 648 – 657 (2006)
- [46] D. A. Guertin, S. Trautmann, and D. McCollum. Cytokinesis in Eukaryotes. *Microbiol. Mol. Biol. Rev.*, **66**(2): 155–178 (2002)
- [47] W.-F. Hoku and R. D. N. Cytokinesis mechanics and mechanosensing. *Cytoskeleton*, **69**(10): 700–709 (2012)
- [48] R. Rappaport. Establishment of the mechanism of cytokinesis in animal cells. *Int. Rev. Cytol.*, **105**: 245–281 (1986)
- [49] J.-H. Zang and J. A. Spudich. Myosin ii localization during cytokinesis occurs by a mechanism that does not require its motor domain. *Proc. Natl. Acad. Sci. U.S.A.*, **95**(23): 13652–13657 (1998)
- [50] M. Zhou and Y.-l. Wang. Distinct Pathways for the Early Recruitment of Myosin II and Actin to the Cytokinetic Furrow. *Mol. Biol. Cell*, **19**(1): 318–326 (2008)
- [51] J. White and G. Borisy. On the mechanisms of cytokinesis in animal cells. *J. Theor. Biol.*, **101**(2): 289 – 316 (1983)
- [52] N. T. L. Rodrigues, S. Lekomtsev, S. Jananji, J. Kriston-Vizi, G. R. X. Hickson, and B. Baum. Kinetochore-localized PP1–Sds22 couples chromosome segregation to polar relaxation. *Nature*, **524**(7566): 489–492 (2015)
- [53] B. Mierzwa and D. W. Gerlich. Cytokinetic Abscission: Molecular Mechanisms and Temporal Control. *Dev. Cell*, **31**(5): 525–538 (2014)
- [54] S. Etienne-Manneville and A. Hall. Rho GTPases in cell biology. *Nature*, **420**(6916): 629–635 (2002)
- [55] C. M. Welch, H. Elliott, G. Danuser, and K. M. Hahn. Imaging the coordination of multiple signalling activities in living cells. *Nat. Rev. Mol. Cell Biol.*, **12**(11): 749–756 (2011)
- [56] M. Werner, E. Munro, and M. Glotzer. Astral signals spatially bias cortical myosin recruitment to break symmetry and promote cytokinesis. *Curr. Biol.*, **17**(15): 1286–1297 (2007)
- [57] J. Betschinger and J. A. Knoblich. Dare to Be Different: Asymmetric Cell Division in *Drosophila*, *C. elegans* and Vertebrates. *Curr. Biol.*, **14**(16): R674–R685 (2004)
- [58] P. Gross, K. V. Kumar, and S. W. Grill. How active mechanics and regulatory biochemistry combine to form patterns in development. *Annu. Rev. Biophys.*, **46**(1): 337–356 (2017)
- [59] B. Goldstein and I. G. Macara. The PAR Proteins: Fundamental Players in Animal Cell Polarization. *Dev. Cell*, **13**(5): 609–622 (2007)
- [60] B. Goldstein and S. Hird. Specification of the anteroposterior axis in *Caenorhabditis elegans*. *Development*, **122**(5): 1467–1474 (1996)
- [61] E. Munro, J. Nance, and J. R. Priess. Cortical Flows Powered by Asymmetrical Contraction Transport PAR Proteins to Establish and Maintain Anterior-Posterior Polarity in the Early *C. elegans* Embryo. *Dev. Cell*, **7**(3): 413 – 424 (2004)
- [62] B. Etemad-Moghadam, S. Guo, and K. J. Kemphues. Asymmetrically distributed par-3 protein contributes to cell polarity and spindle alignment in early *c. elegans* embryos. *Cell*, **83**(5): 743 – 752 (1995)
- [63] E. Knust. Regulation of epithelial cell shape and polarity by cell-cell adhesion. *Mol. Membr. Biol.*, **19**(2): 113–120 (2002)

- [64] B. Mayer, G. Emery, D. Berdnik, F. Wirtz-Peitz, and J. A. Knoblich. Quantitative analysis of protein dynamics during asymmetric cell division. *Curr. Biol.*, **15**(20): 1847 – 1854 (2005)
- [65] V. Shepherd. The cytomatrix as a cooperative system of macromolecular and water networks. volume 75 of *Current Topics in Developmental Biology*, pages 171 – 223. Academic Press (2006)
- [66] M. Mittasch, P. Gross, M. Nestler, A. W. Fritsch, C. Iserman, M. Kar, M. Munder, A. Voigt, S. Alberti, S. W. Grill, and M. Kreysing. Non-invasive perturbations of intracellular flow reveal physical principles of cell organization. *Nat. Cell Biol.*, **20**(3): 344–351 (2018)
- [67] S. Ganguly, L. S. Williams, I. M. Palacios, and R. E. Goldstein. Cytoplasmic streaming in drosophila oocytes varies with kinesin activity and correlates with the microtubule cytoskeleton architecture. *Proc. Natl. Acad. Sci. U.S.A.*, **109**(38): 15109–15114 (2012)
- [68] M. Slabodnick, B. Prevo, P. Gross, and W. Sheung, J. and Marshall. Visualizing cytoplasmic flow during single-cell wound healing in *stentorcoeruleus*. *J. Vis. Exp.*, **82**: e50848 (2013)
- [69] R. E. Goldstein and J.-W. van de Meent. A physical perspective on cytoplasmic streaming. *Interface Focus*, **5**(4) (2015)
- [70] S. N. Hird and J. G. White. Cortical and cytoplasmic flow polarity in early embryonic cells of *Caenorhabditis elegans*. *J. Cell Biol.*, **121**(6): 1343–1355 (1993)
- [71] R. Niwayama, K. Shinohara, and A. Kimura. Hydrodynamic property of the cytoplasm is sufficient to mediate cytoplasmic streaming in the *Caenorhabditis elegans* embryo. *Proc. Natl. Acad. Sci. U.S.A.*, **108**(29): 11900–11905 (2011)
- [72] T. Lecuit and P.-F. Lenne. Cell surface mechanics and the control of cell shape, tissue patterns and morphogenesis. *Nat. Rev. Mol. Cell Biol.*, **8**: 633 EP – (2007)
- [73] C.-P. Heisenberg and Y. Bellaïche. Forces in Tissue Morphogenesis and Patterning. *Cell*, **153**(5): 948–962 (2013)
- [74] A. T. L. Van Lommel. *From Cells to Organs*. Springer (2004)
- [75] R. A. Foty and M. S. Steinberg. The differential adhesion hypothesis: a direct evaluation. *Dev. Biol.*, **278**(1): 255 – 263 (2005)
- [76] P. F. Machado, J. Duque, J. Étienne, A. Martinez-Arias, G. B. Blanchard, and N. Gorfinkiel. Emergent material properties of developing epithelial tissues. *BMC Biol.*, **13**(1): 98 (2015)
- [77] B. Ladoux and R.-M. Mège. Mechanobiology of collective cell behaviours. *Nat. Rev. Mol. Cell Biol.*, **18**(12): 743–757 (2017)
- [78] J. Ranft, M. Basan, J. Elgeti, J.-F. Joanny, J. Prost, and F. Jülicher. Fluidization of tissues by cell division and apoptosis. *Proc. Natl. Acad. Sci. U.S.A.*, **107**(49): 20863–20868 (2010)
- [79] R. Etournay, M. Popović, M. Merkel, A. Nandi, C. Blasse, B. Aigouy, H. Brandi, G. Myers, G. Salbreux, F. Jülicher, and S. Eaton. Interplay of cell dynamics and epithelial tension during morphogenesis of the *Drosophila* pupal wing. *eLife*, **4** (2015)
- [80] M. Popović, A. Nandi, M. Merkel, R. Etournay, S. Eaton, F. Jülicher, and G. Salbreux. Active dynamics of tissue shear flow. *New J. Phys.*, **19** (2017)
- [81] J. Zhou, H. Y. Kim, and L. A. Davidson. Actomyosin stiffens the vertebrate embryo during critical stages of elongation and neural tube closure. *Development*, **136**(4): 677–688 (2009)
- [82] F. Amat, W. Lemon, D. P. Mossing, K. McDole, Y. Wan, K. Branson, E. W. Myers, and P. J. Keller. Fast, accurate reconstruction of cell lineages from large-scale fluorescence microscopy data. *Nat. Methods*, **11**(9): 951–958 (2014)
- [83] L. Wolpert. Positional information and the spatial pattern of cellular differentiation. *J. Theoret. Biol.*, **25**(1): 1 – 47 (1969)
- [84] A. J. Koch and H. Meinhardt. Biological pattern formation: from basic mechanisms to complex structures. *Rev. Mod. Phys.*, **66**: 1481–1507 (1994)
- [85] D. J. Dickinson, W. J. Nelson, and W. I. Weis. A polarized epithelium organized by β - and α -catenin predates cadherin and metazoan origins. *Science*, **331**(6022): 1336–1339 (2011)

- [86] M. Rauzi and P.-F. Lenne. Chapter four - Cortical Forces in Cell Shape Changes and Tissue Morphogenesis. In M. Labouesse, editor, *Forces and Tension in Development*, pages 93–144. Academic Press (2011)
- [87] L. He, X. Wang, H. L. Tang, and D. J. Montell. Tissue elongation requires oscillating contractions of a basal actomyosin network. *Nat. Cell Biol.*, **12**(12): 1133–1142 (2010)
- [88] M. Behrndt, G. Salbreux, P. Campinho, R. Hauschild, F. Oswald, J. Roensch, S. W. Grill, and C.-P. Heisenberg. Forces driving epithelial spreading in zebrafish gastrulation. *Science*, **338**(6104): 257–260 (2012)
- [89] H. Morita, S. Grigolon, M. Bock, S. F. G. Krens, G. Salbreux, and C.-P. Heisenberg. The Physical Basis of Coordinated Tissue Spreading in Zebrafish Gastrulation. *Dev. Cell*, **40**(4): 354–366 (2017)
- [90] S. J. Streichan, M. F. Lefebvre, N. Noll, E. F. Wieschaus, and B. I. Shraiman. Global morphogenetic flow is accurately predicted by the spatial distribution of myosin motors. *eLife*, **7**: e27454 (2018)
- [91] E. Hannezo, J. Prost, and J.-F. Joanny. Instabilities of monolayered epithelia: Shape and structure of villi and crypts. *Phys. Rev. Lett.*, **107**: 078104 (2011)
- [92] J. D. Franke, R. A. Montague, and D. P. Kiehart. Nonmuscle myosin ii generates forces that transmit tension and drive contraction in multiple tissues during dorsal closure. *Curr. Biol.*, **15**(24): 2208–2221 (2005)
- [93] A. C. Martin, M. Kaschube, and E. F. Wieschaus. Pulsed contractions of an actin–myosin network drive apical constriction. *Nature*, **457**(7228): 495–499 (2008)
- [94] A. C. Martin, M. Gelbart, R. Fernandez-Gonzalez, M. Kaschube, and E. F. Wieschaus. Integration of contractile forces during tissue invagination. *J. Cell Biol.*, **188**(5): 735–749 (2010)
- [95] C. Bielmeier, S. Alt, V. Weichselberger, M. La Fortezza, H. Harz, F. Jülicher, G. Salbreux, and A.-K. Classen. Interface contractility between differently fated cells drives cell elimination and cyst formation. *Curr. Biol.*, **26**(5): 563–574 (2016)
- [96] M. A. Wozniak and C. S. Chen. Mechanotransduction in development: a growing role for contractility. *Nat. Rev. Mol. Cell Biol.*, **10**(1): 34–43 (2009)
- [97] T. Iskratsch, H. Wolfenson, and M. P. Sheetz. Appreciating force and shape — the rise of mechanotransduction in cell biology. *Nat. Rev. Mol. Cell Biol.*, **15**(12): 825–833 (2014)
- [98] T. Gregor, D. W. Tank, E. F. Wieschaus, and W. Bialek. Probing the limits to positional information. *Cell*, **130**(1): 153–164 (2007)
- [99] P. C. Martin, O. Parodi, and P. S. Pershan. Unified hydrodynamic theory for crystals, liquid crystals, and normal fluids. *Phys. Rev. A*, **6**: 2401–2420 (1972)
- [100] P. Chaikin and T. Lubensky. *Principles of Condensed Matter Physics*. Cambridge University Press (2000)
- [101] G. Salbreux, J. Prost, and J. F. Joanny. Hydrodynamics of cellular cortical flows and the formation of contractile rings. *Phys. Rev. Lett.*, **103**: 058102 (2009)
- [102] S. de Groot and P. Mazur. *Non-equilibrium Thermodynamics*. Dover Publications (1984)
- [103] A. Katchalsky and P. F. Curran. *Nonequilibrium Thermodynamics in Biophysics*. Harvard University Press (1965)
- [104] L. Landau and E. Lifshitz. *Statistical Physics*. Bd. 5. Elsevier Science (2013)
- [105] L. Onsager. Reciprocal relations in irreversible processes. I. *Phys. Rev.*, **37**: 405–426 (1931)
- [106] L. Onsager. Reciprocal relations in irreversible processes. II. *Phys. Rev.*, **38**: 2265–2279 (1931)
- [107] P. Curie. On symmetry in physical phenomena, symmetry of an electric field and of a magnetic field. *J. Phys.*, **3**: 401 (1894)
- [108] K. Kruse, J. F. Joanny, F. Jülicher, J. Prost, and K. Sekimoto. Generic theory of active polar gels: a paradigm for cytoskeletal dynamics. *Eur. Phys. J. E*, **16**(1): 5–16 (2005)

- [109] J. F. Joanny, F. Jülicher, K. Kruse, and J. Prost. Hydrodynamic theory for multi-component active polar gels. *New J. Phys.*, **9**(11): 422 (2007)
- [110] A. C. Callan-Jones and F. Jülicher. Hydrodynamics of active permeating gels. *New J. Phys.*, **13** (2011)
- [111] F. Jülicher. Active fluids and gels. In *New Trends in the Physics and Mechanics of Biological Systems*. Oxford University Press, Oxford (2009)
- [112] G. Salbreux and F. Jülicher. Mechanics of active surfaces. *Phys. Rev. E*, **96**: 032404 (2017)
- [113] H. Bruus. *Theoretical Microfluidics*. Oxford University Press (2008)
- [114] R. Larson and H. Brenner. *Constitutive Equations for Polymer Melts and Solutions: Butterworths Series in Chemical Engineering*. Elsevier Science (2013)
- [115] H. Berthoumieux, J.-L. Maître, C.-P. Heisenberg, E. K. Paluch, F. Jülicher, and G. Salbreux. Active elastic thin shell theory for cellular deformations. *New J. Phys.*, **16**(6): 065005 (2014)
- [116] B. He, K. Doubrovinski, O. Polyakov, and E. Wieschaus. Apical constriction drives tissue-scale hydrodynamic flow to mediate cell elongation. *Nature*, **508**(7496): 392–396 (2014)
- [117] J. S. Bois, F. Jülicher, and S. W. Grill. Pattern formation in active fluids. *Phys. Rev. Lett.*, **106**: 028103 (2011)
- [118] T. Mammoto and D. E. Ingber. Mechanical control of tissue and organ development. *Development*, **137**(9): 1407–1420 (2010)
- [119] S. Banerjee and M. C. Marchetti. Instabilities and oscillations in isotropic active gels. *Soft Matter*, **7**(2): 463–473 (2011)
- [120] K. V. Kumar, J. S. Bois, F. Jülicher, and S. W. Grill. Pulsatory patterns in active fluids. *Phys. Rev. Lett.*, **112**: 208101 (2014)
- [121] C. A. Weber, C. H. Rycroft, and L. Mahadevan. Differential activity-driven instabilities in biphasic active matter. *Phys. Rev. Lett.*, **120**: 248003 (2018)
- [122] I. M. Sehring, P. Recho, E. Denker, M. Kourakis, B. Mathiesen, E. Hannezo, B. Dong, and D. Jiang. Assembly and positioning of actomyosin rings by contractility and planar cell polarity. *eLife*, **4** (2015)
- [123] T. Moore, S. K. Wu, M. Michael, A. S. Yap, G. A. Gomez, and Z. Neufeld. Self-Organizing Actomyosin Patterns on the Cell Cortex at Epithelial Cell-Cell Junctions. *Biophys. J.*, **107**(11): 2652–2661 (2014)
- [124] E. Hannezo, B. Dong, P. Recho, J.-F. Joanny, and S. Hayashi. Cortical instability drives periodic supracellular actin pattern formation in epithelial tubes. *Proc. Natl. Acad. Sci. U.S.A.*, **112**(28): 8620–8625 (2015)
- [125] S. Banerjee, K. J. C. Utuje, and M. C. Marchetti. Propagating Stress Waves During Epithelial Expansion. *Phys. Rev. Lett.*, **114**(22) (2015)
- [126] O. L. Lewis, R. D. Guy, and J. F. Allard. Actin-Myosin Spatial Patterns from a Simplified Isotropic Viscoelastic Model. *Biophys. J.*, **107**(4): 863–870 (2014)
- [127] V. Ruprecht, S. Wieser, A. Callan-Jones, M. Smutny, H. Morita, K. Sako, V. Barone, M. Ritsch-Marte, M. Sixt, R. Voituriez, et al. Cortical contractility triggers a stochastic switch to fast amoeboid cell motility. *Cell*, **160**(4): 673–685 (2015)
- [128] E. Kreyszig. *Introduction to differential geometry and Riemannian geometry*. University of Toronto Press (1968)
- [129] R. Capovilla and J. Guven. Stresses in lipid membranes. *J. Phys. A*, **35**(30): 6233 (2002)
- [130] W. Helfrich. Elastic Properties of Lipid Bilayers: Theory and Possible Experiments. *Zeitschrift für Naturforschung C*, **28**: 693 (1973)
- [131] J. Sedzinski, M. Biro, A. Oswald, J.-Y. Tinevez, G. Salbreux, and E. Paluch. Polar actomyosin contractility destabilizes the position of the cytokinetic furrow. *Nature*, **476**(7361): 462–466 (2011)

- [132] M. Bergdorf, I. F. Sbalzarini, and P. Koumoutsakos. A Lagrangian particle method for reaction–diffusion systems on deforming surfaces. *J. Math. Biol.*, **61**(5): 649–663 (2010)
- [133] L. Rayleigh. On the instability of jets. *Proc. Lond. Math. Soc.*, **10**(1): 4–13 (1878)
- [134] A. Erzberger. *Actomyosin mechanics at the cell level*. Dissertation, Technischen Universität Dresden (2015)
- [135] M. Cross and H. Greenside. *Pattern Formation and Dynamics in Nonequilibrium Systems*. Cambridge University Press, Cambridge (2009)
- [136] R. Ramaswamy and F. Jülicher. Activity induces traveling waves, vortices and spatiotemporal chaos in a model actomyosin layer. *Scientific Reports*, **6** (2016)
- [137] J. Sethian. *Level Set Methods and Fast Marching Methods: Evolving Interfaces in Computational Geometry, Fluid Mechanics, Computer Vision, and Materials Science*. Cambridge University Press (1999)
- [138] M. Bertalmío, L.-T. Cheng, S. Osher, and G. Sapiro. Variational Problems and Partial Differential Equations on Implicit Surfaces. *J. Comp. Phys.*, **174**(2): 759–780 (2001)
- [139] D. Adalsteinsson and J. A. Sethian. The Fast Construction of Extension Velocities in Level Set Methods. *Journal of Computational Physics*, **148**(1): 2–22 (1999)
- [140] R. Bar-Ziv and E. Moses. Instability and "pearling" states produced in tubular membranes by competition of curvature and tension. *Phys. Rev. Lett.*, **73**: 1392–1395 (1994)
- [141] P. Nelson, T. Powers, and U. Seifert. Dynamical theory of the pearling instability in cylindrical vesicles. *Phys. Rev. Lett.*, **74**: 3384–3387 (1995)
- [142] R. E. Goldstein, P. Nelson, T. Powers, and U. Seifert. Front propagation in the pearling instability of tubular vesicles. *J. Phys. II*, **6**(5): 767–796 (1996)
- [143] D. Sweeton, S. Parks, M. Costa, and E. Wieschaus. Gastrulation in drosophila: the formation of the ventral furrow and posterior midgut invaginations. *Development*, **112**(3): 775–789 (1991)
- [144] A. C. Martin, M. Gelbart, R. Fernandez-Gonzalez, M. Kaschube, and E. F. Wieschaus. Integration of contractile forces during tissue invagination. *The Journal of Cell Biology*, **188**(5): 735–749 (2010)
- [145] F. C. Keber, E. Loiseau, T. Sanchez, S. J. DeCamp, L. Giomi, M. J. Bowick, M. C. Marchetti, Z. Dogic, and A. R. Bausch. Topology and dynamics of active nematic vesicles. *Science*, **345**(6201): 1135–1139 (2014)
- [146] F. Alaimo, C. Köhler, and A. Voigt. Curvature controlled defect dynamics in topological active nematics. *Scientific Reports*, **7**(1): 5211 (2017)
- [147] J. A. Gaunt. The triplets of helium. *Philos. Trans. Royal Soc. A*, **228**: 151–196 (1929)
- [148] T. J. Pedley. Spherical squirmers: models for swimming micro-organisms. *IMA J. Appl. Math.*, **81**(3): 488–521 (2016)
- [149] A. Zöttl and H. Stark. Emergent behavior in active colloids. *J. Phys. Condens. Matter*, **28**(25) (2016)
- [150] A. A. Evans, T. Ishikawa, T. Yamaguchi, and E. Lauga. Orientational order in concentrated suspensions of spherical microswimmers. *Phys. Fluids*, **23**(11): 111702 (2011)
- [151] E. Lauga and T. R. Powers. The hydrodynamics of swimming microorganisms. *Rep. Prog. Phys.*, **72**(9): 096601 (2009)
- [152] J. D. Crawford. Introduction to bifurcation theory. *Rev. Mod. Phys.*, **63**: 991–1037 (1991)
- [153] S. Strogatz. *Nonlinear Dynamics and Chaos: With Applications to Physics, Biology, Chemistry, and Engineering*. Avalon Publishing (2014)
- [154] S. W. Grill and A. A. Hyman. Spindle Positioning by Cortical Pulling Forces. *Dev. Cell*, **8**(4): 461 – 465 (2005)
- [155] M. Schmitt and H. Stark. Marangoni flow at droplet interfaces: Three-dimensional solution and applications. *Phys. Fluids*, **28**(1): 012106 (2016)

- [156] C. A. Whitfield and R. J. Hawkins. Instabilities, motion and deformation of active fluid droplets. *New J. Phys.*, **18**(12): 123016 (2016)
- [157] Z. Izri, M. N. van der Linden, S. Michelin, and O. Dauchot. Self-propulsion of pure water droplets by spontaneous marangoni-stress-driven motion. *Phys. Rev. Lett.*, **113**: 248302 (2014)
- [158] V. D. Sandberg. Tensor spherical harmonics on S^2 and S^3 as eigenvalue problems. *J. Math. Phys.*, **19**(12): 2441–2446 (1978)
- [159] K. Kruse, J. F. Joanny, F. Jülicher, J. Prost, and K. Sekimoto. Asters, vortices, and rotating spirals in active gels of polar filaments. *Phys. Rev. Lett.*, **92**: 078101 (2004)
- [160] L. Giomi. Geometry and topology of turbulence in active nematics. *Phys. Rev. X*, **5**: 031003 (2015)
- [161] T. Frankel. *The Geometry of Physics: An Introduction*. Cambridge University Press (2011)
- [162] G. Arfken and H. Weber. *Mathematical Methods for Physicists*. Elsevier Ltd. (2005)
- [163] R. Seyboldt and F. Jülicher. Role of hydrodynamic flows in chemically driven droplet division. (preprint)
- [164] R. G. Barrera, G. Estevez, and J. Giraldo. Vector spherical harmonics and their application to magnetostatics. *Eur. J. Phys.*, **6**(4): 287 (1985)
- [165] A. Love. *A Treatise on the Mathematical Theory of Elasticity*. Cambridge University Press (2013)
- [166] J. Happel and H. Brenner. *Low Reynolds Number Hydrodynamics*. Nordhoff International Publishing (1973)
- [167] M. Rahimi, A. DeSimone, and M. Arroyo. Curved fluid membranes behave laterally as effective viscoelastic media. *Soft Matter*, **9**: 11033–11045 (2013)
- [168] C. Pozrikidis. *Numerical Computation in Science and Engineering*. Oxford University Press (1998)
- [169] J. G. Oldroyd. On the formulation of rheological equations of state. *Proc. Roy. Soc. A*, **200**(1063): 523–541 (1950)
- [170] N. Sneeuw. Global spherical harmonic analysis by least-squares and numerical quadrature methods in historical perspective. *Geophys. J. Int.*, **118**(3): 707–716 (1994)
- [171] Matlab 2015b. The MathWorks, Natick, MA, USA

Versicherung

Hiermit versichere ich, dass ich die vorliegende Arbeit ohne unzulässige Hilfe Dritter und ohne Benutzung anderer als der angegebenen Hilfsmittel angefertigt habe; die aus fremden Quellen direkt oder indirekt übernommenen Gedanken sind als solche kenntlich gemacht. Die Arbeit wurde bisher weder im Inland noch im Ausland in gleicher oder ähnlicher Form einer anderen Prüfungsbehörde vorgelegt. Die Arbeit wurde in Dresden am Max-Planck-Institut für Physik komplexer Systeme unter der Betreuung von Prof. Frank Jülicher und am Max-Planck-Institut für molekulare Zellbiologie und Genetik unter der Betreuung von Prof. Ivo F. Sbalzarini angefertigt.

Alexander Mietke
Dresden, August 2018